



The University of  
**Nottingham**

UNITED KINGDOM · CHINA · MALAYSIA

# **A model for the role of debris ejection in development of fretting wear**

**TENGTUO ZHU, BEng**

**Thesis submitted to The University of Nottingham**

**for the degree of Doctor of Philosophy**

**Faculty of Engineering**



## Abstract

The paper 'The third-body approach: a mechanical view of wear' by Maurice Godet (Wear, 100 (1984), pp 437–452) was perhaps the first to articulate clearly the key role of the rate of debris expulsion from a fretting contact in controlling the overall rate of wear; the framework of the third body approach was further developed by the concept of tribology circuit by Berthier. Whilst subsequent research over the past four decades has acknowledged this, the role of debris ejection in fretting has been generally addressed qualitatively rather than quantitatively. Moreover, calculation of wear rates in fretting have continued to employ Archard wear equation (or approaches directly derived from it), despite this approach assuming that the rate of wear is controlled by the rate of generation of wear debris (as opposed to the rate of its ejection from the contact).

In this thesis, it is proposed that there are a number of processes which need to take place for fretting wear to proceed. These can be grouped into (i) debris formation within the contact and (ii) debris ejection from the contact. Moreover, it is proposed for the first time that wear can only proceed at the rate of the slower of these two processes – that process being termed the *rate-determining process*. Furthermore, a physically based relationship between the debris-expulsion limited wear rate and the contact size is proposed and demonstrated, namely that the instantaneous rate of wear is inversely proportional to a characteristic dimension of the wear scar. This is a key finding of this thesis which has significant implications for all fretting research and development, whether addressing laboratory testing or service environments.

A key issue resulting from this is that it is recognised that during fretting of contacts with non-conforming geometries (such as cylinder-on-flat or sphere-on-flat) – either in service or in a test environment, the wear scar size increases as wear proceeds, and thus the instantaneous rate of wear decreases. It has been shown in this work for the

first time that the amount of wear in a non-conforming contact geometry can be well approximated from the lateral size of the scar through a simple geometric relationship. This then laid the foundation for the derivation of wear equations for three commonly employed non-conforming pair specimen geometries (cylinder-on-flat, sphere-on-flat and crossed-cylinders); those wear equations all take the form  $V_w = KR^{n-1}E_d^n$  ( $V_w$  is the wear scar volume,  $R$  is the radius of the non-plane specimen(s) in the pair and  $E_d$  is the frictional energy dissipated) where  $n$  varies between 0.67 and 0.8 depending upon the geometry and assumptions made regarding the governing equation. One key assumption is that debris is ejected from the contact only in the direction of the fretting motion, i.e. that side leakage can be ignored. Consideration of experimental data related to cylinder-on-flat contacts (generated within this work) and sphere-on-flat contacts (from the literature) indicated that the validity of this assumption was strongest when the length of the contact was large compared to its width in the fretting direction.

The long-debated role of slip amplitude in fretting has been investigated in terms of its role in debris ejection. Tests were conducted across a range of test durations up to  $10^7$  cycles (such extended test durations are rarely seen in literature), and these extended tests provide new insight into the effects of slip amplitude in the evolution of wear scar. There were two main observations: (i) the change of the wear scar profile (U-shaped or W-shaped) is associated with both the slip amplitude and test duration; (ii) the incubation period can be significantly extended when the slip amplitude is small, suggesting the necessity of long duration to fully reveal the evolution of wear.

## Publications

T. Zhu, P.H. Shipway, W. Sun, *The dependence of wear rate on wear scar size in fretting; the role of debris (third body) expulsion from the contact*, *Wear*, Volumes 440–441, 2019, 203081, ISSN 0043-1648.  
<https://doi.org/10.1016/j.wear.2019.203081>.

T. Zhu, P.H. Shipway, *Contact size and debris ejection in fretting: The inappropriate use of Archard-type analysis of wear data and the development of alternative wear equations for commonly employed non-conforming specimen pair geometries*, *Wear*, Volumes 474–475, 2021, 203710, ISSN 0043-1648.  
<https://doi.org/10.1016/j.wear.2021.203710>.

T. Zhu, P. H. Shipway, *Slip amplitude in fretting: its role in wear rates, debris behaviour and evolution of wear scar shape in tests with an extended number of cycles (In preparation)*

## Acknowledgements

My PhD journey has been unusually long, and it is gratifying to see it through after many difficult times. I want to express my deepest gratitude to my supervisor, Prof. Philip Shipway, without whom completing this thesis would have been impossible. It is a pleasure and my privilege to have had the opportunity to work with Prof. Shipway and learn from him; his tremendous guidance and training was invaluable and helped me become a better researcher. I must thank him for his encouragement and dedication during the rough times. The kindness and patience I received from Prof. Shipway far exceeded the requirement for a supervisor, and I cherish the whole experience. I am also grateful to Prof. Wei Sun for his advice and support at the early stage of my PhD.

I appreciate the friendship I share with my friend and colleague, Adam Kirk. It is a most pleasant surprise to find someone with whom I have so much in common regarding my research area and personal interests, and I will miss our conversations on all kinds of topics. I would also like to thank my colleagues at the ITRC building for creating a supportive and collaborative environment allowing the exchange of ideas. A special thank you goes to my closest friends, Xin Sui, Zi Wang and Wenxuan Peng; I was very fortunate to connect with these remarkable people. Their love, support, laughter and delicious meals have made the journey splendid and unforgettable.

I am grateful to the Senior Research Operations Officer, Donna Astill-Shipman, for assistance in various issues along the way; she has been of more help than she will realise. I would also like to thank the technical team at the University of Nottingham, particularly Tom Buss and Andrew Plummer, for providing training and assistance in conducting experiments, which was essential to this thesis. The financial support provided by the University of Nottingham's OPGR FEE Scholarship is also much appreciated.

---

Most importantly, I must thank my parents, Yuena Zhu and Yingfang Sun, for their unconditional love and endless emotional and financial support throughout my PhD. This thesis is for them.

# Contents

ABSTRACT .....	I
PUBLICATIONS .....	III
ACKNOWLEDGEMENTS.....	IV
CONTENTS.....	VI
NOMENCLATURE.....	IX
ABBREVIATIONS.....	XI
<b>CHAPTER 1 INTRODUCTION .....</b>	<b>1</b>
<b>CHAPTER 2 LITERATURE REVIEW.....</b>	<b>6</b>
2.1 INTRODUCTION.....	6
2.1.1 <i>Wear in sliding and fretting</i> .....	6
2.1.2 <i>The concept of wear rate</i> .....	10
2.2 ANALYSIS OF FRETTING CONTACT.....	16
2.2.1 <i>Hertzian contact mechanics</i> .....	16
2.2.2 <i>Slip regimes</i> .....	20
2.2.3 <i>Fretting loops and the coefficient of friction</i> .....	25
2.3 EVOLUTION OF WEAR IN FRETTING CONTACT .....	31
2.3.1 <i>Fretting stages</i> .....	31
2.3.2 <i>Tribologically transformed structure in fretting</i> .....	35
2.3.3 <i>Energy threshold of the fretting process</i> .....	37
2.3.4 <i>The critical role of the third body in fretting</i> .....	39
2.4 THE ROLE OF CONTACT GEOMETRY IN FRETTING .....	43
2.4.1 <i>Common contact geometries in fretting</i> .....	43
2.4.2 <i>Changing views about the role of contact geometry in fretting</i> .....	44
2.4.3 <i>The effect of contact size on oxygen supply</i> .....	47
2.4.4 <i>The effect of contact size on debris ejection</i> .....	49
2.5 THE ROLE OF SLIP AMPLITUDE IN FRETTING .....	50
2.5.1 <i>The effect of slip amplitude on debris formation</i> .....	51
2.5.2 <i>The effect of slip amplitude on debris ejection</i> .....	53
2.5.3 <i>The effect of slip amplitude on wear rate</i> .....	55
2.6 SUMMARY.....	58
<b>CHAPTER 3 EXPERIMENTAL METHODOLOGY.....</b>	<b>60</b>
3.1 MATERIALS AND SPECIMENS .....	60
3.2 EXPERIMENTAL CONFIGURATION .....	61
3.3 EXPERIMENTAL PROCEDURE .....	65
3.4 EXPERIMENTAL DATA PROCESSING .....	67
3.4.1 <i>Description of fretting loop</i> .....	68
3.4.2 <i>Dissipated energy</i> .....	69
3.4.3 <i>Slip amplitude</i> .....	69
3.4.4 <i>Coefficient of friction</i> .....	71
3.5 WEAR DAMAGE CHARACTERISATION .....	72
3.5.1 <i>Surface topography</i> .....	72
3.5.2 <i>Estimation of wear volume and wear scar width</i> .....	73
3.5.3 <i>Precision and accuracy of measurements</i> .....	74
3.5.4 <i>Nature of wear scar and debris</i> .....	77
<b>CHAPTER 4 THE DEPENDENCE OF WEAR RATE ON WEAR SCAR SIZE IN FRETTING.....</b>	<b>78</b>
4.1 INTRODUCTION AND CHAPTER OUTLINE .....	78
4.2 EXPERIMENTAL RESULTS .....	83

## Contents

---

4.3	DEVELOPMENT OF THE MODEL .....	88
4.3.1	<i>Link between wear scar width and wear volume in a cylinder-on-flat contact.</i> .....	88
4.3.2	<i>Modelling the effect of wear scar size on the wear rate</i> .....	92
4.4	DISCUSSION .....	95
4.4.1	<i>Wear scar characteristics</i> .....	95
4.4.2	<i>Wear rate dependence on contact width in fretting</i> .....	97
4.4.3	<i>Consideration of debris expulsion effects in research programmes</i> .....	98
4.5	CONCLUSIONS .....	99
<b>CHAPTER 5 THE DEVELOPMENT OF ALTERNATIVE WEAR EQUATIONS FOR COMMONLY EMPLOYED NON-CONFORMING CONTACT .....</b>		<b>101</b>
5.1	INTRODUCTION AND CHAPTER OUTLINE .....	101
5.2	DERIVATION OF A WEAR EQUATION FOR CYLINDER-ON-FLAT FRETTING CONFIGURATION .....	108
5.2.1	<i>Errors associated with the approximation</i> .....	112
5.2.2	<i>Experimental verification of the proposed relationship</i> .....	114
5.3	DERIVATION OF WEAR EQUATIONS FOR SPHERE-ON-FLAT AND CROSSED-CYLINDERS FRETTING CONFIGURATIONS 115	
5.3.1	<i>Characteristic wear scar width for sphere-on-flat and crossed-cylinders fretting configurations</i> .....	115
5.3.2	<i>Wear equations based upon a characteristic linear dimension of the wear scar for the sphere-on-flat and crossed-cylinders contact configurations</i> .....	118
5.3.3	<i>Wear equations based upon a characteristic area of the wear scar for the sphere-on-flat contact configuration</i> .....	120
5.3.4	<i>Errors associated with the approximation</i> .....	122
5.3.5	<i>Experimental verification of the proposed relationships for wear scars with equiaxed shapes</i> 125	
5.4	DISCUSSION .....	127
5.4.1	<i>Testing of the wear equations against experimental data</i> .....	127
5.4.2	<i>Dependence of wear on contact geometry and energy dissipated</i> .....	132
5.5	CONCLUSIONS .....	139
<b>CHAPTER 6 THE DEPENDENCE OF WEAR RATE ON SLIP AMPLITUDE .....</b>		<b>141</b>
6.1	INTRODUCTION AND CHAPTER OUTLINE .....	141
6.2	EXPERIMENTAL RESULTS .....	145
6.3	DISCUSSION .....	157
6.3.1	<i>Wear scar characteristics</i> .....	157
6.3.2	<i>Wear rate dependence on slip amplitude in fretting</i> .....	161
6.4	CONCLUSIONS .....	164
<b>CHAPTER 7 CONCLUSIONS .....</b>		<b>165</b>
<b>CHAPTER 8 FUTURE WORK .....</b>		<b>168</b>
<b>BIBLIOGRAPHY .....</b>		<b>171</b>
<b>APPENDIX A .....</b>		<b>178</b>
	DERIVATION OF THE FUNCTION OF DISSIPATED ENERGY IN TERMS OF WEAR SCAR WIDTH.....	178
<b>APPENDIX B.....</b>		<b>182</b>
	DETAILS OF THE METHODOLOGY FOR THE DERIVATION OF THE WEAR EQUATIONS FOR ALL THREE CONTACT CONFIGURATIONS.....	182
B1	CYLINDER-ON-FLAT CONFIGURATION ASSUMING EITHER WEAR SCAR WIDTH OR WEAR SCAR AREA DEPENDENCE OF INSTANTANEOUS WEAR RATE.....	182
B2	SPHERE-ON-FLAT CONFIGURATION ASSUMING WEAR SCAR WIDTH DEPENDENCE OF INSTANTANEOUS WEAR RATE	186
B3	SPHERE-ON-FLAT CONFIGURATION ASSUMING WEAR SCAR AREA DEPENDENCE OF INSTANTANEOUS WEAR RATE	189

B4	CROSSED-CYLINDER CONFIGURATION ASSUMING WEAR SCAR WIDTH DEPENDENCE OF INSTANTANEOUS WEAR RATE	192
B5	THE BETA FUNCTION, GAMMA FUNCTION AND HYPERGEOMETRIC FUNCTION .....	199
<b>APPENDIX C.....</b>		<b>206</b>
	DIMENSIONAL ANALYSIS OF THE FORM OF WEAR EQUATIONS .....	206
C1	LINEAR BASIS OF THE GOVERNING EQUATION .....	208
C2	AREA BASIS OF THE GOVERNING EQUATION FOR CF CONTACT .....	210
C3	AREA BASIS OF THE GOVERNING EQUATION FOR SF CONTACT .....	211
<b>APPENDIX D .....</b>		<b>213</b>
	DETAIL DRAWINGS OF SPECIMENS .....	213

## Nomenclature

Symbol	Quantity	Typical unit
$P$	applied normal load	N
$Q$	cyclic tangential force	N
$Q^*$	amplitude of cyclic tangential force	N
$\Delta$	applied displacement	$\mu\text{m}$
$\Delta^*$	Displacement amplitude	$\mu\text{m}$
$\delta$	actual slip	$\mu\text{m}$
$\delta^*$	slip amplitude	$\mu\text{m}$
$S$	stiffness of system	$\text{N}\cdot\mu\text{m}^{-1}$
$\mu$	coefficient of friction	
$\mu_e$	energy coefficient of friction	
$R$	Cylindrical specimen radius	mm
$N$	test duration	cycle
$f_{\text{Hz}}$	frequency of fretting motion	Hz
$t$	time	s
$T$	temperature	$^{\circ}\text{C}$
$V^+$	volume of the transferred material	$\text{mm}^3$
$V_F^+$	volume of the transferred material on flat specimen	$\text{mm}^3$
$V_R^+$	volume of the transferred material on cylindrical specimen	$\text{mm}^3$
$V^-$	volume of the lost material	$\text{mm}^3$
$V_F^-$	volume of the lost material on flat specimen	$\text{mm}^3$
$V_R^-$	volume of the lost material on cylindrical specimen	$\text{mm}^3$
$v_w$	normalised $V_w$	

$v_w'$	normalised $V_w'$	
$E_d$	dissipated energy	kJ
$E_d'$	Approximated dissipated energy	kJ
$E_{th}$	energy threshold	kJ
$E_{dat}$	energy dissipated above threshold	kJ
$E_{dat}'$	approximated energy dissipated above threshold	kJ
$e_{dat}$	normalised $E_{dat}$	
$e_{dat}'$	normalised $E_{dat}'$	
$D$	total sliding distance	$\mu\text{m}$
$H$	hardness	$\text{kgf}\cdot\text{mm}^{-2}$
$K_A$	Archard wear coefficient	
$k_A$	specific wear rate	$\text{mm}^3\cdot\text{m}^{-1}\cdot\text{N}^{-1}$
$k_e$	energy wear rate	$\text{mm}^3\cdot\text{kJ}^{-1}$
$k$	a parameter describing the instantaneous wear rate	$\text{mm}^4\cdot\text{kJ}^{-1}$
$\theta$	wear scar angle	rad
$x$	wear scar width for CF configuration	mm
$r$	radius of wear scar for SF configuration, being defined as the half of the characteristic wear scar width	mm
$w$	maximum scar width for CC configuration, being defined as the characteristic wear scar width	mm
$L$	wear scar length	mm
$A$	area of the projection of wear scar	$\text{mm}^2$
$R^2$	coefficient of determination	

---

## Abbreviations

---

ASTM	American Society of Testing Materials
BS	British Standard
BSE	back-scattered electron
CC	crossed-cylinders
CF	cylinder-on-flat
CoF	coefficient of friction
ECoF	energy coefficient of friction
EMV	electromagnetic vibrator
FE	finite element
GICoF	geometry independent coefficient of friction
IMS	industrial methylated spirit
LSMB	lower specimen mounting block
LP	low pressure
RDP	rate-determining process
RSD	relative standard deviation
SE	secondary electron
SEM	scanning electron microscopy
SF	sphere-on-flat
TDMS	technical data management streaming
TTS	tribologically transformed structure
USMB	upper specimen mounting block

---



# Chapter 1 Introduction

When two solid bodies are brought into contact and slide over each other, wear may occur on one or both of the surfaces. This phenomenon of material degradation is commonly known as *sliding wear*. The term *fretting* is used to describe small amplitude oscillatory movement between surfaces in contact with each other [1], and as such, any loss of surface material associated with fretting is called *fretting wear*. Fretting occurs in a wide range of service environments where mechanical joints or contacts between components exist, and where the loads on the component results in very small amounts of relative displacement between the two components in contact. The forces which result in fretting in the contact can be excited by a range of system drivers, such as rotation or fluid flow. Examples of fretting in contacts include heat-exchanger bundles in pressurised water reactors, couplings in pumps, press-fits between wheels and axles and splines in aeroengines. Fretting results in damage in terms of fatigue cracking and wear (materials removal), with these two modes of damage being interdependent. Fretting damage therefore results in loss of function; this results in increased service costs due to the need for inspection and repair or replacement, and may lead to catastrophic failure of structures with the hazards associated with that (loss of revenue, environmental damage, loss of life).

This thesis will focus on fretting wear and will not address fretting fatigue. Fretting wear has been considered as a subset of reciprocal sliding wear in the past since the nature of fretting wear is defined by its small scale of displacement amplitude (typically of tens of micrometres [2-4]). However, there are several key differences in terms of the wear mechanisms and the resultant rate of wear which distinguish fretting wear from reciprocating sliding wear or other forms of wear. These differences all originate from a key feature of fretting wear which is that a significant portion of the contact on both of the bodies remains covered (i.e. never out of contact) during the fretting process. This feature resulted in fretting contacts often being described as *closed contacts*.

Sliding wear is the result of the intentional relative movement between surfaces, whilst fretting wear emerges at the place where contacts are designed to be fixed to each other but receives an oscillating motion passively, which is often induced by system vibrations. Damage from fretting can be found in a variety of industries where mechanical joints are subjected to cyclical loading, in particular in the aerospace, power generation and automotive industries [3, 5-7]. Given the nature of the contacts, the fretting motion can also result in damage in the form of fretting fatigue alongside that of fretting wear – and indeed, the development of fretting wear is a significant influence on the development of such fatigue damage. One particular example of fretting damage occurs in the main-shaft spline coupling of an aeroengine, and as engines are developed, the splines typically experience more arduous operating conditions which has necessitated the development of new materials. For example, in the current Rolls-Royce plc Trent series, the torque density carried by the LP shaft is twice that of the previous generation of the aero-engine with this being achieved thanks to the development of new steels, along with the optimised design of the spline profile [8]. The manufacture of the steel (known as BS S132, which is the material of interest for this thesis) involves a process of a triple vacuum melting to improve its purity (reduced inclusion content) and, therefore, its performance against fatigue under conditions of higher bulk and contact stresses [8].

The damage caused by fretting wear can result in the loss of surface material and the loosening of joints, leading to vibration at a greater scale and, as a result, a faster rate of surface degradation. On the other hand, the wear debris in fretting take the form of oxide for metals that have a larger volume than the metals from which they are formed, which may cause seizure of the structure. Whether an increased clearance or seizure occurs is dependent upon the degree of entrapment of debris within the contact. In addition (and particularly when rates of surface degradation are low), fretting can initiate premature fatigue cracks that can lead to the reduction of fatigue strength and the

## Introduction

---

limited life of components, sometimes even catastrophic structure failure [9] (the fatigue failure associated with fretting is known as *fretting fatigue*). However, the scale of the displacement amplitude is so small during the fretting process that the relative motion is difficult to observe, resulting in damage being detected only after a long period of operation.

It was Eden et al. in 1911 [10] who conducted perhaps the first case of fretting wear study (although it was not described as fretting), which was then called *fretting corrosion* as initially suggested by Tomlinson [11] due to the presence of reddish iron oxide. This early description highlights the importance of oxidation in fretting of metals; indeed, following fretting studies have demonstrated that both the mechanical and chemical process are essential to generate wear debris, and that in fact, debris formed after the initial stage are predominately oxide [2]. The complex tribo-chemical nature of fretting is perhaps the reason why that, even after more than a century of research work, a coherent and all-encompassing explanation for fretting wear is still to be established. Fretting wear is sensitive to a large number of variables affecting both the mechanical and chemical aspects of the process [12]. It was suggested by Dombromirski that fretting process may be influenced by more than 50 parameters [13], with perhaps the normal load and displacement amplitude being the most important mechanical variables. Furthermore, it was shown that protective methods (such as coatings, lubrications and change of design etc.) may result in diverse (sometimes even negative) effects on the contacting surfaces in fretting depending upon the conditions [3, 14]. The complexity of nature of fretting process is also reflected by the diversity of predictive models. As outlined by Meng and Ludema [15], whilst numerous models of wear have been proposed throughout the history of wear study, very few of them can be considered robust enough to predict wear because of the wide variety of test configurations and the complexity of the process itself. Hence, a thorough understanding of both the mechanical and chemical nature of the contact (and their

interrelated influences on each other) is critically important in order to facilitate the development of wear models and predict modes of damage.

There are two widely accepted frameworks to prompt the understanding of the fretting process: (i) the Archard wear model [16] along with the energy-wear formulation derived from it [17, 18] (grouped together and termed the Archard-type approach); (ii) the third body approach introduced by Godet [19]. The Archard wear model was initially developed for sliding wear but was nevertheless adopted widely in fretting wear studies. The Archard wear model is mainly used for quantitative analysis when determining a single parameter to characterise the development of wear, i.e. the wear rate, offering a common ground for comparison of experimental results derived under different test conditions. The third body approach, on the other hand, articulates the key role of debris behaviour within the fretting contact due to its closed nature (i.e. the transport of oxygen into the contact to form debris, debris formation, and the transport of debris out of the contact, debris ejection), prompting certain subsequent fretting studies to focus on the investigation of the different effects of variables on the competing process of the formation and ejection of wear debris. There are limitations for both frameworks: the derivation of the wear rate via the Archard wear model usually neglects the effect of debris ejection from the contact, whilst the use of the third body approach is mainly addressed phenomenologically rather than quantitatively; even when quantitative analysis is involved for a problem under the framework of the third body approach, the core of the modelling is still generally based upon the Archard wear model.

There has been some significant progress in understanding the role of debris ejection in fretting contacts with the third body approach being central to these studies. Recent investigations conducted at the University of Nottingham [20-24] focus on examining how different parameters, such as the contact geometry, slip amplitude, temperature and frequency, can influence the transport of debris out of the fretting contact. As a heritage from the previous work at the University of Nottingham, concepts from the third

## **Introduction**

---

body approach will be a focus of this thesis as the current study seeks to develop a model to determine the wear rate (in place of the Archard-type approach) in fretting with the emphasis of the role of debris ejection; the inappropriate use of the Archard-type wear model in fretting will also be discussed. The development of the new model was based on the experimental investigation into the fretting wear behaviour of steel specimen pairs in cylinder-on-flat configuration with different contact geometries over a range of displacement amplitudes and test durations.

## Chapter 2 Literature review

### 2.1 Introduction

#### 2.1.1 Wear in sliding and fretting

Fretting wear is intrinsically related to sliding wear. It is well known that for both sliding wear and fretting wear, it is important to consider both mechanical and chemical process during the development of wear. The mechanical damage to the materials is mainly in the form of fracture, fatigue and particle detachment due to the plastic deformation, and the chemical aspect of the process involves oxidation of the surfaces leading to the generation of reaction products, often influencing the subsequent rate of degradation. Moreover, the chemical and mechanical aspects of the process can exert influences on each other resulting in complex interactions between them; these can be modified further by thermal effects and, more importantly, may even vary with time with the development of the worn contact.

Whilst different definitions of fretting wear have been suggested throughout the history of fretting research, it is, in a simplistic sense, thought of as a branch of reciprocating sliding wear where the amplitude of the motion is relatively small. The similarities observed between fretting wear and sliding wear, together with the fact that sliding wear is usually treated as a more general phenomenon, have resulted in concepts and methods in the analysis of sliding wear being employed in the study of fretting wear. For example, perhaps one of the most fundamental concepts in understanding sliding wear is the Archard wear equation as presented by Archard in 1953 [16], which has been widely employed in the study of wear due to its virtue of simplicity and effectiveness. The starting point of the Archard wear equation is the concept of *true contact area*, which states that the contact between two bodies occurs only over the true contact area instead of the apparent contact area. Archard [25] explained later that

the true contact area is equal to the sum of micro-contacts, which are produced by the mechanical deformation of individual asperities induced by the high local pressure under the applied load. As the contacting surfaces slide over each other, the load carried by individual asperities causes the continuous destruction and formation of micro-contacts and gives rise to detachment of material fragment from the surfaces. With the help of several assumptions, the Archard wear equation links the volume of wear with the normal load, the sliding distance and the hardness of the softer body in the contact pair in the simple linear relationship as follows:

$$V_w = \frac{K_A PD}{H} = k_A PD \quad (2.1)$$

where  $V_w$  is the amount of wear (wear volume);  $P$  is the normal load carried by the contact;  $D$  is the sliding distance;  $H$  is the hardness of the softer of the two contacting surfaces;  $K_A$  is the dimensionless constant commonly known as the *wear coefficient*, which allows the comparison of the wear behaviours across different systems. However, perhaps a quantity defined as  $\frac{K_A}{H}$  (termed as the *specific wear rate*, with the symbol of  $k_A$ ) is more helpful than the dimensionless wear coefficient ( $K_A$ ) and is thus more widely employed for engineering applications. The dimensional specific wear rate ( $k_A$ ) is presented as the wear volume per unit sliding distance per unit of normal force borne across the contact (with typical units of  $\text{mm}^3 \cdot \text{m}^{-1} \cdot \text{N}^{-1}$ ).

The migration of the Archard wear equation from sliding wear to fretting implies that, similar to sliding wear, the degree of damage caused by wear in fretting is expected to be only proportional to the normal load and the sliding distance regardless of other parameters, such as the contact size, displacement amplitude etc. Other concepts such as *mild wear* and *severe wear* as identified by Archard and Hirst [26] for sliding wear have also been used to explain different stages of fretting (as will be described in Section 2.3.1).

With the reduction of the amplitude of the sliding motion, the surfaces in contact can experience a transition from reciprocating sliding wear to fretting wear (in gross slip regime), although the displacement which marks the transition varies widely between different researchers [3, 27, 28]. Vingsbo and Söderberg [4] reviewed a large body of literature concerning how contact conditions change with the displacement amplitude, and recognised that it is difficult to group experimental data from different authors derived under different conditions, quoting [4]: “...Therefore literature data can be incomplete and difficult to interpret, and often only orders of magnitude are relevant...”. Nevertheless, it was suggested that the transition from reciprocating sliding wear to fretting wear may occur between amplitudes of 150-300  $\mu\text{m}$ ; such a transition is illustrated in Figure 2.1 showing the effect of the displacement amplitude on the rate of damage (here the rate of damage is characterised by the specific wear rate,  $k_A$ ).

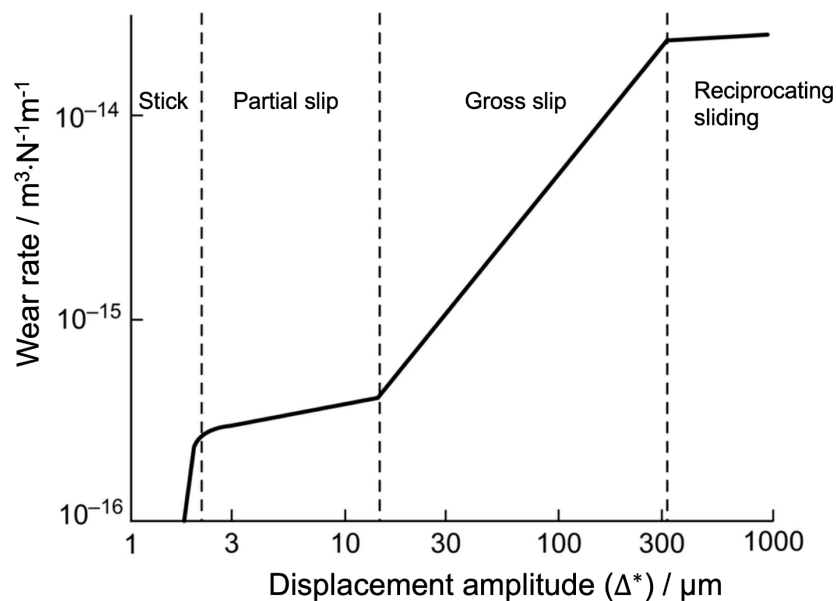


**Figure 2.1: Illustration of the change of specific wear rate with the increase of the displacement amplitude in fretting (from [29] after [4]).**

As can be seen, it is proposed that the specific wear rate is independent of the displacement amplitude in reciprocating sliding wear as predicted by the Archard wear equation. However, Figure 2.1 also indicates that, in gross sliding fretting, the wear rate increased by approximately two orders of magnitude as the displacement amplitude

increases from about 30  $\mu\text{m}$  to 300  $\mu\text{m}$  before entering the regime of reciprocating sliding wear. Although all the numbers in Figure 2.1 are not exact values and they are presented as the scale of change only; the observed variation of the wear rate with the displacement amplitude in fretting wear implies that fretting is perhaps very different from sliding wear, despite the similarities with each other. Perhaps, rather than treating fretting wear as reciprocating sliding wear with small displacement amplitude, it is recognised that there are fundamental differences between these two modes of wear, and hence, simple deployment of the concepts and methods from the analysis of sliding wear may not be helpful in developing understanding of fretting wear. Note that stick, partial slip regime and gross slip regime are different slip regimes that may occur in fretting contacts, and these will be described in detail in Section 2.2.2.

In both sliding wear and fretting wear, the interactions between the mechanical and chemical process can cause the following processes to occur: (i) mechanical deformation at asperity level; (ii) debris formation within the area experiencing the mechanical deformation, depending on chemical reactions with oxygen, which requires the transport of oxygen from the environment to the place where reactions occur; (iii) debris ejection out of the contact to allow further wear take place. However, the closed nature of the contact caused by the small slip amplitude of fretting makes the interaction between the environment and the contact much more difficult than that it is in sliding wear, i.e. the transport of oxygen into the contact from the environment and the transport of the wear debris out of the contact, which can drastically influence the progression of wear. Indeed, the sensitivity of the fretting contact towards the effects of different parameters on the process of debris formation and ejection should be regarded as the key features which distinguish fretting wear from sliding wear, and a separate set of concepts is necessary. As can be seen later in this review, there has been some significant progress on the development of a theoretical framework specifically for fretting, namely the third body approach and its derivatives, but the

Archard wear equation, as developed for sliding wear, is still the major concept used to describe fretting.

### **2.1.2 The concept of wear rate**

A key aim of much research into wear is the development of an understanding of the relationship between the various parameters which describe the *exposure to wear* ( $E$ ) and the *amount of wear* ( $W$ ) that results. There are different ways to define the amount of wear and measuring the volume of material loss is the most typical of these. Alternative measures are possible such as the mass of material removed, or the depth of material removed.

The description of the *exposure to wear* ( $E$ ) can also take many forms. The exposure to wear could be as simple as the duration of materials being exposed to the conditions leading to wear. More complex measures can be employed to describe both the duration and the severity of the exposure. Typical measure of the exposure of wear for sliding wear is the sliding distance, whilst for fretting wear, the frictional energy dissipated is commonly adopted, although it is recognised that neither of these have any time dependency built into them.

In the case of fretting wear, the parameters which might be used to describe the exposure to wear depend upon the nature of that exposure (i.e. whether a time dependency is included or not) and may include the normal force across the contact, the displacement amplitude, the fretting frequency etc. For applications where the occurrence of fretting wear is common, it is important to understand and quantify how changes in these variables affect the evolution of the wear volume, so that damage can be predicted and its effects on the system controlled.

In general terms, the evolution of the amount of wear in terms of the exposure to wear will depend on the test conditions and the material properties; typical examples of the

evolution of wear are illustrated in Figure 2.2. In all the cases as shown in Figure 2.2, there is a period where the wear increases in linear proportion to the exposure, but this may be preceded by an initial transient period in which the relationship between the amount of wear to the exposure might be very different; in other words, the overall wear behaviour can proceed in a non-linear fashion [30].

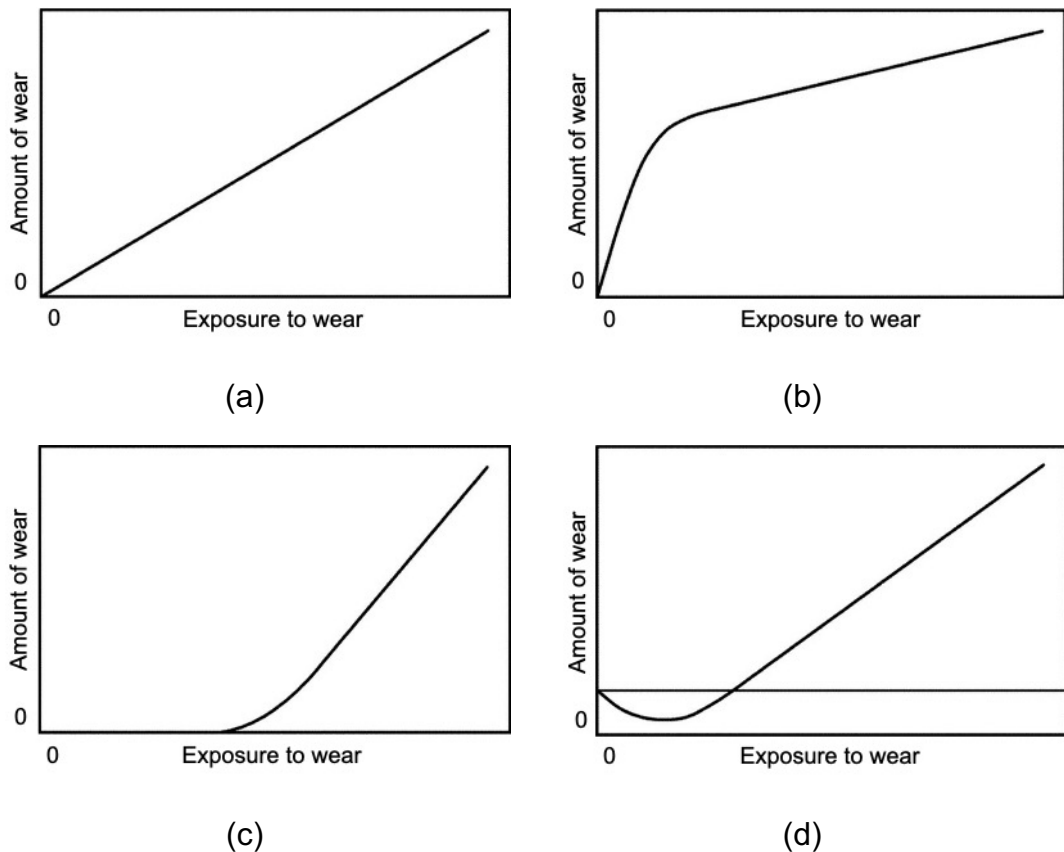


**Figure 2.2: Schematic illustration of the evolution of the wear, namely the amount of wear as a function of the exposure to wear with (a) linear relationship; (b) linear relationship after the transient period of rapid wear; (c) linear relationship after the transient period of wear incubation; (d) linear relationship after the transient period where materials being added up to the surface [29].**

Figure 2.2a illustrates the case where the initial transient period does not exist. Figure 2.2b shows a period of rapid development of wear at beginning of the exposure followed by a period of steady state wear. Figure 2.2c illustrates a case where there is an initial incubation period before wear proceeds a steady rate. Finally, Figure 2.2d illustrates a period of “negative wear” followed by steady state wear (this latter type is

generally observed with wear by hard particles where the wearing agent (e.g. an abrasive) can become embedded in the wearing body).

The development of steady state wear is desired in research when analysing bodies of experimental wear data. The linear relationship allows the aggregation of these data into a single parameter to represent and characterise the overall wear behaviour of the whole body. This single parameter is normally identified as the *wear rate*,  $\frac{dW}{dE}$ . It has been widely recognised that it is essential to derive a constant value of wear rate (also termed the *steady-state wear rate* [30]) to characterise the wear behaviour of different materials under a certain set of test conditions. However, as indicated by Figure 2.2b, Figure 2.2c and Figure 2.2d, in case where non-linear wear behaviour occurs, the average value of  $\frac{dW}{dE}$  itself can be a function of the exposure to wear ( $E$ ), i.e. the average wear rate varies as wear proceeds; in these cases, care must be taken when determining a representative wear rate.

As described in Section 2.1.1, traditionally, the wear rate for sliding wear is derived from Archard's work [16], and the specific wear rate,  $k_A$ , is often employed to describe the wear rate which is assumed to be constant in the steady state. The equivalent definition of the specific wear rate in fretting was proposed by Fouvry and co-workers [31] as shown below:

$$\begin{aligned} D &= 4\delta^* f_{Hz} t = 4\delta^* N \\ E_d &= \bar{\mu} P D \\ V_w &= k_e E_d \end{aligned} \tag{2.2}$$

where  $\delta^*$  is the slip amplitude for each cycle in fretting;  $f_{Hz}$  is the frequency of reciprocal motion;  $t$  is the time;  $N$  is the number of cycles; and  $\bar{\mu}$  is the averaged value of coefficient of friction throughout the process. In fretting, the equivalent term for the total sliding distance is the sum of the slip amplitude for each cycle, which leads to  $D$

being calculated as  $4\delta^* f_{Hz} t$  or  $4\delta^* N$ . The quantity  $\bar{\mu}PD$  is thereby the product of the tangential force (the product of the applied normal load and the coefficient of friction) and the total sliding distance, resulting in the term known as the energy dissipated into the contact,  $E_d$ . Therefore, the specific wear rate in fretting,  $k_e$ , is derived as the constant of proportionality relating the wear volume and the dissipated energy. The constant wear rate in fretting wear,  $k_e$ , is presented as the wear volume per unit of frictional energy dissipated (with typical units of  $\text{mm}^3 \cdot \text{J}^{-1}$ ); itself being derived from the concept espoused by Archard's work but which also accounts for variations in the coefficient of friction. This wear model based upon the dissipated energy has been widely employed in fretting research to characterise the amount of wear [18, 32-36]. In this thesis, all those approaches which are derived from the Archard wear equation will be grouped together and termed *Archard-type approaches*.

It is argued that the Archard-type approach (without considering the transport of debris out of the contact) is not able to account for non-linear wear behaviour [30] and for the differences in wear rates associated with the debris entrapment in the contact. Nevertheless, the use of Archard-type approaches has provided common ground amongst researchers for discussion of the effects of individual variables on fretting and for comparisons of the behaviour of different materials to be made.

As noted by Fillot et al. [37], the Archard-type wear rate in fretting literature is merely the description of the rate associated with the mechanism to remove material from the surfaces. It is essential to recognise that fretting is different from sliding that the scale of the relative oscillatory motion between the contacting surfaces is generally much smaller than the size of the damaged area, meaning that debris ejection from the contact needs to be considered as part of the process of wear [2, 19]. As such, the final measured volumes of wear after exposure depend upon the ability of debris to escape the contact under those conditions. The wear volume in fretting is, therefore, the 'observed' result combining effects of detachment of the wear particles from the

contacting bodies and the subsequent formation and ejection of debris out of the contact, rather than only the volume of material removed from the contacting bodies in sliding wear. It is important to distinguish the nature of wear rate employed in fretting research, i.e. whether the wear rate is referring to the quantity as the observed wear volume per unit energy dissipated (termed as *observed wear rate*) or simply the maximum rate of particle detachments it can achieve under certain test conditions, as derived from the Archard wear equation.

Efforts have been made to modify the Archard-type approach to incorporate the role of oxidation and the existence of the oxide film in contact. Quinn [38, 39] investigated the mild wear in sliding as outlined by Archard and Hirst [26], in which the applied load is relatively low and the presence of the oxide film plays an essential role in modifying the Archard wear coefficient ( $K_A$ ) to account for oxide formation in addition to the particle detachment as presented in the origin work of Archard [16]. It was assumed that the oxide film will start to detach and form particles after the oxide film has grown to reach a critical thickness, and  $K_A$  is dependent upon this process. This modification of the Archard wear equation considered the role of oxidation and thus improved the performance of the model when temperature is elevated; but is nevertheless limited by quantities that cannot be pre-determined when setting up tests (e.g. the local temperature increase in contact and the activation energy for oxidation). Similar research was conducted by Dréano et al. [40, 41] to expand the ability of Archard-type approaches in fretting by examining the effects of tests conditions on the rate of oxidation. The Archard wear coefficient was, again, assumed to be proportional to the oxide thickness, and was found to be strongly dependent upon the environmental temperature. A quantity called *sintering parameter* was introduced as an indicator of the formation of the glaze layer due to the presence of the retained oxide debris in the fretting contact. The sintering parameter can influence the wear rate and thereby was demonstrated to result in a more accurate description of fretting wear. All these

modifications are based upon the Archard-type approaches, which suffer from the same limitation that wear is assumed to be equivalent to the process of debris formation. It is argued that the Archard-type approach (without considering the transport of debris out of the contact) is not able to account for the differences in wear rates associated with differences in debris entrapment in the contact. Even though the presence of the oxide film is recognised, and its effect has been considered when deriving the wear rate, the role of debris escaping out of the contact is still rarely discussed.

All the cases discussed in this section are guided by a common framework of wear analysis which assumes that a representative constant wear rate can be derived which describes the steady state. It is, however, possible that the evolution of wear may exhibit continuous non-linear behaviour, for which the pursuit of a constant wear rate from experimental results can be inappropriate, and an alternative definition of wear rate is required to describe the wear behaviour more accurately. In contrast to the constant wear rate, the concept of the *instantaneous wear rate* is introduced [30] reflecting the rate of the observed amount of wear at any moment of the exposure. It is, in principle, the gradient of the tangent at a certain point during the evolution of wear (examples are given as shown in Figure 2.2), or the derivative of the amount of wear in terms of the exposure. There is no doubt that instantaneous wear rate will capture any non-linear features of the wear process and will be able to account for changes in the operative mechanism of wear; however, it does not possess the virtue of simplicity offered by the Archard-type wear rate and is not a metric that can be used for comparison of different material behaviours under different test conditions. The issue of the balance between the use of a constant wear rate to easily characterise the wear process and the use of an instantaneous wear rate to model the non-linear behaviour remains unaddressed.

## 2.2 Analysis of fretting contact

### 2.2.1 Hertzian contact mechanics

Non-conforming geometries, typically cylinder-on-flat (CF), sphere-on-flat (SF) and crossed-cylinders (CC), are commonly employed in laboratory experiments as representatives of more geometrically complex components in contact as seen in many industrial applications. The analysis for such non-conforming contact under elastic deformation was firstly studied by Hertz [42] (known as *Hertzian contact mechanics*, and was later presented in detail by Johnson [43]), and is useful to understand the initial distribution of the contact pressure and the stress within the contacting bodies.

As illustrated in Figure 2.3, when pressing a cylinder (of radius  $R_1$ ) against another cylinder (of radius  $R_2$ ) with parallel axes and under a normal load ( $P$ ), surfaces will experience elastic deformation, and contact will occur over a rectangular area with the length of  $L$  and the width of  $2a$ ; such a contact is termed a *line contact*. Similarly, if two spherical surfaces are pressed against each other (of radii  $R_1$  and  $R_2$ ) under an applied load, the contact area is a circle of diameter  $2b$ , which is termed a *point contact*. Please note that the line contact is more relevant to this thesis and hence the analysis of which is the focus for the current section. There are some similarities for the analysis of both the line contact and the point contact, and some equations for the point contact are also presented here in this section.

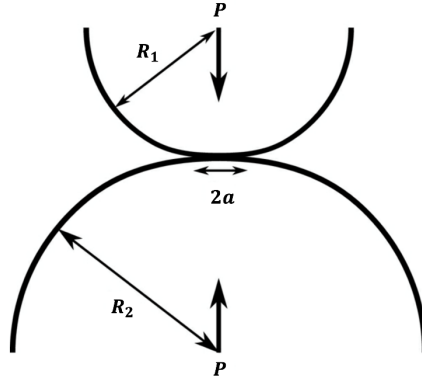


**Figure 2.3: Elastic deformation of a Hertzian line contact between two pressing cylinders of radius  $R_1$  and  $R_2$  under the applied load,  $P$ , forming a rectangular contact area with the length of  $L$  and the contact width of  $2a$ . Note that if a Hertzian point contact is presented here,  $R_1$  and  $R_2$  will be the radii for two pressing spheres, and the contact area will be a circle with the diameter of  $2b$  [43].**

As presented by Johnson [43], the half width of the contact for the Hertzian line contact,  $a$ , can be calculated as shown in Equation 2.3a, and the radius of the contact for the Hertzian point contact,  $b$ , is given by Equation 2.3b.

$$a = \left( \frac{4PR^*}{\pi LE^*} \right)^{\frac{1}{2}} \quad (2.3a)$$

$$b = \left( \frac{3PR^*}{4E^*} \right)^{\frac{1}{3}} \quad (2.3b)$$

For both Equation 2.3a and Equation 2.3b, the definition of  $R^*$  and  $E^*$  are the same.  $R^*$  is the relative radius of curvature of the contacting bodies, which is defined with respect to the radii of the two bodies,  $R_1$  and  $R_2$  as shown in Equation 2.4;  $E^*$  is the relevant elastic modulus (also known as the *reduced modulus*), which is a function of the Young's moduli of the two bodies,  $E_1$  and  $E_2$ , and their corresponding Poisson's ratios,  $\nu_1$  and  $\nu_2$ , as given by Equation 2.5. It should be noted that if one of the contacting bodies is in fact a plane, such as the cylinder-on-flat contact geometry applied in this thesis, the radius of that body is infinite, resulting in the relative radius of curvature being equivalent to the radius of the non-plane body in contact.

$$\frac{1}{R^*} = \frac{1}{R_1} + \frac{1}{R_2} \quad (2.4)$$

$$\frac{1}{E^*} = \frac{(1 - \nu_1)^2}{E_1} + \frac{(1 - \nu_2)^2}{E_2} \quad (2.5)$$

For the line contact, the pressure over the contact,  $p$ , varies with the distance from the centre of the contact (denoted as  $d$ ) in the direction perpendicular to the axis of the cylinder), and hence its distribution as a function of  $d$  is given by Equation 2.6a; for the point contact, the change of the contact pressure is, again, associated with the distance from the centre,  $r$ , but in the radial direction (as shown in Equation 2.6b). For the detail of the derivation of the pressure distribution and following expressions of sub-surface stresses within the contacting bodies, Johnson [43], and Hutchings and Shipway [29] provide further detail.

$$p(d) = \frac{2P}{\pi a L} \sqrt{1 - \frac{d^2}{a^2}} = p_0 \sqrt{1 - \frac{d^2}{a^2}} \quad (2.6a)$$

$$p(r) = \frac{3P}{2\pi b^2} \sqrt{1 - \frac{r^2}{b^2}} = p_0 \sqrt{1 - \frac{r^2}{b^2}} \quad (2.6b)$$

It can be seen from Equation 2.6 that the contact pressure reaches its maximum at the centre of the contact for both cases, i.e.  $d = 0$  or  $r = 0$ ; but falls to zero at the edge of the contact when  $d = a$  or  $r = b$ . The maximum contact pressure,  $p_0$ , can also be expressed in terms of  $R^*$  and  $E^*$  (Equation 2.7a for a line contact, and Equation 2.7b for a point contact):

$$p_0 = \frac{2P}{\pi a L} = \left( \frac{PE^*}{\pi L R^*} \right)^{\frac{1}{2}} \quad (2.7a)$$

$$p_0 = \frac{3P}{2\pi b^2} = \left( \frac{6PE^{*2}}{\pi^3 R^{*2}} \right)^{\frac{1}{3}} \quad (2.7b)$$

The stress within the contacting bodies can be found as function of the maximum contact pressure ( $p_0$ ), the distance from the centre of the contact ( $d$  or  $r$ ) and the depth from the contacting surface ( $z$ ). However, equations of stress will be presented only for

the case of line contact (Equation 2.8). It can be calculated from Equation 2.8c that the maximum shear stress on the axis of loading, which is relevant to consider the damage of material, is  $0.3p_0$ , occurring at the depth of  $z = 0.78a$ . For the point contact, the form of equations is more complex and the stress distribution is associated with the Poisson's ratio (although not particularly sensitive) [29, 43].

$$\frac{\sigma_x}{p_0} = -\frac{1}{a} \left\{ (a^2 + 2z^2)(a^2 + z^2)^{-\frac{1}{2}} - 2z \right\} \quad (2.8a)$$

$$\frac{\sigma_z}{p_0} = -a(a^2 + z^2)^{-\frac{1}{2}} \quad (2.8b)$$

$$\frac{\tau_1}{p_0} = -\frac{1}{a} \left\{ z - z^2(a^2 + z^2)^{-\frac{1}{2}} \right\} \quad (2.8c)$$

where  $\sigma_x$  and  $\sigma_z$  are the principal stresses along the x-axis and z-axis,  $\tau_1$  is the correspond principal shear stress. Figure 2.4 shows the distribution of sub-surface stresses ( $\sigma_x$ ,  $\sigma_z$  and  $\tau_1$ ) and contours of the principal shear stress ( $\tau_1$ ) as presented by Johnson [43].

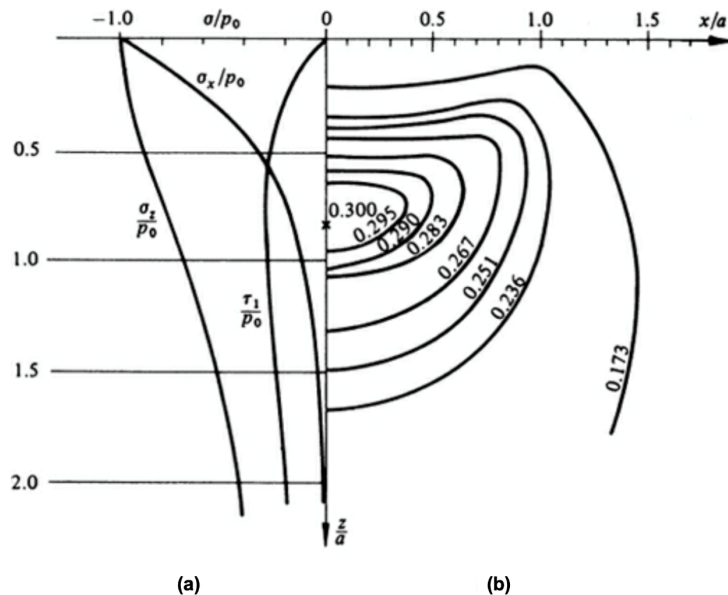
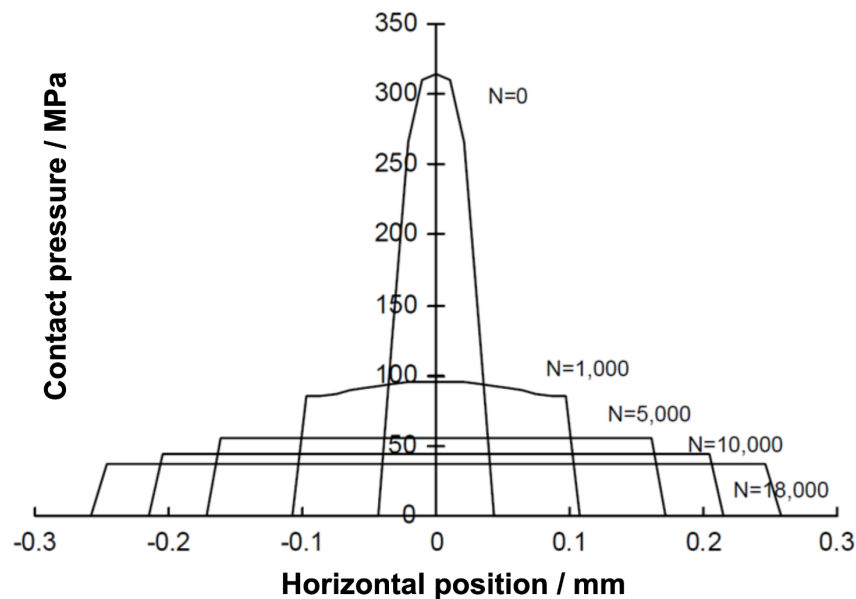


Figure 2.4: Hertzian line contact: (a) distribution of sub-surface stresses along the axis of symmetry; (b) contours of principal shear stress,  $\tau_1$ , showing its maximum value of  $0.3p_0$  at  $z = 0.78$  [43].

It should be noted that the distribution functions outlined in Equation 2.6 and Equation 2.8 are the descriptions of the pressure and stresses only for the initial contact area under loading. However, considering the development of wear for non-conforming contact, the size of the contact will expand continuously throughout the process, which in turn has significant impact on the pressure and stress distributions. Efforts have been made to evaluate the evolution of pressure and stress along the development of wear for non-conforming contact; for example, numerical analysis conducted by McColl et al. [44] demonstrated that, for a cylinder-on-flat contact (producing a line contact, and the radius of the cylindrical specimen is 6 mm), the contact pressure is tending towards a uniformed profile as the test duration increases (shown in Figure 2.5). Similar investigation was carried out by Fouvry et al. [45].



**Figure 2.5:** Distribution of the contact pressure over the width of line contact as the evolution of wear [44].

### 2.2.2 Slip regimes

The Hertzian theory as described in Section 2.2.1 provides an understanding of the initial conditions for non-conforming contact due to the applied normal load. The theory was expanded by Mindlin [46] and Mindlin and Deresiewicz [47] to consider the case

where a cyclic tangential force ( $Q$ ) is also applied to the contact. One important note from the previous section is that the contact pressure achieves its maximum at the centre of the contact area (in the shape of rectangle for line contact, and circle for point contact), and falls to zero at the edge. Methods proposed by Mindlin [46] and Mindlin and Deresiewicz [47] (see the derivation of these methods as explained in detail by Johnson [43]) state that, for a contact where a cyclic tangential force is superimposed over the normal load, some relative displacement may occur between the contacting surfaces at the edge of the contact where the contact pressure is below a threshold. As a result, the whole contact area can be categorised into two regions separated by a boundary denoted as  $c$ , (this boundary is defined as a distance from the centre of the contact beyond which slip may occur): (i) the central region where there is no relative tangential movement between the contacting bodies within the range of  $c$ , termed as the *stuck region*; (ii) the surrounding regions beyond the boundary  $c$ , in which slip can occur between the contacting bodies, termed as the *slip region*.

It should be noted that, as the inner stuck region of the contact remains sticking while the outer slip region of the contact may experience slip, the size of the boundary to separate the stuck region and the slip region ( $c$ ) can vary with test conditions, in particular the normal load, the tangential force and the displacement amplitude. It is also intriguing to notice that a fully stuck contact requires infinite tangential force at the edge of the contact to satisfy the condition of those equations outlined in Johnson's book [43], unless there is an outer slip region surrounding the stuck region. The implication here is that a normally loaded non-conforming contact will always exhibit a slip region under any cyclic tangential loading, and that the key concern is not whether the slip region exists, but rather how the size of it can be influenced under different conditions; note here that the "full stuck" contact in the following contents refers to a contact where slip only occurs at the edge.

As illustrated in Figure 2.6, considering a point contact that is “fully stuck”, with increasing values of the cyclic tangential force,  $Q$ , the annular slip region expands, starting from the edge; the size of the boundary  $c$  will shrink and the central stuck region will eventually diminish as the slip region further penetrating towards the centre of the contact, until slip occurs over the entire contact area when the tangential force reaches the static friction limit (the product of the coefficient of friction and the normal load); i.e.  $Q = \mu P$  ( $\mu$  is the coefficient of friction).

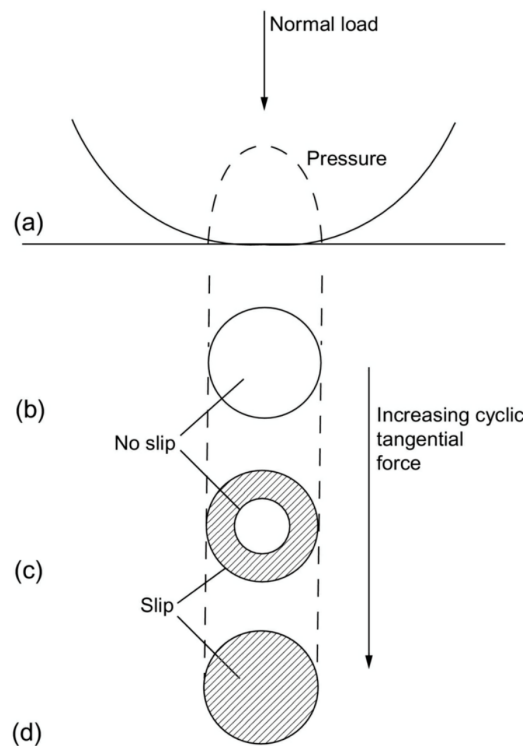


**Figure 2.6: Illustration of (a) the distribution of the contact pressure for a point contact under normal loading; (b) – (d) the plan views of the contact showing a diminishing stuck region as the increase of the cyclic tangential force until slip occurs over the whole contact; the shaded regions presents areas where slip can occur [29].**

With the identification of the stuck region and the slip region, it is reasonable to argue further that there could exist three types of contact, (i) the “fully stuck” contact; (ii) the contact where the stuck region and the slip region co-exist; (iii) and the fully slipping contact. Indeed, each of these three types of contact can correspond to a fretting regime of material behaviour with different damage mechanisms, which will be discussed in the next paragraph.

Vingsbo and Söderberg [4] investigated the interrelated effects of two primary parameters in fretting, namely the normal load (as opposed to the tangential force) and the displacement amplitude, on the size of the boundary which separates the slip region from the stuck region. The general observation was that, with the normal load being fixed, the increase of the amplitude of the cyclic tangential movement is associated with an increase in the extent of slip; a similar effect can be seen by reducing the normal load while fixing the tangential displacement. They introduced the concept of *fretting maps* in 1988, and three regimes of the fretting process were identified as illustrated in Figure 2.7, namely the *stick regime*, the *partial slip regime* (or the *mixed stick-slip regime*) and the *gross slip regime* [4], each with distinctive features of damage. Accordingly, the stick regime is associated with the “fully stuck” contact, the partial slip regime corresponds to the contact with the co-existence of both the stuck region and the slip region, and the gross slip regime is related to the contact where the entire contact is taken over by the slip region.

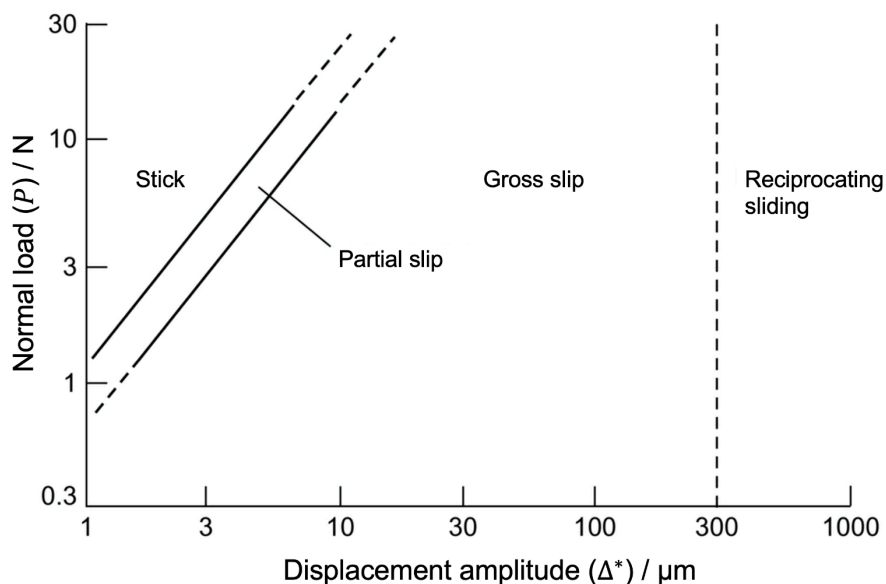


**Figure 2.7: Schematic illustration of the concept of fretting map for a point contact with stainless steel showing regimes of fretting process; different regimes can be achieved by combining different values of the displacement and the normal load (from [29] after [4]).**

The stick regime is featured by limited surface damage. Typically, it is caused by a combination of high normal load and low displacement amplitude. The plastic shearing between surface asperities is limited by the low displacement amplitude, and the entire contacting surface is seized by severe mechanical deformation of surface asperities [48, 49], resulting the entire contact region being “fully stuck” as demonstrated in Figure 2.6b. Hence the contact shows little damage since there is no relative motion.

The partial slip regime or the mixed stick-slip regime is the case where effects of parameters cause the contact to exhibit both the stuck region at the centre and the annular slip region as demonstrated in Figure 2.6c. As described above, the shift from the stick regime to the partial slip can be achieved by increasing the displacement amplitude or reducing the normal load. Damage will occur in the slipping region, with more of the load being carried by the stuck region of the contact as wear takes place. Similar to the stick regime, limited plastic shearing of asperities can be found within the stuck region, but considerable crack formation can be observed at the boundary between the stuck region and the slip region, causing fatigue to be the dominate mode of damage; limited material removal can also be observed within the slip region.

The gross slip regime is defined by significant surface degradation of material removal. As opposed to the stick regime, the gross slip regime occurs when the normal load is low while the displacement amplitude is large, causing the entire contact being covered by the slip region as shown in Figure 2.6d. Within this regime, large amounts of material removal can be observed at a rate that is sufficient to suppress the formation and growth of cracks, resulting the dominate mode of damage being wear. The gross slip regime is the focus of this thesis, and hence the fretting wear behaviour is investigated within this regime.

If the operative regimes during the fretting process are known to be the same, then fretting studies conducted by different researchers may be compared. It is, therefore,

useful to map the wear behaviour of different materials under various conditions in order to identify the fretting regimes [50]. Indeed, fretting regimes can be strongly influenced by different variables, and their combinations; for example, in addition to the normal load and the displacement amplitude, influences of the frequency [4, 51-54] and material type [4, 53, 54] have also been examined. It should be noted, however, whilst the concept of fretting maps is relatively straightforward, the number of experiments it requires to determine the regime boundaries can be significant.

### 2.2.3 Fretting loops and the coefficient of friction

The common practice to determine the fretting regime of material behaviour is by examining the shape of *fretting loop*. A fretting loop is a plot of the cyclic tangential force against the reciprocating displacement for a single cycle of fretting motion. Please note that several terms have been used throughout the literature to describe the tangential force and the displacement imposed to the fretting contact; in this thesis, the applied tangential force within a single cycle is denoted as  $Q$  and, similarly, the applied (far-field) displacement is given by the symbol of  $\Delta$ . The method of plotting of fretting loops was first used by Mindlin and Deresiewicz [47] for their work on analysing the fretting contact, and was later expanded in the work by Vingsbo and Söderberg [4] and Vingsbo et al. [53] to illustrate the concept of fretting maps. Typical shapes of fretting loop in different regimes are presented in Figure 2.8; as the fretting process changes from the stick regime to the gross slip regime, the fretting loop is more open and changes from a line (elastic-only) to an elliptical shape and finally resembles a parallelogram. The change of fretting regime from the stick to the gross slip is similar to the transition described in Figure 2.6, namely that a fretting contact changes from “fully stuck” (although there is elastic deformation in the direction of fretting motion to accommodate the displacement) to a situation where the elastic deformation is overcome so that the edge of the contact starts to slip until the entire contact is sliding with the tangential force remaining constant across the period of sliding. It should be

noted that, under a certain set of test conditions, the fretting regime of the material may persist throughout the test but can also change from one regime to another due to change of the nature of the contact with the evolution of wear. It is, therefore, useful to plot fretting loops as the test evolves. A method to examine the change of fretting regime within a test involves stacking of fretting loops for each cycle to acquire a three-dimensional plot of the tangential force, displacement and number of cycles; this 3D plot is also known as *fretting log*.

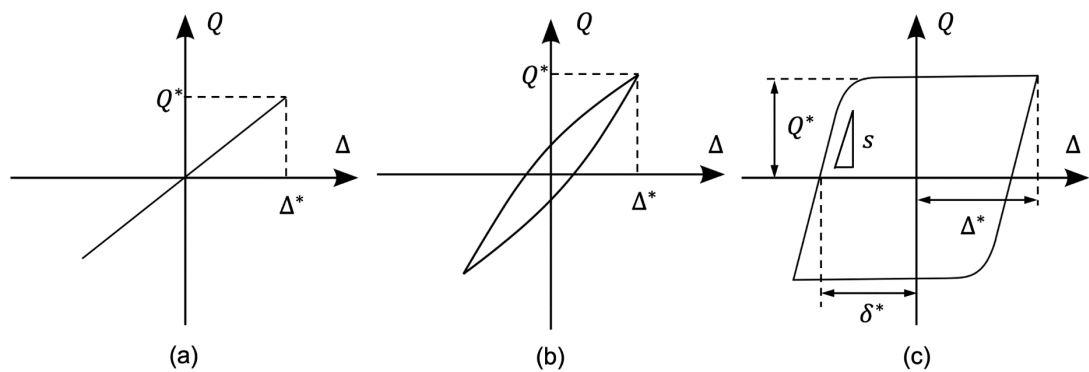


**Figure 2.8: Schematic illustration of the typical shape of the fretting loop within (a) stick regime; (b) partial slip regime; (c) gross slip regime (after [4]).**

As indicated in Figure 2.8, a number of important quantities can be derived from a fretting loop, such as the amplitude of the cyclic tangential force (denoted as  $Q^*$ ), the amplitude of the reciprocal displacement (denoted as  $\Delta^*$ ) and the energy dissipated into the contact per cycle (defined as the work done by the tangential force during a complete cycle; denoted as  $E_d(i)$ , with  $(i)$  indicating  $i^{th}$  cycle), which can be calculated as the area enclosed by the fretting loop (see Section 3.4.2 for the method of determining the dissipated energy in this thesis). It should be noted that the analytical solution for dissipated energy per cycle is very complicated for contact in partial slip as indicated by Johnson [43]. For the contact in gross slip, additional information can also be extracted from the fretting loop, namely the stiffness of the system (denoted as  $S$ ), and the actual slip amplitude (the actual slip of the contact is denoted as  $\delta$ , with  $\delta^*$  referring to its amplitude).

It is important to acknowledge that the applied far-field displacement is not equivalent to the actual slip between the contacting surfaces. As shown in Figure 2.8a, the applied displacement can (in certain cases) be fully accommodated by the elastic deformation of the contact (also known as system compliance), even though the contacting bodies are “fully” stuck to each other. For a contact in the gross slip regime, part of the applied displacement is absorbed by the system compliance; it is until the overcoming of the elastic deformation that the remainder of the displacement can be used to cause the contacting surfaces to slide against each other, hence the actual slip distance will always be smaller than the applied displacement. Please note that the slip amplitude is not easy to physically measure and is commonly determined from fretting loops after the completion of test (see Section 3.4.3 for the description of the method to obtain slip amplitude in this thesis). Such a method, however, was not generally available especially in earlier research, which may cause misinterpretation of the experimental results [24]. To quote Bryggman and Söderberg [52]: “...*the bulk [measured] displacement may be considerably larger than the actual slip amplitude at the interface. The value of the interfacial slip amplitude is difficult to measure experimentally*”. There are some recent works reporting the inappropriate use of the applied displacement amplitude, along with a lack of clarity about the need to distinguish the actual slip from the applied displacement; it is suggested that perhaps the issue is still mainly associated with technical difficulties regarding the measurement of fretting loops [24].

A single characteristic parameter to measure the resistance to the sliding motion, known as the *coefficient of friction*, is often desired in studies of both sliding and fretting wear. In fretting, if a contact in gross slip can be approximated by the Coulomb model, i.e. the tractional force is only dependent upon the normal load [55, 56], which results in the tangential force remaining constant during the sliding period producing a fretting loop akin to the typical shape of a parallelogram. Therefore, a common practice to determine the coefficient of friction in fretting (CoF, denoted as  $\mu$ ) is by defining the

ratio of the amplitude (the maximum value) of the cyclic tangential force to the normal applied load, i.e.  $\frac{Q^*}{P}$ . However, it has been suggested [31, 57-60] that not all cases of fretting contact in gross slip can be described by Coulomb frictional behaviour, i.e. the tangential force may change significantly during the sliding period. By examining fretting loops, it has been identified that there are two common types of non-Coulomb behaviour in fretting: (i) the tangential force remains constant through the majority of the sliding period but rises to a peak at each end of one stroke [33, 61] as shown in Figure 2.9a; (ii) the tangential force increases steadily throughout the sliding period and reaches its maximum at the end of the stroke [62, 63], as illustrated in Figure 2.9b.

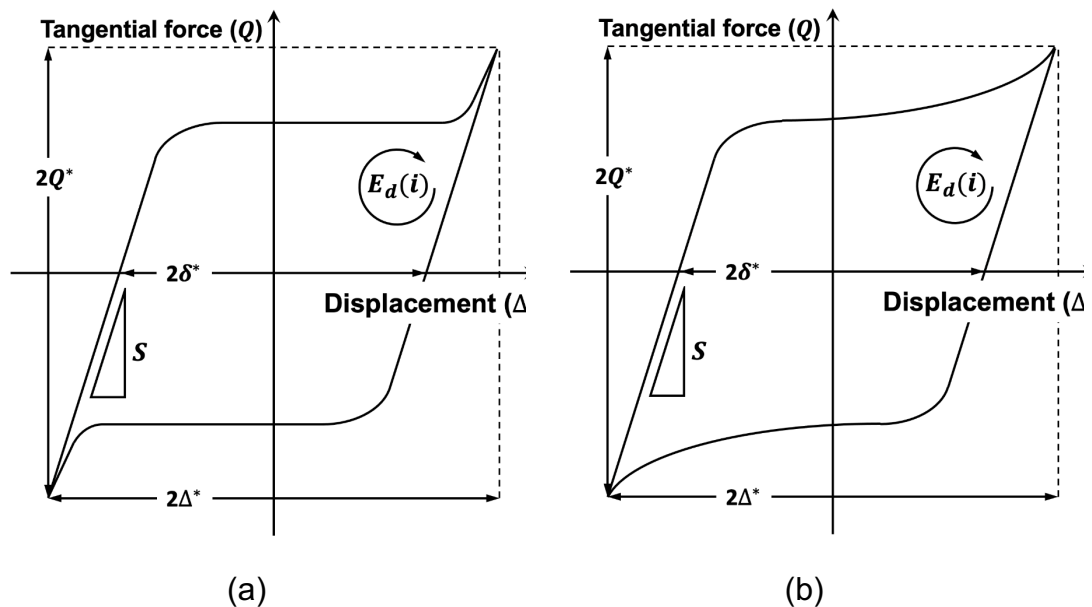


**Figure 2.9: Schematic illustration of fretting loop showing (a) a peak of tangential force at the end of the stroke; (b) a steadily increasing tangential force throughout the sliding (after [64]).**

Several explanations have been proposed to account for the non-Coulomb behaviour. As suggested by Fouvry et al. [33], the peak of tangential force is the result of the physical interactions of material build-up at the edge of the contact as demonstrated in Figure 2.10a termed the *ploughing effect*. It was suggested that the ploughing effect is generally observed in fretting contacts of ductile material and is caused by the material within the contact being pushed towards the edge of the contact due to plastic

deformation. The transferred material is accumulated at the edge, which creates difficulty for the contacting surfaces to slide against each other, unless a larger tangential force is exerted. The work of Dick et al. [61] supported this theory by constructing an FE model based on the cross-sectional profile of the contact with features of transferred material at the edge; the model was able to predict the significant increase of the tangential force at the end of the stroke. However, as Mulvihill et al. [62] noted later, the increasing tangential force cannot be explained by the ploughing effect; points of physical impingement between the contacting surfaces not only exist at the contact edge, but are also distributed throughout the entire contact (as illustrated in Figure 2.10b). These points of impingement are associated with the formation of local pit-peak feature caused by the wear debris modifying the contact profile, acting as the source of the continuous increase of the tangential force during the period of sliding.

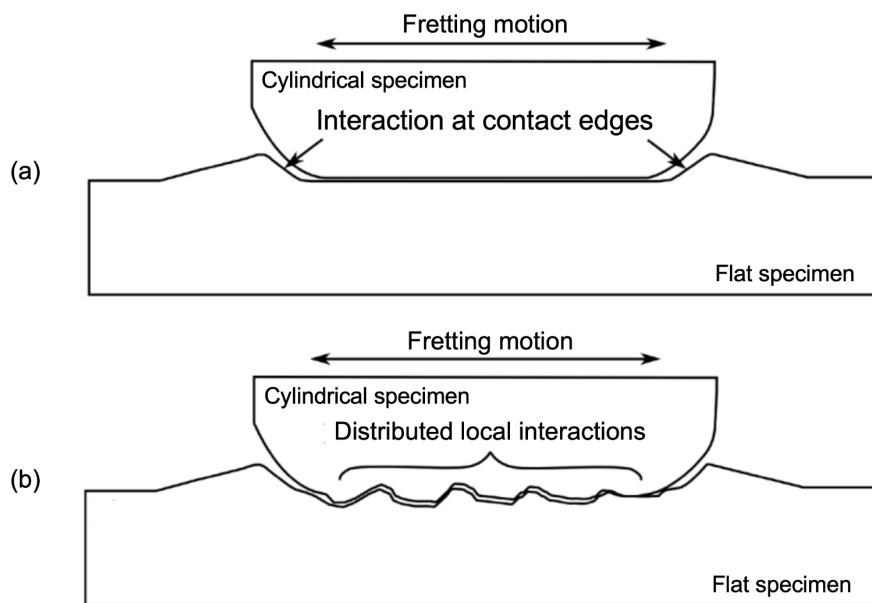


**Figure 2.10: Schematic illustration of the physical interactions between the contacting surfaces (a) at the edge of the contact (the ploughing effect); (b) distributed over the contact area (after [62]).**

In either case, if a fretting contact in gross slip exhibits non-Coulomb behaviour, the classic definition of CoF, as the ratio of the maximum tangential force to the applied normal load, is no longer a representative quantity to account for the significant

variation of the tangential force; in fact, using the maximum value of the tangential force can lead to a significantly overestimated coefficient of friction. An alternative method known as the *energy coefficient of friction* (ECoF, denoted as  $\mu_e$ ) was developed by Fouvry et al. [33] by defining a ratio of the energy dissipated into the contact ( $E_d$ ) to the product of the applied load ( $P$ ) and the total distance of sliding ( $4\delta*N$ ); i.e.  $\frac{E_d}{4P\delta*N}$  (see more details of calculating ECoF in the current study in Section 3.4.4). Please note that applying the ECoF on a contact with Coulomb behaviour will produce the same value as to the classic CoF. The ECoF was originally proposed to address the problem caused by the ploughing effect, but it has been widely accepted in fretting research whenever non-Coulomb behaviour is observed and now exists as an ASTM standard [65]. As reviewed by Llavori et al. [66], among a group of 96 papers associated with studies of fretting in gross slip (published between the year of 2009 to 2019, and the methods of determining the coefficient of friction were specified within), 52% used the classic definition of coefficient of friction, while the energy coefficient of friction was utilised by 35% of those papers. There are other methods to determine the coefficient of friction of the fretting contact, such as the mean coefficient of friction (as introduced by Wang et al. [67]) and the geometry independent coefficient of friction (GICoF, proposed by Jin et al.[64]) which seeks to eliminate the effects of any development of the wear scar geometry on the measured tractional forces during a fretting cycle. Llavori et al. noted in the same work [66] that GICoF is, by their analysis, the most accurate description for non-Coulomb contacts, followed by ECoF while the classic CoF is the worst. Considering the GICoF is a relatively new concept which might require further work to examine its robustness and modification to data processing scripts, ECoF will be used as the method to determine the coefficient of friction in this thesis for the virtue of its simplicity and proven robustness.

## **2.3 Evolution of wear in fretting contact**

### **2.3.1 Fretting stages**

The complete fretting process can be categorised into three sequential stages, namely the initial stage, the intermediate stage and the steady state [2]. The current section will briefly summarise the underlying mechanisms for each stage of fretting, with an emphasis on the fretting process for metallic materials.

In broad terms, the initial stage of fretting wear is featured by adhesive damage, the ploughing effect and resultant material transfer; the intermediate stage is a stage where patches of oxide debris start to develop with the steady state being characterised by the presence of a compact and stable oxide bed. As can be seen later in the current section, the transition from the initial stage to the steady state in fretting is often considered as the contact mechanism changing from severe wear (featuring extensive metallic contact and adhesion) to mild wear (featuring the existence of the oxide film) as outlined by Archard and Hirst for sliding wear [26]. There are similarities in forming metallic particles and oxide debris for both fretting and sliding, but the debris behaviour within the contact, in particular the debris retention (or debris ejection) is very different. This is the key feature which distinguishes fretting wear from sliding wear, and requires the fretting process to reach a steady state so that effects test conditions on the debris behaviour can be compared and understood.

#### **The initial stage**

Before being brought into contact, surfaces of the majority of metals are covered by thin a oxide layer [68]. This oxidation layer separates the metallic surfaces in contact at the beginning of the initial stage in fretting, leading to a relatively low coefficient of friction (CoF). However, such oxide films are often very thin and can be easily removed due to the plastic deformation and the shear stresses in asperity contacts [3], exposing

the metallic surfaces to direct contact with each other. The direct metal-to-metal contact will prompt adhesion and material transfer [69] and cause significant roughening of the contacting surfaces and a high CoF. Godfrey and Bailey [70, 71] indicated that, in the initial stages of fretting wear, significant adhesive damage can be found on the surfaces of several materials such as steel, iron and copper. In particular, values of CoF for mild steel specimens were measured under a variety of loads and displacement amplitudes. In all cases, adhesive wear was observed during the initial stage as indicated by the distinctive peak in the CoF [72]. Berthier [73] performed additional measurements with more details in order to examine the evolution of CoF with the test duration. Overall, the initial stage can be marked as a transition from the interactions of the thin film of oxide on surfaces to direct metallic contact and eventually to the intermediate stage.

### **The intermediate stage**

In the intermediate stage of fretting wear, the generation of oxide debris becomes significant, and patches of oxide debris begin to develop, although the mechanism of oxide formation is less generally agreed upon in the literature. The *tribo-chemical* nature of the fretting process has been widely recognised, indicating that both mechanical and chemical factors are playing significant roles in the formation of oxide debris in fretting [12, 72, 74]. However, arguments revolve around whether metallic surfaces are oxidised with the oxide being subsequently removed from the contacting surfaces [12, 38, 39, 74] or vice versa (i.e. oxide debris is formed from metallic wear particles which were oxidised after being removed from the surface) [70, 71, 75-78].

Uhlig [12] proposed that the generation of oxide debris initiates from the metallic particles (generated during the initial stage resulting from the effects of adhesion and ploughing) and the deformed asperities moving across the contacting surfaces due to the fretting motion. This action produces tracks of exposed metallic surfaces which are immediately oxidised and then scrapped off from these tracks by the next passing

asperity (termed *oxidation-scrape-oxidation*), completing a cyclic process of material detachment and oxidation. The detached particles are converted into fine oxide debris by the abrasive motion of particles against both themselves and the contacting surfaces [12]. In contrast, the measurement of electrical contact resistance during fretting tests by Pendlebury [78] indicates that the occurrence of direct metal-to-metal contact is persistent despite the generation and accumulation of oxide debris within the contact. This observation suggests that it is adhesion that encourages wear to continue and thereby the detachment of metallic particles needs to occur before oxidation. Another source of debris formation is considered to be associated with the *tribologically transformed structure* (TTS), which will be described in Section 2.3.2.

With the formation of oxide debris resulting from the tribo-chemical process in fretting, patches of debris can be created, which may prevent direct metallic contact for some localised areas on fretting surfaces, and hence reduce the overall severity of adhesive wear as seen in the initial stage. Although the reduction of adhesive wear typically reduces the extent of direct metal-to-metal contact and hence leads to a lower CoF, the change of CoF during the intermediate stage could be unstable as patches of oxide debris can experience a continual cycle of breakdown and reforming. Similar to sliding wear, the drive of such cycles of behaviour is the competition between exposure of fresh metal and the process of oxidation. There is, however, an additional factor that needs to be included when considering fretting, namely the physical debris ejection from the contact. It should be noted that in this thesis, the former two processes, i.e. exposure of fresh material and oxidation are combined and together termed *debris formation*.

### **The steady state**

The initial stage and the intermediate stage in fretting focus on the formation of debris and can be considered in the same way as a contact in sliding wear changes its

mechanism from severe wear to mild wear. However, as the competing effects of debris formation and ejection tend towards a balance, more patches of debris can be preserved and they emerge into a compact bed of debris, which marks the fretting process as entering the steady state. In the steady state, the rate of both the processes of debris formation and debris ejection converge [37], so that the thickness of oxide debris layer can be maintained [73, 77]. The CoF is stable and typically lower than in the previous stages. The steady state can be reached quickly within a few tens of thousands of cycles in fretting [28, 50, 79], although the specific duration required for achieving steady state varies with different materials under different test conditions. For example, in Pearson's thesis where same material (see Section 3.1) was employed as the current study for fretting research, the steady state was identified from experimental results as a period with stable CoF; it was found that the steady state can be reached approximately from  $1 \times 10^3$  cycles to  $2.5 \times 10^4$  cycles, depending on test conditions (a higher applied load was associated with a shorter period before the steady state was reached) [79].

It is the nature of fretting that majority of the contacting surfaces stays covered, resulting in the ejection of oxide debris being a crucial factor in the fretting process [73]. To understand the effects of different parameters in fretting is to investigate their influences on the debris behaviour, for which the steady state is the absolute focus for the majority of fretting research. The debris layer in a fretting contact is termed the *third body* as proposed by Godet [19], and the relevant framework to emphasise the effects of the third body in fretting is referred as the third body theory or the third body approach. This framework is significantly opposed to the classical theories of wear, which are based on the interactions of surface asperities. Classical wear mechanisms (such as adhesion, abrasion and fatigue) are considered only as methods for detaching particles from the contacting surfaces, not as the complete processes of wear in fretting. According to Godet et al. [19, 80], the fretting contact is defined as two contacting

surfaces (first bodies) separated by an interposed layer of oxide debris (third body). It is indicated by the third body approach that the progression of wear requires particles to be removed from the first-bodies and subsequently expelled from the fretting contact [80]; therefore the ability of contact to transport oxide debris out of the contact may indeed govern the fretting process [73]. The role of the third body will be discussed in detail in Section 2.3.4.

### 2.3.2 Tribologically transformed structure in fretting

An extended framework was first proposed by Zhang et al. [81] to describe the complex sub-surface damage commonly observed on contacting bodies after fretting, with research by Nurmi et al. [82] presenting perhaps the most comprehensive study of the subject. It has been widely agreed upon that the description of the surface/sub-surface damage structure following fretting can be characterised by three layers with distinctive microstructural features, which are illustrated in Figure 2.11 as presented by Sauger et al. [83, 84]. As shown in Figure 2.11: (i) the top layer is composed of compactly distributed oxide debris; (ii) the middle layer is a region of sub-surface material experiencing severe deformation so that the grains are heavily modified, in particular the orientation and size of grains and is generally termed the *tribologically transformed structure* (TTS) [83-85]; (iii) the bottom layer is a region of plastically deformed bulk material.

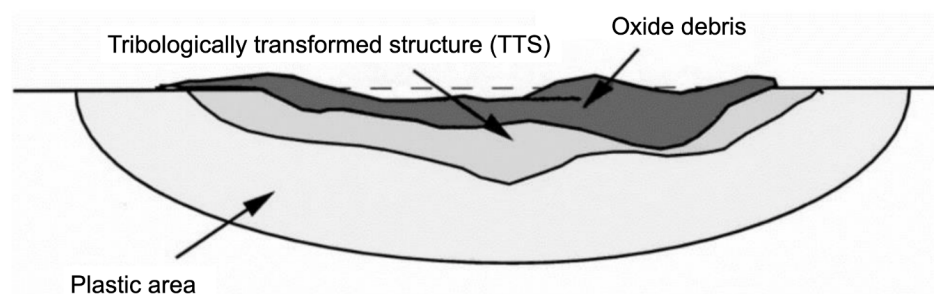


**Figure 2.11: Schematic diagram showing the cross-sectional distribution of different layers of surface and sub-surface material for a fretting wear scar; each layer is characterised by its type of damage [83].**

It was reported that the chemical composition of the TTS exhibits no significant difference from that of the substrate material [83, 84], although there were some other studies showing an elevated oxygen concentration in the TTS [86]. Another commonly observed characteristic is that the TTS tends to have a highly refined microstructure (with grains of the order of tens of nanometres in size), causing the TTS to have significantly increased hardness relative to the bulk material (typically two to three times higher) [83, 84, 87-89]. A critical observation is that the formation of the TTS tends to be associated with cases where the rate of the transport of oxygen into the contact is insufficient to support debris formation [89-91]. In those situations, the observed amount of wear is greatly reduced, although the presence of the TTS generally indicates that significant damage has already occurred within the contact.

With the aid of the concept of the TTS, the mechanisms of forming debris can be described as shown in Figure 2.12 [85] by the following steps. First, the high degree of plastic deformation induces strain hardening of the sub-surface material, resulting in the fast development of the TTS within a short period. As damage proceeds, the TTS can no longer accommodate further plasticity and begins to fragment due to its brittle nature, hence forming metallic wear particles. Under the fretting motion, these metallic particles fracture even further and are oxidised. As a result, oxide debris will accumulate within the fretting contact after a relatively long test duration by consuming the initially formed TTS. However, it is still not clear that whether the formation and degradation of the TTS only occurs at the early stages of a fretting process to initiate the debris formation, or it is indeed a periodic phenomenon throughout the fretting process acting as a continuous source to form oxide debris. The former view is broadly in favour and is supported by the concept of energy threshold (will be described in the following section, Section 2.3.3), whilst evidence exists to support the latter view; for example, a recent study shows that features of the sub-surface damage observed after 100 cycles can still be found after 3 million cycles [92].

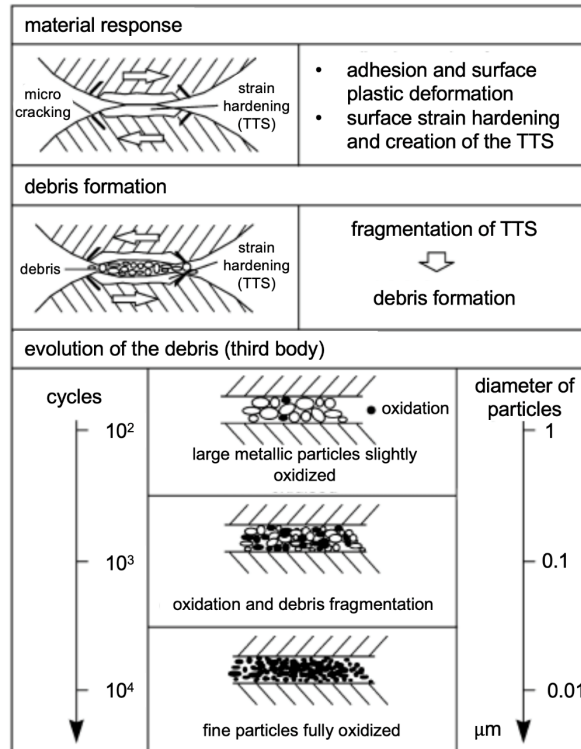


Figure 2.12: Illustration of the formation and the subsequent evolution of oxide debris where the tribologically transformed structure (TTS) is considered as the source of the third body [85].

### 2.3.3 Threshold of the dissipated energy in fretting

The concept that there may exist a threshold of dissipated energy has not been widely recognised [24]. As suggested by Fouvry et al. [17, 31], it is useful to describe the amount of wear (in terms of the net wear volume,  $V_w$ ) as a linear function of the exposure to wear (in terms of the dissipated energy,  $E_d$ ), hence the entire evolution of wear can be characterised by a single parameter, namely the energy wear rate,  $k_e$  (see the description of wear rate in Section 2.1.2). Such a derivation of wear rate generally assumes a direct proportionality between the wear volume and the dissipated energy, i.e. the evolution of wear follows the relationship as shown in Figure 2.2a. This assumption has been doubted by some recent work that indicates that an energy threshold ( $E_{th}$ ) can be found in some particular cases, below which no wear was observed even though damage is being accumulated [83, 93], indicating that the evolution of wear in fretting should have an incubation period before the steady state

as illustrated in Figure 2.2c. The value of  $E_{th}$  was estimated to be ~13 J for fretting tests conducted with steel–alumina specimen pairs; whereas for TiN–alumina specimen pairs, the value of  $E_{th}$  is ~2.3 J [17]. In both cases, the value of the energy threshold is relatively small, which is believed to be associated with the point contact produced by the sphere-on-flat contact configuration. Similar wear behaviour was observed by Ramalho et al. [93] where steel balls were fretted against coated and uncoated flat steel specimens (again, generating a point contact) under conditions of normal laboratory atmosphere and in vacuum; an energy threshold can be observed in all cases, with values ranging from ~1.0 J to ~3.75 J. It was proposed that the development of the TTS and the subsequent formation of wear debris need certain amount of energy to be dissipated in to the contact for recrystallising the microstructure of surfaces; such requirement of the energy input is believed to be associated with the presence of energy threshold [83].

Similarly, fretting tests with cylinder-on-flat configurations have been conducted to investigate the energy threshold by Heredia and Fouvry [94]. In this work, Ti6Al4V specimens were employed and an energy threshold of ~4 kJ was reported, above which the wear volume was, again, described as a linear function of the energy dissipated. The work by Pearson [24] was in accord with the work by Fouvry et al. [17] that, in addition to a single energy-based wear rate, the fretting wear behaviour should also be characterised by the threshold energy; an energy threshold of ~1.1 kJ was reported, which was calculated from the experimental results conducted on the same material used in this thesis. Note that the energy threshold is influenced by the contact configuration; the energy thresholds for tests with cylinder-on-flat configuration are significantly higher than the tens of Joules typically reported for sphere-on-flat configuration.

### 2.3.4 The critical role of the third body in fretting

The debris formed in fretting of steel specimens under normal atmospheric conditions is comprised primarily of iron oxide  $\alpha\text{-Fe}_2\text{O}_3$  with a hematite structure, and relatively small amounts of metallic iron [72, 75, 89]. Similarly, other metallic alloys in fretting tend to produce wear debris in the form of their oxide if oxidation is allowed to occur. Despite the oxide debris being commonly perceived as fine particles, the reported size of oxide debris can cover a wide range from 0.01  $\mu\text{m}$  up to tens of microns [3, 63, 66, 72]. As proposed by Kirk et al. [89], oxide debris is originally small but can agglomerate into debris particles with larger size through the effect of tribo-sintering.

Up to this point in the current section (Section 2.3), the description of the evolution of wear in fretting focuses on the formation of oxide debris. However, the crucial difference between fretting wear and sliding wear, namely the transport of species (i.e. the wear debris and oxygen) cannot be ignored; in particular, the debris retention in the contact or the debris ejection from the contact is a key issue (this concept has already been mentioned a number of times in this thesis, and will be reappearing repeatedly throughout). Whilst the process of debris ejection was well acknowledged in fretting research [2, 3, 76], it was not until the paper of Godet “*The third-body approach: a mechanical view of wear*” [19] that a coherent framework was presented to clearly outline its key role, namely the *third body approach*. This concept was further developed and refined by Godet and co-workers [19, 73, 77, 80, 95], and has become perhaps the most important framework when analysing fretting wear behaviour. It was proposed that a complete definition of a fretting contact should be that of two contacting bodies undergoing fretting motion (first bodies) separated by a debris layer (third body). Note that the third body can either be natural (i.e. wear debris formed during the process) or artificial (e.g. lubricants or external particles deliberately supplied to the contact). In this thesis, fretting behaviour is investigated only for dry contacts hence

only the natural third body will be considered; the term third body, by definition, is equivalent to wear debris for all the following contents.

It was suggested that wear can be analysed through the understanding of the flow of the wear debris during the process, for which Godet applied principles of lubrication theory to the third bodies to analyse their role in the evolution of wear in fretting [19]. He proposed that the presence of the debris layer can change wear behaviour completely: it acts as a film of solid lubricant to separate the contacting bodies (i.e. the first bodies), carries the load and accommodates velocity differences between the first bodies. Indeed, evidence that oxide debris can provide protection against wear in a contact may be found long before the introduction of the third body approach; in the work by Halliday and Hirst [72], it was observed that the high CoF at the early stage of fretting can be restored by continuously removing the wear debris out of the contact. Following on from the third body approach by Godet [19], the role of velocity accommodation provided by the third bodies was later examined by Colombie et al. and Berthier et al. [73, 77]. They suggested that if a debris layer with sufficient thickness can be maintained, then shearing and sliding induced by the fretting motion will be mostly accommodated by the debris layer resulting in reduced deformation in the first bodies. The experimental work by Colombie et al. [77] was carried out by: (i) deliberately removal of oxide debris from the contact; (ii) supply of artificial oxide debris into the contact. The observation was similar to that reported in the work by Halliday and Hirst [72] that the presence of debris layer can provide protection and limit (or even prevent) further surface degradation for the first bodies by forming a compact and stable bed of debris at the interface so that direct metallic contact can be prevented.

As a result, in order for fretting wear to proceed, the removal of surface particles are required to form oxide debris and then, most importantly, to be transported out of the contact [80]. As Godet noted after introducing the third body approach [80], the classical definition of wear as the detachment of particles is only part of the wear process. This

view is supported by Berthier et al. [73, 96] who argued that the evolution of wear in fretting is controlled by both the formation and ejection of debris, rather than only by material removal from the first bodies. With the third body approach, it was argued that a complete description of wear in fretting process should not only include debris formation (as the traditional definition of wear derived from Archard's work [16]), but also the role of debris in modifying the contact and the flow of debris ejection out of the contact. To quote Fillot et al. [37]:

*"...Archard's law... primarily focuses on the process of particle detachment. Its goal is only to measure the matter removed from the rubbing surfaces, without taking into account the way this matter protects the materials in contact from further degradation by accommodating the sliding velocity. This is why, when introducing the concept of the third body to understand wear, the latter is redefined as the ejection of the third body outside the contact".*

The complete description of the fretting wear was further developed by Berthier [96] with the concept of *tribology circuit* being proposed (as illustrated in Figure 2.13). Here, the wear process in fretting is considered as a pipeline with debris flowing from a "source" to a "sink": the process starts with particle detachment from the first bodies and continues with the formation of oxide debris (the "source"); finally, depending upon the accumulation within the contact and other variables that may influence the contact conditions, debris is ejected from the contact at a certain rate (the "sink"). Berthier et al. [73] suggested that fretting wear is primarily influenced by the ability of debris to escape from the contact, and thereby should be understood as a "sink" rather than a "source" problem; i.e. the amount of wear in fretting should be defined as the amount of material being transported out of the contact.

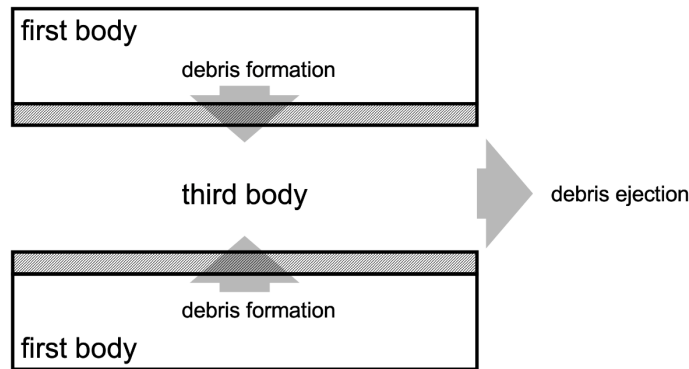


**Figure 2.13: Berthier's illustration of the tribology circuit (after [96]).**

A key aim of much research in fretting wear is the derivation of a single parameter linking the various variables which describe the exposure to wear and the amount of wear that results, namely the wear rate. Many parameters can influence the rate of the evolution of fretting wear by exerting controls over the competition between the formation and ejection of the oxide debris. Although not explicitly stated, the rates of debris formation and ejection from the contact must be equal in the steady state [37]. If the fretting wear is a “sink” problem as suggested by Berthier et al. [73], i.e. the flow of debris out of the contact can determine the observed wear rate, then the effects of various tribological system parameters on the wear rate for fretting needs to be understood from the perspective of their effects on the rate of debris ejection. Indeed, with the framework laid out for the concept of the third body approach, a number of recent papers from the University of Nottingham [20, 23, 24, 97] have examined the effects of various parameters, such as displacement amplitude, temperature, contact geometry and oscillation frequency; irrespective of their focus, the conclusions of these studies converge on a discussion of how the tribological system parameters influence the formation and ejection of debris, and how a change in debris retention or ejection can alter the wear behaviour and therefore the wear rate. Perhaps, amongst all other parameters, the rate of debris expulsion is most sensitive to the size of the contact [98] since this “represents the distance the third body particles must travel [before ejection

from the contact]” [99]. Discussing the effect of the contact size on the debris ejection will be one of the primarily goals for this thesis.

## **2.4 The role of contact geometry in fretting**

### **2.4.1 Common contact geometries in fretting**

In nearly all of the fretting research, simplified geometries are commonly used to investigate the wear behaviour of more geometrically complex components. Those simplified contacts can be categorised into two primary categories, namely the conforming contact and non-conforming contact. Figure 2.14 illustrates some examples of commonly used contacts in fretting research. Conforming contact configurations (e.g. the flat-on-flat contact) were heavily used in early research into fretting since they represent many contacts experiencing fretting wear. However, it is difficult to align conforming surfaces when conducting experiments; moreover, the location of the initiation of wear within the conforming contact (presumably the wear starts at the location where the local pressure is at the maximum) seems to be random, which raises difficulties of predicting (and therefore, controlling) the experimental process [69]. Non-conforming contact configurations, typically cylinder-on-flat (CF), sphere-on-flat (SF) and crossed-cylinders (CC), also replicate contact types seen in many service conditions. However, in contrast to the conforming contacts, the issue associated with alignment can be greatly reduced when non-conforming contacts are adopted. Moreover, the conditions of non-conforming contacts can be theoretically analysed when experiencing elastic loading. As discussed in Section 2.2.1, the contact pressure at the centre of the contact area (the elastic contact area for the CF contact is a rectangle and a circle for the SF contact) is at the maximum but falls to zero at the edges, which enables the location where wear initiates to be more predictable. It should be noted that, whilst the contact size is constant as the tests evolve when a conforming contact configuration is employed (since that the displacements between the two

bodies in a fretting contact are generally very much smaller than the size of the contact), this is not the case for non-conforming geometries. For non-conforming geometries, the contact size increases continuously as wear proceeds (as long as debris can be transported out of the contact), which changes the scale and the distribution of the contact pressure [69].

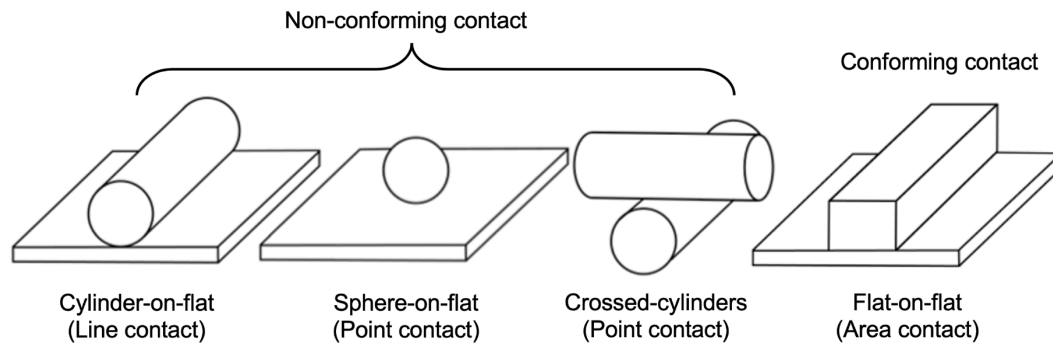


**Figure 2.14: Examples of different contact configurations used in common fretting wear research and their corresponding resulting contact type (after [100]).**

#### 2.4.2 Changing views about the role of contact geometry in fretting

It is generally assumed that contact geometry does not directly influence the wear behaviour, and relatively little work has investigated its effects. The importance of the contact conformity has been overlooked for decades because of the concept of true contact area proposed by Archard, based upon which, Greenwood and Williamson [101] developed a model stating that the true area of contact that will be linearly proportional to the applied load. For example, the size of each micro-contact extends with the increase of the normal load but more asperities are brought into contact leading to the increment of the number of micro-contacts, thus the mean size of each micro-contact remains the same and the true contact area increases linearly. On the other hand, if the applied load is kept as constant, changing the contact size can alter the size and the number of micro-contacts inversely, resulting the true contact area being constant.

According to the model developed by Greenwood and Williamson [101], a change of conformity would not affect the true contact area, and the wear only occurs over the

true contact area; therefore the fretting wear behaviour (normally characterised by the wear volume and wear rate) should be independent upon the contact conformity similar to sliding wear. A contact with large area should lead to a wide but shallow wear scar, whilst a narrow and deep wear scar will result from a contact with small area, but both should have the same wear volume, and therefore the same wear rate. This relationship is expected to be true for both conforming and non-conforming contacts, i.e. regardless of whether the contact size expands throughout the wear process or not, the wear behaviour is expected to be independent of the contact size. This theory has been applied in fretting research, and is attractive in that it allows direct comparison of the wear behaviour between the experimental results acquired from the simplified geometries to those contacts in service with more complex geometries, as well as between tests with different geometries.

However, the significance of debris behaviour (i.e. the debris formation and the debris ejection) in fretting is very different from that in sliding wear and plays a critical role (discussed in Section 2.3.4). As a result, the assumption that the evolution of wear in fretting is independent of the contact geometry should be doubted, since the contact geometry intrinsically influences the size of the contact area (the apparent contact area) and thereby changes the debris formation and ejection in fretting. For example, Waterhouse suggested that fretting contacts can be divided into two categories depending on the behaviour of oxide debris [3, 69]: a surface with shallow dish-like depressions is formed if debris is able to escape from the contact, whilst entrapment of debris leads to small but deep holes. It was found by Kuno and Waterhouse [102] that even the direction of the fretting motion may influence the debris ejection: they conducted fretting test for crossed-cylinders contact configuration with the oscillatory motion being applied on the moving upper specimen in two directions, namely the applied motion perpendicular to the axis of the stationary lower specimen (Figure 2.15a), and the applied motion parallel to the axis of the stationary lower specimen

(Figure 2.15b). The results indicated that the wear in case (a) is significantly more than in case (b), with the difference in the severity of wear by changing the direction of the applied motion only being caused by the ease of oxide debris ejection from the contact, with the debris being seen to protect the contact from the further damage if retained inside the contact. Research work by Jordanoff et al. [103] utilised a rheology law to model the debris behaviour in fretting contacts. It was suggested that the shape of the contact will influence the debris ejection, with this being more significant in the direction of the fretting motion as opposed to perpendicular to it.

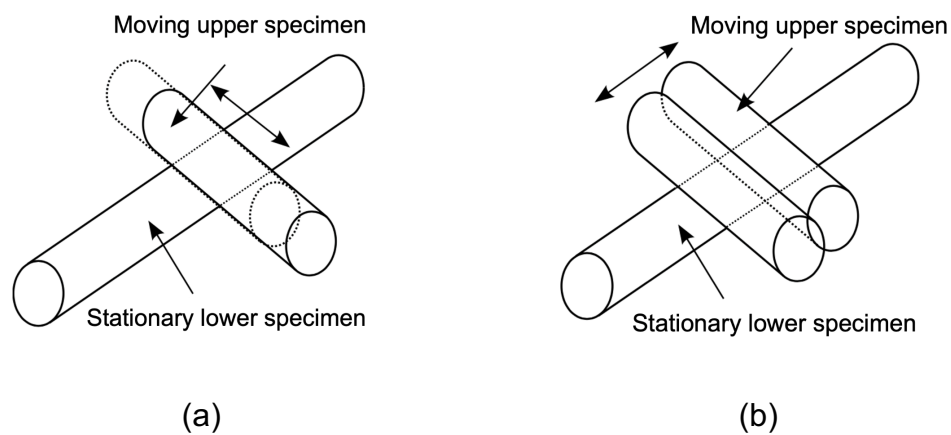


**Figure 2.15: Illustration of the fretting test conducted for crossed-cylinder contact configuration with the oscillatory motion being applied in two different directions: (a) the motion is perpendicular to the axis of the stationary lower specimen; (b) the motion is perpendicular to the axis of the stationary lower specimen [102].**

When a non-conforming contact geometry is employed in fretting research, the contact size increases continuously as the exposure to wear develops, which in turn is perhaps expected to influence the balance between debris formation and ejection. Therefore, to discuss the role of contact geometry in fretting, in particular for non-conforming contacts, is broadly equivalent to examining the effect of contact size. Indeed, recent work which investigated the effect of contact geometry (and therefore the contact size) examined two aspects of the effect of the contact size, namely its effect on the oxygen supply associated with the debris formation and its effect on the debris ejection.

### 2.4.3 The effect of contact size on oxygen supply

Perhaps the first attempt to address the effect of contact size in fretting was conducted by Merhej and Fouvry [36] and Fouvry et al. [18]. It was found that, as the increase of the conformity of the contact area, i.e. as the radius of the cylindrical (or spherical) specimen, the normalised unified energy wear coefficient ( $\overline{\alpha_u}$ ), which is essentially the observed wear rate, is reduced. Note that a new term called the normalised unified energy wear coefficient was introduced in this work, but its core concept is still the Archard-type approach and thus is indeed a normalised wear rate. In another words, with the same level of the exposure to wear, the observed wear volume is reduced with the increase of the contact size. This is completely contradictory to the concept of the true contact area proposed by Archard [25] and its following expansion by Greenwood and Williamson [101], since it suggests that the macroscopic size of the contact area is a controlling factor in fretting. Moreover, in this early research by Fouvry et al. [18], a threshold contact size was proposed as demonstrated in Figure 2.16. It was suggested that the wear rate is influenced by the contact size initially but then becomes independent of it upon it after reaching a threshold value. However, there remains a lack of clarity around whether this threshold contact size truly exists or whether it is an unnecessary term which was introduced to interpret the experimental results. Overall, the concept of threshold contact size is rarely discussed in later works since Fouvry et al. [18].

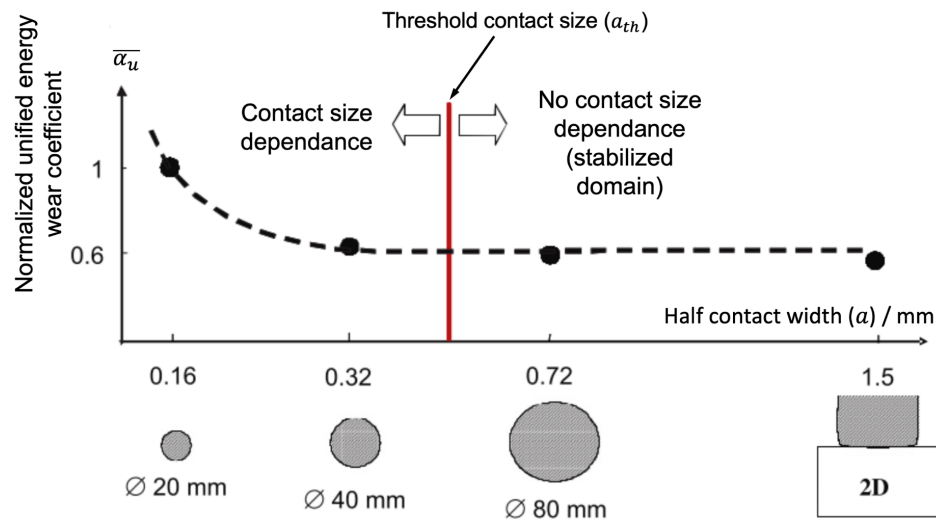


**Figure 2.16: Demonstration of the concept of the threshold contact size in examining the effect of contact size upon observed wear rate for cylinder-on-flat contact configuration [18].**

Similar observations of reduced wear rate with an increase of contact conformity were reported by Warmuth et al. [20, 23]. A more significant observation was that there is a change of fretting wear mechanism from abrasive wear to adhesive wear and metal transfer with pit and peaks across the contacting surfaces as the contact size increased. The formation of oxide debris in fretting process requires a continuous supply of oxygen, and depletion of oxygen can occur if the rate of oxygen transport into the interface is not sufficient to replenish the consumption of oxygen during the fretting process [104, 105]. The contact conformity changes the contact size and thereby influences the distance over which that oxygen must be transported into contact from the environment. It was therefore argued that, as the fretting contact became more conforming, the larger contact size limits the oxygen ability to penetrate across the whole contacts, resulting a higher tendency of more conforming contacts to form a direct metallic contact, the consequence of which is adhesive wear and metal transfer [20, 23]. Such damage does often results in low wear volumes (debris not escaping from the contact) which therefore causes the reduction in the observed wear rate. However, the relative low rate of wear for more-conforming contact does not indicate the low level of damage to

the materials in contact, as proposed Warmuth et al. [23], the pit-peak features caused by the adhesive wear may be significant in terms of the tendency for fretting fatigue.

The argument that a larger contact size can limit the transport of oxygen into the contact has been further developed more recently. Fouvry et al. [90] and Baydoun et al. [106] developed a model to explain the phenomena of the presence of the oxygen-starved areas at the centre of fretting contacts (termed the *adhesive zones*) under certain conditions; such oxygen-starved areas were also previously observed by Warmuth et al. [20, 23] and Fouvry and Merhej [107]. In these adhesive zones, the absence of oxide debris was suggested, again, to be associated with the limited ability of oxygen transport caused by oxygen being consumed in the outer regions of the scar, and thereby the insufficiency of oxygen in the centre of the to support oxide debris formation. In some latter works [91, 106], fretting tests were carried out with conforming contact (flat-on-flat contact configurations): grooves were machined on one of the contacting surfaces paralleling to the direction of fretting motion in order to facilitate the oxygen transport into the contact, and it was shown the adhesive wear zones caused by the oxygen starvation can be significantly reduced with the presence of grooves.

#### **2.4.4 The effect of contact size on debris ejection**

In addition to the effect of contact size on limiting the transport of oxygen into the contact (and therefore the debris formation), its effect on the transport of debris out of the contact is also significant. As discussed in Section 2.3.4, a complete description of the fretting wear process should include debris formation, the role of debris in modifying the contact and debris ejection from the contact. Research since the work by Godet [19] has generally acknowledged the importance of the debris behaviour in fretting (in particular the debris ejection) [73, 77, 80, 96]. It has been recognised that the rate of debris ejection from the contact is dependent upon the contact size [98] since the contact size is the distance for wear debris to travel before being ejected out of the

contact [99]; however, the issue is generally addressed qualitatively rather than quantitatively. Relatively few investigations have been conducted to specifically examine the effect of contact size from the perspective of the debris transport out of the contact. In those recent works as discussed above [18, 20, 23, 34, 36, 90, 107], although the reduction of the observed wear rate was also interpreted as debris being easily entrapped inside the contact, the focus of the arguments is still the oxygen supply in to the contact to form the debris. Moreover, a quantitative analysis of the wear rate being influenced by the difference in debris ejection resulting from the contact size of fretting remains unexamined.

## **2.5 The role of slip amplitude in fretting**

As discussed in Section 2.1.1, fretting wear was conventionally defined as the reciprocating sliding wear with small amplitude of displacement. After the widely recognised work by Vingsbo and Söderberg [4] (shown Figure 2.1), it appears that the most common practice to distinguish fretting wear and reciprocating sliding wear from each other is using displacement amplitude as the criteria. Moreover, with the development of the concept of the fretting map as described in Section 2.2.2, different combinations of normal load and displacement amplitude can strongly influence the fretting regimes and the corresponding damage mechanisms; when the normal load is fixed, the increase of the displacement amplitude can increase the extent of slip across the contacting surfaces, leading to a transition from a partial stick regime to gross slip regime. The displacement amplitude and its role in fretting is, therefore, intrinsically rooted into the core of fretting research. Indeed, many studies have shown that the mechanisms (in terms of the debris formation and ejection), and hence the rate, of fretting wear can be strongly influenced by the displacement amplitude. It should be noted, as outlined in Section 2.2.3, that the amplitude of the applied far-field displacement ( $\Delta$ ) is different from the actual slip ( $\delta$ ) due to the existence of system

compliance [24]. Failing to distinguish between these two terms may lead to a misinterpretation of experimental results. In reality, the actual slip amplitude ( $\delta^*$ ) is the item of interest when researchers discuss the role of displacement amplitude ( $\Delta^*$ ). However, the concepts of the displacement amplitude and the slip amplitude are sometimes somewhat confused in the literature. This issue, coupled with the wide range of test configurations and combinations of different materials, is perhaps one of the reasons why there is still uncertainty around the effects of slip amplitude in fretting, despite slip amplitude being one of the most fundamental elements in fretting wear, which consequently has been studied for a very long time.

In broad terms, slip amplitude, in a similar way to the contact geometry described in Section 2.4.3 and Section 2.4.4, can exert influence on fretting process by influencing debris formation and debris ejection. The influence of slip amplitude on debris formation, although being less commonly discussed in the literature, is through the change of oxygen supply as well as the local temperature caused by the change in rate of energy being dissipated into the contact (i.e. the dissipated power) as the slip amplitude changes. In addition, the slip amplitude changes the ability of debris to escape from the contact, which can disrupt the formation of protective layer of debris and hence influence the rate of wear process.

### **2.5.1 The effect of slip amplitude on debris formation**

In fretting, the closed nature of contact means that there is a significant portion of the contact remains unexposed during the fretting cycle since the amplitude of the motion is much smaller than the contact size. As proposed by Fouvry et al. [108], a larger slip amplitude can open the contact to the environment and thus reduces the portion of the unexposed area, thereby increasing the transport rate of oxygen into the contact (as illustrated in Figure 2.17), which encourages the oxidative mechanism and therefore enhances the formation of oxide debris.

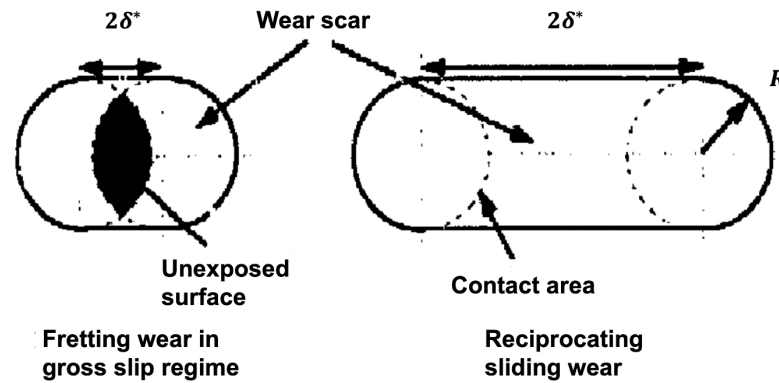


**Figure 2.17: Schematic diagram illustrating the portion of the unexposed surface in fretting being reduced as the increase of slip amplitude (after [108]).**

However, research by Warmuth et al. [20] demonstrated that perhaps the elevated debris formation caused by the larger slip amplitude is not that straightforward. This investigation [20], although being set up primarily for the study of the effect of contact geometry, included slip amplitude as an additional extra variable. As described in Section 2.4.3, the more-conforming contact (with a larger radius of the cylinder specimen, which hence generates contacts with larger size) may restrict the oxygen supply, leading to a higher tendency for direct metallic contact between the two bodies to occur, resulting in pit-peak features and significant sub-surface damage. However, it was also observed that whether the more-conforming (larger) contacts will develop such features is dependent upon the slip amplitude: for the more-conforming contact, larger slip amplitudes are associated with adhesive damage across the contacting surfaces (and the corresponding sub-surface microstructural damage) while the same contact under smaller slip amplitude exhibits the formation of coherent oxide-based debris beds. This observation indicates that, in contrast to the work by Fouvry et al. [108], the increase of the slip amplitude may act to limit the transport of oxygen and hence facilitate the adhesive mechanism. Or, it might also be explained by the theory that the formation of debris bed is restricted when the rate of debris ejection from the contact is high due to the increased slip amplitude, which will be explored in the next section.

These opposite observations associated with the increase of slip amplitude may be explained by the fact that the larger slip amplitude can lead to a larger dissipated power (dissipated energy per unit time, as indicated by Equation 2.9 based on Equation 2.2):

$$\frac{dE_d}{dt} = 4\bar{\mu}\delta^* P f_{Hz} \quad (2.9)$$

this higher power dissipation results in a rise in local temperature and hence the depletion rate of oxygen within the contact is enhanced. As a result, such an increase of oxygen consumption rate is competing against the rate of oxygen transport being brought increased by the more open contact, causing the wear mechanism to exhibit different results under certain test conditions. In the work by Baydoun et al. [91], a concept termed the *adhesive zone* was introduced, which is a central area of a fretting contact which is damaged mainly by adhesion and is surrounded by an area where the presence of oxide debris is prominent. It was found that the size of adhesive zone is independent upon the slip amplitude, suggesting that perhaps two competing factors could be balanced out, the result of which is that the change of overall wear behaviour may seem to be independent of the slip amplitude.

### 2.5.2 The effect of slip amplitude on debris ejection

The effect of slip amplitude on debris ejection is more well-understood compared to its impact on debris formation. As described in the work of Heredia and Fouvry [94], there is a threshold of slip amplitude, below which the wear process seems to cease to occur; it was postulated that a sufficient slip amplitude is required to initiate the wear process in fretting, allowing debris to be ejected from the contact, thereby promoting continuous wear. Fouvry et al. [33] also proposed that the larger slip amplitude can enhance the rate of debris ejection; they argued that, when a larger slip amplitude is employed, debris can be ejected faster and a greater portion of dissipated energy within the contact can thus contribute to the debris formation. Please note that this argument is

based on the assumption that the rate of forming new debris is dependent on the ejection of existing debris. A similar view was proposed by Aldham et al. [109] and Warburton [110] who suggested that larger slip amplitude tends to create a rougher contacting surface and give wear particles a higher velocity, and hence the oxide debris can be transported more efficiently out of the site of generation.

As observed by Fouvry et al. [108], the shape of the wear scar can also be influenced by the slip amplitude. It was found that there seems to exist a transition from W-shaped wear scar (the maximum wear occurs near the edge of the scar while the centre experiences less wear) to U-shaped (the wear is at its maximum at the centre of scar and reduces monotonically towards the edge) with the increase of slip amplitude. The nature of the material at the centre of a W-shaped scar has been the subject of debate: it could be either a build-up of oxide debris at the centre of a U-shaped metal surface [18, 108], or it could be a metallic central region dominated by adhesive damage surrounded by a more worn region associated with the formation of oxide debris [90, 91, 111]. Whilst the nature of W-shaped wear scars is not clear (and indeed may differ in different situations), the occurrence of a U-shaped scar is normally associated the higher rate of debris ejection. The sufficient oxygen supply is also important in determining the type of scar; it was observed by Mi et al.[112] that, under the same set of test conditions except whether the test was conducted in air or in water, the contact producing a W-shaped wear scar in air would instead generate a U-shaped scar in water. It was proposed that the water accelerated the process of debris ejection and washed out those debris which would otherwise have been retained inside the contact and produced a W-shaped scar. It should be noted that this observation is not necessarily strong evidence that a W-shaped wear scar is formed mainly by debris; there is possibility that, at the central region where debris is difficult to escape, the rate of debris formation also ceases, leading to the wear process being almost stopped and the substance at this region is still metal. Moreover, fretting in a water environment is

also likely to reduce the rate of oxygen transport into the scar to form oxide debris. Nevertheless, the observation by Mi et al. [112] appears to support the increased rate of debris ejection associated with the increase of slip amplitude and hence the transition from W-shaped and U-shaped can be observed.

One of the consequences of an increased rate of debris ejection is that the formation of protective debris beds is reduced. It has been found that contacts with larger slip amplitude exhibit a significantly higher degree adhesive damage than those with smaller slip amplitudes [27, 109, 110]. Another piece of evidence was outlined in the work by Hayes and Shipway [97]: in this work, the role of temperature in forming stable debris beds (i.e. glaze layers where the wear rate drops to almost zero) in fretting was investigated. It was found that the temperature at which glaze layer was formed was elevated by the increase of slip amplitude; they proposed that the larger slip amplitude resulted in a higher rate of debris expulsion, thus reducing the residence time of the debris in the contact and thus limiting the tendency of the debris to sinter into a coherent debris bed. This view about the disruptive effect of debris ejection on formation of a protective debris may be used to explain the observation by Warmuth et al. [20] as described in the previous section (Section 2.5.1): here it was postulated that the increase of slip amplitude (and thus the increase in dissipated power in the way that they had conducted their tests) meant that the oxygen could be transported into the contact fast enough, but it is now suggested that the observed effects may be associated with an enhanced rate of debris ejection. The issue about the effect (and their causes) of slip amplitude on fretting remains unresolved with an understanding that the nature of this problem is very complex.

### **2.5.3 The effect of slip amplitude on wear rate**

As emphasised a number of times in the current chapter, the final observed wear rate should be viewed as the result of both the rate of formation and ejection of oxide debris.

The complex nature of the effects of slip amplitude suggests that it is difficult to address the issue individually in terms of debris formation and ejection; perhaps viewing its influence on the combined result of the rate of debris formation and ejection, i.e. the observed wear rate, is more fruitful. Despite the fact that there is a significant variation in reports of how the wear rate is dependent upon the slip amplitude, the general observation is that, before reaching to the reciprocating sliding wear in which the wear rate is independent upon the amplitude of relative motion [16], the wear rate increases with slip amplitude (as demonstrated in Figure 2.1) [4, 18, 27, 33, 72, 81, 91, 108, 111, 113]. The effect of slip amplitude is strong: Vingsbo and Söderberg's [4] widely reproduced figure indicates an increase in wear rate of around two orders of magnitude as the slip amplitude is increased by a factor of around twenty (from  $\sim 15 \mu\text{m}$  to  $\sim 3000 \mu\text{m}$ ). It has been widely recognised that the higher slip amplitude can promote the transport of debris out of the contact, and hence restricts the formation of protective beds of oxide debris and allows the wear process to proceed at a higher rate) [4, 18, 27, 33, 72, 81, 91, 108, 111, 113]. It has been widely recognised that the higher slip amplitude can promote the transport of debris out of the contact, hence restrains the formation of protective beds of oxide debris and allows the wear process to proceed at a higher rate.

However, some have questioned the widely –accepted dependence of the wear rate upon the slip amplitude [24] and have argued that the wear rate should be independent upon the slip amplitude as predicted by Archard wear equation [16]. The experimental evidence, conducted over a range of applied displacement amplitude (from  $\Delta^* = 25 \mu\text{m}$  to  $\Delta^* = 100 \mu\text{m}$ , noting the information about the corresponding slip amplitude was not given) and applied normal load (from  $P = 250 \text{ N}$  to  $P = 650 \text{ N}$ ), indicates that all experimental results can be described by a linear relationship between the dissipated energy and wear volume, as shown in Figure 2.18, which can be characterised simply

by an energy wear rate and an energy threshold for the onset of wear (described in Section 2.3.3), suggesting that the wear rate is thereby independent of slip amplitude.

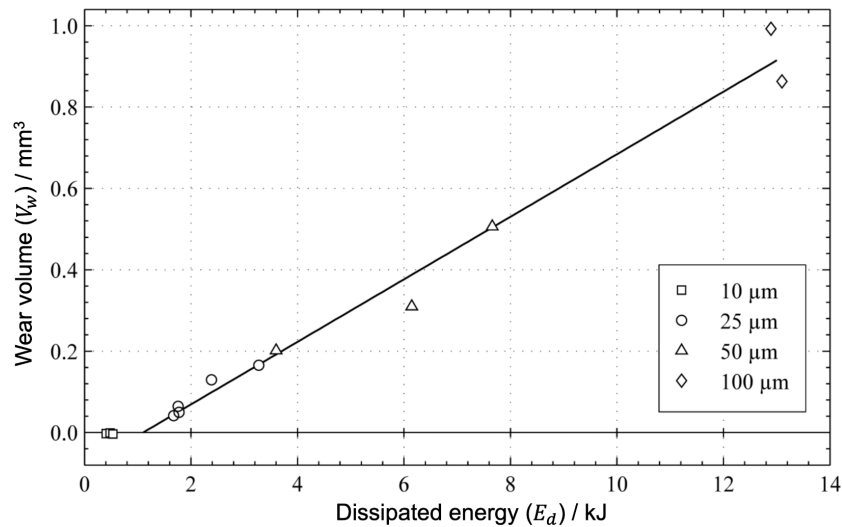


**Figure 2.18: Original representation of the plot showing the wear volume as the function of the dissipated energy with tests conducted with various displacement amplitude (hence the slip amplitude although the exact values of the slip amplitude is unknown) and various normal load (after [24]).**

However, as pointed out by Aldham et al. [109], typical service duration for industrial applications is much longer than the number of cycles that has been employed in literature, a long test duration is necessary when investigating the corresponding effects of different parameters in fretting. The work by Pearson and Shipway [24] suffers from the limitation, which is being shared among many other researches in literature, that the test duration is relatively short (only  $10^5$  cycles); moreover, the coupled effect of the normal load makes the claim of the independence of slip amplitude upon the wear rate unjustified.

Overall, whilst the work of Vingsbo and Söderberg [4] is widely accepted, it does seem to conflict with the equally widely accepted view that we can use an Archard-type analysis for fretting wear, with its focus on wear being proportional to either the total distance slid or total energy dissipated. This conflict indicates that a more holistic understanding of the role of slip amplitude in debris generation (including oxygen transport) and debris ejection is required.

## 2.6 Summary and thesis aims

Understanding both the mechanical and chemical nature of the contact, and their complex interactions, is essential in studies of fretting. The apparent similarities between fretting and sliding lead to the definition of fretting wear as a branch of reciprocating sliding wear with small amplitude of relative motion. However, there are perhaps more differences than similarities when comparing fretting wear and sliding wear, the direct migration of many concepts and methods that were originally developed for sliding wear to the analysis of fretting may perhaps be inappropriate.

In general terms, the following processes must occur in both the fretting and sliding of metals: (i) mechanical deformation at asperity level; (ii) the formation of oxide before debris particles are detached from the surfaces or vice versa; in either case, oxide wear debris is formed at the site of deformation; (iii) the transport of debris out of the contact. However, in contrast to sliding wear, the closed nature of the contact in fretting means that transport processes themselves play a role in and control the rate of the overall process of damage and wear. Specifically, the oxide-based debris formation is influenced by the transport of oxygen into the contact; with sufficient oxygen supply across the contact, the presence of oxide debris helps to prevent severe sub-surface microstructural damage in the metal (this is similar to the transition between severe wear and mild wear in sliding). Similarly, the transport of debris out of the contact has been identified as a key process by a substantial body of fretting research: the presence of debris inside the contact can act to moderate or even prevent surfaces from further damage. It is therefore argued that fretting wear is the result of both debris formation and ejection, and can be considered as a pipeline flowing from the source, which is debris formation, to its sink (i.e. debris ejection). Both processes are strongly influenced by the distance over which active species (i.e. oxygen or debris) are required to travel, resulting in the size of the contact being a critical (but almost always overlooked) factor in fretting. Moreover, in many studies, the size of the contact patch changes

significantly through the course of a test since a non-conforming geometry (such as sphere-on-flat or cylinder-on-flat) is employed, but any effects of this changing size of contact have not been discussed in literature where the conventional Archard-type approach is still the main method for quantitative analysis.

There is clearly an issue to be addressed here: despite the wide general acknowledgement of the role of debris ejection in fretting as a result of Godet's work on third-body effects in fretting from the 1980s, the issue of contact size in fretting (which has a strong influence on that debris ejection) continues to be overlooked. It is stressed that this contact size-effect in fretting is universal (regardless of the conformity of the contact) and needs to be considered both in service environments and in experimental testing. Accordingly, in this thesis, the effects of contact size and displacement amplitude on debris ejection from fretting contacts (and thus upon their overall gross-slip fretting wear behaviour and rates) will be studied using steel-steel specimen pairs in a cylinder-on-flat configuration with cylinders of different radii. The non-conforming nature of the contacts means that, as wear proceeds, the contact sizes will change, and it is hypothesised that the rate of wear will change in light of that. This issue will be explored alongside that of the effect of displacement amplitude on the transport of debris out of the developing contacts.

## Chapter 3 Experimental methodology

### 3.1 Materials and specimens

All of the specimens (both the flat and cylindrical specimens) employed in this thesis were made from a high strength alloy steel (BS S132), which is currently used for the LP shaft of the Rolls-Royce plc Trent series of aero-engines. Raw specimens were cut into blanks with adequate tolerance (~0.5 mm) and then undertaken a heat-treatment process. Details about heat treatment can be found in previous work [114]; key steps are summarised here: specimens were heated at 940 °C for 45 min, then quenched in oil and subsequently tempered at 450 °C for 120 min. Table 3.1 and Table 3.2 [114, 115] present the chemical composition S132 and its mechanical properties after the heat treatment.

**Table 3.1: Chemical composition of the high strength steel used in this work ( / wt. %) [114].**

C	Mo	V	Cr	Si
0.35-0.43	0.8-1.10	0.15-0.25	3.0-3.5	0.1-0.35
Mn	Ni	P	S	Fe
0.4-0.7	<0.3	<0.007	<0.002	Balance

**Table 3.2: Mechanical properties of the high strength steel used in the current study [115].**

$\sigma_y$ / MPa	$\sigma_{ut}$ / MPa	HV30	$E$ / GPa	$\nu$
1247	1697	485±10	206.8	0.28

The tolerance material on all the outer surfaces of heat-treated blanks were ground off to remove the soft decarburised layer generated during the heat treatment. These

specimen blanks were then machined into two categories: (i) flat specimens; (ii) cylindrical specimens with various radii ( $R$ ), namely 6 mm, 15 mm, 80 mm and 160 mm. The final dimensions of both the flat and cylindrical specimens are detailed in Appendix D. The finished surface was required to exhibit a surface roughness ( $Ra$ ) in the range of 0.1 – 0.3  $\mu\text{m}$  for flat specimens and 0.4 – 0.7  $\mu\text{m}$  for cylindrical specimens. For individual specimen quality control, Vickers hardness testing with a 30 kgf applied load (HV30) was performed on three locations of the top surface of the machined specimens to ensure that the required surface hardness (see in Table 3.2) was achieved.

### 3.2 Experimental configuration

In this work, all fretting tests were carried out with a pair of specimens, one flat specimen and one cylindrical specimen with specific radius ( $R$ ), producing a non-conforming contact. The specimen pair was arranged in a cylinder-on-flat configuration as shown in Figure 3.1, creating an initial line contact with the length of  $L = 10$  mm, with the length of the contact perpendicular to the fretting motion. There are some key benefits which support utilisation of the cylinder-on-flat configuration: (i) it replicates well service applications with line contact geometry; (ii) it can reduce the difficulty during the manufacture of specimens (compared with spherical specimens) and the issue associated with specimen alignment in the fretting couple (compared with flat-on-flat configurations); (iii) for the same wear volume, it tends to result in a higher wear depth than flat-on-flat contacts so that any effects of surface preparation (e.g. surface roughness, machining damage) are minimised; (iv), the line contact created by such an arrangement typically evolves into a wear scar with uniform shape, and hence helps to simplify the analysis into a 2D representation; (iv) it allows direct comparison with previous work conducted at the University of Nottingham using the same materials. Due to the nature of non-conforming contacts, the contact will increase its width as wear in the pair progresses (the contact length,  $L$ , is a constant). The relative motion

between the first bodies, i.e. the flat specimen and cylindrical specimen, is induced by the reciprocating movement applied to the cylindrical specimen, resulting in a displacement between the first bodies ( $\Delta$ ) with amplitude  $\Delta^*$ . The load ( $P$ ) applied normal to the contact (as indicated in Figure 3.1) is applied via a dead load and lever arrangement (as illustrated in Figure 3.2).

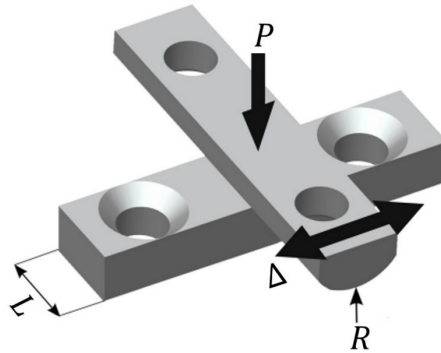


**Figure 3.1: Illustration of the cylinder-on-flat configuration employed in fretting tests for the current study with  $L = 10$  mm and  $R = 6, 15, 80$  or  $160$  mm.**

Care must be taken when machining and aligning the specimen pair as shown in Figure 3.1 to ensure an evenly distributed load. Deviations from an ideal cylinder-on-flat configuration will be quickly compensated once wear starts to take place (the depth of wear is generally much greater than machining tolerances). However, misalignment during assembly will result in a non-uniform wear scar shape, hence losing the simplicity of the geometry by employing the cylinder-on-flat configuration; care is taken to maintain alignment and to scrap results from any pairs where the post-test scar shape indicated misalignment.

Figure 3.2 is a diagram showing all the main components of the fretting test rig used in this work. The rig was initially designed and manufactured by Pearson [79] to study the effects of different parameters in fretting, namely the applied load ( $P$ ), the displacement amplitude ( $\Delta$ ), the temperature ( $T$ ), the frequency ( $f_{Hz}$ ) and the test duration ( $N$ ). The functionality of each principal component of the test rig can be found in Pearson's thesis [79]. Warmuth further extended the rig's capacity [116], allowing fretting tests at higher

frequency (from  $f_{Hz} = 20$  Hz up to  $f_{Hz} = 200$  Hz) to be carried out (see the details of the modification in Warmuth's work [116]).

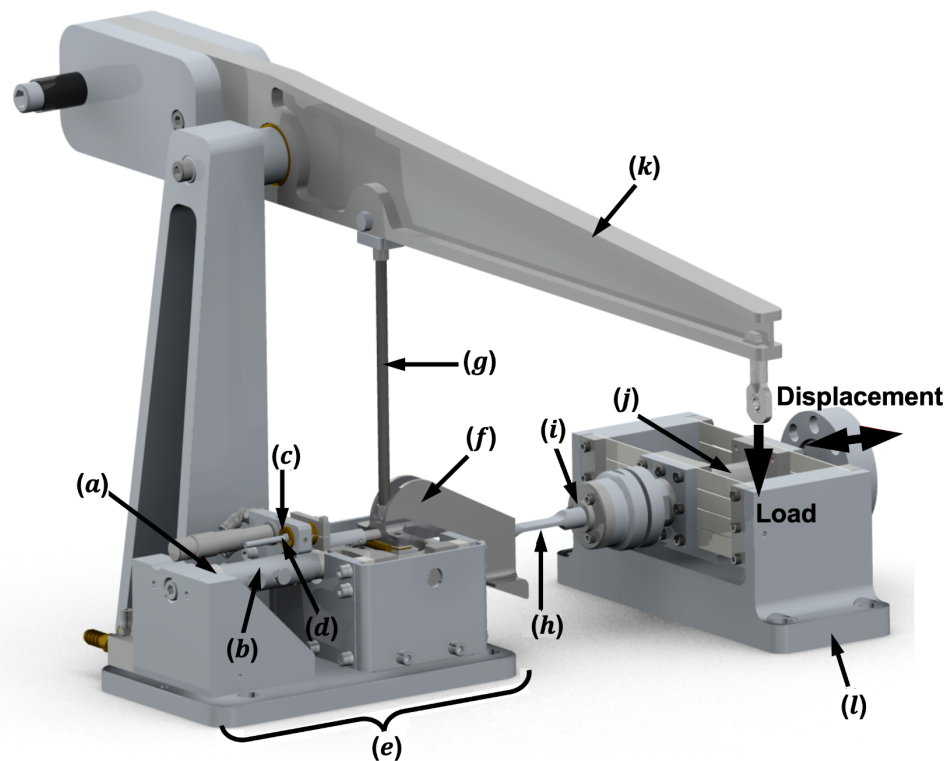


**Figure 3.2: Diagram of the fretting test rig for the current study with its main components: (a) load cell; (b) water cooled spacer; (c) water cooled displacement sensor mount; (d) capacitance displacement sensor; (e) lower specimen mounting block (LSMB); (f) upper specimen mounting block (USMB); (g) load pin; (h) drive linkage; (i) alignment coupling; (j) stinger housing; (k) load bar; (l) linear guide vane assembly (after [116]).**

Note that the sources of the applied displacement and load are not shown in Figure 3.2 for the clarity of illustration. In practice, the flat and cylindrical specimens are mounted on their corresponding mounting blocks, i.e. the flat specimen to the lower specimen mounting block (LSMB, component *e* in Figure 3.2) and the cylindrical specimen to the upper specimen mounting block (USMB, component *f*). The orthogonally crossed configuration for the flat and cylindrical specimens, as shown in Figure 3.1, can be achieved by securing the USMB to the alignment coupling (component *i*). A deadweight is placed at the end of a cantilevered load bar (component *k*), producing a downward force amplified by five times due to the leverage structure of the load bar. The amplified force is transmitted through the load pin (component *g*) and applied on

top of the USMB, with the intention of creating a uniformly distributed normal force ( $P$ ) on the cylindrical specimen. As described earlier in this section, the relative motion between the flat and cylindrical specimens is produced by an oscillating movement applied on USMB, and thus the cylindrical specimen, whilst the LSMB is stationary. Such displacement on USMB ( $\Delta$ ) is driven by an electromagnetic vibrator (EMV) at a designated frequency ( $f_{Hz}$ ) through a flexible drive linkage (component  $h$ ), which was designed specifically [116] to allow a slight degree of misalignment during the specimen pair assembly and to be tolerant of the small vertical displacement of the upper specimen associated with the development of wear during the course of a test.

The reciprocating lateral displacement of the USMB ( $\Delta$ ), and thus the cylindrical specimen, is measured by a CS08 Micro-Epsilon capacitance sensor (component  $d$ ). This displacement information is used to control the force output from the EMV to achieve the designated displacement amplitude ( $\Delta^*$ ) throughout the test. Since the nature of the contact is evolving (both geometrically and in terms of the nature of the materials at the surface), the tangential force ( $Q$ , with amplitude of  $Q^*$ ) required from the EMV changes accordingly (the maximum force output from the EMV is  $\sim 2$  kN). The tangential force is monitored by a Kistler 9132BA slimline piezoelectric load cell (component  $a$ ) located on a stationary element of LSMB. The details regarding the experimental configuration for mounting both the capacitance sensor and the load cell on the LSMB can be found in Figure 3.3 Please note that Figure 3.3 contains some additional components (component  $m$  to component  $p$ ) that are not initially presented in Figure 3.2; the numbering order in both figures is consistent.

Both data of the displacement and the tangential force are sampled and recorded in a data file (in the file format of TDMS, a file format developed by National Instruments™) at a rate of 200 measurements for each fretting cycle throughout the test irrespective of the fretting frequency.

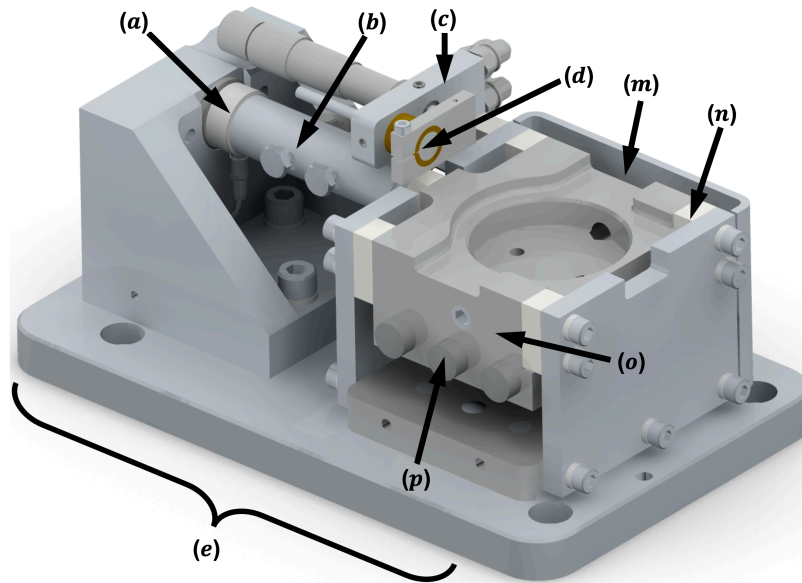


Figure 3.3: Diagram of the lower specimen mounting block (LSMB) in greater detail showing the experimental configuration of: (a) load cell; (b) water cooled spacer; (c) water cooled displacement sensor mount; (d) capacitance displacement sensor; (e) lower specimen mounting block (LSMB); (m) side plate (the side plate on the other side is removed in this diagram to reveal the cartridge heater inside); (n) one of the thermal barriers; (o) main body of the mounting block to contain specimens; (p) one of the cartridge heaters (after [116]).

### 3.3 Experimental procedure

The preparation work on specimen pair (one flat specimen and one cylindrical specimen) for each fretting test involves thorough demagnetisation and surface degreasing before rinsing with acetone to remove water residue. After this, specimens are sprayed with industrial methylated spirit (IMS) to remove acetone and thoroughly dried with an air duster.

After preparing the specimen pair, specimens are attached to mounting blocks, which are subsequently assembled in the fretting test rig. To arrange the specimens in a cylinder-on-flat configuration, the flat and cylindrical specimens need to be mounted on the LSMB and the USMB, respectively. Figure 3.4 is a simplified illustration showing the essential components of the fretting test rig. Details about the transmission of the applied load ( $P$ ) and the displacement ( $\Delta$ ) from their sources to the wear contact have been described in Section 3.2. Here is a short review:  $P$  can be applied to the USMB

through a leveraged dead weight, while  $\Delta$  is generated by the EMV and applied to the cylindrical specimen. With the successful assembly of specimen pair to the test rig, test parameters including the displacement amplitude ( $\Delta^*$ ), the frequency ( $f_{Hz}$ ), the temperature ( $T$ ) and the test duration ( $N$ ) can be designated using the control software developed by Pearson [79]. It should be noted that although normal load ( $P$ ) can be defined in the control system for records and further calculations, physical masses need to be placed at the end of the cantilevered load bar.

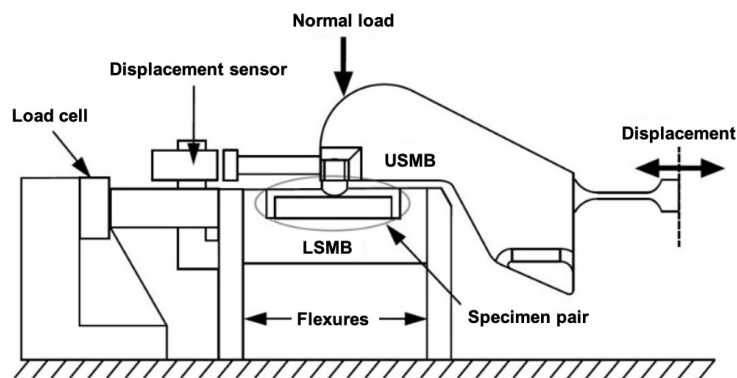


**Figure 3.4: Schematic diagram illustrating the essential components of the fretting test rig in this thesis (after [116]).**

Throughout the test, the relative displacement ( $\Delta$ , with amplitude of  $\Delta^*$ ) between the USMB and LSMB is monitored using a capacitance displacement sensor; the tangential traction force across the specimen pair contact,  $Q$  (with amplitude of  $Q^*$ ) is measured by a piezoelectric load cell. Both the tangential traction force and the relative displacement are sampled and recorded 200 times per fretting cycle.

With the completion of the fretting test, the upper specimen fixture (including components  $f$  and  $h$  in together with the cylindrical sample) is carefully removed by disassembly of the coupling (component  $i$ ) which allows access to the lower specimen. Samples of ejected debris accumulated outside the wear contact are collected in an airtight container for further analysis. The damaged area on each sample in the specimen pair is swabbed with cotton wool and subsequently rinsed with IMS to remove

oxide debris that is loosely attached to the surface of the wear scar, leaving the debris that has been firmly adhered to the surface intact.

### 3.4 Experimental data processing

The majority of the raw data in the TDMS data file are three columns of data: the values of tangential traction force ( $Q$ ) and the displacement ( $\Delta$ ) and the corresponding cycle count. Several quantities of interest need to be determined by processing the raw data, with these being essential to understand the wear contact under different test conditions, namely the system stiffness, the dissipated energy into the contact, the slip amplitude and the coefficient of friction. Please note that these quantities of interest can be determined for each cycle of a test. It is, therefore, necessary to distinguish the notations representing an individual cycle (with  $(i)$  indicating  $i^{th}$  cycle) from those representing the whole test (without  $(i)$ ).

As indicated previously, the 200 measurements of the force and displacement are recorded for each cycle, resulting in the size of the raw data file being directly proportional to the test duration ( $N$ ). In this work, the size of the generated data file ranged from 2.5 MB ( $N = 500$  cycles) to 50 GB ( $N = 1 \times 10^7$  cycles); in particular, the volume of raw data caused significant problems in data processing when the fretting test performed over a long test duration. It was found that the data processing script developed by Pearson [79] was unable to process data files beyond the size of 5GB (when  $N = 1 \times 10^6$  cycles) due to the inefficient use of data structure and memory overflow. A new version of the data processing script was developed and a benchmark test to process a 500 MB data file was carried out. It was demonstrated that the new script outperformed the previous version by a factor of ten (the processing time is reduced from  $\sim 30$  min to  $\sim 3$  min). Moreover, it can process large data files beyond 5GB which cannot be dealt with by the previous version of the data processing script.

### 3.4.1 Description of fretting loop

A fretting loop can be produced with the measurements of the tangential force ( $Q$ ) and displacement ( $\Delta$ ) for each cycle of a test. Within a single fretting cycle, each fretting loop displays the values of tangential force as a function of displacement. An idealised gross slip fretting loop is shown in Figure 3.5 as the representative of those observed in fretting tests.

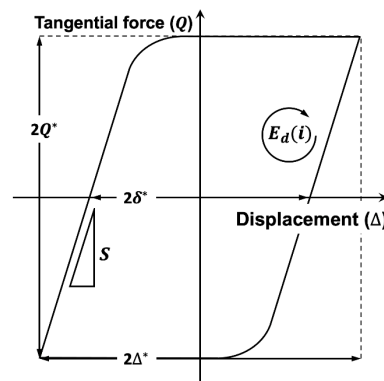


**Figure 3.5: Schematic illustration of an idealistic fretting loop in the gross slip regime.**

The general shape of a fretting loop resembles a parallelogram. The steep vertical sides are related to the region of elastic deformation of the contact; thus, a linear increase in tangential force ( $Q$ ) can be observed with increased applied displacement ( $\Delta$ ). Once the tangential force is above a particular value, the contact begins to slide, and the tangential force remains constant until the displacement amplitude ( $\Delta^*$ ) is reached; the horizontal upper and lower sides of the fretting loop are associated with this sliding period. The gradient of the vertical sides is defined as the system stiffness ( $S$ ). It should be noted, however, that the system stiffness represents the overall compliance of the whole system, which is the stiffness from all the components within the system, and is thereby different from the contact stiffness (identified as the cause of elastic deformation within the contact [24, 31]). In this thesis, the contact stiffness cannot be directly measured, and therefore it is the system stiffness ( $S$ ) being used for further analysis. The value of  $S$  is determined as  $33.3 \pm 3 \text{ N} \cdot \mu\text{m}^{-1}$ , which is calculated as

the average from fretting loops of various experiments across this work. There is loop-to-loop variation within a test and for illustrations relating to loop shapes, average fretting loops can be used.

### 3.4.2 Dissipated energy

The energy dissipated in the contact for each cycle ( $E_d(i)$ ) can be interpreted as the area enclosed by the fretting loop at the corresponding cycle, which is defined as:

$$E_d(i) = \int_{-\Delta^*}^{\Delta^*} Q(\Delta) d\Delta \quad (3.1)$$

Therefore, the total energy dissipated into the contact throughout the test ( $E_d$ ) can be calculated as the summation of the dissipated energy for each cycle:

$$E_d = \sum_{i=1}^N E_d(i) \quad (3.2)$$

where  $N$  is the test duration (i.e. number of cycles).

The calculation method to obtain the dissipated energy for each cycle of a particular test ( $E_d(i)$ ) from its raw data is described in Pearson's work [79], and the total dissipated energy ( $E_d$ ) for that test is the sum.

### 3.4.3 Slip amplitude

It is essential to recognise that the actual slip within the contact ( $\delta$ ) should be distinguished from the applied displacement ( $\Delta$ ) on the USMB, the difference being associated with the elastic displacements due to system (including contact) compliance. The slip amplitude ( $\delta^*$ ) is always less than the applied displacement amplitude ( $\Delta^*$ ) and can be considered as the displacement in the loop when the lateral force is zero (i.e. when the elastic displacement is zero). The slip amplitude ( $\delta^*$ ) cannot be directly measured and needs to be calculated from the far-field measurements of the applied

displacement amplitude ( $\Delta^*$ ) by processing of the recorded fretting loops (see Figure 3.5). It remains difficult to calculate the slip amplitude ( $\delta^*$ ) on the fly during the test, especially at higher test frequencies, and this is done by post-processing. As such, displacement control is based upon  $\Delta^*$  and not  $\delta^*$ . In the current study, the slip amplitude for each cycle of a test was calculated from the collection of raw data, the method of which can be found in Pearson's work [79]. It was found that values of  $\delta_n^*$  are stable throughout the test, and the deviation is negligible; the relative standard deviation (RSD, defined as the ratio of the standard deviation to the mean) is always smaller than 5% when the test reaches the steady-state. As a result, the slip amplitude to represent the whole test ( $\delta^*$ ) can be determined as the average of those values for each cycle ( $\delta^*(i)$ ):

$$\delta^* = \frac{1}{N} \sum_{i=1}^N \delta^*(i) \quad (3.3)$$

More commonly, the slip amplitude ( $\delta^*$ ) can be determined from the fretting loop by measuring the distance between the origin and the displacement when the tangential force reaches zero ( $Q = 0$ ). The relationship between displacement amplitude and slip amplitude can be formulated as follows:

$$\delta^* = \Delta^* - \frac{Q^*}{S} \quad (3.4)$$

It is clear that these are not linearly dependent upon each other; changes that affect  $Q^*$  (such as applied load and coefficient of friction) will result in a change in  $\delta^*$  even if  $\Delta^*$  is maintained constant. In addition, the validity of the assumption of a constant system stiffness,  $S$ , needs to be explored. As indicated by Equation 3.4, a more significant proportion of the applied displacement is accommodated by the elastic deformation of the contact when larger normal loads are applied, with increases resulting in no slip in the contact when  $\frac{Q^*}{S}$  reaches  $\Delta^*$ .

### 3.4.4 Coefficient of friction

The common definition of the coefficient of friction (CoF) for each cycle ( $\mu(i)$ ) is the ratio of the maximum tangential force in the cycle ( $Q^*(i)$ ) to the applied normal load ( $P$ ):

$$\mu(i) = \frac{Q^*(i)}{P} \quad (3.5)$$

As described in Chapter 2, this approach is appropriate if specimens are sliding freely against each other without the local pit-peak feature across the contact or the effect of ploughing (i.e. subjected to Coulomb's friction law), hence producing a fretting loop with the shape identical to that as shown in Figure 3.5. However, to account for non-Coulomb friction (i.e. for variation of the tangential force during the part of a fretting cycle where gross slip is occurring), an alternative definition of CoF was developed by Fouvry et al. [33], which is commonly known as the energy coefficient of friction (ECoF, denoted as  $\mu_e$ ). The value of ECoF for each cycle ( $\mu_e(i)$ ) can be calculated as:

$$\mu_e(i) = \frac{E_d(i)}{4P\delta^*(i)} \quad (3.6)$$

which is the ratio of the energy dissipated in a fretting loop and the product of the distance slid and the normal force applied to the contact. Values of ECoF for different fretting tests were compared with CoF, and it found that ECoF is more representative for the current study; hence ECoF is used for the following analysis in this work. As the dissipated energy and the slip amplitude for each cycle can be calculated from raw data, the ECoF for each cycle can also be determined using Equation 3.6. Similar to the slip amplitude, statistical analysis shows that the value of  $\mu_e(i)$  is stable throughout the test, with the RSD smaller than 3% when the test reaches the steady-state. The averaged value of  $\mu_e(i)$  is used as the representative for individual test:

$$\mu_e = \frac{1}{N} \sum_{n=1}^N \mu_e(i) \quad (3.7)$$

### 3.5 Wear damage characterisation

Following a fretting test, fretting damage was evaluated by conducting profilometric scanning on the wear scar, which gives surface topography information. From this, the wear scar width and the wear volume can be estimated. The distribution of wear debris on the surface was characterised using scanning electron microscopy (SEM). Additional examinations on cross-sectioned cylindrical specimens were carried out to identify the nature of damage beneath the surface of the wear scar.

#### 3.5.1 Surface topography

Two types of profilometers, namely Bruker Contour GT-I and Alicona G5, were used for this thesis to scan the damaged area on both the flat and cylindrical specimens; the scanning areas for both the flat and cylindrical specimens are demonstrated in Figure 3.6. The length of the scanning area is 10.5 mm for flat specimens and 13 mm for cylindrical specimens, while the width of the scanning varies according to the width of the wear scar. It has been observed that the wear scar width in the current study ranges from ~0.3 mm to ~9 mm; therefore, a wide range of the width of the scanning area is required. The extra space on the scanning area allows a slight misalignment during the measurement and is essential to calculate the reference surface.

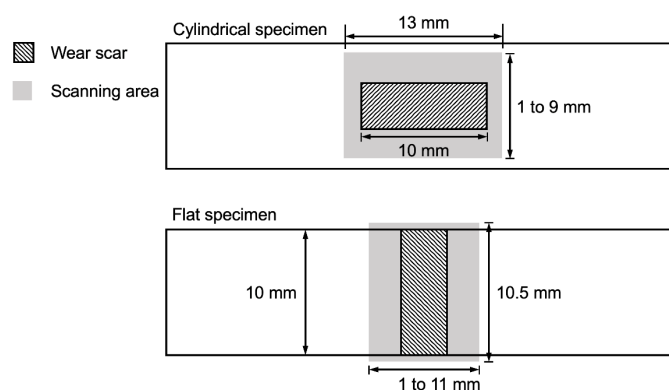
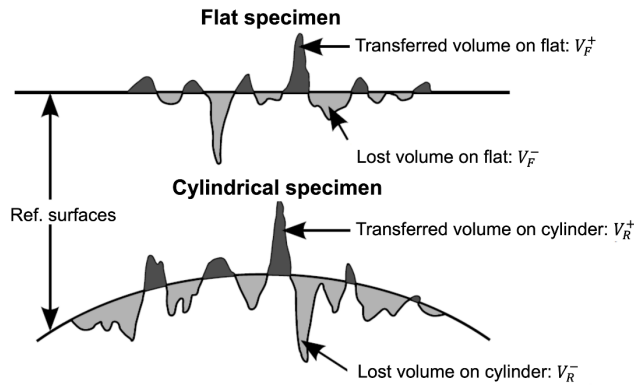


Figure 3.6: Illustration of the scanning area for both the flat and cylindrical specimens.

### 3.5.2 Estimation of wear volume and wear scar width

A reference surface must be determined to represent the surface before the test to estimate the wear volume. The reference surface is defined as the best-fit plane of all surface profiles outside the wear scar for both the flat and cylindrical specimens. The calculation method to determine the reference surface needs the information collected from the extra space of the scanning area; the detail of the calculation method can be found in Pearson's work [79]. It is suggested by Elleuch et al. [32] that the transferred material is defined as the material above the reference surface, with volume  $V^+$ , composed of the transferred volume on the flat ( $V_F^+$ ) and the cylindrical specimen ( $V_R^+$ ). In contrast, the material below the reference surface is regarded as lost material with volume  $V^-$ , as the summation of the lost volume on the flat ( $V_F^-$ ) and the cylindrical specimen ( $V_R^-$ ). The definition of the material transferred, and the material lost is illustrated in Figure 3.7. The overall net wear volume ( $V_w$ ) is defined in Equation 3.8.



**Figure 3.7: Schematic diagram to illustrate the assessment of material transferred and material loss with respect to the reference surfaces [32].**

$$V^+ = V_F^+ + V_R^+ \quad (3.8a)$$

$$V^- = V_F^- + V_R^- \quad (3.8b)$$

$$V_w = -(V^+ + V^-) \quad (3.8c)$$

As described in Section 3.2, the cylinder-on-flat configuration employed in the current study produces a line contact for specimens. Such a line contact typically develops into

a uniform wear scar as the progress of wear. It is, therefore, feasible to use a single average profile to represent the whole damaged area on specimens. This representative profile across the damaged area can be generated by taking the average of individual profiles across the wear scar width. As illustrated in Figure 3.8a (schematically) and Figure 3.8b (using example data from a R160 specimen pair following  $N = 5 \times 10^6$  cycles), the wear scar width ( $x$ ) was determined from the average profile of the wear scar on the flat specimen and defined as the width of the central portion of the wear scar that lay below the reference surface.

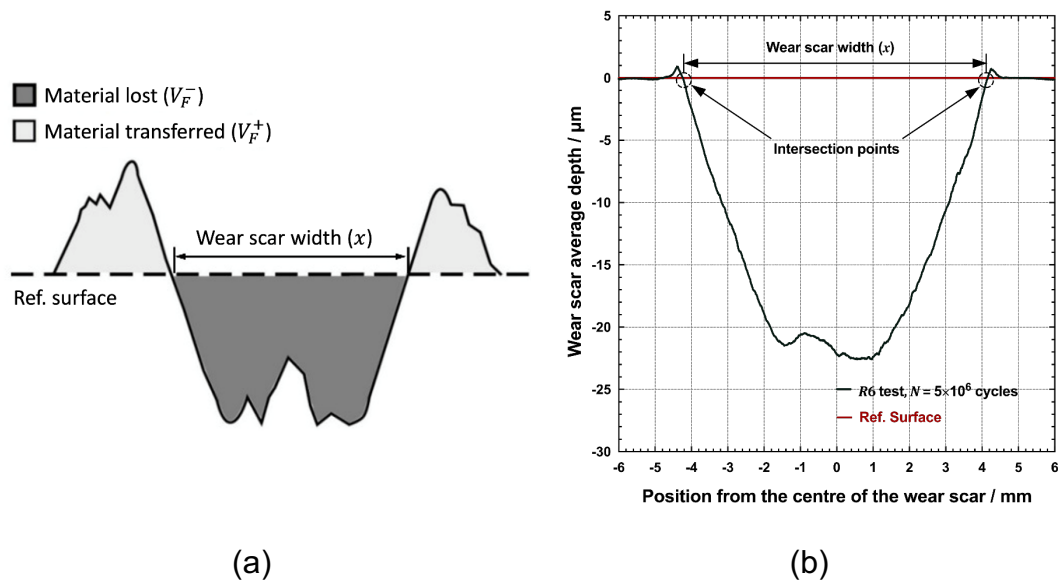


**Figure 3.8:** (a) Illustration of the assessment of material lost and material transferred with respect to the reference surface and the definition of wear scar width; (b) example of the determination of wear scar width from the average surface profile for a R160 test at  $N = 5 \times 10^6$  cycles.

### 3.5.3 Precision and accuracy of measurements

The surface topography of specimen pairs was initially measured with the Bruker Contour GT-I at the beginning of this PhD programme, but the machine was no longer available after the first year, which led to the switch of profilometer to the Alicona G5. Therefore, the Alicona G5 was used to measure the majority of experimental results in this work, and the difference between the data acquired by those two profilometers was

compared. It was found that the measurements for surface topography on tested specimens from both the Bruker Contour GT-I and the Alicona G5 are almost identical, with differences of less than 4%. Several duplicated measurements were taken to examine the repeatability (as defined by the relative standard deviation, RSD) of estimating the wear volume and the wear scar width. It found that the RSD is always smaller than 5% for both the estimated wear volume and wear scar width obtained from Bruker Contour GT-I and Alicona G5 measurements, indicating a high repeatability of measurements.

However, the difference between repeatability (in another word, precision) and accuracy needs to be distinguished. While repeatability concerns the closeness of the measurements to each other, accuracy describes the closeness of the measurements to the actual value. One of the critical contributions from this work is the observation of the geometric relationships of wear volume ( $V_w$ ) and wear scar width ( $x$ ) for cylinder-on-flat specimen pairs for a non-conforming contact in fretting. This observation requires an accurate estimation of wear volume and wear scar width to assert its validity.

To investigate the accuracy of the estimated wear volume and wear scar width, two cylindrical specimens (one with a radius of 6 mm and the other with a radius of 160 mm) were taken for dummy tests. Materials on top of the specimens were ground off to a random depth leaving a flat surface with a length of  $L$  and width of  $x$ , as shown in Figure 3.9. This operation on cylinders ensures that the material removal can be characterised precisely by the minor segment of the cylinder as indicated by Equation 4.2, which is stated here that:

$$V_w = L \left( R^2 \arcsin \left( \frac{x}{2R} \right) - \frac{x}{4} \sqrt{4R^2 - x^2} \right) \quad (3.9)$$

The volume of material removal from the top of dummy specimens and the corresponding wear scar width were estimated using the set of methods described in

Section 3.5.2 for the measurements from both the Bruker Contour GT-I and Alicona G5 profilometers.

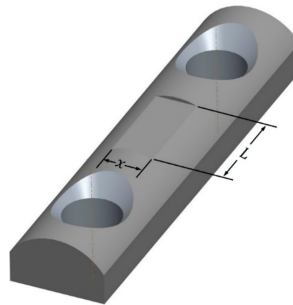


**Figure 3.9: Illustration of the material removal from the top of specimens to evaluate the accuracy of estimations of wear volume and wear scar width.**

Figure 3.10 compares the idealised wear volume (Equation 3.9) against their measured values for the measurements from both the Bruker Contour GT-I and Alicona G5 profilometers. The negligible difference between the data acquired from both the profilometers is demonstrated again, which is smaller than 2% for dummy specimens. The error between the predicted data and the actual value for dummy tests is generally slight, but the error is better for the *R6* cylindrical specimen than for the *R160*, 1.6% versus 8.5%, suggesting that there could exist a systematic error when estimating wear volume and wear scar width, especially for *R160* tests.

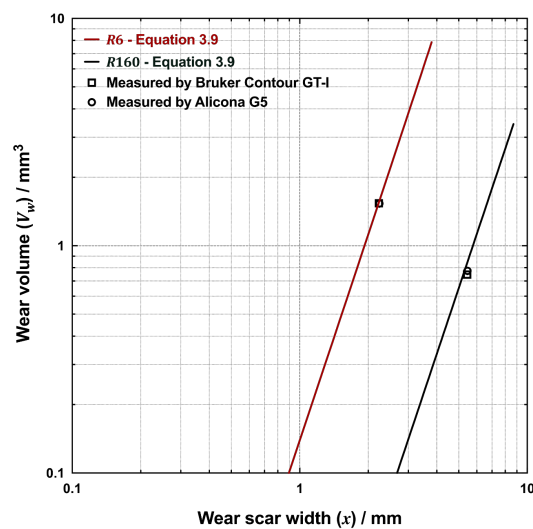


**Figure 3.10: Plot of the wear scar width against wear volume for dummy tests conducted with *R6* and *R160* cylindrical specimens to demonstrate the accuracy of the set of methods to estimate wear volume and wear scar width used in this work.**

### 3.5.4 Nature of wear scar and debris

SEM was used to characterise the wear scar and the distribution of the oxide debris with a Philips XL3 microscope; either secondary electron (SE) or backscattered electron (BSE) imaging techniques were applied based on the type of features being examined. Images were taken at a working distance of 10 mm with an accelerating voltage of ~20 kV. Using the SE detector enables the acquisition of high-resolution optical images to examine topographical features but provides little information about the composition of the material being scanned. In contrast, BSE imaging is beneficial since it allows oxide debris (with its lower average atomic number) to be readily distinguished from the metallic substrates due to its lower imaging brightness.

Cross-sectioning was performed on several cylindrical specimens to allow the characterisation of substrates beneath the surfaces of wear scars. Sectioned samples were obtained with the help of a high-speed slitting wheel, followed by mounting in conductive phenolic resin. A progressive grinding procedure was carried out to polish the surface with silicon carbide papers at increasingly fine grades and finished by polishing with a 1  $\mu\text{m}$  diamond paste. The surface was etched with 5% nital (a solution containing nitric acid and alcohol) to reveal the material's microstructure before being examined via SEM.

## **Chapter 4 The dependence of wear rate on wear scar size in fretting**

### **4.1 Introduction and chapter outline**

Classically, wear is considered to be a process of particle detachment from the surfaces in contact. This is the central concept of Archard's wear model (initially derived for sliding wear and not for fretting wear) [16], which relates the amount of wear (the material removal from the surface, i.e. the wear volume) with the exposure to wear (a combination of the sliding distance and the applied load). As noted by Fillot et al. [37], concepts and terms used in the fretting literature, such as wear rate and wear mechanism, were inherited from the classical Archard approach, where the wear rate describes the rate of material removal from the surfaces. However, in fretting, this debris is easily trapped in the contact region due to the small displacement amplitude (typically tens of micrometres) [2], with the removal of this debris being required for further wear to take place. Therefore, it is argued that the Archard-type approach (without considering the transport of debris out of the contact) is not able to account for the differences in wear rates associated with differences in debris entrapment in the contact.

The concept of the third-body in fretting was introduced by Godet in 1984 [19], who argued that the wear process and rate are the result of the competition between debris formation and ejection. In his early work, Hurricks [2] proposed that the wear particles are first detached from the surface and then oxidised and ground into fine debris, finally forming a debris layer. This layer was referred to as the 'third body' by Godet [19], who suggested the third bodies can act to accommodate velocity and carry load (the concept of which was borrowed from principles of lubrication theory). To some extent, debris provides protection against wear by the formation of stable beds of debris within the contact of fretting. Therefore, in order for wear to occur, debris needs to be

## The dependence of wear rate on wear scar size in fretting

detached from the first bodies and then ejected from the contact, with the rate of wear thereby being controlled by the rheology of the third bodies [73, 80].

The commonly used term wear rate simply refers to the ratio linking the amount of wear (in terms of the observed wear volume) with the exposure to wear defined by tribological system parameters (in terms of the energy dissipated). Since fretting wear itself represents the consequences of both debris formation and ejection, it should be noted that the measured wear volume contains the information related to the complete wear process. Berthier and co-workers [37, 96] therefore suggested that it is not appropriate to interpret wear rate as the rate of particles detachment since the elimination of wear debris from the contact is vital for the development of wear; they illustrated this concept via a tribology circuit as shown in Figure 4.1(a). It is argued that the wear rate is controlled by balancing the competition between the corresponding debris formation and ejection rates. Figure 4.1(b) indicates that the system will tend towards an equilibrium between the formation and ejection of debris [37]; any change in contact would trigger an increase or decrease in the corresponding rate of debris formation or ejection, altering the equilibrium state and influencing the observed wear rate.

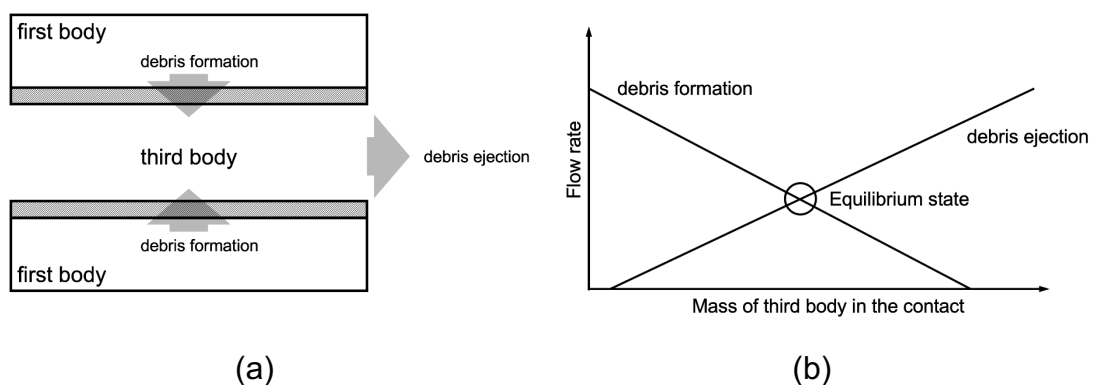


**Figure 4.1: (a) Berthier's illustration of the tribology circuit [96]; (b): illustration of the competition between debris formation and debris ejection [37] for a fretting contact.**

Waterhouse suggested that fretting contacts can be divided into two categories depending on the behaviour of oxide debris [3]. A surface with shallow dish-like depressions is formed if debris is able to escape from the contact, whilst entrapment of debris leads to small but deep holes. More recent work [20, 23, 24, 97] has examined the various tribological system parameters in fretting, such as displacement amplitude, temperature and oscillation frequency, to understand their influence on the formation and ejection of debris and the corresponding wear rate. However, relatively little work has investigated the effect of contact geometry, despite the fact that a large variety of contact geometries have been employed in experimental research. In general, these contact geometries can be divided into two primary categories, namely non-conforming contacts and conforming contacts. The use of non-conforming contacts (e.g. cylinder-on-flat and sphere-on-flat) is widespread because it replicates contact types seen in many service conditions but even when this is not the case, it aids reproducible laboratory experimentation in that it reduces problems associated with specimen alignment. As observed by Fouvry and co-workers [18, 36] and Warmuth et al. [20, 23], the observed wear rate was significantly reduced with increasing contact conformity (i.e. as the radius of curvature of the non-plane body increased). They argued that such reduction in wear rate is associated with the change of fretting wear mechanism (from abrasive wear to adhesive wear) and the increased entrapment of wear debris, noting that both can occur as contact conformity is increased. These investigations of the effect of contact geometry focussed on the role of the third body, which are in line with the work of Godet [19] and Berthier et al. [37, 73, 96]. The third-body approach, together with more recent work on the effect of contact geometry in fretting, point to the critical roles of debris kinematics and contact geometry in the fretting wear process.

It is recognised that when a non-conforming geometry is employed in fretting research, the contact size increases continuously as wear occurs, which in turn is expected to influence the balance between debris formation and ejection. It is suggested that the

## The dependence of wear rate on wear scar size in fretting

observed wear rate is the lesser of (i) the rate of removal from the wearing surfaces to form debris and (ii) the rate of removal of that debris from the contact; a schematic diagram illustrating this hypothesis is presented in Figure 4.2 where the lines represent the maximum rates of both debris formation and debris ejection that the contact may sustain under certain conditions as a function of wear scar width. In cases where debris ejection is the rate-determining step, the contact size will thus exert an influence on the wear rate. In such cases, the observed wear rate is thus a function of the amount of wear (as opposed to being assumed to be constant). It is noted that although the contact size can also influence debris formation by changing the transport of oxygen into the contact, this aspect of the effect of contact size is not the subject of this thesis. To be more specific, the debris formation in Figure 4.2 is only associated with the process of particle detachment from first bodies as outlined in Archard-type approaches.

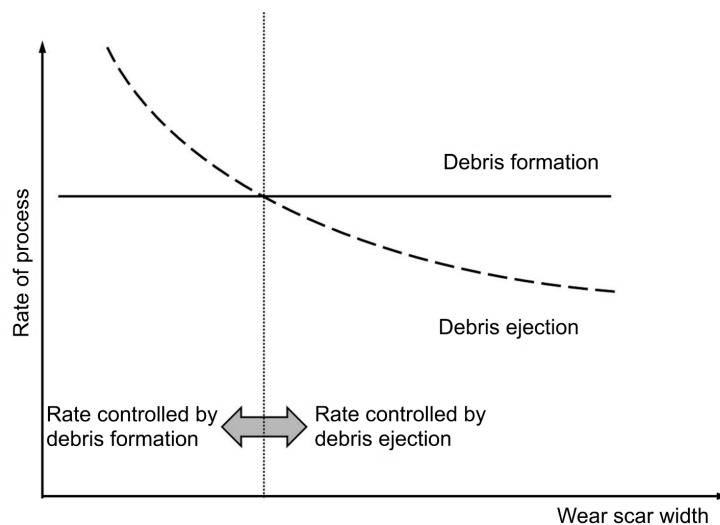


**Figure 4.2: Schematic diagram illustrating the dependence of rates of wear and debris ejection on wear scar width, with regions where debris formation and debris ejection are the rate-determining processes (i.e. the process with the lower of the two rates at any scar width).**

In the current chapter, a cylinder-on-flat configuration was employed (as shown in Figure 3.1), and the evolving contact was characterised by the wear scar width. A wide range of test durations (from  $N = 5 \times 10^2$  cycles to  $N = 5 \times 10^6$  cycles) and two different initial geometries (cylindrical specimens with 6 mm and 160 mm radii, denoted as  $R6$

and  $R160$ , respectively) were employed to obtain different wear scar widths and rates of scar width development. It is argued that changing wear scar width should alter the rate of debris ejection from the contact and thus control the observed wear rate when debris ejection is rate-determining. An analytical wear model is presented, which describes the dependence of the wear rate on wear scar width for a cylinder-on-flat contact across a range of wear scar widths, which are associated with both different initial geometries and different amounts of wear.

Details about the specimens, the test rig and the experimental procedures employed in the current chapter are described in Chapter 3. This thesis is focussed upon the debris ejection behaviour in the gross slip regime, and hence the combination of experimental parameters must serve this purpose to ensure that the contact will remain in gross slip regime throughout the test. To minimise undesirable effects associated with large changes in the tractional load (such as the EMV response and changes in system elastic deformations), a constant normal load was selected, with this being  $P = 450$  N to allow direct comparison with experimental data from the previous bodies of work conducted upon this test apparatus. A constant displacement amplitude of  $\Delta^* = 50$   $\mu\text{m}$  was employed since, again, under this combination of load and applied displacement, gross-slip could be assured irrespective of small changes in the coefficient of friction. The radii of the cylindrical specimens ( $R6$  and  $R160$ ) were chosen to maximise the dissimilarity of the resultant contact size development whilst ensuring that specimens could be readily and reproducibly manufactured. Furthermore, previous work on the effect of contact geometry by Warmuth [116] laid the foundation for this thesis, hence the same specimen geometry was chosen for the consistency of the research. Test conditions for this chapter are detailed in Table 4.1 as below:

Table 4.1: Summary of the fretting test conditions for Chapter 4.

---

Normal load ( $P$ ) / N	450
Displacement amplitude ( $\Delta^*$ ) / $\mu\text{m}$	50
Cylindrical specimen radius ( $R$ ) / mm	6, 160
Test duration ( $N$ ) / $\cdot 10^3$ cycles	0.5, 5, 20, 100, 500, 1000, 2000, 3500, 5000
Frequency ( $f_{\text{Hz}}$ ) / Hz	20
Temperature ( $T$ ) / $^{\circ}\text{C}$	Ambient temperature

---

## 4.2 Experimental results

Figure 4.3 shows  $V_w$  as a function of  $E_d$  for both the  $R6$  pairs and the  $R160$  pairs. It can be seen that, for equivalent dissipated energies, wear volumes are higher for the  $R6$  pairs than for the  $R160$  pairs. Moreover, for both pair types, it can be seen that the wear rate (adopting the traditional concept of observed wear rate, which is defined as wear volume per unit energy dissipated) decreases with increasing energy dissipated. Figure 4.3b illustrates that whilst the wear volume increases with dissipated energy from the outset for  $R6$  pairs, there is an incubation period for the  $R160$  pairs of at least  $\sim 5$  kJ before a measurable wear volume was observed. It should be noted that several (up to six) replicated tests were carried out to investigate repeatability. It was found that the repeatability (as defined by the relative standard deviation, RSD) of both dissipated energy and net wear volume was always less than 10%, and in some cases, much less. Values of RSD for dissipated energy of all repeated tests were found to be smaller than 3%.

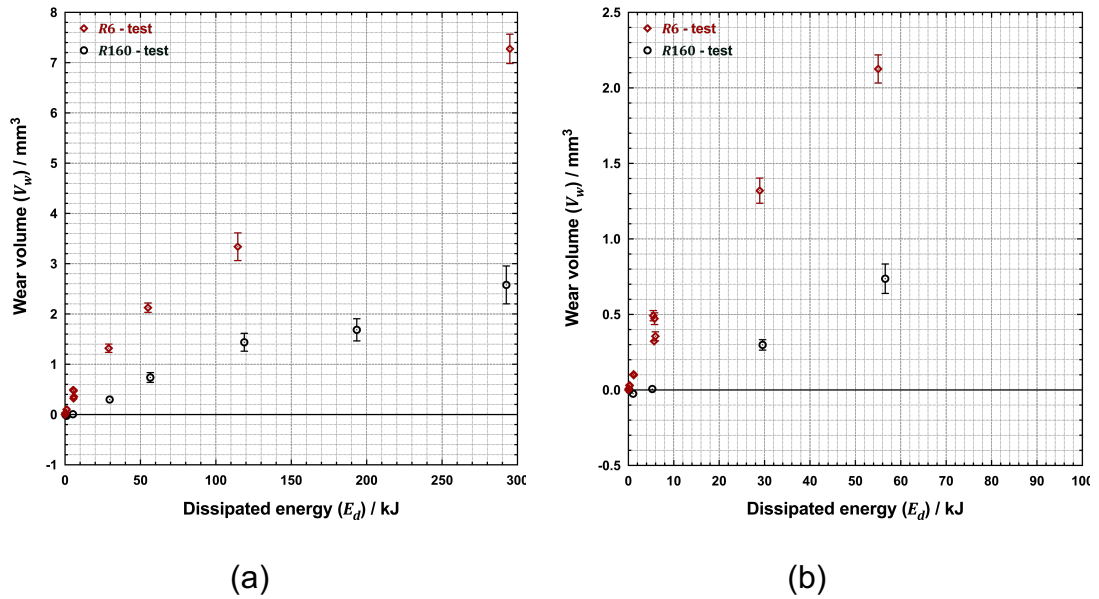
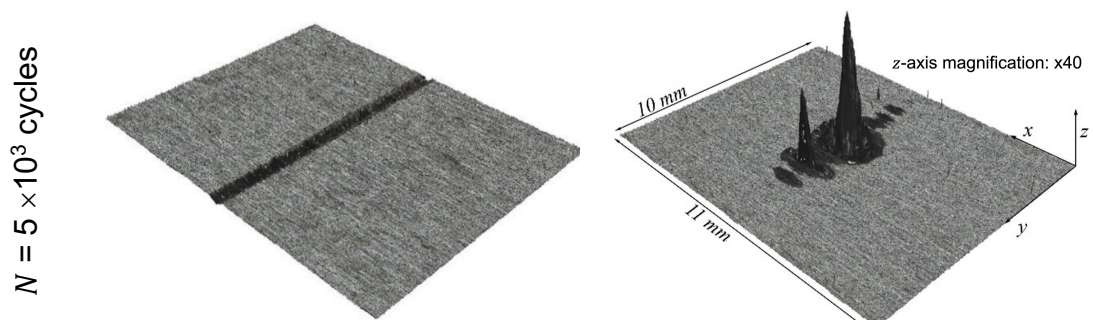
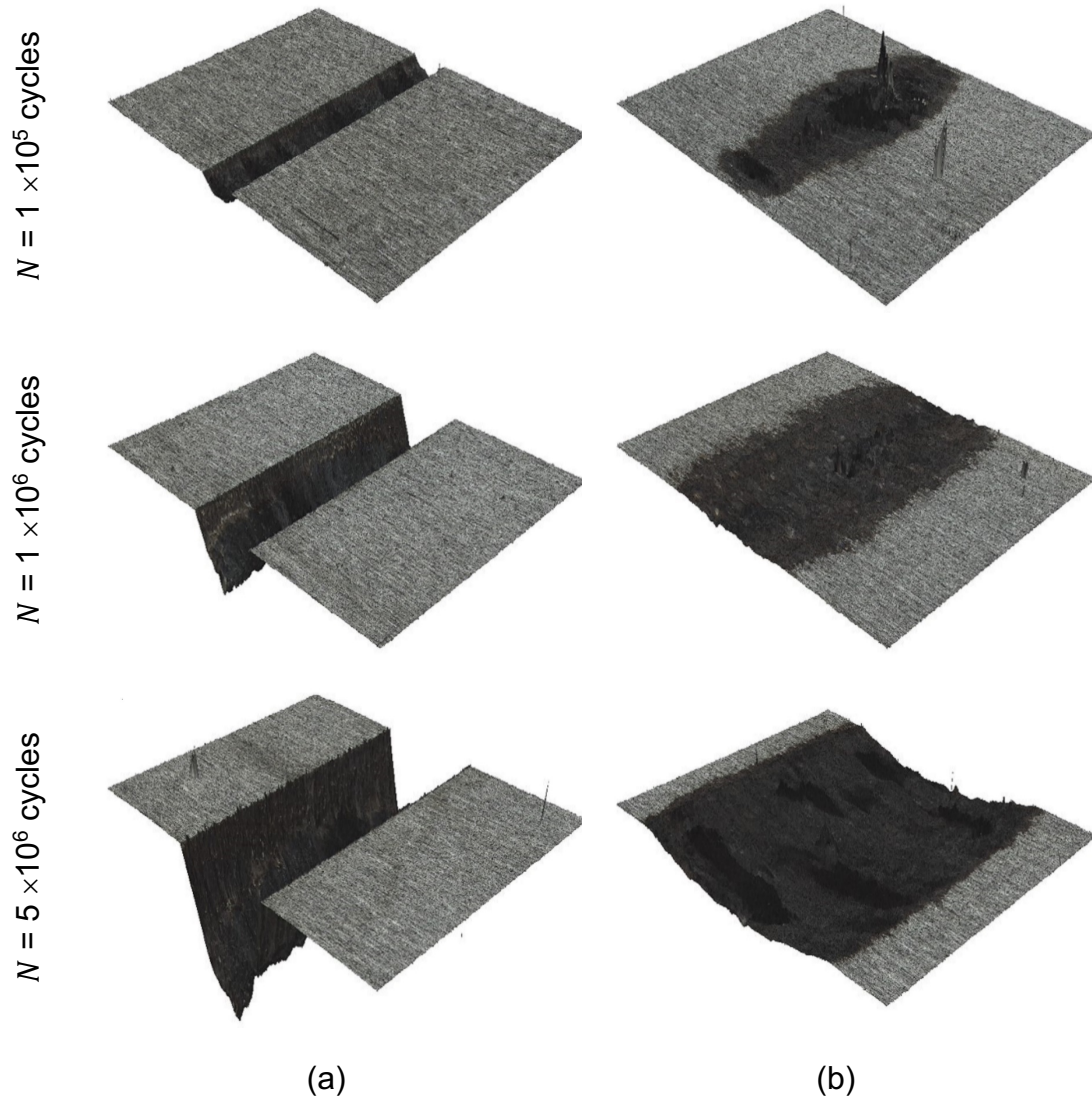


Figure 4.3: Net wear volume as a function of dissipated energy for fretting tests conducted with R6 pairs and R160 pairs: (a) data from all tests conducted for this chapter; (b) detailed view for tests where the dissipated energy was less than 100 kJ, giving a clearer view of the initiation behaviour; error bars are displayed.

Figure 4.4 presents the 3D profilometric representations of the wear scars on the flat specimens for selected tests with both R6 pairs (left column) and R160 pairs (right column) as a function of test duration. Each scanning area is fixed as 10.5 mm in length and 11 mm in width (as described in Section 3.5.1). It has been noticed that the size of the wear scar changes dramatically. The width of the scanning area is fixed at 11 mm to allow direct comparison across different radii and test durations. Please note that the magnification normal to the plane is 40 times greater than that within the plane.



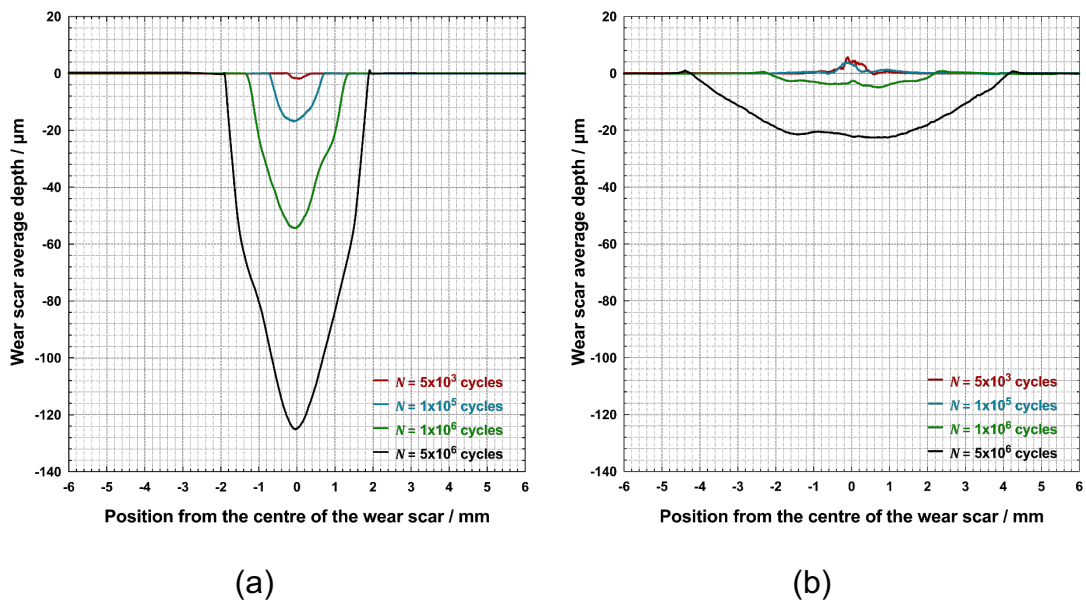


**Figure 4.4: Surface topography images of wear scar on flat specimens for selected fretting tests conducted over a range of test durations, from  $N = 5 \times 10^3$  cycles to  $N = 5 \times 10^6$  cycles: (a)  $R6$  pairs; (b)  $R160$  pairs. The magnification in all images is 40 times in the  $z$ -direction (to provide scale, the height of the peak in the  $R160$  pair after  $N = 5 \times 10^3$  cycles is  $\sim 150 \mu\text{m}$ ); images are acquired from Alicona G5.**

As shown in Figure 4.4, for the  $R6$  pairs, the wear scars are seen to be of uniform width for all examined test durations, and they grow in both width and depth as the cycle count increases. However, as observed previously [20], the more-conforming  $R160$  pairs exhibit the formation of localised pit-peak features in the early stages of the wear scar development (from  $N = 5 \times 10^3$  to  $N = 1 \times 10^5$  cycles); these features result from a metallic transfer between the specimens. It is notable that these features have largely

been eliminated after  $N = 1 \times 10^6$  cycles, following which a wide but relatively uniform wear scar is observed.

Figure 4.5 shows the average profiles of wear scars on flat specimens (derived from the data of the type presented in Figure 4.4) for fretting tests conducted with *R6* and *R160* pairs. Figure 4.5a indicates that a U-shaped wear profile for *R6* pairs is formed as early as after  $N = 5 \times 10^3$  cycles, and this then develops in depth and width as the test duration increases. In contrast, for *R160* pairs, tests with up to  $N = 1 \times 10^5$  cycles (a common set-up for the value of test duration in previous studies at the University of Nottingham [79, 116, 117]) show no significant material removal from the flat specimen; however, the development of a U-shaped wear scar is clearly observed after  $N = 1 \times 10^6$  cycles, growing in both depth and width as the cycle count increases.



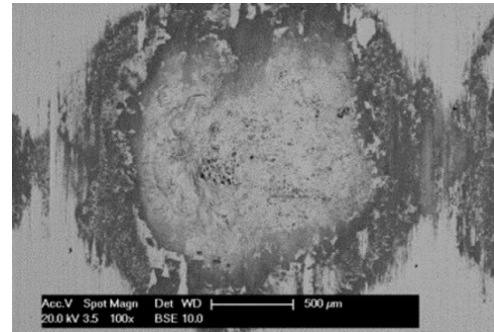
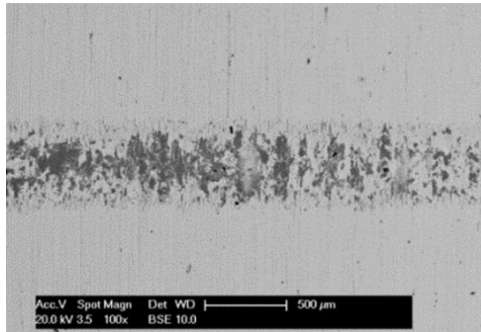
**Figure 4.5: Averaged profiles of fretting wear scar on flat specimens for selected fretting tests conducted over a range of test durations, from  $N = 5 \times 10^3$  cycles to  $N = 5 \times 10^6$  cycles; (a) *R6* pairs; (b) *R160* pairs; profilometry data acquired from Alicona G5.**

Figure 4.6 shows BSE-SEM images of the wear scars on the flat specimens for the *R6* (left column) and *R160* (right column) specimen pairs as a function of test duration. In this imaging mode, oxide debris has lower contrast than metallic debris in the fretting

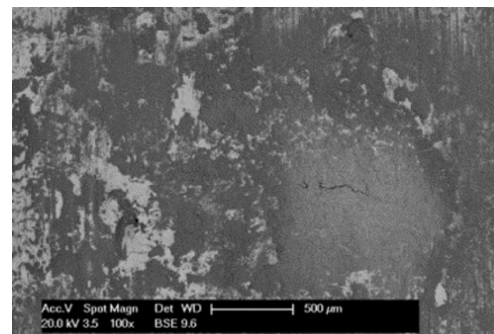
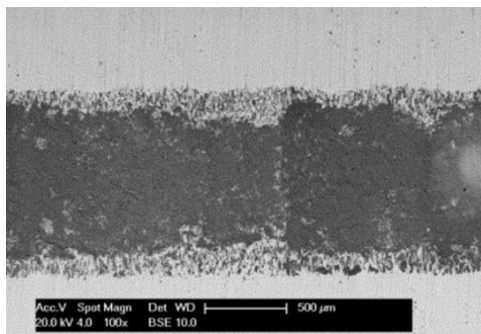
## The dependence of wear rate on wear scar size in fretting

scars due to its lower average atomic number. For the *R6* pairs, it can be seen that the fretting scar is only sparsely covered in oxide after  $N = 5 \times 10^3$  cycles, but that an oxide debris bed has fully covered the scar following  $N = 1 \times 10^5$  cycles. This oxide bed is seen to be non-uniform, with evidence at  $N = 5 \times 10^6$  cycles that the oxide delaminates locally and thus exposes the underlying metallic material to wear further. In contrast, in the *R160* pairs, the pit-peak features observed in the early stages ( $N = 5 \times 10^3$  cycles) are seen to have a predominantly metallic character, indicating that they are formed by metallic transfer between the specimens. After  $N = 1 \times 10^5$  cycles, the surface is covered mainly by an oxide debris bed, although patches where there is no oxide coverage exist. This situation remains after  $N = 1 \times 10^6$  cycles, and it is only after  $N = 5 \times 10^6$  cycles that the oxide coverage in the fretting scar is largely uniform. Indeed, after  $N = 5 \times 10^6$  cycles, there are no significant differences in the oxide coverage in the wear scar between the *R6* and the *R160* pairs.

$N = 5 \times 10^3$  cycles



$N = 1 \times 10^5$  cycles



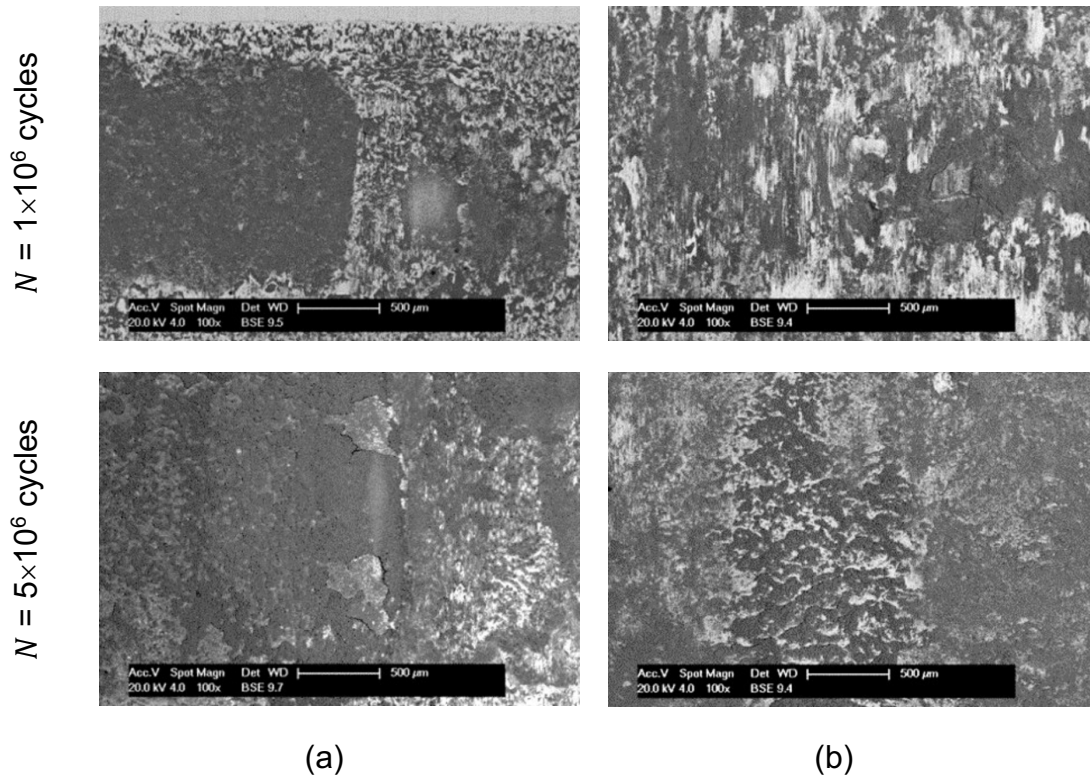
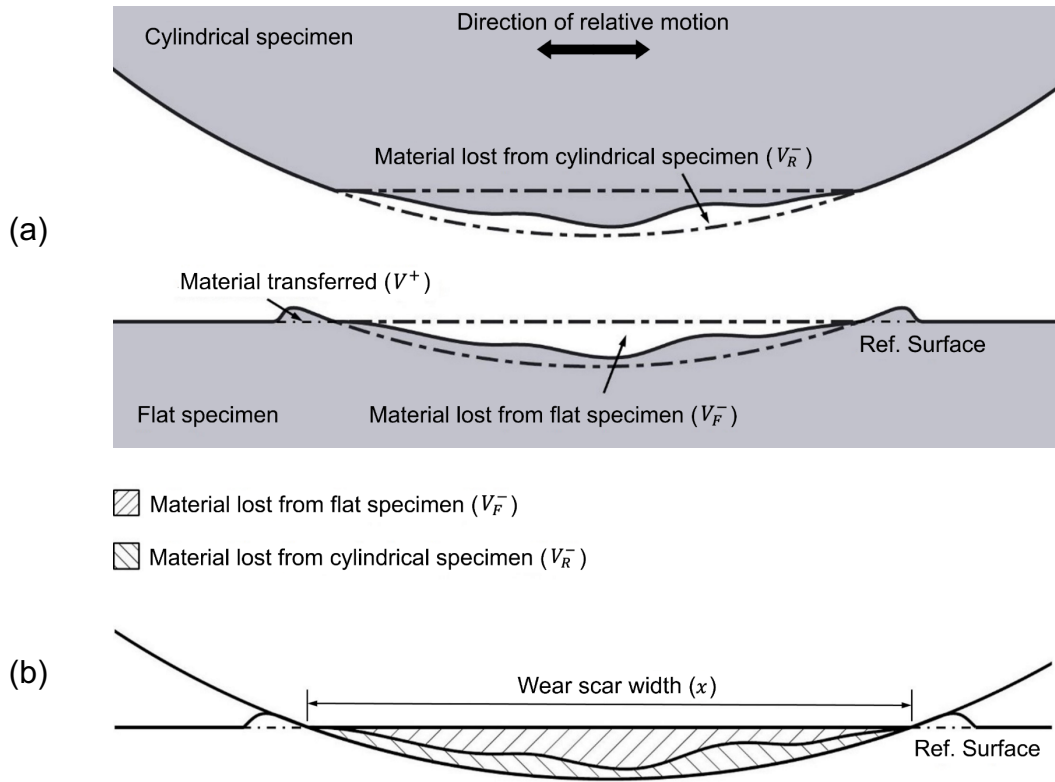


Figure 4.6: BSE images of the top view of the fretting wear scar on flat specimens for fretting tests conducted over a range of test durations, from  $N = 5 \times 10^3$  cycles to  $N = 5 \times 10^6$  cycles with (a) R6 specimen pairs; (b) R160 specimen pairs.

### 4.3 Development of the model

#### 4.3.1 Link between wear scar width and wear volume in a cylinder-on-flat contact.

To facilitate the development of a model which allows the dependence of the fretting wear rate upon the scar width to be developed (see Section 4.3.2), a mathematical relationship between the wear scar width and volume is required; such a relationship is proposed, based upon the assumptions espoused in Figure 4.7. Since the wear scar width is large compared with the slip amplitude, it is assumed that the wear scar on the flat and cylindrical specimens have the same width and indeed share the same profile. It is also assumed that any ploughed material is small and does not result in significant errors in measurement of the wear scar width.



**Figure 4.7: (a) A typical contact of high strength steel after fretting test with a small amount of transferred material at the edge, illustrating the assumption (b) that the combined wear on the two specimens result in a total worn volume equivalent to the minor segment of the cylinder.**

With these assumptions, then it can be seen that the total wear volume (i.e. the combined material lost from the cylindrical and the flat specimens) is simply the volume of the minor cylindrical segment of intersection between the flat and cylindrical specimens (Figure 4.7b). Hence, Equation 3.8c,  $V_w = -(V^+ + V^-)$ , can be approximated as:

$$V_w \approx -V^- = -(V_R^- + V_F^-) \quad (4.1)$$

Therefore, the relationship between wear scar width ( $x$ ) and the volume ( $V_w$ ) can be described as follows:

$$V_w = L \left( R^2 \arcsin \left( \frac{x}{2R} \right) - \frac{x}{4} \sqrt{4R^2 - x^2} \right) \quad (4.2)$$

It is noted that in the following derivation,  $x \geq 0$ . Moreover, in the current experimental configuration, the value of wear scar width,  $x$ , cannot exceed 10 mm since this is the width of the cylindrical specimen as indicated in Figure 3.1; in addition,  $L = 10$  mm in the experimental configuration employed.

Figure 4.8 shows the measured wear volumes plotted against the measured wear scar widths, with the geometrical relationship indicated by Equation 4.2. It should be noted that the data in Figure 4.8 contain additional experimental results for the *R6* pairs outside of the tests reported in this chapter (the additional tests were conducted with the same specimen configuration and material and at the same load and fretting frequency (i.e.  $P = 450$  N and  $f_{Hz} = 20$  Hz, but with  $\Delta^*$  between 10 and 25  $\mu\text{m}$  and  $\Delta^* = 100$   $\mu\text{m}$ ). The data presented relate to wear scars where the scar is broadly uniform in width across the scar; as can be seen in Figure 4.4, a uniform scar was formed in the *R6* pairs following test durations as low as  $N = 5 \times 10^3$  cycles, whereas for the *R160* pairs, much longer test durations were required ( $N = 1 \times 10^5$  cycles) before a sensible and representative estimate of a scar width could be made. As such, the data for the *R160* pairs do not exist at the lower values of width and volume due to the wear scar not being fully formed in these cases.

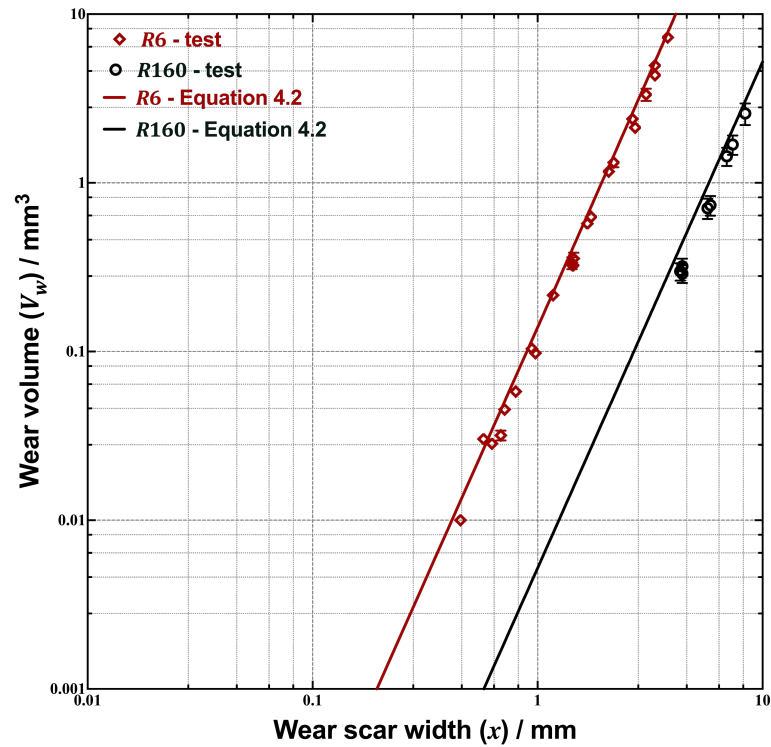


Figure 4.8: Plot of the wear scar width against net wear volume for fretting tests conducted with *R6* and *R160* pairs at varying displacement amplitude from  $\Delta^* = 10 \mu\text{m}$  to  $\Delta^* = 100 \mu\text{m}$  with  $P = 450 \text{ N}$ ; error bars are displayed.

Figure 4.8 illustrates that for the fully formed wear scars, the measured data fit well with the idealised geometrical relationship, but the fit is better for the *R6* pairs than for the *R160* pairs. The average difference between the predicted and measured volumes for a given scar width were  $14 \pm 8\%$  and  $22 \pm 7\%$  for the *R6* and *R160* pairs respectively (with the uncertainty representing the standard deviation of the difference). It is notable that the measured wear volume for a given scar width is always less than predicted value, as would be expected given the assumptions made; in addition, there is no clear trend in the fractional difference in wear scar width across the range examined. However, the accuracy of the estimation of wear volume and wear scar width should be taken into consideration. The accuracy investigation described in Section 3.5.3 indicated that there is a systematic bias between the predicted and measured volumes with the set of methods employed in this work, especially for *R160* tests. The existence of such systematic error suggests that the fit for *R160* tests as shown in Figure 4.8 might be improved by a reasonable amount.

#### 4.3.2 Modelling the effect of wear scar size on the wear rate

In the literature addressing the third-body approach in fretting, it is suggested that in certain circumstances, the rate of wear in a fretting contact is limited by the rate of debris ejection from the contact (as opposed to the rate of material removal from the opposing surfaces). A schematic diagram suggesting how this may relate to the size of the wear scar was presented earlier in Figure 4.2. It is proposed that the debris flow will be parallel to the slip direction with a velocity (displacement of debris particle per cycle) which is a function of many of the experimental parameters (such as slip amplitude, applied load, temperature, etc.); however, given that none of these were changed during the experiment, it is assumed that any changes in the debris flow during these tests will be associated only with changes in the width of the wear scar as the test proceeds. The physics of the dependence of the debris flow on the wear scar width is not fully understood; however, two proposals are offered, both of which lead to the same dependence of wear rate upon the scar width:

- It may be assumed that the debris flow velocity is independent of the wear scar width, which means that the residence time of any debris particle within the contact increases with the wear scar width. If it is assumed that, for wear to proceed, debris must be continually eliminated from the contact, and that the rate of debris elimination controls the rate of wear, then it is proposed that the wear rate will be proportional to the inverse of the debris residence time, i.e.  $\frac{1}{x}$ .
- Alternatively, it may be assumed that the flow of particles is proportional to the gradient of their concentration between where they are formed (in the contact) and where they are eliminated (the edge of the contact). If it is assumed that their concentrations at the point of formation and elimination are fixed, then the gradient is simply controlled by the wear scar width, again leading to the hypothesis that the wear rate will be proportional to  $\frac{1}{x}$ .

As such, for situations where debris ejection from the contact is the rate determining step (i.e. the region to the right of the vertical line in Figure 4.2),

$$\frac{dV_w}{dE_d} = \frac{k}{x} \quad (4.3)$$

where  $k$  is a parameter describing the scar width-dependent wear rate of the contacting pair, which itself can be dependent upon other fretting parameters such as normal load and slip amplitude.

So far, relationships between the wear volume and the wear scar width (Equation 4.2), and the wear scar width and the wear rate (Equation 4.3) have been determined.

Finding the derivative of  $V_w$  in terms of  $x$  from Equation 4.2 results in the following equation (see Appendix A for details):

$$\frac{dV_w}{dx} = \frac{x^2 L}{2\sqrt{4R^2 - x^2}} \quad (4.4)$$

Substituting Equation 4.4 into Equation 4.3 gives:

$$\frac{dE_d}{dx} = \frac{x^3 L}{2k\sqrt{4R^2 - x^2}} \quad (4.5)$$

which can be integrated to yield the following expression which describes the relationship between  $E_d$  and  $x$  only when  $E_d \geq E_{th}$  (see Appendix A for details of derivation):

$$E_d = mL \left( 16R^3 - \sqrt{4R^2 - x^2}(8R^2 + x^2) \right) + E_{th} \quad (4.6)$$

where  $m = \frac{1}{6k}$  and  $E_{th}$  is the energy dissipated when wear first occurs (i.e. when  $x$  first becomes a positive number).  $E_{th}$  is often referred to as the threshold energy for onset of wear [24, 83].

Although a derivation of an equation describing the direct relationship between  $E_d$  and  $V_w$  is not trivial (see Appendix A for that derivation), a set of parametric equations based on wear scar width was established:

$$V_w = L \left( R^2 \arcsin \left( \frac{x}{2R} \right) - \frac{x}{4} \sqrt{4R^2 - x^2} \right) \quad (4.7a)$$

$$E_d = mL \left( 16R^3 - \sqrt{4R^2 - x^2} (8R^2 + x^2) \right) + E_{th} \quad (4.7b)$$

That is, both  $E_d$  (Equation 4.7a) and  $V_w$  (Equation 4.7b) can be evaluated at a certain value of  $x$  to form  $(E_d, V_w)$  as a point on the trajectory describing the curve of  $V_w$  as a function of  $E_d$ . Equation 4.7b is transformed into a linear function in the form of  $E_d = aX + E_{th}$  by assigning  $\left( 16R^3 - \sqrt{4R^2 - x^2} (8R^2 + x^2) \right)$  to  $X$  and  $mL$  to  $a$  (as shown in Equation 4.8). As such, constants  $m$  and  $E_{th}$  were determined by solving the linear equation by using the transformed experimental results for both the  $R6$  and  $R160$  tests.

$$E_d = mL \left( 16R^3 - \sqrt{4R^2 - x^2} (8R^2 + x^2) \right) + E_{th}$$

↓

$$E_d = aX + E_{th} \quad (4.8)$$

Although these two specimen pair geometries ( $R6$  and  $R160$ ) appear to exhibit very different wear rates overall, i.e. the traditional concept of observed wear rate, defined as wear volume per unit energy dissipated, (and those rates change with the cycle count), constants  $m$  and  $E_{th}$  evaluated for these two geometries are rather similar. The values of  $m$  are as follows (with subscripts indicating the radius of the cylindrical specimen in the pair):  $m_6 = 2.29 \text{ kJ}\cdot\text{mm}^{-4}$  and  $m_{160} = 2.67 \text{ kJ}\cdot\text{mm}^{-4}$ , a difference of less than 15%; the corresponding values of  $E_{th}$  for these two sets of data are:  $E_{th_6} = 0.418 \text{ kJ}$  and  $E_{th_{160}} = 0.702 \text{ kJ}$  (a difference of less than 50%). To demonstrate that this methodology is appropriate and that it robustly describes these two sets of data and their evolutions with the test duration, two curves were calculated based on the

parametric equations defined by Equation 4.7a and Equation 4.7b for  $R6$  and  $R160$  tests with common values of  $m$  and  $E_{th}$ , i.e. the only different value used during the calculation is the radius of cylindrical specimen; specifically, the mean values of  $m$  and  $E_{th}$  were employed, namely  $m = 2.48 \text{ kJ}\cdot\text{mm}^{-4}$  and  $E_{th} = 0.560 \text{ kJ}$ . Figure 4.9 shows the experimental data plotted against the calculated values for both  $R6$  and  $R160$  pairs; the validity of the methodology and hypothesis is clear from the correlation between the data and the predictions.

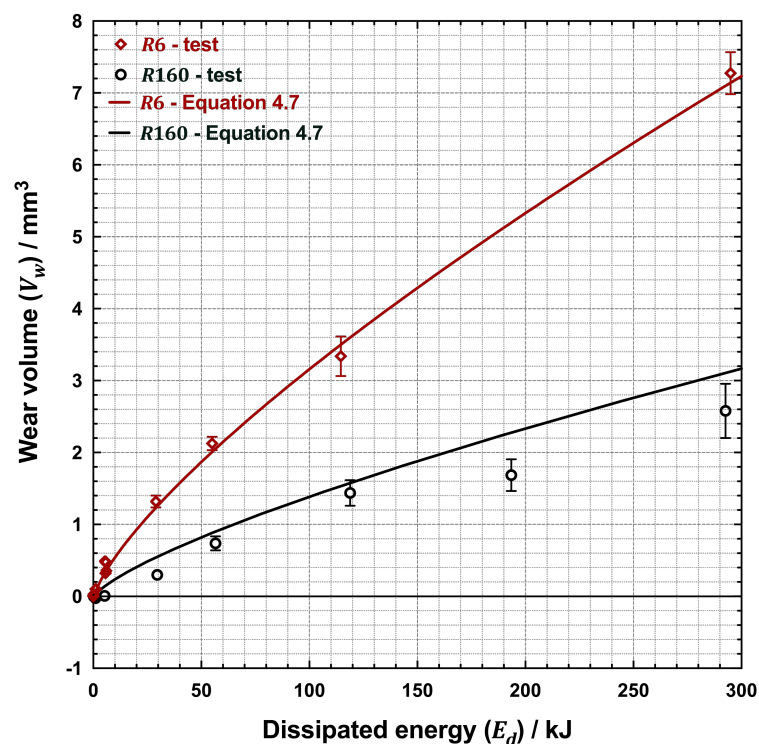


Figure 4.9: A comparison between the experimental data and the calculated values based on the parametric equations defined by Equation 4.7a and Equation 4.7b showing the wear volume as a function of dissipated energy for fretting tests conducted with  $R6$  pairs and  $R160$  pairs; error bars are displayed.

## 4.4 Discussion

### 4.4.1 Wear scar characteristics

In previous research that has examined the effects of specimen geometry on the fretting wear behaviour of non-conforming contact pairs [18, 20, 23, 36], it can be seen that more conforming contacts result in lower wear rates (as has been seen in

this chapter). In the study conducted by Warmuth et al. which used the same steel as in the current study [20, 23], it was observed that *R6* geometries resulted in U-shaped wear scars, whereas *R160* geometries resulted in large pits and peaks on the wear surfaces which were associated with metallic transfer between the specimens. However, in these papers, the fretting tests were conducted only for a relatively short test durations ( $N = 1 \times 10^5$  cycles). It was proposed by Warmuth et al. [23] that these pit-peak features were formed when the rate of oxygen ingress into the contact was too low to result in oxidation of the nascent metal surfaces formed as part of the wear process before metal-to-metal transfer could occur, and that more conforming contacts restricted this oxygen ingress due to the larger widths of the fretting contacts.

In the current study, it can be seen that these pit-peak features were never observed for tests with the *R6* geometry (additional tests with test durations as low as  $N = 500$  cycles were conducted, but U-shaped scars were always observed), and it is proposed that this is due to the ease of oxygen ingress into these contacts. However, whilst the pit-peak features were observed for tests with small numbers of cycles ( $N < 1 \times 10^5$  cycles) with the *R160* pairs, they were eliminated at higher numbers of cycles ( $N > 1 \times 10^6$  cycles), despite the fact that the scar widths were getting larger as the wear proceeded (which presumably further restricts oxygen ingress into the scar). It is proposed that whilst oxygen ingress into the scar will become more limited by increases in the wear scar width associated with wear, the corresponding increase in the restriction of wear debris expulsion from the contact (and the associated reduction in wear rate) is the dominant effect; hence, as the scars grow at higher numbers of cycles, the oxygen ingress ceases to be a rate-determining process, RDP, (and thereby a mechanism-determining process), with the debris expulsion from the scar taking this role. Please note here that, when considering the evolution of the wear contact for *R160* pairs, the adhesive wear observed at the early stage is not necessarily due to the depletion of oxygen being transported into the contact, and could be in fact initial

transient adhesion before the steady state is established where debris ejection is the RDP throughout the test (as illustrated in Figure 2.2c). Nevertheless, the main argument here remains intact that, for the test conditions employed in the current study, the transport of oxide debris out of the contact is dominating the fretting process.

It should also be noted that the pit-peak features exhibited at the early stage of tests with R160 pairs (i.e. where  $N < 1 \times 10^5$  cycles) are generally circular in shape as shown in Figure 4.4 and Figure 4.6 rather than forming uniformly in a rectangular shape as might be expected for a line contact. Similar observations can be found on previous works conducted in the University of Nottingham utilising the same testing rig [116, 117]. As discussed in Chapter 3, specimen surface tolerance and imperfect alignment mean that there will be variations in the initial pressure distribution on the contact. Under normal conditions of wear, any such variations are rapidly eliminated since the highest pressures also result in the highest rates of surface recession. However, where adhesive (metal-to-metal contact without sufficient oxidation) occurs, material can be laterally transported to form a metallic peak which this carries a higher proportion of the load, thus exacerbating further damage in this region and growth of the pit-peak feature.

These observations also indicate the need to examine the mechanisms of fretting wear across a wide range of durations; it was proposed in earlier work [23] that the pit-peak features may be significant in terms of the tendency for fretting fatigue. However, for many components in service, the numbers of fretting cycles are much larger than those typically employed in laboratory tests; given the changes in mechanism observed here, it is argued that misleading conclusions may be drawn if the test conditions do not replicate those seen in service or can be demonstrated to have reached a steady-state.

### **4.4.2 Wear rate dependence on contact width in fretting**

Whilst the general concept of the competition between debris-formation and debris-expulsion to control the wear mechanisms and rates of wear has been well accepted

since the publications of Godet and co-workers [19], a physically-based quantitative model is initially outlined in this study which proposes that in situations where the rate of wear in fretting is limited by debris expulsion from the contact, the wear rate is inversely proportional to the width of the scar. The model is dependent upon the observation that the total wear volume of the fretting pair is very close to that of a minor segment of the cylinder defined by the wear scar width. The model is in good agreement with the experimental data and is able to predict the evolution of wear volumes with fretting duration for two very different contact geometries in which the wear volumes are clearly seen to be very dependent upon these geometrical differences.

It is not clear where the transition from the debris-formation controlled regime and the debris-expulsion controlled regime occurs (see Figure 4.2), but given the correlation between the experimental data and the predictions based upon the hypothesis, it may be assumed that this transition occurs at relatively small wear scar widths (i.e. the wear rate is debris-expulsion controlled from an early stage). The exceedingly high rates of wear that the model predicts as the scar width tends towards zero are not observed for two reasons; (i) the minimum scar widths (at the beginning of the test) are finite due to elastic deformation; the initial Hertzian contact widths (full width) under the test conditions are 111  $\mu\text{m}$  and 572  $\mu\text{m}$  for the *R6* and *R160* pairs respectively; (ii) at small scar widths, debris expulsion ceases to be the rate-determining mechanism, with the rate of debris formation itself taking that role instead.

### **4.4.3 Consideration of debris expulsion effects in research programmes**

As discussed, the role of debris expulsion from a fretting contact is more significant than it is in sliding wear in controlling both the rates and mechanisms of wear. However, much fretting research (particularly that which seeks to develop new fretting resistant materials or compares the behaviour of different materials) simply considers the wear rates without considering whether the effects observed are associated with changes in

the rate of debris formation or with changes in the rate of debris ejection from the contact.

Although this chapter has focussed on the influence of the wear scar size (both initial size and evolved size in a non-conforming contact due to the wear process itself) on the rates of wear (controlled by debris expulsion), it is recognised that many other factors also control debris expulsion from the scar, including initial geometry (e.g. flat-on-flat, sphere-on-flat) and contact size, fretting stroke, fretting frequency, temperature, hardness of the contacting materials etc [21, 22, 97, 118, 119]. As such, it is argued that consideration of debris expulsion from a contact (in particular, via SEM analysis of the wear scars) is a critical part of research in the field of fretting, and that caution needs to be exercised when comparing wear rates in situations in which an analysis of the debris expulsion from the contact has not been considered.

### **4.5 Conclusions**

In fretting, the wear rate can be either controlled by the rate of debris formation within the contact or by the rate of debris ejection from the contact. In the current chapter, the concept of the rate-determining process (RDP) is suggested to analyse the wear behaviour in fretting, which proposes that both the debris formation and ejection will have a maximum rate at which they can be sustained under certain conditions, and the observed wear rate is determined by the process with the smallest of these maximum rates. It was observed in this chapter that, in fretting wear of contacts with a cylinder-on-flat geometry (where contact size increases continuously with the exposure to wear), the observed wear rate is controlled by the process of debris being transported out of the contact, which is dependent upon the evolving size of the wearing contact (and thereby being the RDP). In contrast to the constant wear rate that is widely adopted in fretting research, the instantaneous wear rate is used in the current chapter, which has been shown to be inversely proportional to the wear scar width, meaning that changes

in wear rate with initial contact geometry and the duration of fretting can be quantitatively explained. The validity of the model is demonstrated by its ability to account for significant differences in measured wear rate (with either geometry of test duration). The model thus indicates that fretting wear is contact size-dependent and cannot be described adequately by an Archard-type formulation. It is noted that this conclusion relates only to a cylinder-on-flat configuration, and that for other contact geometries (e.g. annular ring contact or sphere-on-flat contact), the dependence of the rate of debris expulsion from the contact on the contact size will be different.

For the geometry employed in this work, the development of the relationship between wear scar width and wear rate required a relationship between the wear scar volume and width. A simple geometrical relationship was proposed and validated by the agreement between the measured data and predicted values.

Finally, it is noted that for the *R160* contact pairs, the wear mechanism changed with the test duration. At low cycles (up to  $N = 1 \times 10^5$  cycles), the rate of oxygen ingress to the wearing surfaces in the contact was not high enough to facilitate the development of an oxide debris bed between the first bodies, and this resulted in pit-peak features on the contact surfaces which were associated with metallic transfer between the specimens. As the test duration was extended (above up to  $N = 1 \times 10^6$  cycles), the rate at which debris was expelled from the contact reduced the overall wear rate sufficiently, so that the rate of oxygen ingress was high enough to facilitate the formation of an oxide debris bed, and a U-shaped wear scar was formed (as was always observed for the less conforming *R6* pairs). This observation indicates that care must be taken in fretting testing to ensure that the duration is long enough to ensure that steady-state wear mechanisms are operative.

# **Chapter 5 The development of alternative wear equations for commonly employed non-conforming contact**

## **5.1 Introduction and chapter outline**

Fretting wear differs from sliding wear in a variety of ways, the most significant being that in fretting, the magnitude of the relative displacement between the bodies is generally much smaller than the size of the contact between those bodies, meaning that debris ejection from the contact needs to be considered as part of the process of continual wear [2, 19]; more specifically, the concept of the “tribology circuit” proposes that in fretting, wear debris elimination from the contact is required for wear to proceed [96]. It is recognised that the rate of debris ejection from the contact will depend upon the size of the contact itself [98] since this is the representative of the travelling distance of debris before being transported out of the contact [99].

As discussed in Chapter 4, fretting wear of metals under conditions where debris predominantly consists of metal oxides, there are two key processes, either of which may be the factor that controls the observed rate of wear:

- the rate of formation of the oxide debris (itself dependent amongst other things upon the rate of oxygen ingress into the contact [23, 91, 106]);
- the rate of debris ejection from the contact (itself dependent amongst other things upon the contact size and the rheology of the bed [99] and the tendency for the oxide debris particles to agglomerate and potentially sinter [21, 97, 120]).

At the start of a test, there will be a transient period where (amongst other things [121]) the debris bed in the contact is building towards a steady state thickness [99]. Once steady state is reached, the rate of debris formation and the rate of its ejection from the contact must be equal [37].

There has been significant recent research progress in considering the effect of transport processes in fretting, both in terms of transport of key species into the contact (in particular oxygen) [106] and in terms of transport of debris out of the contact (as discussed in Chapter 4). Which of these processes is rate-determining will depend upon the conditions under which the fretting is taking place; in particular, it is noted that both transport of oxygen into the contact and transport of debris out of the contact depend upon the physical size of the wear scar. The work considered in the current thesis only addresses situations where debris ejection is rate determining (i.e. it does not address situations where transport of oxygen into the contact is rate-determining). The recent work by Baydoun et al. [106] indicates that transport of oxygen into the contact will tend to become the rate-determining as the contact size increases and as the time-based rate of wear (i.e. volume lost per unit time) increases.

In concluding that the wear rate may (under certain circumstances) be dependent upon the size of the contact means that under those circumstances, descriptions of wear rate using Archard-type approaches are no longer adequate. Although not explicitly stated, it is implicitly assumed in the Archard-type approaches that the wear rate is governed by the rate of debris formation alone, with this being independent of any transport of species either in or out of the contact.

The influence of contact size on the rate of fretting may be less of an issue in test programmes where comparisons between different materials or different test conditions are the primary aim of the research, as long as the tests are all conducted with a contact of the same size and with a geometry where the contact size does not change during the course of the test. However, for a variety of reasons, laboratory fretting testing is very often conducted using non-conforming specimen pair configurations where the size of the contact changes as the test proceeds; common geometries of this type are (i) cylinder-on-flat (CF); (ii) sphere-on-flat (SF); (iii) crossed-cylinders (CC). In such configurations, the influence of the radii of the non-plane bodies on the wear rate is well

## The development of alternative wear equations for commonly employed non-conforming contact

known [18, 20, 23, 90, 107]. In such cases, the wear scar increases in size (in a manner dependent upon the geometry of the two first bodies) as wear proceeds [18], and this will result in a change in the rate of debris flow from the contact as the test proceeds. Fillot et al.[37] noted that in the steady state, the rate of formation of debris and the rate of debris flow from the contact must be equal. This idea was developed in the previous chapter where the concept of the rate-determining process was outlined; in this, rates of the two processes (debris formation and debris ejection from the contact) are considered separately, with the process with the lower of the two rates at any point in a test being termed the rate-determining process. The two rates as a function of wear scar width are illustrated schematically in Figure 5.1<sup>1</sup> which indicates that for a non-conforming specimen pair configuration (where the wear scar grows as a test proceeds), a change in the rate-determining process may occur during a test as the wear scar grows in size due to continued material removal. It is therefore argued that a nominal measure of the wear scar size (related perhaps to the initial contact size or to the final size [18, 90, 107]) is not sufficient in analysis of the evolution of fretting, and that the evolution of the scar size throughout a test needs to be considered and understood.

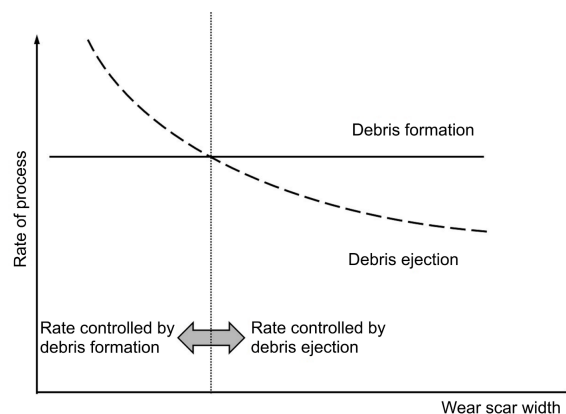


**Figure 5.1: Schematic diagram illustrating the dependence of rates of debris formation and debris ejection on wear scar width, with regions where debris formation and debris ejection are the rate-determining processes (i.e. the process with the lower of the two rates at any scar width) being identified.**

<sup>1</sup> Please note that Figure 5.1 is simply a re-presentation of Figure 4.2 and is reproduced here simply to aid the flow of this chapter

In the previous chapter where the concept of the rate-determining process was proposed, it was demonstrated that for cylinder-on-flat fretting of a high strength steel (with the fretting motion perpendicular to the axis of the cylinder as shown in Figure 5.2<sup>2</sup>), the instantaneous wear rate was inversely proportional to the wear scar width,  $x$  (the scar width being as indicated in Figure 5.2), indicating that the wear rate was being controlled by debris ejection from the contact for almost the entire duration of each of these tests (i.e. that the period where debris formation was the rate determining process as indicated in Figure 5.1 could be neglected). This dependence of wear rate on the contact size invalidates the concept of a constant wear rate in configurations with non-conforming pairs in situations where debris ejection is the rate-determining process and means that Archard-type approaches (with the total amount of wear being proportional to some measure of the exposure to wear) are not appropriate in the analysis of the evolution of wear in such situations.

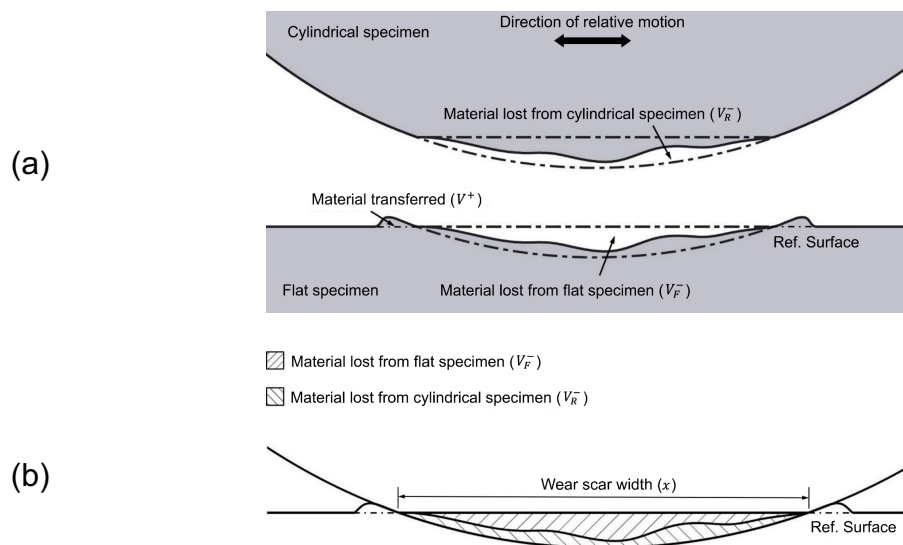


**Figure 5.2: (a) Schematic diagram of distribution of wear across two specimens in a cylinder-on-flat fretting pair (with a small amount of transferred material at the edge), illustrating the assumption (b) that the combined wear on the two specimens result in a total net wear volume equivalent to the minor segment of the cylinder.**

<sup>2</sup> Please note that Figure 5.2 is a re-representation of Figure 4.7 and, similar to Figure 5.1, is reproduced here simply to aid the flow of this chapter

## The development of alternative wear equations for commonly employed non-conforming contact

---

In the previous chapter, data were presented relating to the evolution of wear volume ( $V_w$ ) with frictional energy dissipated ( $E_d$ ) in fretting for two different geometries of cylinder-on-flat contact, specifically with a cylinder radius,  $R$ , of both 6 mm and 160 mm; these were termed  $R6$  and  $R160$  pairs respectively. As can be seen, the evolution of wear volume with energy dissipated was very different for the two different geometries, and previously, it had been suggested that the Archard-type wear rate was therefore a function of contact geometry [18, 20, 23, 90, 107]. However, it was demonstrated in the previous chapter that these two data sets could be reconciled via the concept of the instantaneous wear rate being proportional to the instantaneous wear scar width; the lines predicting the evolution of wear volume with energy dissipated shown in Figure 4.9 were both derived from the formulation:

$$\frac{dV_w}{dE_d} = \frac{k_1}{x} \quad (5.1)$$

where:

$$k_1 = f(P, \delta^*, T, f_{Hz} \dots)$$

indicating that  $k_1$  is a function of a number of important parameters in the fretting wear test including the normal load carried by the contact ( $P$ ), the slip amplitude ( $\delta^*$ ), the temperature ( $T$ ), the fretting frequency ( $f_{Hz}$ ) along with the material properties of the two bodies. However, in Chapter 4 and also in the current chapter,  $k_1$  is considered to be a constant since the experimental test parameters upon which  $k_1$  is dependent are held constant in the tests from which the experimental results were derived.

As suggested in the previous chapter, the physical rationale behind the form of Equation 5.1 was based upon either the distance which debris particles need to travel before leaving the contact or upon the concentration gradient down which the debris flow occurs. In the cylinder-on-flat fretting configuration, it was assumed that debris flow was primarily in the direction of the fretting displacement, with this being promoted not

only by the action of the displacement itself, but also by the fact that the dimension of the approximately rectangular wear scar parallel to the fretting displacement was small compared to its dimension perpendicular to the fretting direction.

Despite the comments made in the previous chapter, it is also recognised here that the form of the Equation 5.1 could also be rationalised in terms of the flow rate of debris out of the contact being inversely proportional to the area of the contact ( $A = xL$ ) since  $L$  is a constant in a line contact such as the one employed in this thesis. From this, it might be inferred that the flow rate of debris out of the contact is in fact proportional to the pressure in the contact (namely  $\frac{P}{A}$ ), although it is also recognised that the shape of the contact (i.e. the aspect ratio in the case of a rectangular wear scar) is also expected to affect debris flow. The possibility of this being a contact pressure effect is highlighted here since, whilst these two different physical underpinnings are indistinguishable for a line contact, they would lead to different outcomes for an initially point contact (such as sphere-on-flat or crossed-cylinders) which is to be addressed in this chapter.

A key issue in the previous chapter where this concept was first proposed for a cylinder-on-flat fretting contact was that Equation 5.1 could not be readily transformed into a relationship directly describing the dependence of the wear volume ( $V_w$ ) upon the energy dissipated ( $E_d$ ). Instead, both  $V_w$  and  $E_d$  were described individually as a function of the wear scar width ( $x$ ) and cylinder radius ( $R$ ) (amongst other things), yielding a set of parametric equations as follows (originally presented as Equation 4.7):

$$V_w = L \left( R^2 \arcsin \left( \frac{x}{2R} \right) - \frac{x}{4} \sqrt{4R^2 - x^2} \right) \quad (5.2a)$$

$$E_d - E_{th} = m_1 L \left( 16R^3 - \sqrt{4R^2 - x^2} (8R^2 + x^2) \right) \quad (5.2b)$$

where  $E_{th}$  is the energy dissipated when wear first begins to occur (often referred to as the threshold energy for onset of wear [24, 83]) and  $m_1$  is a constant related to  $k_1$  from

## The development of alternative wear equations for commonly employed non-conforming contact

---

Equation 5.1, such that  $m_1 = \frac{1}{6k_1}$ . As such, the way that the wear scar volume evolved with energy dissipated for two very different geometries was rationalised for the first time. Curves were generated from Equation 4.7 (or Equation 5.2) for both *R6* and *R160* pairs using the same values of  $m_1$  (i.e. with the same values of  $k_1$ ) and the same values of  $E_{th}$  for the two cases; these curves were plotted against the experimental data and are shown in Figure 4.9. It can be seen that this approach describes these data well, thus validating the hypotheses that underpin Equation 5.1.

It is noted that the term  $(E_d - E_{th})$  represents the frictional energy dissipated above the threshold energy for wear to commence. This will be termed  $E_{dat}$  in the current chapter (the subscript “*dat*” being an acronym for “dissipated above threshold”) such that  $E_{dat} = E_d - E_{th}$ .

Despite the success of this formulation in rationalising the data presented in Figure 4.9, it is recognised that it fails to provide a direct description of the relationship between the wear volume ( $V_w$ ), the cylinder radius ( $R$ ) and the energy dissipated ( $E_d$ ) which is needed to support an understanding of the dependence of the wear volume upon the latter two parameters. Moreover, the formulation of Equation 5.2 was only derived for a cylinder-on-flat contact and given that other configurations with non-conforming specimen pairs are commonly used in fretting research, there is a need to derive similar equations for those configurations, and in doing so, consider the two plausible forms of the governing equation, namely that the instantaneous wear rate is inversely proportional to a characteristic linear dimension of the scar or that it is proportional to the contact pressure (and thus inversely proportional to the area of the contact). As such, this current chapter seeks to develop an equation (which will be termed *the wear equation*) for situations where a non-conforming specimen pair configuration is employed and where the wear rate is controlled by debris-ejection from the contact; for each of the non-conforming specimen pair configurations commonly employed in

fretting research (namely cylinder-on-flat (CF), sphere-on-flat (SF) and crossed-cylinder (CC) geometries), wear equations will be derived which directly describe the relationship between the wear volume ( $V_w$ ), the energy dissipated ( $E_d$ ), the relevant geometrical parameters and the initial proposed governing equations.

Additional fretting tests were conducted in exactly the same way as those presented in the previous chapter but with different cylinder radii in the contact pair, namely 15 mm ( $R15$ ) and 80 mm ( $R80$ ). Again, details about the specimens, the test rig and the experimental procedures employed in the current chapter are described in Chapter 3; test conditions for this chapter are detailed in Table 5.1 as below:

**Table 5.1: Summary of the fretting test conditions for the additional tests for which data are presented in Chapter 5.**

Normal load ( $P$ ) / N	450
Displacement amplitude ( $\Delta^*$ ) / $\mu\text{m}$	50
Cylindrical specimen radius ( $R$ ) / mm	15, 80
Test duration ( $N$ ) / $10^6$ cycles	1, 2, 5
Frequency ( $f_{Hz}$ ) / Hz	20
Temperature ( $T$ ) / $^{\circ}\text{C}$	Ambient temperature

## 5.2 Derivation of a wear equation for cylinder-on-flat fretting configuration

In the previous chapter, a parametric relationship between wear scar width and wear volume was derived for the cylinder-on-flat configuration (re-presented in this chapter as Equation 5.2) based upon the governing equation (re-presented in this chapter as Equation 5.1) which is valid in describing both of the proposals under consideration, namely (i) that the instantaneous wear rate is inversely proportional to a characteristic linear dimension of the scar or (ii) that the instantaneous wear rate is proportional to

## The development of alternative wear equations for commonly employed non-conforming contact

the contact pressure (and thus inversely proportional to the area of the contact). The geometric relationship that the wear volume can be determined via wear scar width as outlined in Equation 5.2 is fundamental for the concept of instantaneous wear rate. This geometric relationship is further validated with additional experimental results on *R15* and *R80* specimen pairs as shown in Figure 5.3. Similar to Figure 4.8, a good fit between the measured data and the idealised geometrical relationship can be observed for all specimen pairs, however, the fit is reduced slightly as the contact conformity increases, i.e. from *R6* to *R160*. The average difference between the predicted and measured volumes for a given scar width were  $14\pm 8\%$ ,  $13\pm 7\%$ ,  $17\pm 4\%$ , and  $22\pm 7\%$  for the *R6*, *R15*, *R80* and *R160* pairs respectively (with the uncertainty representing the standard deviation of the difference).

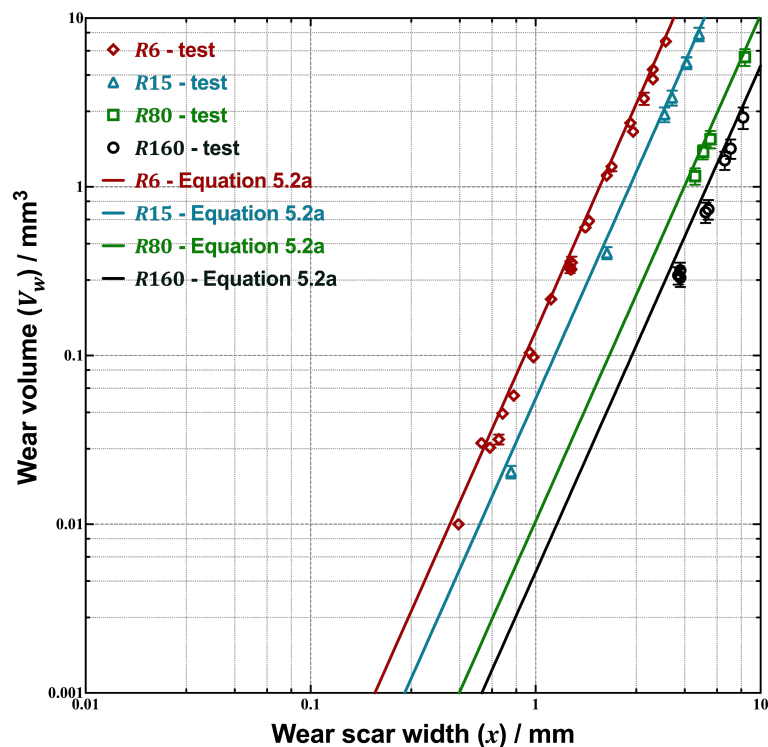


Figure 5.3: Plot of the wear scar width against net wear volume for fretting tests conducted with *R6*, *R15*, *R80* and *R160* pairs at varying displacement amplitude from  $\Delta^* = 10 \mu\text{m}$  to  $\Delta^* = 100 \mu\text{m}$  with  $P = 450 \text{ N}$ ; error bars are displayed.

To simplify the development of a wear equation, the wear scar angle,  $\theta$ , is now selected as the measure of the progress of wear for a specimen pair (as opposed to the wear scar width,  $x$  as was previously selected).

As previously demonstrated, the total wear volume across the two samples of a cylinder-on-flat specimen pair is well described by the minor segment of a cylinder defined by the chord of intersection between the cylinder and plane specimens (see Figure 5.2). The extent of wear is thus described by the angle  $\theta$  as illustrated in Figure 5.4, where the wear scar width,  $x$ , is equal to  $2R\sin(\theta)$ .

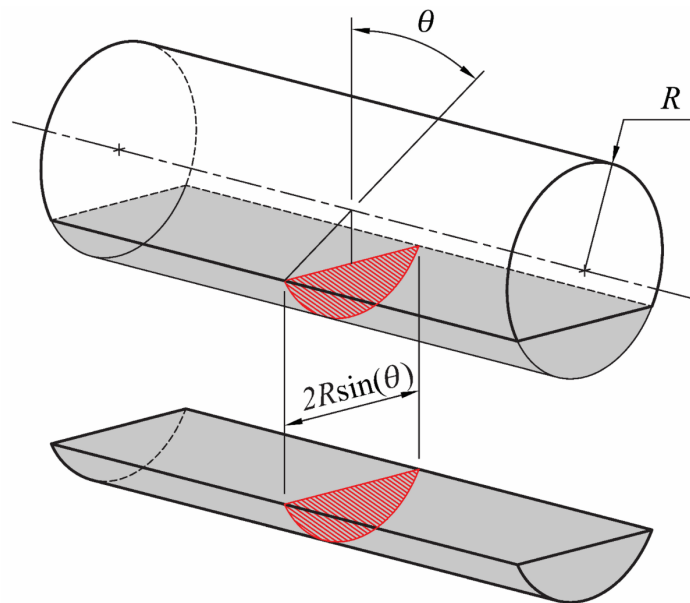


Figure 5.4: Illustration of the relationship between the wear volume (the minor segment of the cylinder) and its corresponding wear scar angle for the cylinder-on-flat fretting geometry.  $0 \leq \theta \leq \frac{\pi}{2}$ .

Using the wear scar angle,  $\theta$  ( $0 \leq \theta \leq \frac{\pi}{2}$ ), allows the parametric equations (Equations 5.2a and 5.2b) to be rewritten as follows (see Appendix B, Section B1):

$$V_w = LR^2(\theta - \sin(\theta) \cos(\theta)) \quad (5.3a)$$

$$E_{dat} = m_1 LR^3(\cos(3\theta) - 9\cos(\theta) + 8) \quad (5.3b)$$

Conducting Taylor series expansions for both Equation 5.3a and Equation 5.3b and taking their first non-constant polynomial terms (since these are the dominating terms),

## The development of alternative wear equations for commonly employed non-conforming contact

---

approximations for the wear volume and the energy dissipated above the threshold (denoted as  $V_w'$  and  $E_{dat}'$  respectively) can be written as follows:

$$V_w' = \frac{2}{3}LR^2\theta^3 \quad (5.4a)$$

$$E_{dat}' = 3m_1LR^3\theta^4 \quad (5.4b)$$

As can be seen in the next section (Section 5.2.1), the error associated with the approximations for a cylinder-on-flat contact is relatively low. As such, it is reasonable to assume that  $V_w \approx V_w'$  when  $E_{dat} = E_{dat}'$  for all  $\theta$ , with the approximation being better for smaller values of  $\theta$ . The formulation of a direct relationship between the wear volume ( $V_w$ ) and the energy dissipated above the threshold ( $E_{dat}$ ) is now simply derived by eliminating the wear scar angle,  $\theta$ , from the approximated equations 5.4a and 5.4b, yielding the following relationship:

$$\begin{aligned} V_w &= 2 \left(\frac{1}{3}\right)^{1.75} \left(\frac{L}{m_1^3}\right)^{0.25} R^{-0.25} E_{dat}^{0.75} \\ &= K_1 R^{-0.25} E_{dat}^{0.75} \end{aligned} \quad (5.5)$$

In the previous chapter, the threshold energy ( $E_{th}$ ) for the system in question was derived as 0.560 kJ, meaning that  $E_{th}$  was therefore comparatively small in the context of the maximum values of energy being dissipated in those tests of around 300 kJ (see Figure 4.9). In situations like this (i.e. tests where the maximum duration is much greater than the duration at which wear is first observed to commence), it seems reasonable therefore to neglect this threshold energy to enable further simplification of the function to take place. This assumption that  $E_{th} \approx 0$  allows a further simplification of Equation 5.5 to yield:

$$V_w = K_1 R^{-0.25} E_d^{0.75} \quad (5.6)$$

It is recognised that if there is an obvious threshold energy at which wear is first observed in a fretting test dataset, then Equation 5.5 could readily be employed in preference to Equation 5.6. However, Equation 5.6 allows data to be processed where the threshold energy,  $E_{th}$ , cannot be readily identified from the dataset available.

### 5.2.1 Errors associated with the approximation

The parametric equations given by Equation 5.3 have been shown to be able to describe well the dependence of wear volume on both the energy dissipated and the geometry of the system for the data presented in Figure 4.9. The approximations of these equations to the forms presented in Equation 5.4 have then allowed the derivation of the wear equations as presented in Equations 5.5 and 5.6. However, the error in moving between the exact equations (Equation 5.3) to the approximate equations (Equation 5.4) needs to be understood since the validity (or otherwise) of Equations 5.5 and 5.6 are dependent upon this.

Figure 5.5 shows the relationships between the normalised energy dissipated above the threshold energy ( $e_{dat} = \frac{E_{dat}}{m_1 LR^3}$ ) and the normalised wear volume ( $v_w = \frac{V_w}{LR^2}$ ) for the exact equations (Equation 5.3) alongside the equivalent for the approximated equations (Equation 5.4); from the exact form, Equation 5.3 indicates that the allowable range of  $e_{dat}$  is between 0 and 8 and that the allowable range of  $v_w$  is between 0 and  $\frac{\pi}{2}$  when  $\theta$  is within the range that  $0 \leq \theta \leq \frac{\pi}{2}$ . It should be noted that in Figure 5.5, the axes are normalised to the maximum values,  $\max(e_{dat})$  and  $\max(v_w)$ , respectively ( $\max(e_{dat}) = 8$ ,  $\max(v_w) = \frac{\pi}{2}$ ). It can be seen that the wear volume given by approximated equations is always less than that given by the exact equations for the same value of normalised energy. The error in the wear volume ( $\varepsilon_V$ ) associated with the approximated form when  $e_{dat} = e_{dat}'$  is given by:

$$\varepsilon_V = \frac{v_w' - v_w}{v_w} \quad (5.7)$$

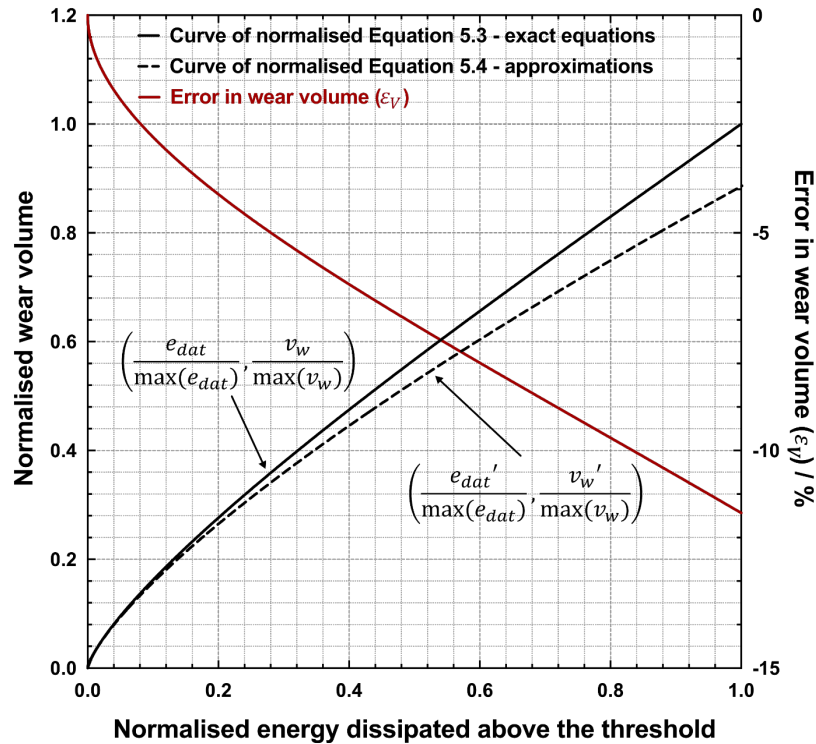


Figure 5.5: Plot of normalised energy dissipated above the threshold against normalised wear volume for both the exact (Equation 5.3) and approximate equations (Equation 5.4) for a cylinder-on-flat contact across the full range of allowable values of  $e_{dat}$  along with the fractional error in the wear volume across the same range.

Figure 5.5 shows that the fractional difference between the normalised wear volume given by the exact and the approximated equations ( $\varepsilon_V$ ) increases as  $e_{dat}$  increases, but with the magnitude of the error never being greater than 12%. In the previous chapter, the maximum value of  $\theta$  observed in the test programme (which included fretting test durations of up to  $5 \times 10^6$  cycles) was 0.32 rad which leads to a fractional error,  $\varepsilon_V$ , of only  $\sim 0.5\%$ . As such, it can be concluded that the errors in making the approximations of the Taylor series expansions for cylinder-on-flat fretting configurations are small compared to other sources of error, such as in the measurement of experimental data. As such, the wear equation (Equation 5.6) is considered a valid equation, with the errors associated with the approximations required for its derivation being of an acceptable magnitude for any amount of wear.

### 5.2.2 Experimental verification of the proposed relationship

The wear data from a cylinder-on-flat fretting contact previously presented in Figure 4.9 are replotted in the form indicated by Equation 5.6 (i.e. now using the term  $R^{-0.25}E_d^{0.75}$  as the abscissa) and presented in Figure 5.6. Please note that data additional to those presented in Figure 4.9 are also included in Figure 5.6; these data relate to tests conducted in exactly the same way as those presented in the previous chapter but with different cylinder radii in the contact pair ( $R15$  and  $R80$ ). It can be seen that the experimental data generated with the four different geometrical configurations are well described across the range of test durations by the function presented in Equation 5.6. The dashed lines in Figure 5.6 represent the region of 95% confidence intervals for the overall fitting line.

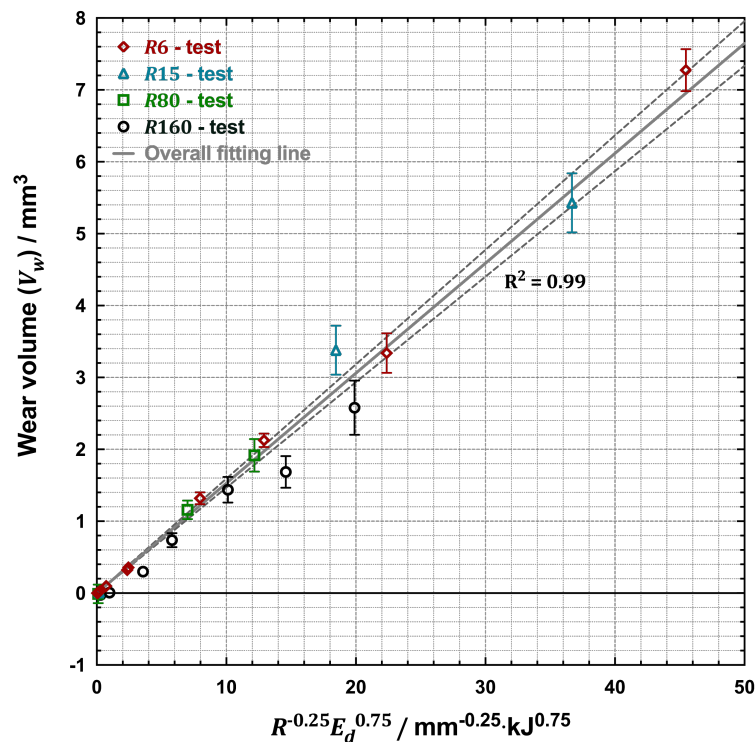


Figure 5.6: Wear volumes from cylinder-on-flat fretting tests of a high strength steel plotted as a function of  $R^{-0.25}E_d^{0.75}$ . The data relating to tests with cylinders with radii of 6 mm and 160 mm ( $R6$  and  $R160$  respectively) are from Figure 4.9; data related to tests with cylinders with radii of 15 mm and 80 mm ( $R15$  and  $R80$  respectively) are additional data which relate to experiments with identical materials conducted under the same fretting conditions, but simply with different cylinder radii; error bars are displayed.

### **5.3 Derivation of wear equations for sphere-on-flat and crossed-cylinders fretting configurations**

The concept that the instantaneous wear rate may be inversely proportional to a characteristic linear dimension of the scar or that it may be proportional to the contact pressure (and thus inversely proportional to the area of the contact) lead to two different potential governing equations in the case of initially point contacts (i.e. sphere-on-flat and crossed-cylinders geometries). Wear equations based upon the governing equation which states that the instantaneous wear rate is inversely proportional to a characteristic linear dimension of the scar will be derived for the SF and CC contact configurations; however, due to the complexities of the analysis, the wear equation based upon the governing equation which states that the instantaneous wear rate is proportional to the contact pressure (and thus inversely proportional to the area of the contact) will be derived only for the SF contact configuration.

#### **5.3.1 Characteristic wear scar width for sphere-on-flat and crossed-cylinders fretting configurations**

The work on the cylinder-on-flat contact configuration presented in Section 5.2 is simply an extension of the work in the previous chapter where Equation 5.1 was first proposed. In those cylinder-on-flat fretting tests where the fretting motion is perpendicular to the axis of the cylinder and the wear scar dimension perpendicular to the fretting direction are generally much larger than its dimension parallel to the fretting motion, it was assumed that the debris flow velocity out of the contact was parallel to the direction of the fretting motion; moreover, at any point in the evolution of the wear scar, it was assumed the wear scar width,  $x$ , was the same across the length of the contact and could therefore be readily defined.

As for the cylinder-on-flat (CF) case, it is assumed that the total wear volume across the two components of a SF specimen pair can be described by the spherical cap of intersection of the sphere with the plane. Similarly, it is again assumed that the total

wear volume across the two components of a CC specimen pair can be described by the volume of intersection of two crossed cylinders. The extent of wear for both cases is defined by the wear scar angle  $\theta$  as illustrated in Figure 5.7.

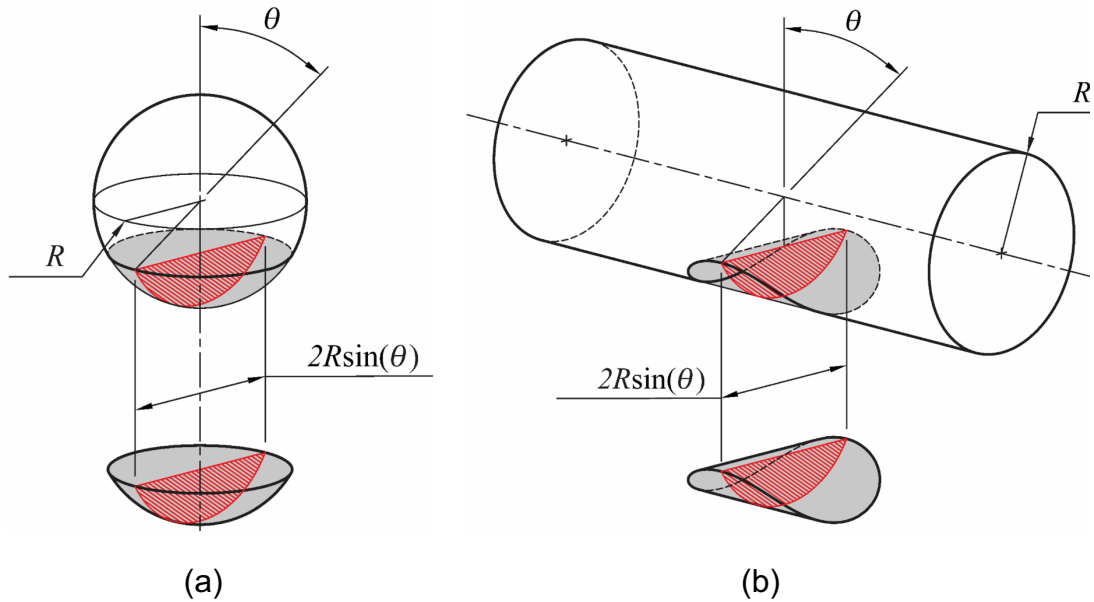
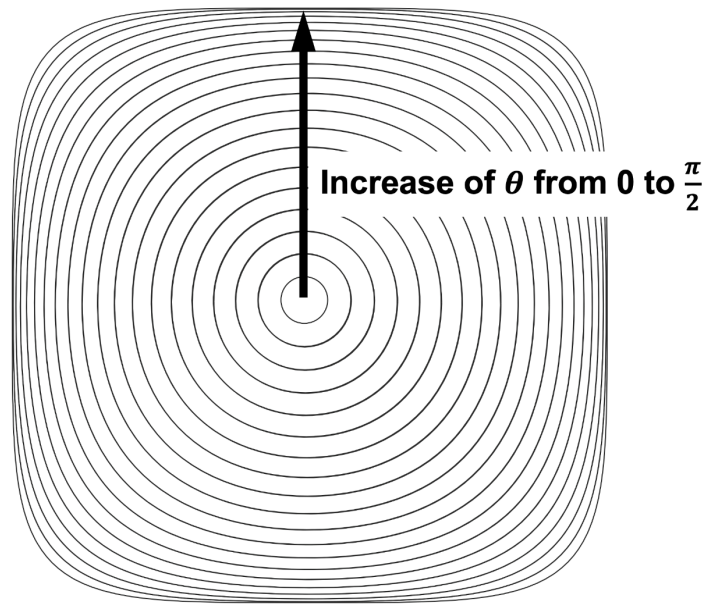


Figure 5.7: Illustration of the relationship between the wear volume (defined by a spherical cap) and its corresponding wear scar angle for (a) the sphere-on-flat; (b) the crossed-cylinders geometry.  $0 \leq \theta \leq \frac{\pi}{2}$ . The wear volume for the sphere-on-flat configuration is defined by a spherical cap, while the wear volume for the crossed-cylinders is the intersection of two crossed cylinders.

As can be seen from Figure 5.7, there is no geometrically straightforward measure (akin to the uniform wear scar width  $x$  which was used to characterise the wear scar for the CF geometry) by which the wear scar can be characterised for either the SF or the CC fretting configurations. In both cases, the wear scar shape will be equiaxed (assuming that the slip amplitude is small compared to the width of the wear scar); in the case of the SF configuration, the shape of the wear scar projection will be a circle, whereas for the CC geometry, whilst the projection of the wear scar remains equiaxed as wear progresses, its shape changes from circle in the early stages towards a square as wear progresses as illustrated in Figure 5.8.



**Figure 5.8: Illustration of the shape change of the projection of the wear scar for the crossed-cylinders configuration as wear progresses.**

Whilst the fretting displacement will tend to promote debris flow parallel to it, the equiaxed nature of the scars (on sphere-on-flat and crossed-cylinders configurations) will mean that some (perhaps a significant fraction) of the debris will escape the scar from the sides of the contact (termed *side-leakage* [103]) which means that such debris will have a component of its velocity perpendicular to the fretting direction. As such, there is no intuitively obvious definition of the wear scar width in the direction of the fretting motion over which the debris needs to travel to exit the wear scar.

Despite this complexity, a simple proposal is made at this stage, namely that a characteristic wear scar width can still be defined both for the sphere-on-flat (SF) and the crossed-cylinders (CC) configurations, with this being the largest value of the scar width parallel to the direction of fretting since it is argued this will be rate-controlling in terms of the debris flow of out of the scar. As such, the characteristic wear scar width for the SF contact is the diameter of the circular wear scar as illustrated in Figure 5.7a (termed as  $2r$ ), which is equal to  $2R\sin(\theta)$ ; similarly, the characteristic wear scar for the CC contact is the maximum of wear scar width as shown in Figure 5.7b (termed as  $w$ ), which is also equal to  $2R\sin(\theta)$ .

### 5.3.2 Wear equations based upon a characteristic linear dimension of the wear scar for the sphere-on-flat and crossed-cylinders contact configurations

With the definition of the characteristic wear scar width for both the SF and CC configurations as described in the previous section (Section 5.3.1), the same assumption that the instantaneous wear rate is inversely proportional to the characteristic wear scar width is adopted in each case (Equation 5.8a is the governing equation for the SF while Equation 5.8b is for the CC):

$$\frac{dV_w}{dE_d} = \frac{k_2}{2r} \quad (5.8a)$$

$$\frac{dV_w}{dE_d} = \frac{k_3}{w} \quad (5.8b)$$

where:

$$k_2 = g(P, \delta^*, T, f_{Hz} \dots)$$

$$k_3 = h(P, \delta^*, T, f_{Hz} \dots)$$

indicating that  $k_2$  and  $k_3$  are functions of various test parameters as previously defined. Please note that, similar to  $k_1$ ,  $k_2$  and  $k_3$  are treated as constants in the current chapter.

Using same methodology as outlined for the CF contact configuration (as outlined in Section 5.2), parametric equations for the wear volume and the energy dissipated above the threshold energy functions of the wear scar angle  $\theta$  can be derived for both the SF (Equation 5.9a and Equation 5.9b) and CC (Equation 5.10a and Equation 5.10b) as follows (with details of their derivation being presented in Appendix B, Section B2 and Section B4):

$$V_w = \frac{\pi R^3}{12} (\cos(3\theta) - 9 \cos(\theta) + 8) \quad (5.9a)$$

$$E_{dat} = m_2 \pi R^4 (\sin(4\theta) - 8 \sin(2\theta) + 12\theta) \quad (5.9b)$$

**The development of alternative wear equations for commonly employed non-conforming contact**

---

$$V_w = \frac{\pi R^3}{16} (\cos(3\theta) + 2\cos(2\theta) - 17\cos(\theta) + 14) \quad (5.10a)$$

$$E_{dat} = m_3 \pi R^4 (9\sin(4\theta) + 16\sin(3\theta) - 120\sin(2\theta) - 48\sin(\theta) + 204\theta) \quad (5.10b)$$

By performing Taylor series expansions for both Equations 5.9 and 5.10 and again taking their first non-constant polynomial terms, the wear volume and the energy dissipated above the threshold can be approximated for both the SF (Equation 5.11a and Equation 5.11b) and CC (Equation 5.12a and Equation 5.12b) configurations:

$$V_w' = \frac{\pi R^3 \theta^4}{4} \quad (5.11a)$$

$$E_d' = \frac{32}{5} m_2 \pi R^4 \theta^5 \quad (5.11b)$$

$$V_w' = \frac{\pi R^3 \theta^4}{4} \quad (5.12a)$$

$$E_{dat}' = \frac{384}{5} m_3 \pi R^4 \theta^5 \quad (5.12b)$$

Again, as shown in a following section concerning error analysis for both the sphere-on-flat and crossed-cylinders contact (Section 5.3.4), the error associated with the approximation is relatively low, which leads to the conclusion that  $V_w \approx V_w'$  when  $E_{dat} = E_{dat}'$  for all  $\theta$ , with the approximation being better for smaller values of  $\theta$ . The formulations of a direct relationship between the wear volume ( $V_w$ ) and the energy dissipated above the threshold ( $E_{dat}$ ) for the SF and CC configurations are now simply derived by eliminating the wear scar angle,  $\theta$ , from the approximated equations presented in Equations 5.11 and 5.12, yielding the following relationship in the case of SF (Equation 5.13) and CC (Equation 5.14) configurations respectively:

$$\begin{aligned} V_w &= \frac{1}{4} \left( \frac{5}{32} \right)^{0.8} \left( \frac{\pi}{m_2^4} \right)^{0.2} R^{-0.2} E_{dat}^{0.8} \\ &= K_2 R^{-0.2} E_{dat}^{0.8} \end{aligned} \quad (5.13)$$

$$\begin{aligned}
 V_w &= \frac{1}{4} \left( \frac{5}{384} \right)^{0.8} \left( \frac{\pi}{m_3^4} \right)^{0.2} R^{-0.2} E_{dat}^{0.8} \\
 &= K_3 R^{-0.2} E_{dat}^{0.8}
 \end{aligned} \tag{5.14}$$

Using the aforementioned assumption that  $E_{th} \approx 0$  as discussed for the cylinder-on-flat contact, further simplification of both Equation 5.13 and Equation 5.14 can be carried out to yield simplified wear equations for the SF (Equation 5.15) and CC (Equation 5.16) configurations in fretting:

$$V_w = K_2 R^{-0.2} E_d^{0.8} \tag{5.15}$$

$$V_w = K_3 R^{-0.2} E_d^{0.8} \tag{5.16}$$

It is worth noting that the forms of the wear equations for both SF and CC configurations are identical, i.e. both take the form  $V_w \propto R^{-0.2} E_d^{0.8}$  as indicated in Equation 5.15 and Equation 5.16. As shown in Figure 5.8, the shape of wear scar for CC contact is close to a circle when  $\theta$  is small, which is very similar to that of the SF contact. Furthermore, the method outlined in this chapter involves the Taylor expansion of the parametric equations of  $V_w$  and  $E_{dat}$  at the point of  $\theta = 0$ , followed by elimination of the internal variable  $\theta$ . The implication is that the approximation can capture the exact behaviour of the functions when  $\theta = 0$ , with the performance of the approximation being gradually reduced with the increase of  $\theta$ . As such, the similarity between Equation 5.15 and Equation 5.16 is associated with the similarity of the contacts when  $\theta$  is small and the nature of the Taylor expansion.

### **5.3.3 Wear equations based upon a characteristic area of the wear scar for the sphere-on-flat contact configuration**

Further to the assumptions made in the derivation of the wear equations in Section 5.3.2, a second proposal of the governing equation for the instantaneous wear rate is considered here for both the sphere-on-flat and the crossed-cylinder contact, namely

## The development of alternative wear equations for commonly employed non-conforming contact

---

that the instantaneous wear rate is inversely proportional to the *area* of the wear scar<sup>3</sup>. It should be noted that the relationship between the area ( $A$ ) and angle ( $\theta$ ) of the wear scar for the SF configuration can be readily described as  $A = \pi R^2 \sin^2(\theta)$  where the radius of the circular wear scar is equal to  $R \sin(\theta)$  as illustrated in Figure 5.7. However, an equivalent relationship is difficult to formulate for the CC configuration; as shown in Figure 5.8, the evolution of the wear scar shape for the CC is complex and requires further analysis which is beyond the scope of this thesis. As a result, the derivation of the wear equation based upon the second form of the governing equation related to the area of the contact (Equation 5.17) will be carried out only for the SF contact:

$$\frac{dV_w}{dE_d} = \frac{k'_2}{A} \quad (5.17)$$

where:

$$k'_2 = g(P, \delta, T, f_{Hz} \dots)$$

suggesting that  $k'_2$  is a function of various test parameters as previously defined but, again, is treated as a constant for the derivation of the wear equation.

Using the assumption above, and the same methodology as outlined in the previous sections (Section 5.2 and Section 5.3.2): the derivation of the parametric equations of wear volume and dissipated energy in terms of wear scar angle, followed by Taylor expansion of the parametric equations and the elimination of the variable  $\theta$ , an equivalent wear equation can be derived. The details of the methodology are presented in Appendix B, Section B3.

Parametric equations can be derived as follows:

---

<sup>3</sup> For the CF configuration, the hypotheses that the wear rate is inversely proportional to  $x$  or that it is inversely proportional to  $A$  lead to the same equation (since  $A = x L$  where  $L$  is a constant). As such, it is not considered further here.

$$V_w = \frac{\pi R^3}{12} (\cos(3\theta) - 9 \cos(\theta) + 8) \quad (5.18a)$$

$$E_{dat} = m'_2 \pi^2 R^5 (-3 \cos(5\theta) + 25 \cos(3\theta) - 150 \cos(\theta) + 128) \quad (5.18b)$$

Performing Taylor expansions on Equation 5.18 to approximate the wear volume and the energy dissipated above the threshold gives:

$$V_w' = \frac{\pi R^3 \theta^4}{4} \quad (5.19a)$$

$$E_{dat}' = 40 m'_2 \pi^2 R^5 \theta^6 \quad (5.19b)$$

Given that the error associated with the approximation is relatively low (Section 5.3.4), eliminating the internal variable  $\theta$  yields the following relationship:

$$\begin{aligned} V_w &= \frac{1}{4} \left( \frac{1}{40} \right)^{0.67} \left( \frac{1}{\pi m'_2{}^2} \right)^{0.33} R^{-0.33} E_{dat}^{0.67} \\ &= K'_2 R^{-0.33} E_{dat}^{0.67} \end{aligned} \quad (5.20)$$

Equation 5.20 is further simplified by assuming  $E_{th} \approx 0$  to give the wear equation derived from the area based governing equation for the SF contact:

$$V_w = K'_2 R^{-0.33} E_d^{0.67} \quad (5.21)$$

### 5.3.4 Errors associated with the approximation

In previous sections (Section 5.3.2 and Section 5.3.3), the approximated parametric equations have allowed wear equations for the sphere-on-flat and the crossed-cylinders configurations to be derived for all three cases, i.e. (a) the wear equation for the SF contact from the linear basis of the governing equation; (b) the wear equation for the CC contact from the linear basis of the governing equation; (c) the wear equation for the SF contact from the area basis of the governing equation. However, as discussed in Section 5.2.1, the errors associated with moving from the exact parametric equations (Equation 5.9, Equation 5.10 and Equation 5.18) to the approximated

## The development of alternative wear equations for commonly employed non-conforming contact

---

parametric equations (Equation 5.11, Equation 5.12 and Equation 5.19) by performing Taylor expansion need to be understood in order that the validity of the approximation can be assessed.

The method by which the errors associated with the approximation are as described in Section 5.2.1 and will not be described again in detail, with simply the outputs being presented. Figure 5.9 shows the relationship between the normalised energy dissipated above the threshold energy and the normalised wear volume across the full range of allowable wear scar angles  $\theta$  ( $0 \leq \theta \leq \frac{\pi}{2}$ ) for the exact equations. Alongside is plotted the equivalent relationship for the approximated equations across the same range. It should be noted that in Figure 5.9, the axes are normalised to the maximum values,  $\max(e_{dat})$  and  $\max(v_w)$  respectively. It can be seen from Figure 5.9 that across the full range of allowable wear scar angles, the magnitude of the fractional error in the wear volume associated with the approximations ( $\varepsilon_V$  defined in Equation 5.7) is never greater than 11% for case (a); 13% for case (b); and 19% for case (c). As such, it is suggested that wear equations (Equation 5.15, Equation 5.16 and Equation 5.21) (which have been derived from the Taylor series expansions and the additional assumption that  $E_{th} \approx 0$ ) are valid equations for all three cases, with the errors associated with the approximations required for derivations being of an acceptable magnitude for any amount of wear.

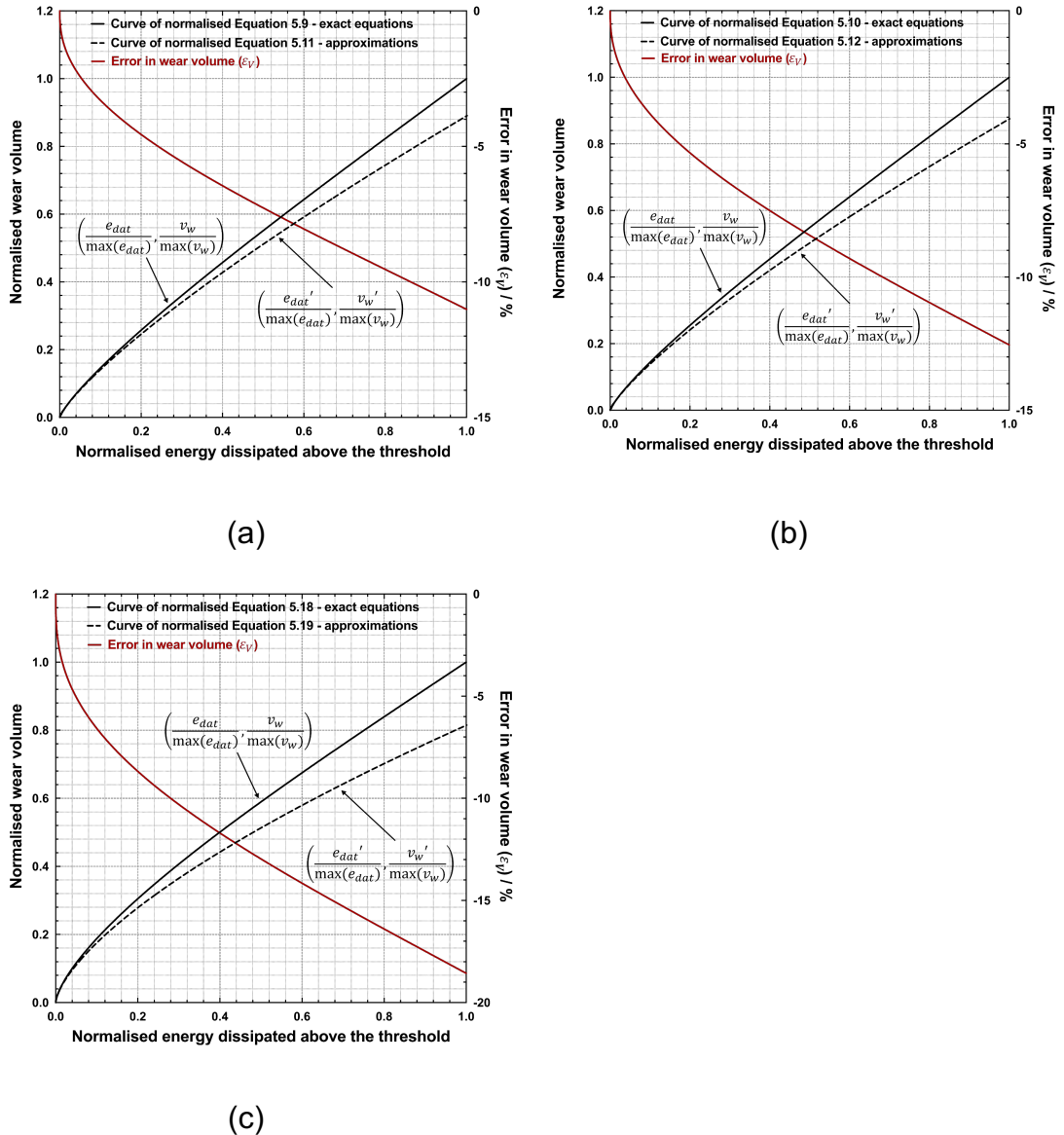


Figure 5.9: Plot of normalised energy dissipated above the threshold against normalised wear volume for both the exact and approximate across the full range of allowable values of  $e_{dat}$  along with the fractional error in the wear volume across the same range for all three cases: (a) SF contact with linear-based governing equation; (b) CC contact with linear-based governing equation; (c) SF contact with area-based governing equation.

The normalised expressions of the energy dissipated above the threshold and the wear volume for all three cases in the current section (Section 5.3) are summarised in Table 5.2 as below. In addition, Table 5.2 presents the maximum values of  $e_{dat}$  and  $v_w$  for all three cases as well as their corresponding values of maximum error as indicated in Figure 5.9.

**The development of alternative wear equations for commonly employed non-conforming contact**

**Table 5.2: Summary of the normalised expressions, the maximum values and the maximum error when analysing the errors associated with the approximations for all three cases.**

contact configurations	normalised expressions	maximum values	maximum error
SF (linear)	$e_{dat} = \frac{E_{dat}}{m_2 \pi R^4}$ $v_w = \frac{V_w}{\pi R^3}$	$\max(e_{dat}) = 6\pi$ $\max(v_w) = \frac{2}{3}$	11%
CC (linear)	$e_{dat} = \frac{E_{dat}}{m_3 \pi R^4}$ $v_w = \frac{V_w}{\pi R^3}$	$\max(e_{dat}) = 102\pi - 64$ $\max(v_w) = \frac{3}{4}$	13%
SF (area)	$e_{dat} = \frac{E_{dat}}{m'_2 \pi^2 R^5}$ $v_w = \frac{V_w}{\pi R^3}$	$\max(e_{dat}) = 128$ $\max(v_w) = \frac{2}{3}$	19%

**5.3.5 Experimental verification of the proposed relationships for wear scars with equiaxed shapes**

Experimental data are available in the literature [107] against which the two wear equations (Equations 5.15 and Equation 5.21) for the sphere-on-flat contact configuration can be tested. The data relate to fretting wear of a 52100 steel pair with a sphere-on-flat geometry, with a constant slip amplitude of 72  $\mu\text{m}$ . Three sphere radii were examined, namely 9.525 mm, 25.4 mm and 50 mm; it should be noted that different loads were employed for tests with the three different radii to ensure that the initial Hertzian contact pressure was the same across all three geometries. The wear data are presented in Figure 5.10 in the form of wear volume as a function of energy dissipated for the three different geometries along with the lines of best fit as proposed in the original paper; it can be seen that the evolution of the wear scar volume with energy is strongly influenced by the geometry of the contacting pairs, with the gradient of the regression lines (previously termed the *wear rate*) decreasing as the radius of

the spherical body was increased. These data are now replotted in the forms indicated by Equation 5.15 (using the term  $R^{-0.2}E_d^{0.8}$  as the abscissa) and by Equation 5.21 (using the term  $R^{-0.33}E_d^{0.67}$  as the abscissa) and are presented in Figure 5.11a and Figure 5.11b respectively. It can be seen (Figure 5.11) that the experimental data generated with the different geometrical configurations and test durations are reasonably described by either the function presented in Equation 5.15 (Figure 5.11a) or the function presented in Equation 5.21 (Figure 5.11b), although it is recognised that the data for the three different sphere radii do still form distinct populations in both cases, indicating that the assumptions made in the derivation of either equation are not entirely valid.

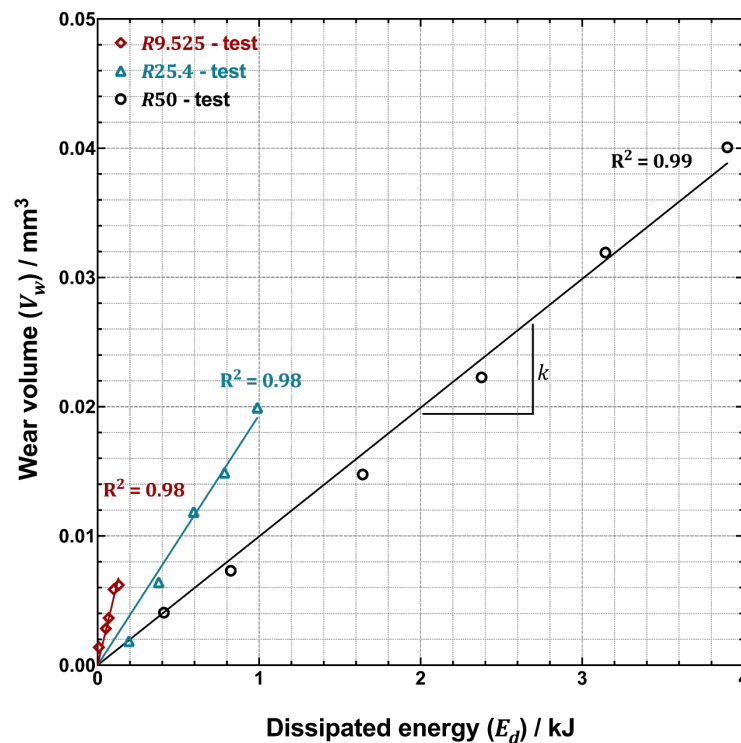


Figure 5.10: Plot of experimental data from the literature [107] showing the wear volume as a function of dissipated energy for fretting of a high-strength steel conducted with a sphere-on-flat arrangement with three different sphere radii (namely R9.525 pairs, R25.4 pairs and R50 pairs).

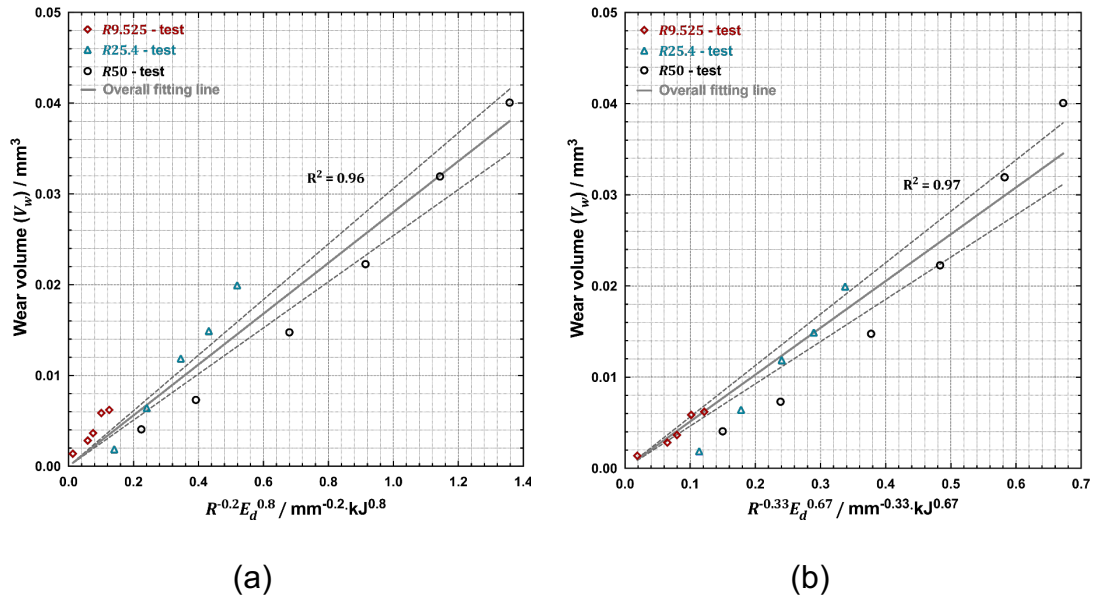


Figure 5.11: Replot of data from Figure 5.10 showing the wear volumes from sphere-on-flat fretting tests of a high strength steel [107] plotted as a function of (a)  $R^{-0.2} E_d^{0.8}$ ; (b)  $R^{-0.33} E_d^{0.67}$ . The data relate to tests with different sphere radii of 9.525 mm, 25.4 mm and 50 mm.

## 5.4 Discussion

### 5.4.1 Testing of the wear equations against experimental data

The third body approach [19] and the concept of the tribology circuit [96] both highlight the importance of debris ejection from the contact as a critical part of the ongoing process of wear, with the concept of the rate-determining process (RDP) as discussed in the previous chapter (either debris formation or debris ejection from the contact) being based upon these. It was shown that the rate of debris ejection from the contact was inversely proportional to the wear scar width for a cylinder-on-flat fretting configuration, and the parametric equations derived from it demonstrated that the evolution of the wear scar volume with the energy dissipated in the test was non-linear (i.e. Archard-type approaches are not appropriate descriptions of behaviour for fretting in contacts where debris ejection is the RDP). However, in the work of the previous chapter, the governing formulation was presented in the form of parametric equations which obscured the relationship desired of a wear equation, namely the direct

**The development of alternative wear equations for commonly employed non-conforming contact**

relationship between the wear volume and a measure of the exposure to wear (in this case, the frictional energy dissipated). In the current chapter, a wear equation has been derived for the cylinder-on-flat (non-conforming) contact geometry which is based upon the same assumptions as employed in the derivation of the parametric equations, namely that the rate of wear is always controlled by debris ejection from the contact (as opposed to debris formation within the contact) and that the threshold energy dissipated (below which there is no wear) is negligible. The wear equation derived is presented in a summary table (Table 5.3).

**Table 5.3: Summary of the wear equations for the three different non-conforming contact configurations considered in this work, namely cylinder-on-flat, sphere-on-flat and crossed-cylinders with both the linear and area bases of the governing equation as indicated.**

Contact configurations	Wear equation
Cylinder-on-flat (linear or area)	$V_w = K_1 R^{-0.25} E_d^{0.75}$
Sphere-on-flat (linear)	$V_w = K_2 R^{-0.2} E_d^{0.8}$
Crossed-cylinders (linear)	$V_w = K_3 R^{-0.2} E_d^{0.8}$
Sphere-on-flat (area)	$V_w = K_2' R^{-0.33} E_d^{0.67}$

The success in providing a coherent framework to understand the differences in development of wear volume in a cylinder-on-flat fretting test as a function of the contact geometry (as can be seen by comparison of Figure 4.9 and Figure 5.6) gives support to the underlying assumptions upon which the model development was based, primarily that of wear rate being inversely proportional to either the width or area of the wear scar (these two being equivalent here).

The assumption that the instantaneous wear rate is inversely proportional to the width of the wear scar was employed for the derivation of the equivalent equations for the sphere-on-flat and crossed-cylinders specimen pair configurations (also shown in the

## **The development of alternative wear equations for commonly employed non-conforming contact**

---

summary Table 5.3). In both of these cases, it is recognised that these begin as point contacts and that the wear scars remain largely equiaxed as they grow. The assumption is still made in the derivation of the equations that the debris flow out of the contact which occurs in the direction of fretting motion flow controls the wear rate and that the rate is therefore controlled by the largest dimension of the wear scar in that direction; as such, whilst side-leakage of debris from the contact may occur, it is assumed to have no significant influence on the wear rate. Whilst this was a very reasonable assumption for the cylinder-on-flat contact (where the dimension of the wear scar perpendicular to the direction of displacement was relatively large and therefore side-leakage was likely to be a small fraction of the overall debris ejection from the contact), it is clearly less so for these equiaxed contact geometries where side-leakage [19] is a reasonable expectation [77, 96] and may be significant. The equation for development of wear volume for a sphere-on-flat fretting contact based upon the assumption that instantaneous wear rate is inversely proportional to the wear scar radius has been tested against experimental data (Figure 5.11a) for tests conducted with spheres of different radii. In Figure 5.11a, the populations associated with the three sphere radii are still distinct (this is in contrast to the equivalent situation for the cylinder-on-flat configuration as presented in Figure 5.6) and this demonstrates that this wear equation derived is less well able to account for the effect of sphere radius; it is suggested that this indicates that the assumption that side-leakage of debris can be neglected when considering the (rate-determining) rate of debris ejection from the contact is less valid for the sphere-on flat geometry than it is for the cylinder-on-flat geometry. Despite this, the fit of data to the derived form of the wear equation indicated in Figure 5.11a is still reasonable, indicating the concept of the wear rate being dependent upon the size of the wear scar has clear validity here.

The assumption in the model that debris is removed from the contact in the direction of the fretting motion and that side-leakage can be ignored has been demonstrated to be

## The development of alternative wear equations for commonly employed non-conforming contact

wanting via the analysis of the sphere-on-flat experimental data where the wearing contact remains equiaxed throughout the process. More broadly, it is therefore concluded that the significance of side leakage (and therefore the validity of the assumptions made in the derivation of the new wear equations) might depend upon the aspect ratio of the contact or whether the shape of wear scar can be characterised by a 2D representation (i.e. with a uniform wear scar shape, such as CF contact) or a 3D representation (i.e. geometries such as SF and CC contacts) as illustrated schematically in Figure 5.12. In this regard, it is noted that for the CF contact, the aspect ratio of the contact patch changes as wear occurs, with the influence of side-leakage increasing as wear proceeds; this increasing influence of side leakage results in a decrease in the validity of the assumptions upon which the new wear equations are based. Moreover, it is noted that the initial geometrical arrangement will influence how the aspect ratio changes throughout a test. For example, CF contacts with the same applied load but a different line length would be expected to perform very differently as a result of differences in the way that the aspect ratio would vary with wear volume. Similarly, a contact with uneven shape of wear scar may suffer from the stronger effect of side-leakage, which might require further refinement of the model presented in this work.

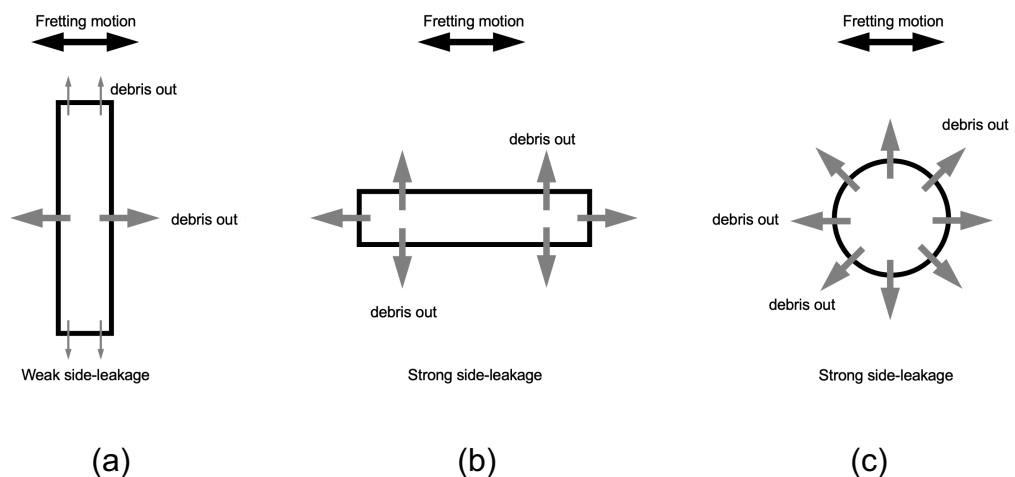


**Figure 5.12: Illustration of the effect of aspect ratio or the shape of a fretting contact on side-leakage (a) high aspect ratio; (b) low aspect ratio; (c) ununiform shape.**

### **The development of alternative wear equations for commonly employed non-conforming contact**

---

It is noted that the form of Equation 5.1 used for the broadly rectangular wear scar formed in the cylinder-on-flat contact configuration was also consistent with the assumption that the instantaneous wear rate is inversely proportional to the contact area, a position which would accord with the work in this area which likens the particle bed to a fluid which either flows or is squeezed out of the contact [99, 103] This second assumption was tested for the case of the sphere-on-flat contact resulting in a wear equation with a slightly different form (Equation 5.21) which is again included in the summary table (Table 5.3). Comparison of Figure 5.11a and Figure 5.11b indicates that, whilst the data are fully in accord with the concept of the instantaneous wear rate being related to the size of the contact, the area-derived form of the wear equation is not better in accord with the experimental data than the linear-derived form. When the assumptions and the fit to the data for the sphere-on-flat configuration are compared with those for the cylinder-on-flat configuration, it is suggested that the essentially two-dimensional situation of the cylinder-on-flat configuration is preferred: in this case, the debris flow is predominantly parallel to the direction of fretting, driven both by the fretting motion itself and by the fact that the scar dimension in the fretting direction is small compared to its dimension perpendicular to the fretting motion (with this short distance driving the flow as indicated in the governing equations).

It is noted that no suitable experimental data has been found in the literature against which the form of the wear equation for the crossed-cylinders contact geometry can be tested. However, given the similarity of the developing contact shape between the sphere-on-flat geometry and the crossed-cylinders geometry, especially at the early stage of a wear test where the projection of the wear scar is still approximately a circle, it is reasonable to conclude that the wear equation for the latter geometry has similar validity to that of the former geometry.

#### 5.4.2 Dependence of wear on contact geometry and energy dissipated

The equations for the different contact geometries and assumptions regarding the governing equation are presented in summary in Table 5.3. In all four cases, the equations take the form (when threshold energy is assumed to be negligible compared to the total dissipated energy into the contact):

$$V_w = KR^{n-1}E_d^n \quad (5.22)$$

It can be shown that  $K$  is directly proportional to the parameter in governing equation,  $k$ , by the relationship of  $K = \lambda k^n$ , where  $\lambda$  is the constant generated during the derivation and is independent of any fretting parameters. Please note that, unlike  $k$  which has the unit of  $\text{mm}^4 \cdot \text{kJ}^{-1}$ ,  $K$  will have units which depend upon the pair geometry and assumptions regarding the governing equation; also, it is noted that (in contrast to the units of the constant in Archard-type formulations),  $K$  will not have units which have a clearly recognisable physical meaning and this fact will make the approach being proposed intrinsically less attractive than the traditional approach to the those engaged in research and development in this area. However, it is also recognised that the general form of wear equation for fretting developed in the current work (as indicated by Equation 5.22) is generated as the result of mathematical approximations of those parametric equations based upon a simple, yet reasonable assumption underpinned by the physical phenomenon for fretting wear. Although the final form of the equation may seem similar to those power law equations with empirical exponents generated by data-fitting of experimental results, the method outlined in the current study is fundamentally different from them. The derivations of those wear equations as described in Appendix B give no indication that the radius exponent can be related to the exponent of the dissipated energy,  $n$ , by  $n - 1$ ; yet the wear equations (as summarised in Table 5.3) derived in this work demonstrate the existence of such relationship between exponents of radius and dissipated energy at least for all four

## **The development of alternative wear equations for commonly employed non-conforming contact**

---

cases presented in the current chapter. Dimensional analysis as presented in Appendix C indicates that the appearance of such relationship between the exponents in Equation 5.22 is not entirely by coincidence.

It was the apparent differences in the fretting wear rates observed as a function the radius of the non-plane members when using both cylinder-on-flat and sphere-on-flat geometries [18, 20, 23, 90, 107] that prompted the research in this area (both in the previous chapter and in the work reported herein), with its focus on the effect of the developing contact size on the rate of wear. The equations presented in Table 5.3 allow the dependence of the development of wear volume on the details of the selected test specimen pair geometry to be accounted for; it has been shown that for all three geometrical configurations examined and with the assumptions of both the linear and area dependencies of the instantaneous wear rate, the radius exponent  $n - 1$  is within the range of  $-0.33 \leq n - 1 \leq -0.2$ , which indicates that for a given energy dissipated, the wear volume will decrease with increasing radius of the non-plane specimen in each case. This is a direct result of the fact that as the specimen radius increases, the scar size will be larger for a given worn volume, with that larger wear scar size then reducing the flow rate of the debris from the contact (Equation 5.1, Equation 5.8a, Equation 5.8b and Equation 5.17) and thus reducing the observed rate of wear. However, it is recognised that the dependence on the specimen geometry is relatively weak; for example, for the cylinder-on-flat contact geometry, an increase in the cylinder radius by a factor of  $\sim 27$  (as in the experiments reported in Figure 4.9 and Figure 5.6) is predicted to result in a reduction in the wear volume (all other things being equal) by a factor of only  $\sim 2.3$ . Notwithstanding, for the first time, these equations have provided a means of incorporating characteristics of the specimen test geometry into the wear equation with the success of this approach being demonstrated most strongly for the cylinder-on-flat test configuration (Figure 5.6) but also for the sphere-on-flat test

configuration (Figure 5.11) to a lesser extent (the difference being associated with the effects of side-leakage of debris as previously discussed).

Perhaps more significant is the proposed dependence of the wear volume on the energy dissipated. Archard's wear equation [16] was derived for sliding wear, and describes the rate of debris generation in a sliding contact. It has been argued previously (an argument which is reinforced here) that simply applying this equation (or those of other Archard-type approaches) to fretting contacts where debris elimination from the contact is the rate-determining process is not appropriate [37]. The equations (Table 5.3) derived in this chapter do (for the first time) take account of the size of the wear scars for the three contact geometries considered with two hypotheses regarding the governing equations, but also give an indication as to why Archard-type equations have been employed so widely in analysis of fretting data. The dependence of wear volume on dissipated energy takes the form as indicated in Equation 5.22, where across the three geometries examined and with the assumptions of both the linear and area dependencies of the instantaneous wear rate,  $0.67 \leq n \leq 0.8$ . The fact that these exponents are not far removed from unity (this being the exponent associated with the Archard-type equations) means that the fitting of experimental data to an equation of the form  $V_w = k_e E_d + c$  (where  $k_e$  is considered to be the wear rate and  $c$  is a constant representing an initial transient in wear associated with bedding-in [30]) is often apparently quite successful. It is noted that  $c$  is often set to zero, with this being a necessary assumption in the many cases reported in the literature where the wear rate  $k_e$  is derived from tests conducted with a single value of energy dissipated,  $E_d$ .

To illustrate this, a dataset was formed of 1001 equally-spaced points in  $E_d$  and values of wear volume calculated for each of those points according to the relationship as indicated by Equation 5.22 (i.e. the form  $V_w = \eta E_d^{0.75}$  associated with a cylinder-on-flat contact configuration, where  $\eta = K_1 R^{-0.25}$ , which is a constant when treating  $K_1$  and  $R$  are constants). Linear regressions of the form  $V_w = k_e E_d$  and  $V_w = k_e E_d + c$  were then

## The development of alternative wear equations for commonly employed non-conforming contact

applied to this dataset. The regression lines to these data are shown in Figure 5.13:, where the solid line represents the data of the form  $V_w = \eta E_d^{0.75}$  and the dashed lines represent the two different forms of linear regression to these data; it can be seen that it is apparently not unreasonable to apply a linear relationship of either of these types to such a dataset (in both cases, the coefficient of determination,  $R^2$ , is greater than 0.99). Moreover, with the natural errors associated with experimental data, the apparent appropriateness of a linear fit to a set of experimental data of this form is even more understandable.

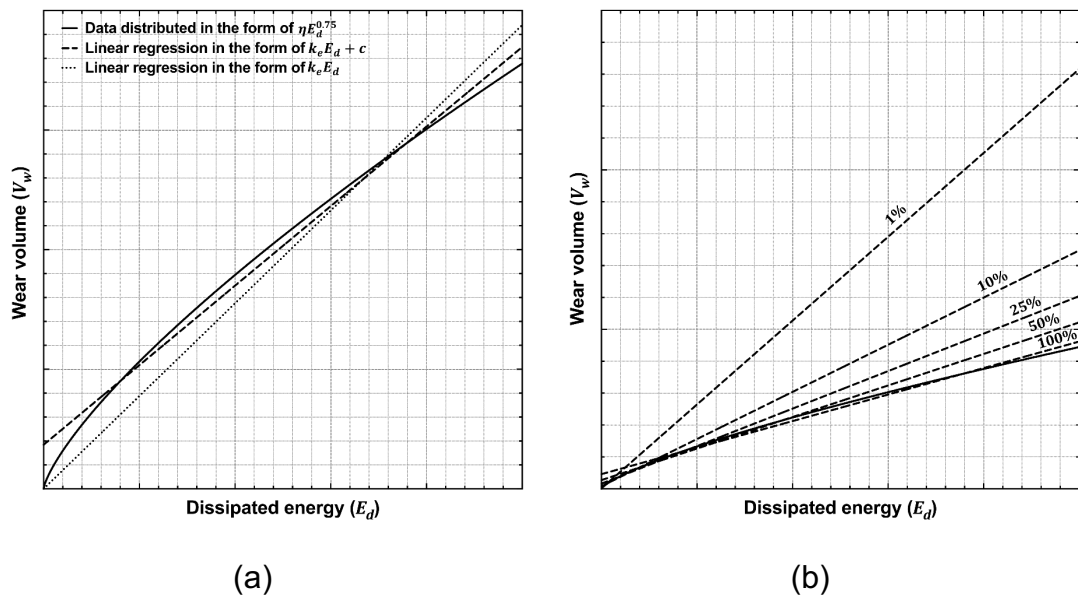


**Figure 5.13: Schematic diagram showing data distributed in the form  $V_w = \eta E_d^{0.75}$  (solid line) along with linear regressions to those data; (a) linear fit in the form  $V_w = k_e E_d$  (long dashes) and  $V_w = k_e E_d + c$  (short dashes); (b) linear regression in the form  $V_w = k_e E_d + c$  to data from tests of five different durations; the test with the longest duration (in terms of  $E_d$  is labelled 100%) with the four shorter tests having a maximum dissipated energy of 1%, 10%, 25% and 50% of that of the longest test. The linear regressions to the datasets from the tests with the five different durations are as indicated by the dashed lines.**

If it is (incorrectly) assumed is that the relationship between wear volume ( $V_w$ ) and energy dissipated ( $E_d$ ) (or any similar measure of the exposure to wear) is in fact linear (of the general form  $V_w = k_e E_d + c$ ), then given that enough data have been gathered to identify the value of the initial transient ( $c$ ) and to ensure that steady-state conditions have been established, the duration of the test (in terms of the total energy dissipated)

should not affect the value of the wear rate derived. (It is noted that in previous work, it is not clear that the tests lengths were always adequately long, especially for more-conforming contact geometries, to allow steady state conditions to be established as can be seen by a comparison of the data in references [23] and in the previous chapter). However, if it is instead assumed (as is argued here) that the data actually take the form  $V_w = \eta E_d^{0.75}$ , the gradient of any linear regressions to such data will depend upon the duration of the test (i.e. the maximum value of  $E_d$  in the dataset). This is schematically illustrated in Figure 5.13b; here five tests are simulated with the only difference between those tests being their duration (in terms of  $E_d$ ). The four shorter tests have durations of 1%, 10%, 25% and 50% of that of the longest test. Linear regressions (of the type  $V_w = k_e E_d + c$ ) are applied over the data from the five test durations (labelled 100% for the test with the longest duration and then 1%, 10%, 25% and 50% for those of the shorter durations). It is notable again that in each of these cases, the coefficient of determination,  $R^2$ , is greater than 0.99. It can be thus seen that the  $k_e$  (traditionally assumed to be the wear rate) is strongly dependent upon the duration of the test, with this gradient decreasing as the duration of the test,  $E_d$ , is increased. To give some measure of the significance of these changes, the variation in  $k$  with the test duration (represented by  $E_d$ ) is presented in Figure 5.14. The implication of this is that when employing a non-conforming geometry for a fretting test programme, if two otherwise identical tests are conducted with different test durations, then the gradient,  $k_e$  (of the general form  $V_w = k_e E_d + c$ ), of the linear regression to the resulting data is dependent upon the ratio of the test durations. For example, whichever form (either  $V_w = k_e E_d + c$  or  $V_w = k_e E_d$ ) is assumed, increasing the test duration by a factor of 10 leads to a reduction of  $k_e$  (the Archard-type wear rate) to 56% of its former value. In fact, the linear regression line is close to the tangent line of the data distribution; the gradient of the linear regression can be approximated as the derivative of Equation

**The development of alternative wear equations for commonly employed non-conforming contact**

5.22, i.e. it can be shown that as  $E_d$  increases by a factor of  $\alpha$ , the derivative of  $V_w$  with respect to  $E_d$  changes by a factor of  $\alpha^{n-1}$ :

$$E_d \rightarrow \alpha E_d$$

$$\frac{dV_w}{dE_d}(\alpha E_d) = \alpha^{n-1} \frac{dV_w}{dE_d}(E_d) \quad (5.23)$$

(with  $n$  being defined as in Equation 5.22) and thus the change of  $k_e$  (the Archard-type wear rate) follows a similar pattern.

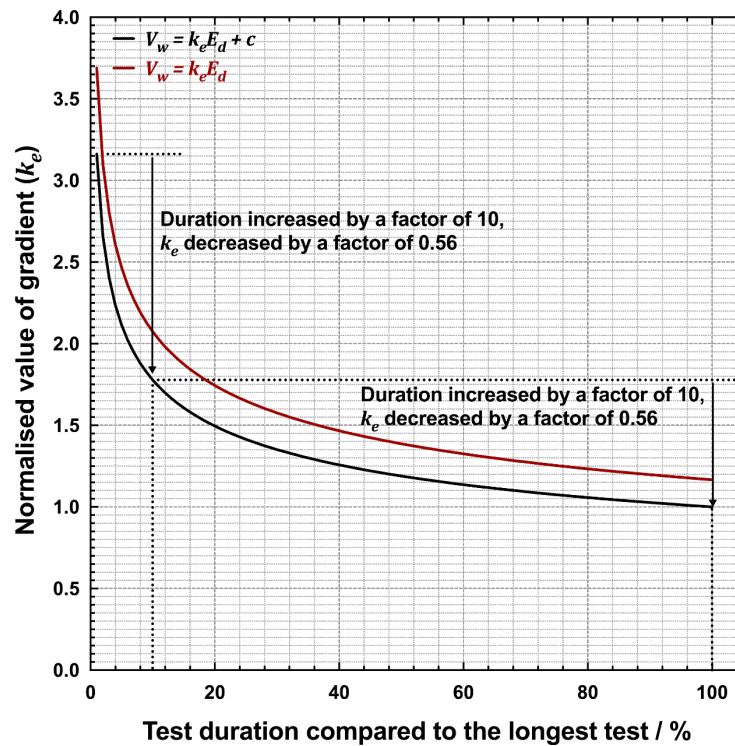


**Figure 5.14: Normalised values of the gradients ( $k_e$ ) of linear regressions to data of the form  $V_w = \eta E_d^{0.75}$  with for data of a range of durations,  $E_d$ , compared to that of the duration of the longest dataset. Linear regressions both of the form  $V_w = k_e E_d$  and  $V_w = k_e E_d + c$  are shown. The values of  $k_e$  have been normalised to that resulting from the regression of the form  $V_w = k_e E_d + c$  to the longest dataset.**

To further illustrate this, linear regression (to the general form  $V_w = k_e E_d + c$ ) was applied to the experimental data presented in Figure 4.9 for the 6 mm radius cylinders for different maximum test durations; in each case all the data available both at and below the defined test duration were employed for the linear regression. The gradient of the linear regression ( $k_e$ ) to the experimental data is plotted against the test duration

as shown in Figure 5.15; it can be seen that  $k_e$  falls as the test duration was increased, but that in all cases, the coefficient of determination remained high, giving (false) confidence that the experimental data were well described by the form of the equation  $V_w = k_e E_d + c$ . The ratio of dissipated energy between the test with the largest and smallest duration here is  $\sim 50$ . The ratio  $\alpha^{n-1}$  (as shown in Equation 5.23, with  $\alpha = 50$  and  $n = 0.75$ ) indicates that the gradient of the linear regression ( $k_e$ ) should be  $\sim 2.65$  times larger at the smallest duration than at the largest, with the data in Figure 5.15 demonstrating an equivalent ratio of 2.26. The accord between observations and predictions here adds further weight to this approach.

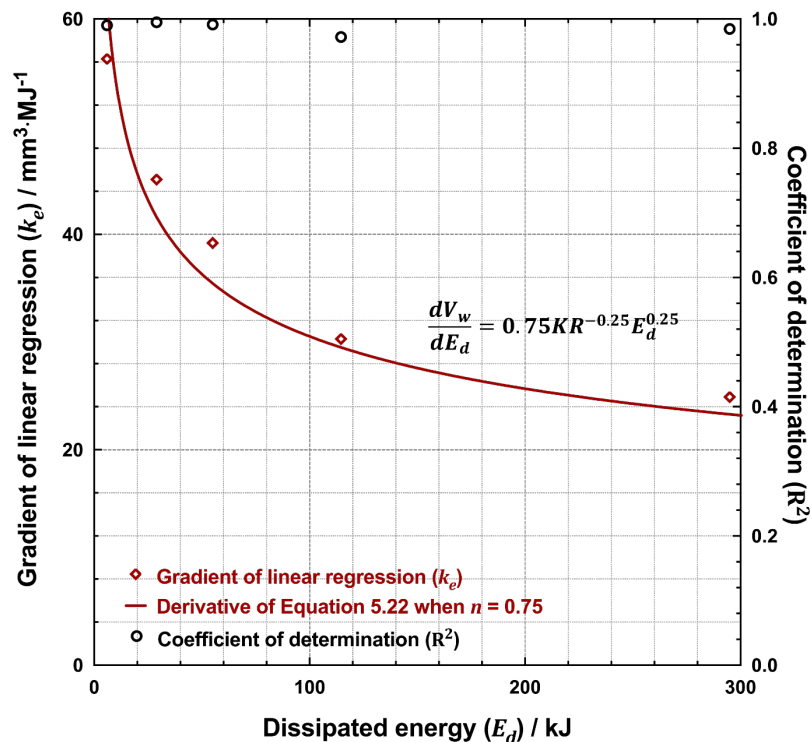


Figure 5.15: Plot of gradients,  $k_e$ , (of the form  $V_w = k_e E_d + c$ ) along with the associated coefficients of determination from linear regression of the data for the 6 mm radius cylinders presented in Figure 4.9 as a function of the maximum energy included in the linear regression.

As such, it has been shown that for fretting conditions where debris ejection from the contact is the rate-determining process, linear regression to the general form  $V_w = k_e E_d + c$  generally produces a good fit to the data, but that the high quality of the fit unfortunately provides misplaced assurance that the gradient of such a regression can

## **The development of alternative wear equations for commonly employed non-conforming contact**

---

be regarded as the wear rate. The proposed form of the relationship when debris transport is the RDP ( $V_w = KR^{n-1}E_d^n$ ), which is more appropriate than those based upon an Archard-type approach, indicates the dependence upon both the geometrical make-up of the contact ( $R$ ) and the duration of the test ( $E_d$ ) since both of these affect the development of the size of the contact. It is recognised that  $K$  itself (similar to the constant  $k$  in the governing equation as highlighted in Equation 5.1 and Equation 5.8 from where it was derived) is likely to be a function of many other parameters which are regarded as variable in the fretting test such as applied load, slip amplitude, environmental temperature, fretting frequency etc. However, this constant  $K$  is independent of test durations and contact geometry, and thereby will facilitate understanding of the development of wear in fretting, both in service and in laboratory testing. Whilst these equations have been derived for specific test geometries, the need to consider debris ejection from the contact as a potential rate-determining process is general to all situations where fretting occurs; moreover, it is argued that in any situation where debris ejection is seen to be rate-determining (irrespective of geometry), the instantaneous wear rate will be inversely proportional to a characteristic dimension of the size of the wear scar related either to the distance over which debris have to migrate before they can be ejected or to the area of the contact. For laboratory tests where a non-conforming specimen pair geometry is employed, it is recognised that it is helpful to have data across a wide range of values of dissipated energy, or to have data with the specimen pairs having non-plane specimens over a range of radii, and to plot those data via the appropriate form of wear equation  $V_w = KR^{n-1}E_d^n$ .

## **5.5 Conclusions**

It has been shown that under certain circumstances, the instantaneous wear rate in fretting is either inversely proportional to a characteristic dimension of the wear scar (the maximum size of the scar parallel to the direction of fretting) or is inversely

proportional to the wear scar area. This means that when non-conforming specimen pair geometries are employed in fretting testing (where the scar size grows as wear proceeds), then the instantaneous wear rate changes as the test proceeds. One outcome of this assertion is that the traditional concept of wear rate for such a test is meaningless since it is constantly changing.

Wear equations have been generated for three commonly employed non-conforming specimen pair geometries with the assumptions of both linear and area dependencies of the instantaneous wear rate which describe the evolution of wear volume with test duration (which is here described by the frictional energy dissipated). The basis of these equations is that of debris-flow out of the contact, and it is shown that the simple assumption that the debris flow rate is inversely proportional to the maximum size of the scar parallel to the direction of fretting is most reasonable when that dimension of the scar is small compared to the size of the scar in other directions. As such, the validity of the equations developed is much higher for cylinder-on-flat test configurations than it is for sphere-on-flat or crossed-cylinders test configurations.

Examination of the form of the wear equations developed provides an understanding of how Archard-type approaches have been inappropriately employed for so long in fretting research, despite the wide consensus regarding the validity of Godet's third body approach and Berthier's tribology circuit which highlight the key role of debris ejection from the contact; moreover, it also provides an indication as to how the test duration will affect the traditional measure of the wear rate derived from inappropriate application of an Archard-type equation to such data.

# Chapter 6      The dependence of wear rate on slip amplitude

## 6.1 Introduction and chapter outline

There is a substantial body of research that indicates that there is a threshold of slip amplitude in fretting below which the wear process can no longer take place [9, 24, 27, 81, 94, 122-124]. It is believed that, with the closed nature of fretting contact, a sufficient slip amplitude is necessary to initiate the process of debris ejection out of the contact to allow the progression of wear. However, the reported values for such a threshold vary widely: the critical slip amplitude was found up to 70  $\mu\text{m}$  in some early reports [27, 81], while more recent works indicated that the critical value should be around 10  $\mu\text{m}$  [24, 94]. It was argued by Pearson and Shipway [24] that these differences could be explained by the fact that the concepts of displacement amplitude ( $\Delta^*$ ) and slip amplitude ( $\delta^*$ ) are often confused, where the former incorporates the system compliance and is thereby always larger than the latter; these two quantities are related to each other by the equation of  $\delta^* = \Delta^* - \frac{Q}{S}$  as shown in Equation 3.4 (Section 3.4.3) where terms are as previously defined. It was suggested [24] that the lack of necessary techniques in early investigations resulted in the so-called “slip amplitude” referred in those literatures are in fact the applied displacement amplitude, and the actual slip amplitude of these compliant systems could be small.

We should note here that the definition of the threshold slip amplitude, although without being explicitly defined, is based on the observation from experimental results that the wear volume becomes negligible below the threshold. With the fact that small slip amplitude are often closely associated with a small dissipated energy, and there also exists a threshold of energy in fretting below which wear ceases (described in Section 2.3.3), Pearson and Shipway argued [24] that it is still not clear whether the negligible wear volume is caused by the small slip amplitude or instead that the total dissipated

energy required to initiate damage has not been reached; it seems the latter argument is favoured by them from the discussion presented in their work. Small slip amplitude is also associated with partial slip regime in fretting (described in Section 2.2.2), in which a portion of the contact area does not slip under the imposed fretting conditions. The contact in partial slip regime exhibits a stuck region at the centre with limited abrasive damage near the edge, which could be used as an explanation for the almost zero wear volume observed induced by small slip amplitude.

Nevertheless, despite the difference in the value of threshold slip amplitude, it is generally agreed upon that, with a fixed test duration and normal load, the wear volume increases rapidly with the increase of slip amplitude, once the threshold has been overcome. Within the framework of an Archard-type approach, such observation often leads to the conclusion that the wear rate increases monotonically with slip amplitude until the transition to reciprocating sliding wear, upon which the wear rate will be independent of the slip amplitude as predicted by Archard wear equation [16]. Indeed, this dependence of wear rate upon slip amplitude in fretting has been reported by many researchers [4, 18, 27, 33, 72, 81, 91, 108, 111, 113], among which the work by Vingsbo and Söderberg [4] is the most renowned and widely recognised (as shown in Figure 2.1). However, the source of data upon which Vingsbo and Söderberg's work was built [4] was conducted under different test configurations and materials. As demonstrated by Knudsen and Massih [125] by reproducing Vingsbo and Söderberg's work with original data which was used in constructing Figure 2.1, it is likely that the simple relationship indicated between wear rate and slip amplitude is an over-simplification.

With the understanding of the existence of an energy threshold in fretting and the realisation that the concepts of displacement amplitude and slip amplitude were not explicitly distinguished at the time of Vingsbo and Söderberg, Pearson and Shipway [24] presented a formula to calibrate the wear rate (as the energy wear rate  $k_e$ ) derived from experimental results which had not considered these two issues. They proposed

## The dependence of wear rate on slip amplitude

---

that the true wear rate ( $k'_e$ ) was related to the  $k_e$  by the equation of  $\frac{k_e}{k'_e} = 1 - \frac{Q^*}{S\Delta^*} - \frac{E_{th}}{4\Delta^*Q^*N}$ ,

and concluded that the true wear rate is in fact independent upon the slip amplitude.

However, it is suggested here that the work of Pearson and Shipway [24] has presented unjustified conclusions based upon a paucity of data, specifically that their use of a fixed (and small – only  $10^5$ ) number of fretting cycles meant that the effects of slip amplitude and total energy dissipated were confused.

Please note that nearly all the arguments about the role of slip amplitude in the current section are based on experimental results which are conducted in a relatively short test duration [109], compared with the service time of engineering components in applications. Hence it is not clear whether the conclusions drawn by those observations can adequately characterise the wear process given that steady state may not always have been achieved (even if the researchers suggest that it has). More importantly, as emphasised many times in the current thesis, a fretting wear process should focus on both debris formation and debris ejection indicated by the third body approach [19] and the concept of tribology circuit [96], rather than considering material removal only suggested by the Archard wear equation [16]. However, when discussing the effect on slip amplitude (and many other fretting parameters) on the wear rate, it is the Archard-type wear rate that most researchers employ as the basis, which this thesis argues is not normally appropriate.

To fully understand the role of slip amplitude in fretting, its effects on the debris formation and ejection must be discussed individually, which requires studies to understand the underlying mechanisms and RDPs so that a coherent physical model can be established. It has been generally accepted that an increased slip amplitude can enhance the rate of debris ejection [33, 109]. However, care needs to be taken in studies involving non-conforming contact geometries where a larger slip amplitude can

produce a larger contact over a fixed number of cycles which may then result in reduction in wear rate associated with the increased contact size.

In Chapter 4, a governing equation was proposed linking the instantaneous wear rate with the wear scar width, which provides a method to address the effect of contact size in modelling the evolution of wear (the equation is restated here in the current chapter as Equation 6.1):

$$\frac{dV_w}{dE_d} = \frac{k}{x} \quad (6.1)$$

Unlike the traditional Archard-type wear rate, which is assumed to be a constant regardless of the exposure of wear, the implication of Equation 6.1 is that (with a non-conforming contact geometry) the wear rate falls continuously with the development of wear. The parameter  $k$  in Equation 6.1 acts as single parameter characterising the instantaneous wear rate for tests under certain conditions, which presumably is a function of various fretting parameters such as the normal load and slip amplitude, but, importantly, is independent upon the contact geometry and the test duration. This governing equation was solved analytically by assuming a geometric relationship between the wear volume and the wear scar width, generating a set of parametric equations. The concept was developed further in Chapter 5 to produce a general form of wear equation which states that, for non-conforming configuration (CF, SF or CC contact), the wear volume can be calculated as shown in Equation 5.22 (which is restated here as Equation 6.2), whose validity was tested with extra data from literature as demonstrated in Chapter 5.

$$V_w = KR^{n-1}E_d^n \quad (6.2)$$

In light of this, the question to be addressed in the current chapter is clear: assuming that debris ejection is still the RDP, what is the dependency of  $k$  upon the slip amplitude? (i.e. is the ability of the contact to expel debris influenced by the slip amplitude?) Details

## The dependence of wear rate on slip amplitude

---

about the specimens, the test rig and the experimental procedures employed in the current chapter are described in Chapter 3; test conditions for this chapter are detailed in Table 6.1 as below:

**Table 6.1: Summary of the fretting test conditions for the additional tests for which data are presented in Chapter 6.**

---

Normal load ( $P$ ) / N	450
Displacement amplitude ( $\Delta^*$ ) / $\mu\text{m}$	10, 15, 20, 25, 50, 100
Cylindrical specimen radius ( $R$ ) / mm	6
Test duration ( $N$ ) / $\cdot 10^6$ cycles	1, 5, 10
Frequency ( $f_{Hz}$ ) / Hz	20
Temperature ( $T$ ) / $^{\circ}\text{C}$	Ambient temperature

---

## 6.2 Experimental results

Examination of experimental data shows that in the early stages of the test, fretting loops were unsteady, but steady state was quickly achieved with the loops remaining stable throughout the rest of test. Averaged fretting loops over the last 10% of the test were calculated and examples such loops from tests with durations of  $N = 5 \times 10^6$  cycles and with a range of displacement amplitudes from  $\Delta^* = 10 \mu\text{m}$  to  $\Delta^* = 50 \mu\text{m}$  are presented in Figure 6.1a. Figure 6.1b compares the averaged fretting loops from the first 10%, the mid 10% and the last 10% of one example test after reaching its steady-state; the example test was conducted with  $\Delta^* = 25 \mu\text{m}$  and  $N = 5 \times 10^6$  cycles, demonstrating that those loops in Figure 6.1a are indeed characteristic of their corresponding tests. Within each loop, it can be seen that after the period of elastic deformation induced by the stiffness of system, the tangential force ( $Q$ ) within contact increases during the relative motion between first bodies. The system stiffness  $S$  (i.e. the gradient of the elastic part of the fretting loops) was calculated to be  $33 \pm 3 \text{ N} \cdot \mu\text{m}^{-1}$ .

It should be noted that the maximum tangential forces exhibited in tests conducted with  $\Delta^* = 10 \mu\text{m}$  and  $\Delta^* = 15 \mu\text{m}$  are similar to each other, but significantly lower than those observed in the tests conducted with larger displacement amplitudes. Experimental data from tests conducted with  $\Delta^* = 100 \mu\text{m}$  are used in the current study, but the maximum duration of these tests was  $N = 1 \times 10^6$  cycles; it is noted here that their fretting loops exhibit a system stiffness within the range identified for the loops presented in Figure 6.1 along with a similar maximum tangential force ( $Q^*$ ). A characteristic tangential force for the loop is often presented in the form of  $\mu_e$ , and the dependence of  $\mu_e$  with  $\Delta^*$  (and therefore with  $\delta^*$ ) will be presented later (Figure 6.3).

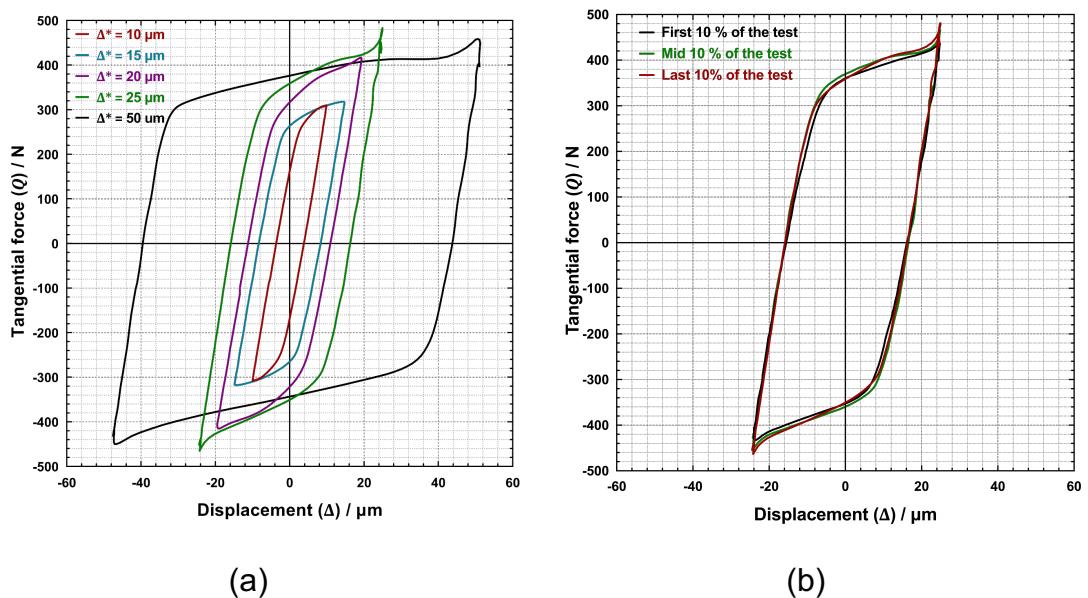


Figure 6.1: Plot of averaged fretting loops for tests: (a) with varying displacement amplitudes from  $\Delta^* = 10$  to  $50 \mu\text{m}$ , and  $P = 450 \text{ N}$ ; experiments were conducted with  $N = 5 \times 10^6$  cycles and the loops shown are the average over the last 10% of the test; (b) from the first 10%, the mid 10% and the last 10% of the test conducted with  $\Delta^* = 25 \mu\text{m}$  and  $N = 5 \times 10^6$  cycles, demonstrating the characteristic nature of fretting loops in Figure 6.1a.

As discussed in Chapter 2, distinguishing slip amplitude ( $\delta^*$ ) from displacement amplitude ( $\Delta^*$ ) is important as the former represents the actual slip occurring between first bodies, and it can be calculated from the fretting loops by removing the elastic displacements from the loop. The method to calculate  $\delta^*(i)$  (slip amplitude for each cycle of a test) has been described in Section 3.4.3, and from this a single quantity to

## The dependence of wear rate on slip amplitude

---

characterise the slip amplitude for the whole test ( $\delta^*$ ) can be determined as the average of  $\delta^*(i)$ . However, it is also a common practice to estimate  $\delta^*$  from fretting loops to have a board understanding of how  $\delta^*$  deviates from  $\Delta^*$ ; for instance, as shown in Figure 6.1, the slip amplitude of the test conducted with  $\Delta^* = 50 \mu\text{m}$  for  $N = 5 \times 10^6$  cycles is  $41 \mu\text{m}$ . In the current study, for tests with different displacement amplitudes, varying from  $\Delta^* = 10 \mu\text{m}$  to  $\Delta^* = 100 \mu\text{m}$ , their corresponding slip amplitudes across different test durations are steady. The statistical analysis of slip amplitudes shows that variations of  $\delta^*$  for each  $\Delta^*$  at different number of cycles are small, with the RSD (relative standard deviation, defined as the ratio of one standard deviation to the mean) from the minimum of 0.5% for  $\Delta^* = 20 \mu\text{m}$  to the maximum of 20.9% for  $\Delta^* = 10 \mu\text{m}$ . The average values and variation of  $\delta^*$  across different test durations for each  $\Delta^*$  are presented in Table 6.2 located at the end of this section (those values of  $\delta^*$  for each individual test were calculated as the average of  $\delta^*(i)$ ). The following analysis to understand the dependence of wear rate upon displacement amplitude (therefore, the slip amplitude) will be based on the average value of  $\delta^*$ .

Figure 6.2 is a plot of evolution of ECoF ( $\mu_e(i)$ ) over a test of duration of  $N = 5 \times 10^6$  cycles for two displacement amplitudes, namely  $\Delta^* = 10 \mu\text{m}$  and  $\Delta^* = 50 \mu\text{m}$ . As it can be seen, the change of  $\mu_e(i)$  throughout the test follows a similar fashion for both displacement amplitudes. The increase of  $\mu_e(i)$  is rapid at the beginning of the test, followed by a quick fall-back to a relatively steady value. which is characterised by small fluctuations around that steady value. This pattern of the change of  $\mu_e$  is in line with those results reported in literature [66, 111, 117, 120, 126] and is observed for all the tests conducted in the current study. Therefore, similar to the analysis of fretting loops in Figure 6.1, the averaged value of ECoF over the last 10% of the test duration was calculated to represent  $\mu_e$  for each individual test.

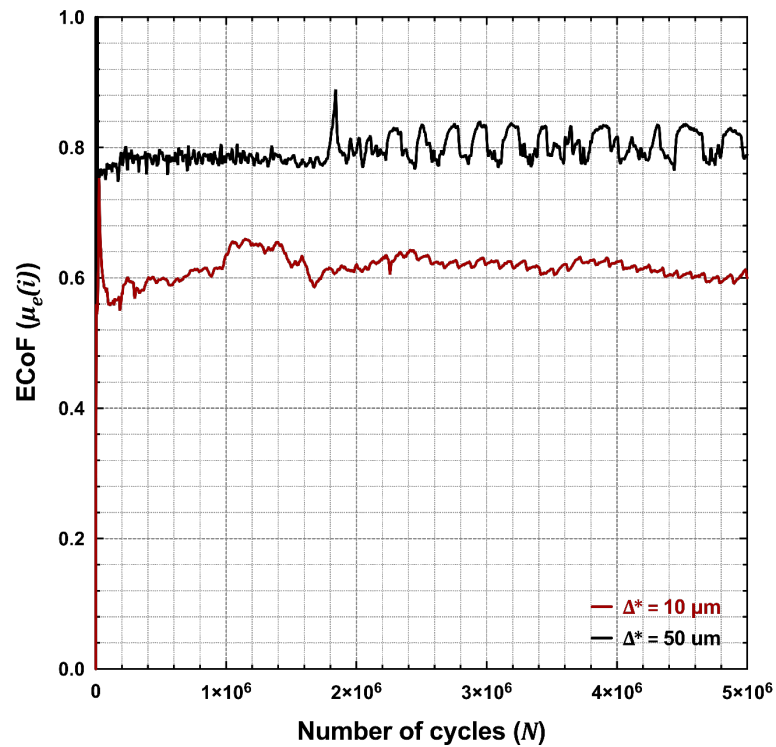


Figure 6.2: Plot of evolution of ECoF ( $\mu_e(i)$ ) over a test of  $N = 5 \times 10^6$  cycles for two displacement amplitudes, namely  $\Delta^* = 10$  and  $\Delta^* = 50 \mu\text{m}$ .

The average values of ECoF ( $\mu_e$ ) calculated from each test in the current study is plotted against the corresponding slip amplitude ( $\delta^*$ ) in Figure 6.3; the error bar on the graph marks the standard deviation range of  $\mu_e$  for each test. As it can be seen, values of  $\mu_e$  across different test durations for each slip amplitude are reasonably stable. The overall trend is that  $\mu_e$  increases rapidly from a value around 0.6 to around 0.8 as the slip amplitude is increased from  $\sim 5 \mu\text{m}$  to  $\sim 15 \mu\text{m}$  and then remains stable at around 0.8 as the slip amplitude is further increased. Averaged ECoF across different test durations can be determined, the values of which are summarised in Table 6.2.

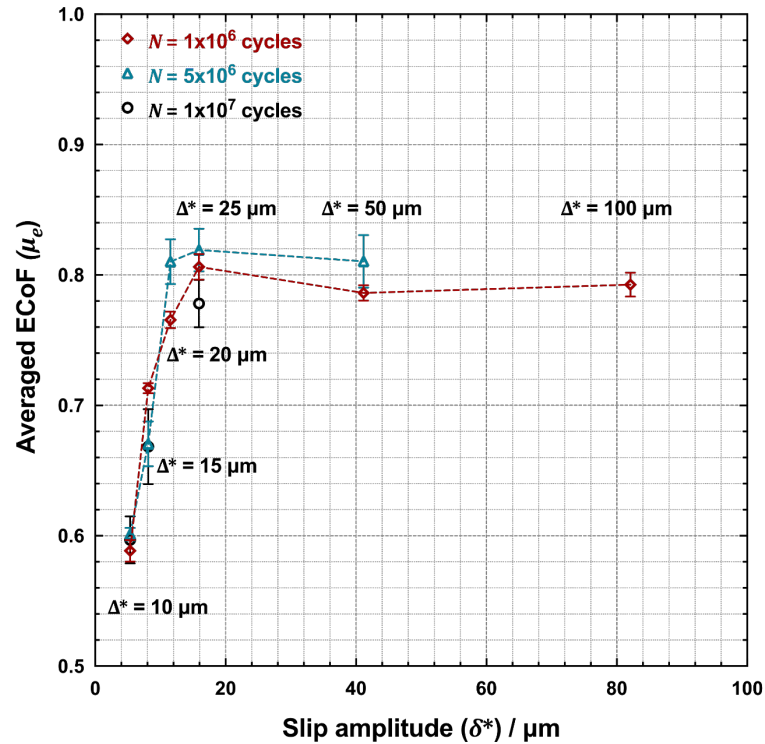
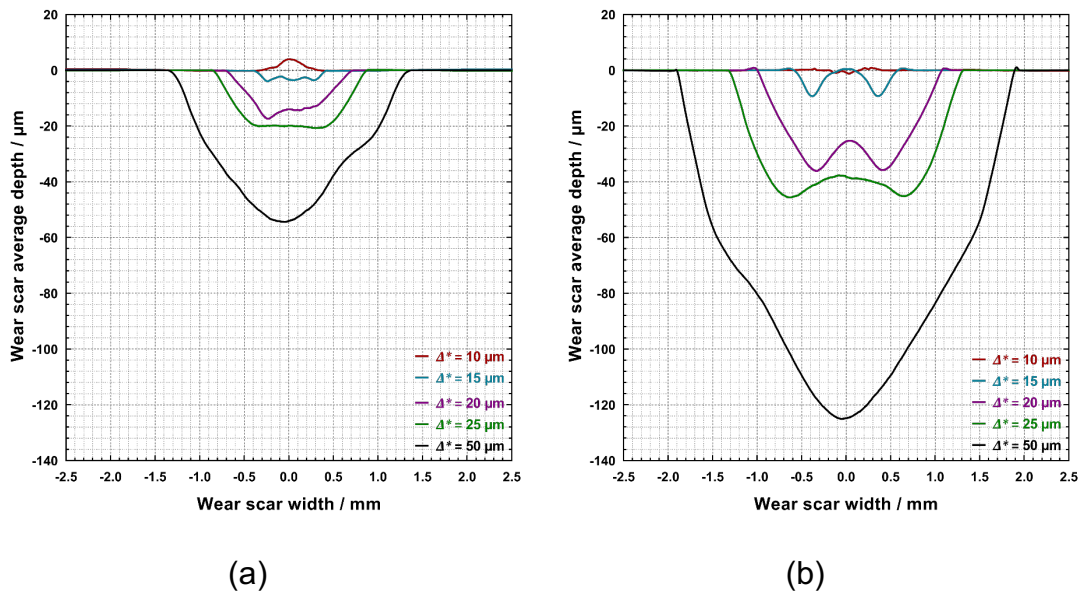


Figure 6.3: Plot of averaged ECoF against slip amplitude for tests of varying duration ( $N = 1 \times 10^6$  cycles,  $5 \times 10^6$  cycles and  $1 \times 10^7$  cycles); values of ECoF were taken as the average of the last 10% of test duration.

Figure 6.4 shows the averaged profile of wear scars on flat specimens for tests conducted with varying displacement amplitude, from  $\Delta^* = 10 \mu\text{m}$  to  $\Delta^* = 50 \mu\text{m}$  for  $N = 1 \times 10^6$  cycles and for  $N = 5 \times 10^6$  cycles. Figure 6.4 illustrates that all wear scars develop as expected in both depth and width as the increase of test duration, except for tests conducted with  $\Delta^* = 10 \mu\text{m}$ . For  $\Delta^* = 10 \mu\text{m}$ , it appears that no clear evidence of the evolution of wear scar in terms depth or width is observed at least until  $N = 5 \times 10^6$  cycles.

A U-shaped wear profile is clearly developed for tests with  $\Delta^* = 50 \mu\text{m}$ . As demonstrated in the results reported in the Chapter 4, such shape of wear scar is formed early in the test (it is observed as early as  $N = 5 \times 10^3$  cycles). In contrast, for the tests conducted with displacement amplitudes within the range from  $\Delta^* = 15 \mu\text{m}$  to  $\Delta^* = 25 \mu\text{m}$ , the wear scar starts to show the early sign of forming a W-shape by  $N = 1 \times 10^6$  cycles, with a W-shape wear scar being fully developed by  $N = 5 \times 10^6$  cycles.

For example, the wear scar of the test conducted at  $\Delta^* = 25 \mu\text{m}$  seems to be at the edge of the transition from U-shape to W-shape after  $N = 1 \times 10^6$  cycles, and appears to exhibit features from both shapes; however, when the test duration reaches  $N = 5 \times 10^6$  cycles, the W-shape of the wear scar has more fully developed.



**Figure 6.4: Averaged profiles of fretting wear scar on flat specimens for fretting tests at varying displacement amplitudes, from  $\Delta^* = 10 \mu\text{m}$  to  $\Delta^* = 50 \mu\text{m}$ . Experiments were conducted with (a)  $1 \times 10^6$  cycles (b)  $5 \times 10^6$  cycles; profilometry data acquired from Alicona G5.**

To further investigate the development of W-shaped scars, some further extended tests with  $N = 1 \times 10^7$  cycles were carried out, and the average profiles of their corresponding wear scars are presented in Figure 6.5. As can be seen, for tests conducted with  $\Delta^* = 25 \mu\text{m}$ , the wear scar at  $N = 1 \times 10^7$  cycles clearly demonstrate a properly formed W-shape. The fully developed W-shaped wear scar for tests with  $\Delta^* = 15 \mu\text{m}$  at  $N = 5 \times 10^6$  cycles is more developed for higher test durations. The wear scar of  $\Delta^* = 10 \mu\text{m}$  test exhibits the most dramatic change during the process when the test duration is elongated to  $N = 1 \times 10^7$  cycles: the wear scar appears to very little worn after  $N = 5 \times 10^6$  cycles but forms a clear W-shape after  $N = 1 \times 10^7$  cycles.

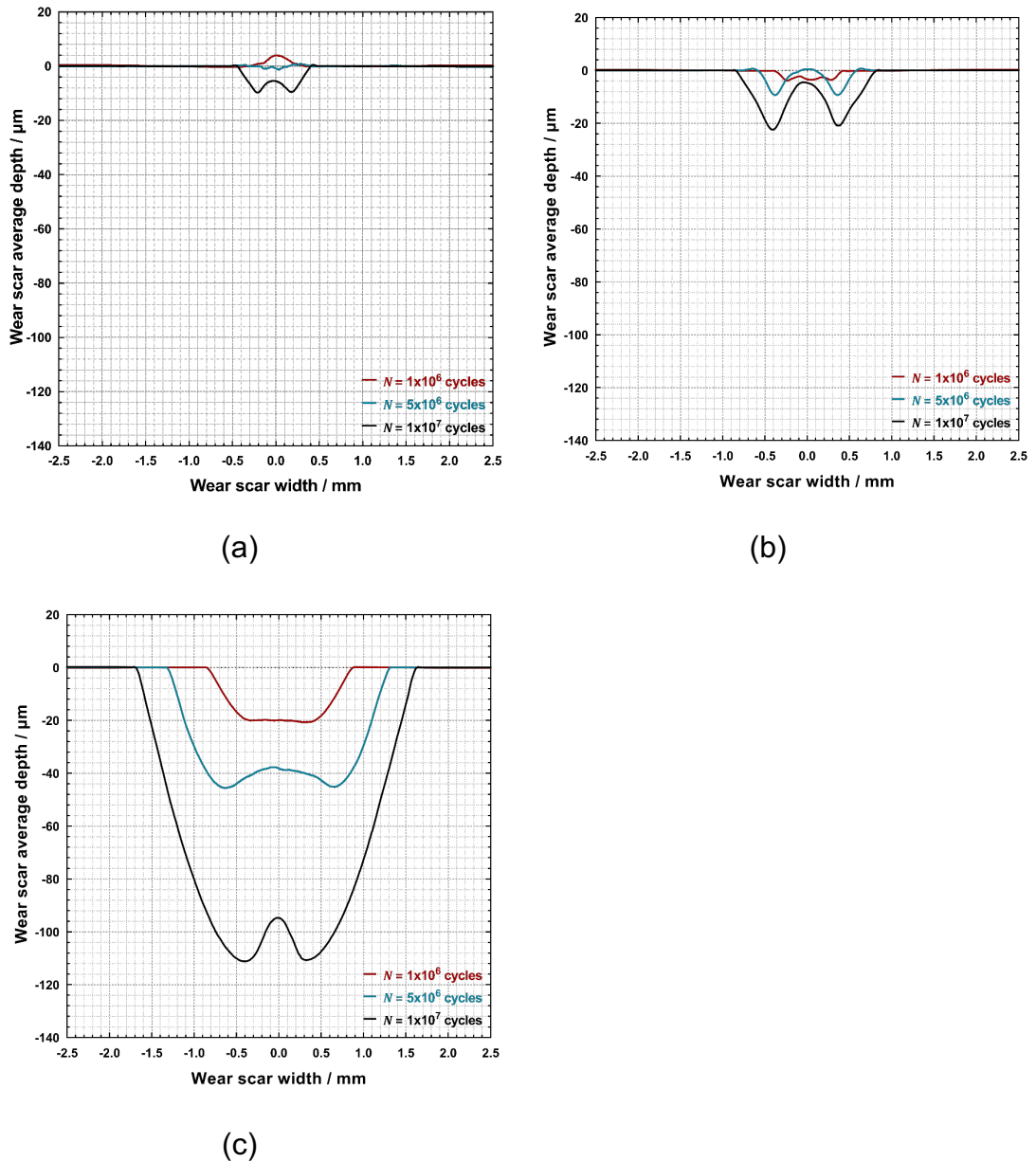
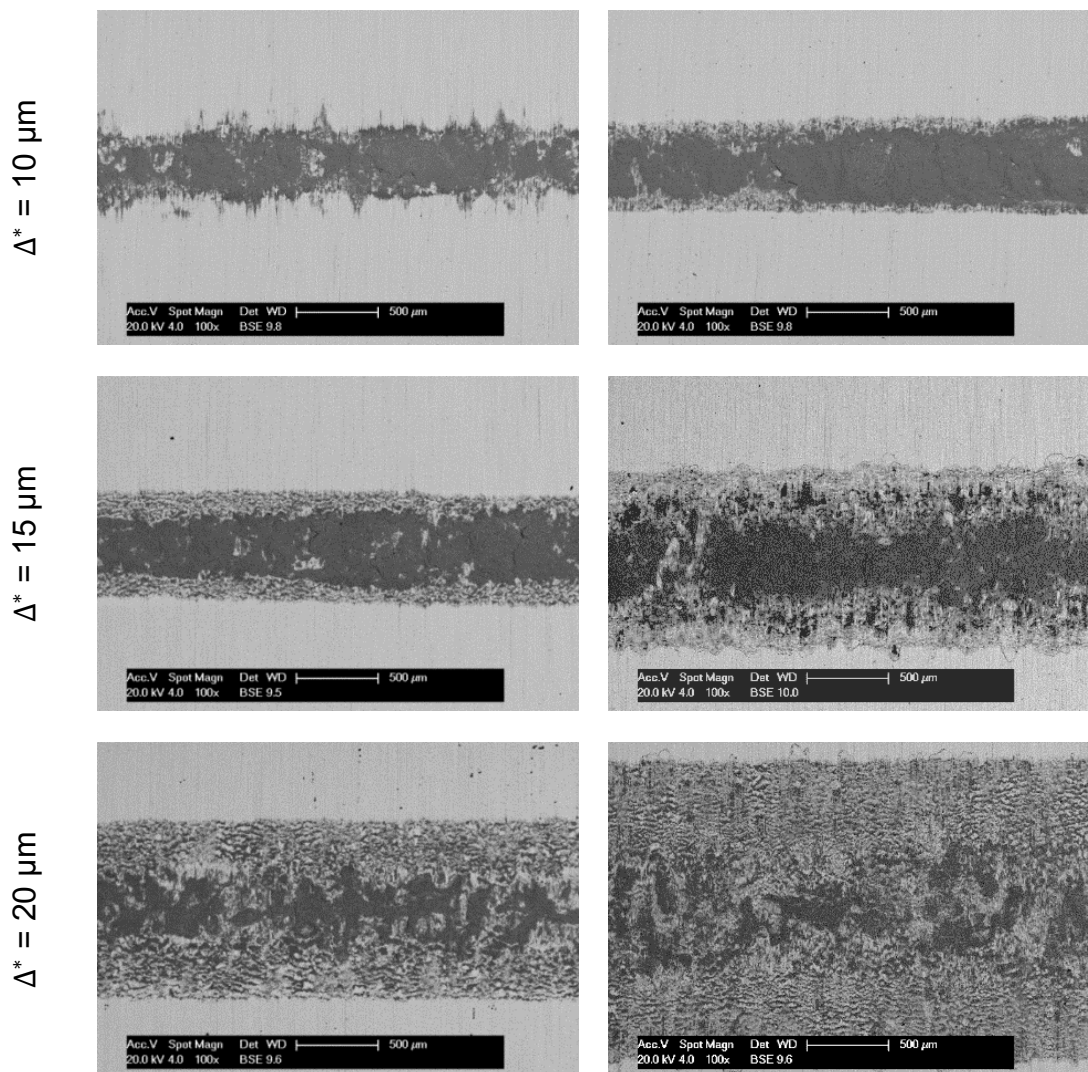
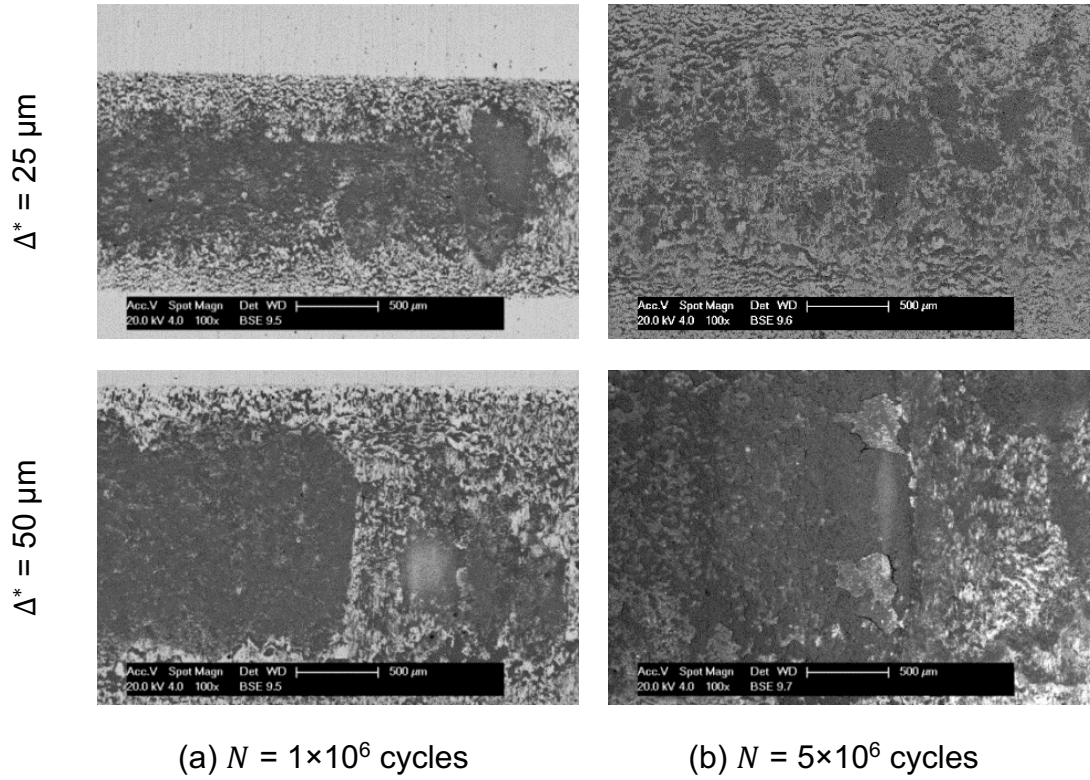


Figure 6.5: Evolution of averaged profiles of fretting wear scar on flat specimens as a function of test duration (1, 5 and  $10 \times 10^6$  cycles) for three different applied displacement amplitudes; (a)  $\Delta^* = 10 \mu\text{m}$ ; (b)  $\Delta^* = 15 \mu\text{m}$ ; (c)  $\Delta^* = 25 \mu\text{m}$ ; profilometry data acquired from Alicona G5.

Figure 6.6 provides the top view BSE microscopy images of the tests conducted for the current study. A relationship between the displacement amplitude (thus the slip amplitude) and the debris retention within the contact can be observed. It clearly shows that as the increase of displacement amplitude, wear scar size is increased but the oxide debris is more sparsely distributed across the wear scar leaving the underlying metallic material more exposed. For tests conducted at  $\Delta^* = 10 \mu\text{m}$ , the existence of a

compact oxide bed across the wear scar can be observed. Such an oxide bed is still developed for the test with  $\Delta^* = 15 \mu\text{m}$ , except that it only exists at the centre of wear scar, while the metallic surface is more prominent towards the edge of wear scar. This trend of the oxide bed being unevenly distributed across the wear scar is continued and amplified for the rest of tests in the current study. The BSE images of the wear scar of  $\Delta^* = 50 \mu\text{m}$  also indicate the possibility that a coherent oxide bed may form within the wear scar which then delaminates due to the relative motion between first bodies.





**Figure 6.6: BSE images at low magnification  $\times 100$  of the wear scar on flat specimens for fretting tests conducted with  $R6$  at varying displacement amplitudes, from  $\Delta^* = 10 \mu\text{m}$  to  $\Delta^* = 50 \mu\text{m}$ , with  $P = 450 \text{ N}$  at (a)  $1 \times 10^6$  cycles; (b)  $5 \times 10^6$  cycles from the top view.**

The previous chapter (Chapter 5) indicates that the traditional concept of wear rate (Archard-type) fails to give accurate description of fretting wear test when a non-conforming contact geometry is employed, because the wear scar size is constantly changing. A more realistic form of wear equation for the cylinder-on-flat configuration based on the assumption that the debris flow rate should be inversely proportional to the characteristic dimension of wear scar (outlined in Equation 6.2, with  $n = 0.75$ ).

As all the specimens in the current study have the same radius ( $R$ ), the radius in the equation above can be considered as a constant, and therefore Equation 6.2 can be reduced into a more general form as shown in Equation 6.3a:

$$V_w = \eta E_d^{0.75} \quad (6.3a)$$

$$\eta = KR^{-0.25} \quad (6.3b)$$

$$K = \lambda k^{0.75} \quad (6.3c)$$

$$V_w = \lambda k^{0.75} R^{-0.25} E_d^{0.75} \quad (6.3d)$$

where  $\eta$  is the quantity as the product of  $K$  and  $R^{-0.25}$  (Equation 6.3b), and as described in Chapter 5,  $K$  is related to the parameter in the governing equation,  $k$ , by Equation 6.3c.

Employing Equation 6.3a allows Figure 6.7 to be developed as below. In this figure, the ability of Equation 6.3a (therefore, Equation 5.22, with  $n = 0.75$  for cylinder-on-flat fretting contact) to describe wear volume as a sub-linear function of dissipated energy is further demonstrated. Similar to Figure 5.6, linear functions can be used to well describe the relationship between the wear volume ( $V_w$ ) and the transformed dissipated energy (using the term  $E_d^{0.75}$  as the abscissa) for different groups of  $\Delta^*$ . The coefficient of determination,  $R^2$ , is generally high ranging from  $R^2 = 0.93$  to  $R^2 = 0.99$ . It should be noted that, whilst a  $R^2$  above 0.9 suggests a good accordance between the experimental data and the values predicted by the model, the goodness of fit improves slightly with the increase of  $\Delta^*$ : when compared with the test results carried out with other values of  $\Delta^*$ , the goodness of fit is reduced for tests conducted with  $\Delta^* = 10 \mu\text{m}$  and  $\Delta^* = 15 \mu\text{m}$  as indicated by Figure 6.7. In this figure, tests conducted in the current chapter can be easily distinguished by their corresponding displacement amplitude. The values of  $\eta$  (and hence  $K$ ) can, therefore, be determined from Figure 6.7 as the gradient for each group of  $\Delta^*$ .

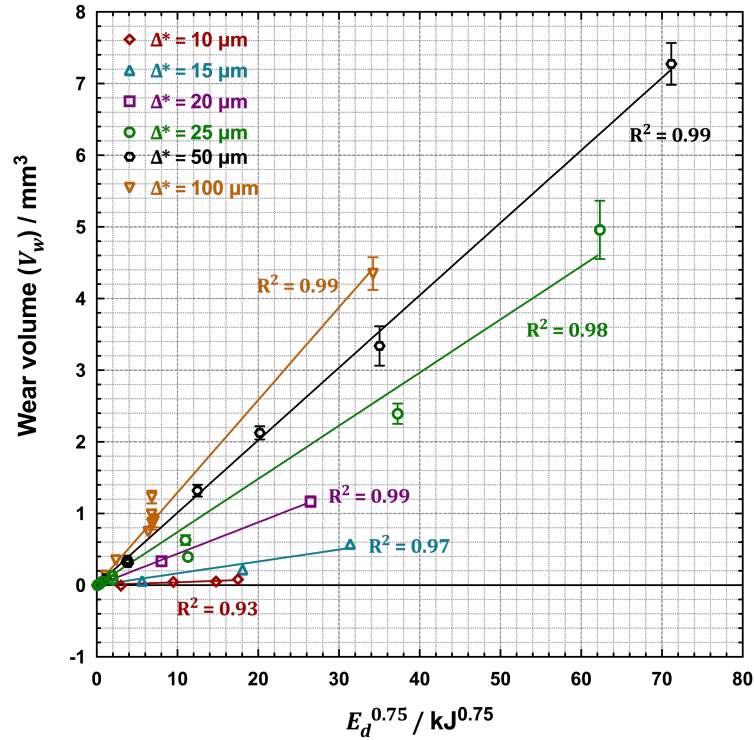


Figure 6.7: Plot of wear volume against  $E_d^{0.75}$  as suggested by Equation 6.3a for tests conducted with varying displacement amplitude and number of cycles. It can be seen that  $\eta$  in Equation 6.3a (indicated by the gradient of the line) is strongly dependent upon displacement amplitude; error bars are displayed.

With the determination of  $\eta$  and  $K$ , values of  $k$  can be calculated through Equation 6.3b and Equation 6.3c, which are plotted against their corresponding slip amplitude and presented in Figure 6.8 and summarised in Table 6.2; the error bar in the graph represents the 95% confidence range of those values. Please note that, although  $\eta$  and  $K$  can be easily calculated after transforming the values of dissipated energy to their power of 0.75 (i.e.  $E_d^{0.75}$ ), it is recognised that the unit of  $K$  depends on the choice of contact geometry and the assumption for the governing equation (indicated by Equation 5.22), and hence lacks a readily apparent physical meaning. In contrast, the parameter  $k$  in the governing equation (Equation 6.1), although has not been assigned with a physical quantity, is easier to explain and understand; thus, further discussions will be focused on  $k$ . As it can be seen, the change of  $k$  is dramatic when displacement amplitude is within the range from  $\Delta^* = 10 \mu\text{m}$  to  $\Delta^* = 25 \mu\text{m}$ , then its rate of change slows down as slip amplitude increases further. It should be noted that one key

observation from experimental results in this section is that there seems to exist a correspondence of the changes in  $\mu_e$ , the wear scar shape and  $k$  as the displacement amplitude increases; these data are presented together in Table 6.2.

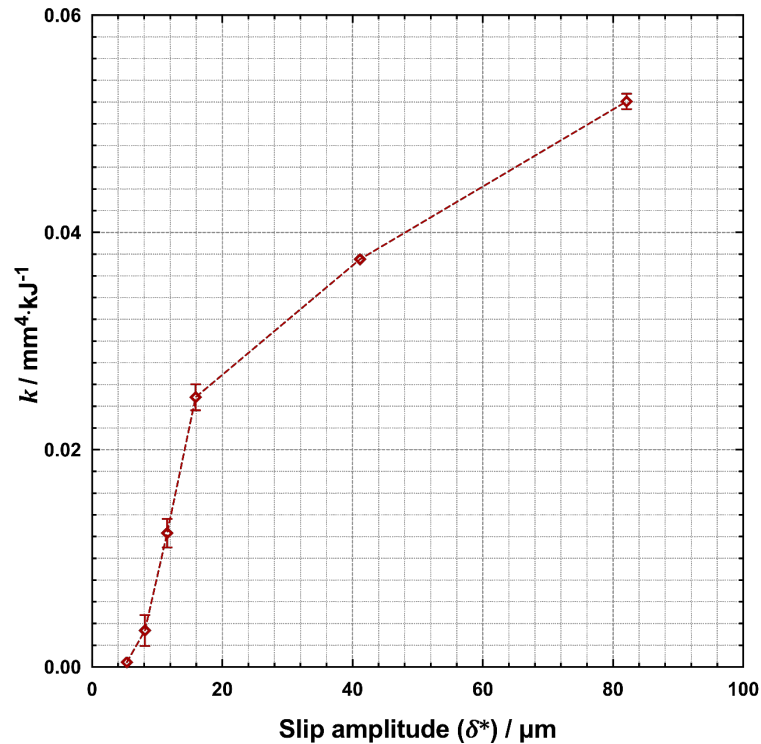


Figure 6.8: Plot of  $k$  (as indicated in Equation 6.1 as the parameter describing the instantaneous wear rate) as function of slip amplitude.

Table 6.2: Summary of the change of  $\delta^*$  with the corresponding evolution of  $\mu_e$  and  $k$  as  $\Delta^*$  increases.

$\Delta^* / \mu\text{m}$	$\delta^* / \mu\text{m}$	$\mu_e$	$k / \text{mm}^4 \cdot \text{kJ}^{-1}$
10	$5.36 \pm 1.12$	$0.61 \pm 0.01$	0.0004
15	$8.12 \pm 0.27$	$0.67 \pm 0.04$	0.0034
20	$11.54 \pm 0.06$	$0.78 \pm 0.01$	0.0123
25	$15.91 \pm 1.85$	$0.80 \pm 0.02$	0.0248
50	$41.14 \pm 0.46$	$0.79 \pm 0.01$	0.0375
100	$82.08 \pm 0.58$	$0.79 \pm 0.01$	0.0521

### 6.3 Discussion

#### 6.3.1 Wear scar characteristics

A small slip amplitude is generally associated with small wear volume if other parameters are fixed, and indeed this is demonstrated by the experimental results presented in this chapter. However, it is widely acknowledged that, when the slip amplitude is below a critical value, the process of wear would cease to occur [24, 27, 81, 94] since the debris is unable to be ejected with small slip amplitude, regardless the change of other parameters. Whilst the value for such threshold of slip amplitude in early reports in literature may suffer from failing to distinguish the slip amplitude from displacement amplitude and hence may not be quoted directly, the general understanding is that the critical line is drawn when the slip amplitude ( $\delta^*$ ) is around 10  $\mu\text{m}$ . As summarised in Table 6.2, with the test configuration employed in this thesis, there are three displacement amplitudes whose equivalent slip amplitude is below or close to 10  $\mu\text{m}$ ; namely the cases where  $\Delta^* = 10 \mu\text{m}$ ,  $\Delta^* = 15 \mu\text{m}$  and  $\Delta^* = 20 \mu\text{m}$ , with corresponding slip amplitudes of  $\delta^* = 5 \mu\text{m}$ ,  $\delta^* = 8 \mu\text{m}$  and  $\delta^* = 11 \mu\text{m}$ .

As pointed out by Aldham et al. [109], very long test durations are necessary in fretting to avoid the generation of unrepresentative measurements, and thereby the misinterpretation of data. The threshold slip amplitude is often derived from the measurement of where wear volume is negligible, and hence the identification of a threshold may be influenced by the test duration; indeed, this concern is reflected on Figure 6.4 and Figure 6.5. As shown in Figure 6.4 and Figure 6.5, the slip amplitude beyond the threshold of  $\sim 10 \mu\text{m}$  leads to the monotonic increase of both the width and depth of wear scars with the increase of slip amplitude. However, it is observed in Figure 6.4a that, as early as  $N = 1 \times 10^6$  cycles, the wear scar for  $\Delta^* = 20 \mu\text{m}$  ( $\delta^* = 11 \mu\text{m}$ ) has already developed a wear scar with a wear volume of  $\sim 0.34 \text{ mm}^3$  (exhibiting the mixed feature of W-shaped and U-shaped); in contrast, the wear scar for  $\Delta^* = 15$

$\mu\text{m}$  ( $\delta^* = 8 \mu\text{m}$ ) is much less developed but still visible ( $V_w = 0.06 \text{ mm}^3$ ), and the wear scar for  $\Delta^* = 10 \mu\text{m}$  ( $\delta^* = 5 \mu\text{m}$ ) is almost zero. However, as the test duration continues to increase to  $N = 5 \times 10^6$  cycles (shown in Figure 6.4b), the development of wear scar conducted with these values of slip amplitude demonstrates a different picture than that at  $N = 1 \times 10^6$  cycles: the already developed wear scar for  $\delta^* = 11 \mu\text{m}$  grows continuously ( $V_w = 1.17 \text{ mm}^3$ ), and the wear scar for  $\delta^* = 8 \mu\text{m}$  starts to show the feature of W-shaped wear scar with the wear volume of  $0.22 \text{ mm}^3$  while it is still difficult to observe the progress of wear for  $\delta^* = 5 \mu\text{m}$ . Further increase of test duration to  $N = 1 \times 10^7$  cycles (rarely seen in literature) as shown in Figure 6.5 demonstrates that the wear scar for  $\delta^* = 8 \mu\text{m}$  evolves further with its volume reached to  $0.57 \text{ mm}^3$ ; but more importantly, the unexpected development of wear scar for the case of  $\delta^* = 5 \mu\text{m}$  can finally be observed ( $V_w = 0.09 \text{ mm}^3$ ). Please note that perhaps more repeated tests at the long test duration for  $\delta^* = 5 \mu\text{m}$ ,  $\delta^* = 8 \mu\text{m}$  and  $\delta^* = 11 \mu\text{m}$  are required to reduce uncertainties (the source of uncertainties being the stability of testing rig and the error in measurements); it is nevertheless argued here that the evolution of the wear scars for  $\delta^* = 5 \mu\text{m}$ ,  $\delta^* = 8 \mu\text{m}$  and  $\delta^* = 11 \mu\text{m}$  under different test durations challenge the view about threshold slip amplitude.

In literature, the low wear volume associated with the small slip amplitude may also be explained by the contact being in partial slip regime, which may be supported by the fretting loops of the type presented in Figure 6.1 and the ECoF data presented in Figure 6.2 and Figure 6.3. It seems from these figures that the fretting loops are not fully developed for the cases of  $\Delta^* = 10 \mu\text{m}$  and  $\Delta^* = 15 \mu\text{m}$  ( $\delta^* = 5 \mu\text{m}$  and  $\delta^* = 8 \mu\text{m}$  respectively), and their ECoF are lower than others by  $\sim 25\%$ . However, microscopic examinations on the surfaces of these wear scars (Figure 6.6) suggest that there is no evidence of a stuck region on the wear surfaces for both the case of  $\Delta^* = 10 \mu\text{m}$  and  $\Delta^* = 15 \mu\text{m}$ , either after  $N = 1 \times 10^6$  cycles nor after  $N = 5 \times 10^6$  cycles. In fact, compact debris beds can be identified to cover those surfaces, and the coverage of the oxide

debris is more sparsely distributed across the wear scar for the increased slip amplitude. It is suggested that the low ECoF and the non-fully developed fretting loop for the case of  $\Delta^* = 10 \mu\text{m}$  and  $\Delta^* = 15 \mu\text{m}$  are not caused by the change of regime as suggested by the work of Pearson and Shipway [24]; instead, the variation of debris distribution suggests that it was the presence of the debris bed acting to separate the first bodies that caused the reduction in ECoF and the change of shape in fretting loops.

As indicated by Equation 2.9, a higher slip amplitude suggests a higher power being dissipated into the contact (if fretting frequency is held constant), which is often considered to cause a rise of surface temperature and thereby a higher tendency of debris to sinter together. If the surface temperature rise caused the increase of slip amplitude is the dominating factor, then a more compact debris bed is expected on the contact with larger slip amplitude and a sparser debris bed should be found when the slip amplitude is small. However, this expectation is in contrast to the observations as shown in Figure 6.6, which is in accord with the observations in literature [27, 109, 110]. It is therefore suggested that the effects of any temperature rise caused by the increase of slip amplitude is not a dominating factor. It is recognised that further cross-sectional investigation would be useful to identify any changes in the sub-surface damage as a function of slip amplitude.

With the evidence presented in this chapter, it is proposed that, when there is no change of fretting regime and that debris ejection remains the RDP. The evolution of wear in fretting follows a similar pattern of development; namely that, similar to the observations in Chapter 4, there is an incubation period for the fretting contact to develop into the steady-state, beyond which the evolution of wear will subsequently exhibit a non-linear behaviour as indicated by Equation 6.2. This incubation period is normally characterised by test duration as well as by the threshold energy, and, as already demonstrated by the results in this work, their values are strongly influenced by the test conditions and contact geometries. For example, the test with  $\Delta^* = 10 \mu\text{m}$

( $\delta^* = 5 \mu\text{m}$ ) requires a very long test duration to reach the steady-state, which is longer than  $N = 5 \times 10^6$  cycles (with  $E_d = \sim 20 \text{ kJ}$ ) and shorter than  $N = 1 \times 10^7$  cycles (with  $E_d = \sim 45 \text{ kJ}$ ). The requirement of the incubation period for the case of  $\Delta^* = 15 \mu\text{m}$  ( $\delta^* = 8 \mu\text{m}$ ) is arguably around  $N = 1 \times 10^6$  cycles ( $E_d = \sim 10 \text{ kJ}$ ) where wear can be observed even though its amount is relatively small; for the case of  $\Delta^* = 20 \mu\text{m}$  ( $\delta^* = 11 \mu\text{m}$ ) and beyond, the incubation period is much shorter; for example, as demonstrated in Chapter 4, for  $\delta^* = 41 \mu\text{m}$ , i.e.  $\Delta^* = 50 \mu\text{m}$ , the wear scar has already been established by the time when  $N = 5 \times 10^3$  cycles, with  $E_d = 0.02 \text{ kJ}$ . The variation of the incubation period for different slip amplitude emphasises the argument that perhaps the attempt to use a unified threshold of test duration or dissipated energy below which the wear will not occur to characterise the wear process is not appropriate, each test with different conditions may report a different value of threshold; the same argument can also challenge the concept of the threshold of slip amplitude.

It is suggested here, rather than creating concepts of threshold to artificially distinguish the mechanisms of fretting wear, perhaps viewing the wear behaviour under different conditions as different members from the same family can provide a better foundation in developing a more thorough understanding of fretting wear. To accomplish this goal, as argued many times in this thesis already, a long enough test duration is required to ensure that steady state has been reached. To demonstrate the necessity of applying long test durations, Figure 6.7 has been reproduced (shown in Figure 6.9) with data associated with two sets of different test durations, each set characterised by a dashed line. It can be seen from Figure 6.9 that experimental results conducted under the same test duration can be in fact fitted with a straight line. Such interpretation of data is commonly seen across a large body of literatures [24, 27, 81], which can lead to false assurance to the concept of threshold. For example, if the investigation was carried out at  $N = 1 \times 10^6$  cycles, then an energy threshold of  $E_d = \sim 10 \text{ kJ}$  may be reported; but a different value of energy threshold can be found if the test duration is elongated to  $N =$

## The dependence of wear rate on slip amplitude

$5 \times 10^6$  cycles. Moreover, as the test duration increases, the so-called “threshold of slip amplitude” will reduce its value continuously, until the slip amplitude is so small that the contact falls into the partial slip regime.

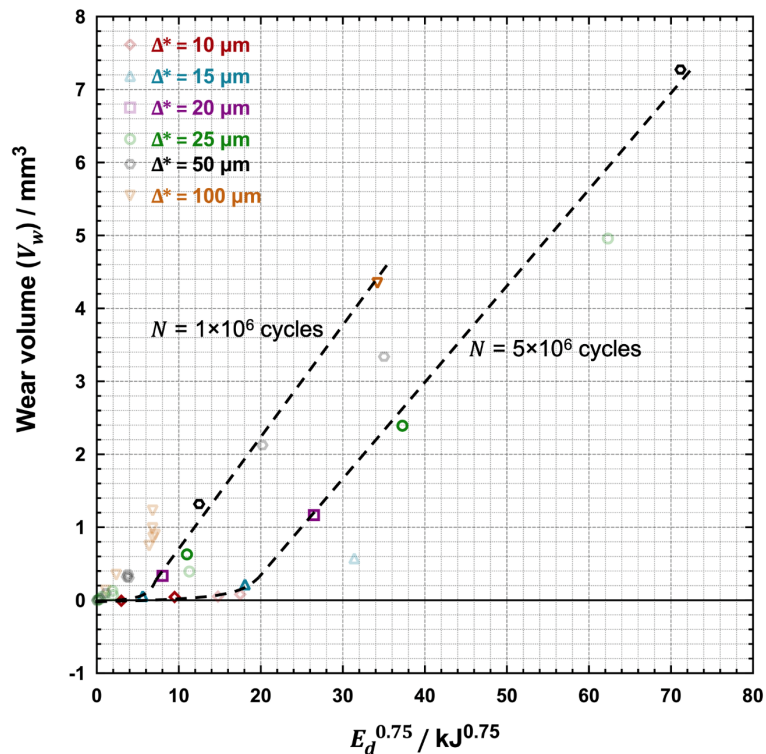


Figure 6.9: Illustration of the common practice to fit experimental data with straight lines where test durations are fixed by reproducing Figure 6.7 with original data displayed with a higher transparency;  $E_d^{0.75}$  is used as the exposure to wear for the purpose of demonstration.

### 6.3.2 Wear rate dependence on slip amplitude in fretting

A demonstrably sufficiently long test duration is suggested as essential when conducting fretting studies. The complete definition of wear incorporates both the process of debris formation and ejection as postulated by the third body approach [19] and the concept of tribology circuit [96]. In this work, it is suggested that, if the debris ejection is the RDP (as argued in the previous section), the instantaneous wear rate is inversely proportional to the contact size by a parameter  $k$  (as indicated in Equation 6.1), and relationship between the wear volume and the dissipated energy can be described by a non-linear equation as outlined in Equation 6.2. Whilst it is believed that

the larger slip amplitude can enhance the debris ejection [33, 109, 110], such enhancement is competing against the opposite effect brought by the larger contact size due to the large slip amplitude. To separate the role of slip amplitude from the contact size on debris ejection, the values of  $K$  for each slip amplitude can be determined from Figure 6.7, which is used to calculate their corresponding values of  $k$  as presented in Figure 6.8. As suggested in Chapter 4, the value of  $k$  can be interpreted as the ability of the contact to eject oxide debris, and is found to be strongly dependent upon the slip amplitude as indicated by Figure 6.8. It is recognised that the physical meaning of  $k$  (although a physical quantity has not been assigned to it) is very different from the Archard-type wear rate. Nevertheless, the evolution of  $k$  with the increased slip amplitude exhibits a similar pattern which has been observed by those investigations about the dependence of Archard-type wear rate upon the slip amplitude as by many studies in literature [4, 18, 27, 33, 72, 81, 91, 108, 111, 113].

Figure 6.8 indicates that the increase of the slip amplitude can indeed cause the rise of the debris ejection. The reduced debris ejection rate associated with small slip amplitude suggests a longer residence time of debris being retained inside the contact, and a higher likelihood of debris agglomeration / sintering to form a compact debris bed. Even though increasing the slip amplitude can enhance the debris ejection, the debris at the centre of wear scar is still more difficult to be removed, which may cause the compact debris bed being formed mainly at the centre if not being able to cover the whole contact (as shown in Figure 6.6); such change in the distribution of oxide debris is reflected by the change of  $k$ . The development of  $k$  also implies that the ability of the contact to remove debris may approach towards a plateau since the rate of change of  $k$  falls with increasing slip amplitude. If it is assumed that (in the same vein as the proposal of Vingsbo and Söderberg [4] as shown in Figure 2.1)  $k$  may reach a plateau value (above which it is independent of slip amplitude), then such a plateau value has not been reached at least by  $\delta^* = 82 \mu\text{m}$ . More tests with larger slip amplitudes are

## **The dependence of wear rate on slip amplitude**

---

required to reveal the evolution of  $k$  after  $\delta^* = 82 \mu\text{m}$ ; equally importantly, more investigations of the dependence of  $k$  at higher slip amplitudes are required to understand the underlying physical mechanisms of wear.

The main observation from Figure 6.4 and Figure 6.5 is that shape of wear scar is influenced by the slip amplitude: with the fixed test durations, a W-shaped wear scar is associated with smaller slip amplitudes and U-shaped wear scar can be found when slip amplitude is larger, which is in accord with observations in literature [90, 91, 108, 111]. It is demonstrated in Figure 6.5c that, as the increase of test duration (as well as the energy) from  $N = 1 \times 10^6$  cycles to  $N = 5 \times 10^6$  cycles, the shape wear scar for  $\delta^* = 16 \mu\text{m}$  ( $\Delta^* = 25 \mu\text{m}$ ) changes from U-shaped to W-shaped and it is recognised that this may be influenced by the commensurate increase in the wear scar width. It is proposed here that, whilst the increase of the slip amplitude can reinforce the debris ejection, its enhancing effect is compensated by the growing contact size. As such, the difficulty of the debris expulsion from the centre of the wear scar is increased since the distance from the centre to the edge is the largest for debris to travel across the contact, the result of which is the W-shaped wear scar. Although the nature of those W-shaped and U-shaped wear scar requires further cross-sectional investigations, the implication from Figure 6.5c is that, with the ability to transport debris out the contact defined by a certain slip amplitude, all wear scars (in tests with non-conforming geometries) may eventually develop into a W-shaped wear scars as contact size increases; the contact size at which the transition to a W-shaped scar occurs will increase with increasing slip amplitude. The test duration required for such transition to occur is influenced by the debris ejection associated with different slip amplitude; more investigations are clearly needed in this area.

## 6.4 Conclusions

With the evidence presented in this work, reducing the slip amplitude leads to the formation of a more compact debris bed across the contact, which is associated with reduced debris ejection and hence the increased residence time for debris inside the contact. As such, reduced ECoF and less developed fretting loops are observed for test conducted with small amplitude. In tests with non-conforming contacts, the enhancement of debris ejection by the increase of slip amplitude is competing against the opposite effect associated with increases in the contact size; the wear equation generated in Chapter 4 (the governing equation for the instantaneous wear rate) and Chapter 5 (general wear equation in a non-linear form) can help to separate the effect of the slip amplitude from the effect of the contact size. However, the standard of “long test duration” to reveal the development of wear is influenced by the test conditions. In this chapter, it was found that the test duration required for wear to occur is increased by the reduction of slip amplitude; in particular, test duration in the order of tens of millions of cycles is needed for tests with  $\delta^* = 5 \mu\text{m}$  cycles.

The value of  $k$ , the parameter describing the instantaneous wear rate, which is independent of the contact size, can be determined from the transformed experimental data by plotting the wear volume against the quantity of  $E_d^n$  (where  $n = 0.75$  if cylinder-on-flat configuration is employed). The parameter  $k$ , which was found to be independent of the contact geometry (as demonstrated in Chapter 4), has been shown to be strongly dependent upon the slip amplitude. Whilst the methods outlined in thesis provide a first attempt to understand the dependence of wear rate on slip amplitude without the effect of contact size, the nature of the change of  $k$  in terms of slip amplitude requires further investigation.

## Chapter 7      Conclusions

The influence of debris ejection from fretting contacts on their wear behaviour has been qualitatively understood since the work of Godet in the 1980s, but in analysis of wear data, this influence continues to be overlooked. The key objective of this thesis was to address this issue qualitatively for the first time, with this involving an analysis of how debris ejection from the contact is dependent upon physical dimensions of the contact patch. Fretting wear experiments employing a cylinder-on-flat sample configuration were conducted which allowed the change in instantaneous wear rate throughout a test (as the size of the wearing contact increased) to be monitored. An analytical model to determine the wear rate based on the contact geometry and the role of debris flow was developed. The model is able to account for differences in Archard-type wear rates observed in tests conducted with the apparently different (and evolving) contact geometries over a range of durations.

The model developed is based upon a physical understanding of the process of fretting wear of metals, where it is proposed that the progression of wear requires the formation of oxide debris and the subsequent transport of debris out of the contact due to the closed nature of the contact. This concept has been extended in this thesis by proposing that both the process of debris formation and ejection will have a maximum possible rate under a given set of conditions, and the observed wear rate is governed by the process with the least of these maximum rates; the limiting process has been termed the rate-determining process (RDP). As highlighted in this thesis, identification of the RDP is critical in improving understanding of the rates of wear in fretting.

The model that has been developed states that, when debris ejection is the RDP, the contact size exerts its influence on the overall wear rate by controlling the rate of debris ejection, with it being demonstrated that the rate of debris ejection is inversely

proportional to a characteristic dimension of the contact characterised by a single parameter  $k$  where:

$$\frac{dV_w}{dE_d} = \frac{k}{x}$$

It is proposed that this contact size-effect is universal for fretting analysis. If the contact size remains unchanged as wear proceeds (such as when conforming contacts are employed), then the rate of debris ejection (hence the observed wear rate) will be constant, although it is noted that this constant is dependent upon the contact size selected. One important implication of this is that, when comparing wear rates from different research reports, quoting the observed Archard-type wear rate without the information related contact size is of little value. In such case, the single parameter  $k$ , which is irrelevant to the change of contact size, can be used for the characterisation of experimental results.

Solutions of the governing equation of the model were targeted for three commonly-used non-conforming contact geometries in fretting research (namely cylinder-on-flat, sphere-on-flat and crossed-cylinders). Key for this derivation is the assertion that the wear volume in fretting can be calculated from the contact size via a simple geometrical relationship, along with the logically-argued assertion that the recession rate of the surfaces is the same at any point within the contact. By making suitable approximations, equations were derived for the three geometry-types which were observed to have the non-linear form as:  $V_w = KR^{n-1}E_d^n$ .

The error associated with approximations during the derivation of these wear equations were generally small (typically less than ~0.5% in the cases considered in this thesis). This alternative model to the Archard-type approach was applied to experimental fretting wear data from tests conducted with cylinder-on-flat and sphere-on flat contact geometries. The model is less successful in predicting the results from equiaxed

## Conclusions

---

contact patches (sphere-on-flat contact) than from a contact where the contact size perpendicular to the fretting direction is large (cylinder-on-flat). It is concluded that the performance of the model falls as effect of side-leakage increases. Despite the success of the model presented in this thesis for two-dimensional contacts, its boundary and the scope of applicability should be further investigated. Moreover, the model requires extension so that the role of side-leakage of debris from fretting contacts can be understood and quantified.

The new wear equation for fretting of non-conforming contacts was applied to improve the understanding of the effect of slip amplitude. It was demonstrated using two-dimensional contacts that the value of  $k$  increases monotonically with fretting slip amplitude but its value seems to approach a plateau at high values of slip amplitude (around 82  $\mu\text{m}$ ) showing a similar pattern described in the seminal work of Vingsbo and Söderberg. It was proposed that the small value of  $k$  associated with smaller slip amplitudes is caused by the restricted debris ejection rate (i.e. per unit time), which provides sufficient residence time for debris to form compact debris beds which resist debris expulsion from the contact; in contrast, the enhanced debris ejection caused by larger slip amplitudes disrupts the formation of such a protective layer and promotes debris expulsion. However, further investigation is required to provide a physically-based understanding of the underlying mechanisms by which  $k$  is dependent upon slip amplitude and the associated change of wear scar profile (U-shaped or W-shaped).

## Chapter 8 Future work

As discussed, an assumption has been made throughout this thesis that debris is expelled from the contact with its velocity being parallel to the direction of fretting, which means that side leakage of debris is assumed to be negligible. However, it was suggested that the poorer fit to experimental data in cases where the contact is equiaxed indicates that side-leakage should not be ignored, and work needs to be conducted which addresses the role of side leakage (and identifies when it can be ignored). It is noted that when stronger side-leakage occurs, the transport of debris out of the contact may cease to be the RDP, since the size of contact itself (in the direction of fretting motion) may no longer limit the debris ejection, causing the debris formation to take the determinant role (similar to sliding wear). Perhaps the most efficient way to address this is to employ conforming contacts with different aspect ratios. Overall, more experimental investigations are required to reveal the long-term behaviour of contact with different shapes and aspect ratio. All these efforts will be critical to understand the boundary and the scope of the applicability of the simple model presented in this work.

In addition to the debris formation and ejection being the potential RDP in fretting, the transport of oxygen into the contact may be a third potential RDP. While a model based on debris ejection has been proposed in this thesis and models for debris formation have been outlined in Archard-type approach, models considering the effects of fretting parameters on oxygen transport are required. Moreover, since the change of contact conditions may trigger the change of RDP and hence the instantaneous wear rate during a test, an attempt to provide a coherent framework incorporating all the potential RDPs would be significant to prompt the understanding of fretting.

One of the most important contribution of this thesis is the proposal of the instantaneous wear rate being inversely proportional to the contact size when debris ejection is the RDP. Whilst experimental results (either generated in this thesis or extracted from

external source in literature) were used to verify the governing equations for CF and SF contact configurations, as well as the general wear equations that were subsequently derived from them, the data for CC contact is missing. In addition, the general wear equation for CC contact may take a different form if considering different radii of cylinders (assumed to be the same in this thesis) or different crossing angle between two cylinders (assumes to be perpendicular to each other); either of these extra considerations are commonly seen in industry. Perhaps more significantly, there is a need to extend the findings and conclusions of this work to work with conforming contacts. As part of this, there is a need to consider whether steady—state wear can always be achieved in conforming contacts of any size (i.e. will wear naturally stifle itself as it does in partial-slip) and whether the proposal that the maximum debris ejection rate is proportional to the inverse of the contact size continues to hold as the contact size increases.

The successful employment of the proposed governing equation suggests that the roles of fretting parameters can be understood regardless of the contact size. It is noted that the instantaneous wear rate is characterised by a single parameter  $k$ , which is proposed to be a function of different parameters. There are many directions that can be taken in the future to refine the governing equation by understanding the relationship of  $k$  as functions of parameters of interest; for example, the relationship between  $k$  and the slip amplitude can be further investigated so that an equation of  $k$  in terms of slip amplitude could be derived; tests with larger slip amplitude (larger than  $82\ \mu\text{m}$ ) should be conducted to reveal the further evolution of  $k$ . Moreover, the governing equation opens up endless possibilities to understand how other parameters such as normal load, frequency and temperature can influence the value of  $k$ , with the aim being to identify their exact equations; the proposed instantaneous wear rate may also be applied to different materials and conforming contacts in the future. With the understanding of the roles of fretting parameters on the value of  $k$ , their effects could be compared with

those investigations where the traditional measure of wear rate were applied; finding out both the similarity and difference between these two methods would be of significant value.

## Bibliography

1. ASTM, *Standard Terminology Relating to Wear and Erosion*. ASTM International, 2015. **ASTM G40-15**.
2. Hurricks, P.L., *The mechanism of fretting - a review*. *Wear*, 1970. **15**(6): p. 389 - 409.
3. Waterhouse, R.B., *Fretting Corrosion*. International Series of Monographs on Material Science and Technology, ed. D.W. Hopkins. Vol. 10. 1972: Pergamon Press. 88.
4. Vingsbo, O. and S. Söderberg, *On fretting maps*. *Wear*, 1988. **126**(2): p. 17.
5. Waterhouse, R.B., *Occurrence of fretting in practice and its simulation in the laboratory*, in *Materials Evaluation Under Fretting Conditions*, S. Brown, Ed., Editor. 1982, ASTM International. p. 3-16.
6. Brown, S., Ed., *Material Evaluation Under Fretting Conditions*. ASTM International. Vol. STP780-EB. 1982, West Conshohocken, PA.
7. Wallace, W., D.W. Hoepfner, and P.V. Kandachar, *AGARD Corrosion Handbook. Volume 1. Aircraft Corrosion: Causes and Case Histories*. 1985, Advisory Group for Aerospace Research and Development, NATO.
8. Ford, T., *Mainshafts for the trent*. *Aircraft Engineering and Aerospace Technology*, 1997. **69**(6): p. 555-560.
9. Bill, R.C., *Fretting wear and fretting fatigue—how are they related*. *Journal of Lunrication Technology*, 1983. **105**(2): p. 230-238.
10. Eden, E.M., W.N. Rose, and F.L. Cunningham, *The endurance of metals: experiments on rotating beams at University College, London*. *Proceedings of the Institution of Mechanical Engineers*, 1911. **8**(1): p. 829-880.
11. Tomlinson, G.A., *The rusting of steel surfaces in contact*. *Proceedings of the Royal Society of London. Series A, Containing Papers of a Mathematical and Physical Character*, 1927. **115**(771): p. 472-483.
12. Uhlig, H.H., *Mechanism of fretting corrosion*. *Journal of Applied Mechanics – Transactions of the ASME*, 1954. **21**: p. 401-407.
13. Dobromirski, J., *Variables of Fretting Process: Are There 50 of Them?*, in *Standardization of Fretting Fatigue Test Methods and Equipment*, M. Attia and R.B. Waterhouse, Editors. 1992. p. 60-66.
14. McColl, I.R., R.B. Waterhouse, S.J. Harris, and M. Tsujikawa, *Lubricated fretting wear of a high-strength eutectoid steel rope wire*. *Wear*, 1995. **185**(1–2): p. 203-212.
15. Meng, H.C. and K.C. Ludema, *Wear models and predictive equations: their form and content*. *Wear*, 1995. **181 - 183**: p. 443 - 457.
16. Archard, J.F., *Contact and rubbing of flat surfaces*. *Journal of Applied Physics*, 1953. **24**(8): p. 981-988.
17. Fouvry, S., P. Kapsa, T. Liskiewicz, S. Hannel, and E. Sauger, *An energy description of wear mechanisms and its applicatons to oscillation sliding contacts*. *Wear*, 2003. **255**(1 - 6): p. 287 - 298.
18. Fouvry, S., C. Poulins, and S. Deyber, *Impact of contact size and complex gross–partial slip conditions on Ti–6Al–4V/ Ti–6Al–4V fretting wear*. *Tribology International*, 2009. **42**(3): p. 460 - 473.
19. Godet, M., *The third-body approach: a mechanical view of wear*. *Wear*, 1984. **100**(1 - 3): p. 437 - 452.
20. Warmuth, A.R., S.R. Pearson, P.H. Shipway, and W. Sun, *The effect of contact geometry on fretting wear rates and mechanism for a high strength steel*. *Wear*, 2013. **301**(1 - 2): p. 491 - 500.
21. Pearson, S.R., P.H. Shipway, J.O. Abere, and R.A.A. Hewitt, *The effect of temperature on wear and friction of a high strength steel in fretting*. *Wear*, 2013. **303**(1-2): p. 622-631.

22. Lemm, J.D., A.R. Warmuth, S.R. Pearson, and P.H. Shipway, *The influence of surface hardness on the fretting wear of steel pairs-Its role in debris retention in the contact*. Tribology International, 2014. **81**: p. 258-266.
23. Warmuth, A.R., P.H. Shipway, and W. Sun, *Fretting wear mapping: The influence of contact geometry and frequency on debris formation and ejection for a steel-on-steel pair*. Proceedings of the Royal Society of London. Series A. Mathematical, Physical and Engineering Sciences, 2015. **471**(2178).
24. Pearson, S.R. and P.H. Shipway, *Is the wear coefficient dependent upon slip amplitude in fretting? Vingsbo and Söderberg revisited*. Wear, 2015. **330 - 331**(May - June 2015): p. 93 - 102.
25. Archard, J.F., *Elastic deformation and the laws of friction*. Proceedings of the Royal Society of London. Series A. Mathematical, Physical and Engineering Sciences, 1957. **243**(1233): p. 190-205.
26. Archard, J.F. and W. Hirst, *The wear of metals under unlubricated conditions*. Proceedings of the Royal Society of London. Series A. Mathematical, Physical and Engineering Sciences, 1956. **236**(1206): p. 397-410.
27. Ohmae, N. and T. Tsukizoe, *The effect of slip amplitude on fretting*. Wear, 1974. **27**(3): p. 281-294.
28. Chen, G.X. and Z.R. Zhou, *Study on transition between fretting and reciprocating sliding wear*. Wear, 2001. **250**(1-12): p. 665-672.
29. Hutchings, I.M. and P.H. Shipway, *Tribology: friction and wear of engineering materials*. 2017: Butterworth-Heinemann.
30. Blau, P.J., *How common is the steady-state? The implications of wear transitions for materials selection and design*. Wear, 2015. **332-333**(May-June): p. 1120-1128.
31. Fouvry, S., P. Kapsa, H. Zahouani, and L. Vincent, *Wear analysis in fretting of hard coatings through a dissipated energy concept*. Wear, 1997. **203-204**: p. 393-403.
32. Elleuch, K. and S. Fouvry, *Wear analysis of A357 aluminium alloy under fretting*. Wear, 2002. **253**(5): p. 662-672.
33. Fouvry, S., P. Duó, and P. Perruchaut, *A quantitative approach of Ti-6Al-4V fretting damage: friction, wear and crack nucleation*. Wear, 2004. **257**(9): p. 916-929.
34. Elleuch, K. and S. Fouvry, *Experimental and modelling aspects of abrasive wear of a A357 aluminium alloy under gross slip fretting conditions*. Wear, 2005. **258**(1-4): p. 40-49.
35. Fouvry, S., V. Fridrici, C. Langlade, P. Kapsa, and L. Vincent, *Palliatives in fretting: a dynamical approach*. Tribology International, 2006. **39**(10): p. 1005-1015.
36. Merhej, R. and S. Fouvry, *Contact size effect on fretting wear behaviour: application to an AISI 52100/AISI 52100 interface*. Lubrication Science, 2009. **21**: p. 83 - 102.
37. Fillot, N., I. Iordanoff, and Y. Berthier, *Wear modeling and the third body concept*. Wear, 2007. **262**(7 - 8): p. 949 - 957.
38. Quinn, T.F.J., *Role of oxidation in the mild wear of steel*. British Journal of Applied Physics, 1962. **13**(1): p. 33.
39. Quinn, T.F.J., *Oxidational wear*. Wear, 1971. **18**(5): p. 413-419.
40. Dréano, A., S. Fouvry, and G. Guillonéau, *A tribo-oxidation abrasive wear model to quantify the wear rate of a cobalt-based alloy subjected to fretting in low-to-medium temperature conditions*. Tribology International, 2018. **125**: p. 128-140.
41. Dreano, A., S. Fouvry, S. Sao-Joao, J. Galipaud, and G. Guillonéau, *The formation of a cobalt-based glaze layer at high temperature: A layered structure*. Wear, 2019. **440-441**: p. 203101.

42. Hertz, H., *On the contact of rigid elastic solids and on hardness, chapter 6: Assorted papers by H. Hertz*. 1882, MacMillan, New York.
43. Johnson, K.L., *Contact Mechanics*. 1985: Cambridge University Pres.
44. McColl, I.R., J. Ding, and S.B. Leen, *Finite element simulation and experimental validation of fretting wear*. *Wear*, 2004. **256**(11): p. 1114-1127.
45. Fouvry, S., C. Paulin, and T. Liskiewicz, *Application of an energy wear approach to quantify fretting contact durability: Introduction of a wear energy capacity concept*. *Tribology International*, 2007. **40**(10-12): p. 1428-1440.
46. Mindlin, R.D., *Compliance of elastic bodies in contact*. *Journal of Applied Mechanics*, 1949. **16**: p. 259-268.
47. Mindlin, R.D. and H. Deresiewicz, *Elastic spheres in contact under varying oblique forces*. *Journal of Applied Mechanics*, 1953. **20**: p. 327-344.
48. Zhou, Z.R., S. Fayeulle, and L. Vincent, *Cracking behaviour of various aluminium alloys during fretting wear*. *Wear*, 1992. **155**(2): p. 317-330.
49. Zhou, Z.R. and L. Vincent, *Mixed fretting regime*. *Wear*, 1995. **181**: p. 531-536.
50. Zhou, Z.R., K. Nakazawa, M.H. Zhu, N. Maruyama, P. Kapsa, and L. Vincent, *Progress in fretting maps*. *Tribology International*, 2006. **39**(10): p. 1068-1073.
51. Söderberg, S., U. Bryggman, and T. McCullough, *Frequency effects in fretting wear*. *Wear*, 1986. **110**(1): p. 19-34.
52. Bryggman, U. and S. Söderberg, *Contact conditions in fretting*. *Wear*, 1986. **110**(1): p. 1-17.
53. Vingsbo, O., M. Odfalk, and N. Shen, *Fretting maps and fretting behavior of some FCC metal alloys*. *Wear*, 1990. **138**(1-2): p. 153-167.
54. Odfalk, M. and O. Vingsbo, *Influence of normal force and frequency in fretting*. *Tribology Transactions*, 1990. **33**(4): p. 604-610.
55. Coulomb, C.A., *Théorie des machines simples, en ayant égard au frottement de leurs parties, et a la roideur des cordages*. Mémoires de mathématique et de physique, présentés à l'Académie royale des sciences, 1785.
56. Popova, E. and V.L. Popov, *The research works of Coulomb and Amontons and generalized laws of friction*. *Friction*, 2015. **3**(2): p. 183-190.
57. Magaziner, R., O. Jin, and S. Mall, *Slip regime explanation of observed size effects in fretting*. *Wear*, 2004. **257**(1-2): p. 190-197.
58. Lee, H. and S. Mall, *Fretting behavior of shot peened Ti-6Al-4V under slip controlled mode*. *Wear*, 2006. **260**(6): p. 642-651.
59. Paulin, C., S. Fouvry, and C. Meunier, *Finite element modelling of fretting wear surface evolution: Application to a Ti-6Al-4V contact*. *Wear*, 2008. **264**(1-2): p. 26-36.
60. Everitt, N.M., J. Ding, G. Bandak, P.H. Shipway, S.B. Leen, and E.J. Williams, *Characterisation of fretting-induced wear debris for Ti-6Al-4 V*. *Wear*, 2009. **267**(1-4): p. 283-291.
61. Dick, T., C. Paulin, G. Cailletaud, and S. Fouvry, *Experimental and numerical analysis of local and global plastic behaviour in fretting wear*. *Tribology international*, 2006. **39**(10): p. 1036-1044.
62. Mulvihill, D.M., M.E. Kartal, A.V. Olver, D. Nowell, and D.A. Hills, *Investigation of non-Coulomb friction behaviour in reciprocating sliding*. *Wear*, 2011. **271**(5-6): p. 802-816.
63. Hintikka, J., A. Lehtovaara, and A. Mäntylä, *Normal displacements in non-Coulomb friction conditions during fretting*. *Tribology International*, 2016. **94**: p. 633-639.
64. Jin, X., W. Sun, and P.H. Shipway, *Derivation of a wear scar geometry-independent coefficient of friction from fretting loops exhibiting non-Coulomb frictional behaviour*. *Tribology International*, 2016. **102**: p. 561-568.
65. ASTM, *Standard Guide for Determining Friction Energy Dissipation in Reciprocating Tribosystems (ASTM G203-10)*. 2016, ASTM International: West Conshohocken, PA.

66. Llavori, I., A. Zabala, A. Aginagalde, W. Tato, J. Ayerdi, and X. Gómez, *Critical analysis of coefficient of friction derivation methods for fretting under gross slip regime*. Tribology International, 2020. **143**: p. 105988.
67. Wang, D.G., D.Z. Song, X.R. Wang, D.K. Zhang, C.L. Zhang, and J.A. Araújo, *Tribo-fatigue behaviors of steel wires under coupled tension-torsion in different environmental media*. Wear, 2019. **420**: p. 38-53.
68. Rabinowicz, E., *Friction and Wear of Materials, 2nd Edition*. 2013: Wiley.
69. Waterhouse, R.B., *Fretting Wear*, in *ASM Handbook: Friction, Lubrication, and Wear Technology*, P.J. Blau, Editor. 1992, ASM International. p. 243-255.
70. Godfrey, D. and J.M. Bailey, *Coefficient of friction and damage to contact area during the early stages of fretting I: Glass, copper, or steel against copper*, in *National Advisory Committee for Aeronautics Collection 1953*, NACA.
71. Bailey, J.M. and D. Godfrey, *Coefficient of friction and damage to contact area during the early stages of fretting II: steel, iron, iron oxide, and glass combinations*, in *National Advisory Committee for Aeronautics Collection 1954*, NACA.
72. Halliday, J.S. and W. Hirst, *The fretting corrosion of mild steel*. Proceedings of the Royal Society of London. Series A. Mathematical, Physical and Engineering Sciences, 1956. **236**(1206): p. 411-425.
73. Berthier, Y., L. Vincent, and M. Godet, *Velocity accommodation in fretting*. Wear, 1988. **125**(1 - 2): p. 25 - 28.
74. Stott, F.H., J. Glascott, and G.C. Wood, *Factors affecting the progressive development of wear-protective oxides on iron-base alloys during sliding at elevated temperatures*. Wear, 1984. **97**(1): p. 93-106.
75. Feng, I.M. and B.G. Rightmire, *An experimental study of fretting*. Proceedings of the Institution of Mechanical Engineers, 1956. **170**(1): p. 1055-1064.
76. Waterhouse, R.B. and D.E. Taylor, *Fretting debris and the delamination theory of wear*. Wear, 1974. **29**(3): p. 8.
77. Colombie, C., Y. Berthier, A. Floquet, L. Vincent, and M. Godet, *Fretting: Load carrying capacity of wear debris*. Journal of Tribology-Transactions of the ASME, 1984. **106**(April): p. 194-201.
78. Pendlebury, R.E., *Unlubricated fretting wear of mild steel surfaces in air at room temperature: II electrical contact resistance measurements and the effect on wear of intermittent loading*. Wear, 1987. **118**(3): p. 341-364.
79. Pearson, S.R., *The effects of nitriding on the fretting wear of a high strength steel at ambient temperature and elevated temperature*, in *Department of Mechanical, Material and Manufacturing Engineering*. 2013, University of Nottingham.
80. Godet, M., *Third-bodies in tribology*. Wear, 1990. **136**(1): p. 29 - 44.
81. Zhang, X.S., C.H. Zhange, and C.L. Zhu, *Slip amplitude effects and microstructural characteristics of surface layers in fretting wear of carbon steel*. Wear, 1989. **134**(2): p. 297-309.
82. Nurmi, V., J. Hintikka, J. Juoksukangas, M. Honkanen, M. Vippola, A. Lehtovaara, A. Mäntylä, J. Vaara, and T. Frondelius, *The formation and characterization of fretting-induced degradation layers using quenched and tempered steel*. Tribology International, 2019. **131**: p. 258-267.
83. Sauger, E., S. Fouvry, L. Ponsonnet, P. Kapsa, J.M. Martin, and L. Vincent, *Tribologically transformed structure in fretting*. Wear, 2000. **245**(1-2): p. 39-52.
84. Sauger, E., L. Ponsonnet, J.M. Martin, and L. Vincent, *Study of the tribologically transformed structure created during fretting tests*. Tribology International, 2000. **33**(11): p. 743-750.
85. Zhou, Z.R., E. Sauger, J.J. Liu, and L. Vincent, *Nucleation and early growth of tribologically transformed structure (TTS) induced by fretting*. Wear, 1997. **212**(1).

## Bibliography

---

86. Xin, L., Z.H. Wang, J. Li, Y.H. Lu, and T. Shoji, *Microstructural characterization of subsurface caused by fretting wear of Inconel 690TT alloy*. Materials Characterization, 2016. **115**: p. 32-38.
87. Blanchard, P., C. Colombie, V. Pellerin, S. Fayeulle, and L. Vincent, *Material effects in fretting wear: application to iron, titanium, and aluminum alloys*. Metallurgical Transactions A, 1991. **22**(7): p. 1535-1544.
88. Fayeulle, S., P. Blanchard, and L. Vincent, *Fretting Behavior of Titanium Alloys*. Tribology Transactions, 1993. **36**(2): p. 267-275.
89. Kirk, A.M., P.H. Shipway, W. Sun, and C.J. Bennett, *The effect of frequency on both the debris and the development of the tribologically transformed structure during fretting wear of a high strength steel*. Wear, 2019. **426-427**: p. 694-703.
90. Fouvry, S., P. Arnaud, A. Mignot, and P. Neubauer, *Contact size, frequency and cyclic normal force effects on Ti-6Al-4V fretting wear processes: An approach combining friction power and contact oxygenation*. Tribology International, 2017. **113**(September 2017): p. 460-473.
91. Baydoun, S. and S. Fouvry, *An experimental investigation of adhesive wear extension in fretting interface: Application of the contact oxygenation concept*. Tribology International, 2020. **147**: p. art. no. 106266.
92. Juoksukangas, J., V. Nurmi, J. Hintikka, M. Vippola, A. Lehtovaara, A. Mäntylä, J. Vaara, and T. Frondelius, *Characterization of cracks formed in large flat-on-flat fretting contact*. International Journal of Fatigue, 2019. **124**: p. 361-370.
93. Ramalho, A., A. Merstallinger, and A. Cavaleiro, *Fretting behaviour of W-Si coated steels in vacuum environments*. Wear, 2006. **261**(1): p. 79-85.
94. Heredia, S. and S. Fouvry, *Introduction of a new sliding regime criterion to quantify partial, mixed and gross slip fretting regimes: Correlation with wear and cracking processes*. Wear, 2010. **269**(7): p. 515-524.
95. Berthier, Y., L. Vincent, and M. Godet, *Velocity accommodation sites and modes in tribology*. European journal of mechanics. A. Solids, 1992. **11**(1): p. 35-47.
96. Berthier, Y., *Experimental evidence for friction and wear modeling*. Wear, 1990. **139**(1): p. 77 - 92.
97. Hayes, E.K. and P.H. Shipway, *Effect of test conditions on the temperature at which a protective debris bed is formed in fretting of a high strength steel*. Wear, 2017. **376 - 377**(Part B): p. 1460 - 1466.
98. Godet, M., D. Play, and D. Berthe, *An attempt to provide a unified treatment of tribology through load carrying capacity, transport and continuum mechanics*. Journal of Tribology-Transactions of the ASME, 1980. **102**(2): p. 153-164.
99. Fillot, N., Y. Berthier, and I. Iordanoff, *Simulation of wear through mass balance in a dry contact*. Journal of Tribology-Transactions of the ASME, 2005. **127** (1): p. 230-237.
100. Neu, R.W., *Progress in standardization of fretting fatigue terminology and testing*. Tribology International, 2011. **44**(11): p. 1371-1377.
101. Greenwood, J.A. and J.B.P. Williamson, *Contact of nominally flat rough surfaces*. Proceedings of the Royal Society of London. Series A. Mathematical, Physical and Engineering Sciences, 1966. **295**: p. 300-319.
102. Kuno, M. and R.B. Waterhouse. *The effect of oscillatory direction on fretting wear under crossed cylinder contact conditions*. in *Proc. Conf. Eurotrib*. 1989.
103. Iordanoff, I., Y. Berthier, S. Descartes, and H. Heshmat, *A review of recent approaches for modeling solid third bodies*. Journal of Tribology-Transactions of the ASME, 2002. **124**(4): p. 725-735.
104. Mary, C., T. Le Mogne, B. Beaugiraud, B. Vacher, J.M. Martin, and S. Fouvry, *Tribochemistry of a Ti alloy under fretting in air: evidence of titanium nitride formation*. Tribology letters, 2009. **34**(3): p. 211-222.

105. Mary, C., S. Fouvry, J.M. Martin, and B. Bonnet, *Pressure and temperature effects on Fretting Wear damage of a Cu–Ni–In plasma coating versus Ti17 titanium alloy contact*. *Wear*, 2011. **272**(1): p. 18-37.
106. Baydoun, S., P. Arnaud, and S. Fouvry, *Modelling adhesive wear extension in fretting interfaces: An advection-dispersion-reaction contact oxygenation approach*. *Tribology International*, 2020. **151**: p. art. no. 106490.
107. Fouvry, S. and R. Merhej, *Introduction of a power law formulation to quantify the contact size effects on friction and wear responses of dry oscillating sliding contacts: Application to a chromium steel interface*. *Wear*, 2013. **301**: p. 34-46.
108. Fouvry, S., P. Kapsa, and L. Vincent, *Quantification of fretting damage*. *Wear*, 1996. **200**(1 - 2): p. 10.
109. Aldham, D., J. Warburton, and R.E. Pendlebury, *The unlubricated fretting wear of mild steel in air*. *Wear*, 1985. **106**(1-3): p. 177-201.
110. Warburton, J., *The fretting of mild steel in air*. *Wear*, 1989. **131**(2): p. 365-386.
111. Baydoun, S., S. Fouvry, S. Descartes, and P. Arnaud, *Fretting wear rate evolution of a flat-on-flat low alloyed steel contact: A weighted friction energy formulation*. *Wear*, 2019. **426**: p. 676-693.
112. Mi, X., Z.B. Cai, X.M. Xiong, H. Qian, L.C. Tang, Y.C. Xie, J.F. Peng, and M.H. Zhu, *Investigation on fretting wear behavior of 690 alloy in water under various temperatures*. *Tribology International*, 2016. **100**: p. 400-409.
113. Fantetti, A., L.R. Tamatam, M. Volvert, I. Lawal, L. Liu, L. Salles, M.R.W. Brake, C.W. Schwingshackl, and D. Nowell, *The impact of fretting wear on structural dynamics: Experiment and Simulation*. *Tribology International*, 2019. **138**: p. 111-124.
114. Mohd Tobi, A.L., J. Ding, S. Pearson, S.B. Leen, and P.H. Shipway, *The effect of gross sliding fretting wear on stress distributions in thin W-DLC coating systems*. *Tribology International*, 2010. **43**(10): p. 1917-1932.
115. Leen, S.B., I.J. Richardson, I.R. McColl, E.J. Williams, and T.R. Hyde, *Macroscopic fretting variables in a splined coupling under combined torque and axial load*. *Journal of Strain Analysis for Engineering Design*, 2001. **36**: p. 481 - 497.
116. Warmuth, A.R., *The effect of contact geometry and frequency on dry and lubricated fretting wear*, in *Department of Mechanical, Material and Manufacturing Engineering*. 2014, University of Nottingham.
117. Jin, X., *Investigation of the interrelated effects of temperature and frequency on fretting wear*, in *Department of Mechanical, Material and Manufacturing Engineering*. 2017, University of Nottingham.
118. Jin, X., P.H. Shipway, and W. Sun, *The role of frictional power dissipation (as a function of frequency) and test temperature on contact temperature and the subsequent wear behaviour in a stainless steel contact in fretting*. *Wear*, 2015. **330-331**: p. 103-111.
119. Jin, X., W. Sun, and P.H. Shipway, *The role of geometry changes and debris formation associated with wear on the temperature field in fretting contacts*. *Tribology International*, 2016. **102**: p. 392-406.
120. Kirk, A.M., P.H. Shipway, W. Sun, and C.J. Bennett, *Debris development in fretting contacts: debris particles and debris beds*. *Tribology International*, 2019. **149**: p. art. no. 105592.
121. Liu, Y.F., T. Liskiewicz, and B. Beake, *Dynamic changes of mechanical properties induced by friction in the Archard wear model*. *Wear*, 2019. **428-429**: p. 366-375.
122. Feng, I.M. and H.H. Uhlig, *Fretting corrosion of mild steel in air and in nitrogen*. *Journal of Applied Mechanics – Transactions of the ASME* 1954. **21**: p. 395 - 400.
123. Toth, L., *The investigation of the steady stage of steel fretting*. *Wear*, 1972. **20**(3): p. 277-286.

## Bibliography

---

124. Pendlebury, R.E., *Formation, readhesion and escape of wear particles in fretting and sliding wear in inert and oxidizing environments*. *Wear*, 1988. **125**(1-2): p. 3-23.
125. Knudsen, J. and A.R. Massih, *Evaluation of fretting wear data with the aid of mechanism-maps*. 2005.
126. Barman, K., P.H. Shipway, K.T. Voisey, and G. Pattinson, *The role of a thermally sprayed cuniin underlayer in the durability of a dry-film lubricant system in fretting—a phenomenological model*. *Tribology International*, 2018. **123**: p. 307-315.
127. Gradshteyn, I.S. and I.M. Ryzhik, *Table of Integrals, Series, and Products (Seventh Edition)*. 7 ed. 2007, USA: Academic Press. 408.
128. Artin, E., *The Gamma Function*. Dover edition ed. 2015: Dover Publications, Inc.

## Appendix A

### Derivation of the function of dissipated energy in terms of wear scar width

The volume of a minor segment of a cylinder (parallel to the cylinder axis) is given by the following equation:

$$V_w = L \left( R^2 \arcsin \left( \frac{x}{2R} \right) - \frac{x}{4} \sqrt{4R^2 - x^2} \right) \quad (A.1)$$

where terms are as previously defined. In the current study, it is proposed that the instantaneous wear rate  $\frac{dV_w}{dE_d}$  is dependent upon the scar width ( $x$ ) as follows:

$$\frac{dV_w}{dE_d} = \frac{k}{x}$$

which can be rewritten as follows:

$$\frac{dV_w}{dx} \frac{dx}{dE_d} = \frac{k}{x} \quad (A.2)$$

$\frac{dV_w}{dE_d}$  can be calculated by differentiating Equation A.1 with respect to  $x$ , which gives:

$$\begin{aligned} \frac{dV_w}{dx} &= LR^2 \frac{d}{dx} \left( \arcsin \left( \frac{x}{2R} \right) \right) - \frac{L}{4} \frac{d}{dx} \left( x \sqrt{4R^2 - x^2} \right) \\ &= LR^2 \frac{1}{\sqrt{4R^2 - x^2}} - \frac{L}{4} \frac{4R^2 - 2x^2}{\sqrt{4R^2 - x^2}} \\ &= \frac{x^2 L}{2\sqrt{4R^2 - x^2}} \end{aligned} \quad (A.3)$$

Substituting Equation A.3 into Equation A.2 gives:

$$dE_d = \frac{x^3 L}{2k\sqrt{4R^2 - x^2}} dx \quad (A.4)$$

## Appendix A

---

which can be integrated as follows:

$$E_d = \frac{L}{2k} \int \frac{x^3}{\sqrt{4R^2 - x^2}} dx$$

Defining that:

$$f(x) = \frac{x^3}{\sqrt{4R^2 - x^2}}$$

$$u = x^2$$

then:

$$E_d = \frac{L}{2k} \int f(x) dx$$

$$du = 2x dx$$

This returns:

$$\int f(x) dx = \int \frac{ux}{\sqrt{4R^2 - u}} \frac{du}{2x} = \frac{1}{2} \int \frac{u}{\sqrt{4R^2 - u}} du$$

Defining:

$$v = 4R^2 - u$$

then:

$$dv = -du$$

Combining  $u(x)$ ,  $v(u)$  and their corresponding differentiation into  $\int f(x)$  and rearranging the equation yields:

$$\int f(x) dx = \frac{-1}{2} \int \frac{4R^2 - v}{\sqrt{v}} dv = \frac{1}{2} \int \sqrt{v} dv - 2R^2 \int \frac{1}{\sqrt{v}} dv$$

And thus:

$$\int f(x)dx = \frac{1}{3}v^{\frac{3}{2}} - 4R^2v^{\frac{1}{2}} + c_1$$

By substituting the expressions for  $v(u)$  and  $u(x)$ :

$$\begin{aligned} \int f(x)dx &= \frac{1}{3}(4R^2 - u)^{\frac{3}{2}} - 4R^2(4R^2 - u)^{\frac{1}{2}} + c_1 \\ &= \frac{1}{3}(4R^2 - x^2)^{\frac{3}{2}} - 4R^2(4R^2 - x^2)^{\frac{1}{2}} + c_1 \\ &= \sqrt{4R^2 - x^2} \left( \frac{1}{3}(4R^2 - x^2) - 4R^2 \right) + c_1 \\ &= -\frac{1}{3}\sqrt{4R^2 - x^2}(8R^2 + x^2) + c_1 \end{aligned}$$

Therefore:

$$E_d = \frac{L}{2k} \left( -\frac{1}{3}\sqrt{4R^2 - x^2}(8R^2 + x^2) \right) + \frac{L}{2k}c_1$$

Simplifying the terms here yields:

$$E_d = -mL \left( \sqrt{4R^2 - x^2}(8R^2 + x^2) \right) + C \quad (A.5)$$

where  $C = \frac{1}{2k}c_1$  and  $m = \frac{1}{6k}$ .

To evaluate the integration constant,  $C$ , it is noted that in a fretting contact, there is a threshold of energy dissipated,  $E_{th}$ , below which  $x = 0$  (i.e. there is no wear) [24, 83]; in this region, Equation A.5 does not describe the relationship between  $E_d$  and  $x$ . However, once  $E_d$  has exceeded  $E_{th}$ , then wear occurs (and thus  $x > 0$ ). Evaluating Equation A.5 when  $E_d = E_{th}$  and  $x = 0$  yields the following:

$$E_{th} = -mL(16R^3) + C$$

and thus:

$$C = E_{th} + 16mLR^3$$

The final equation for  $E_d$  in terms of  $x$  is therefore as follows:

$$E_d = mL \left( 16 R^3 - \sqrt{4R^2 - x^2} (8R^2 + x^2) \right) + E_{th} \quad (A.6)$$

## Appendix B

### Details of the methodology for the derivation of the wear equations for all three contact configurations

The steps to determine the relationship between wear volume ( $V_w$ ) and dissipated energy ( $E_d$ ) for all three configurations (cylinder-on-flat, sphere-on-flat and crossed-cylinders) are identical, and can be categorised as follows:

- (i) derive an expression for  $V_w$  in terms of radius ( $R$ ) and wear scar angle ( $\theta$ );
- (ii) differentiate the expression to yield  $\frac{dV_w}{d\theta}$ ;
- (iii) determine the derivative of  $E_d$  with respect to  $\theta$ ,  $\frac{dE_d}{d\theta}$ , based on the assumption that the wear rate is inversely proportional to the wear scar width or on the assumptions that wear rate is inversely proportional to the wear scar area;
- (iv) integrate  $\frac{dE_d}{d\theta}$  to find an expression for  $E_d$  (and  $E_{dat}$ ) in terms of  $\theta$ ;
- (v) express  $V_w$  and  $E_{dat}$  as an infinite sum of polynomial terms (Taylor series) and approximate their expressions by taking their first non-constant polynomial terms;
- (vi) express  $V_w$  as a function of  $E_{dat}$ .

#### B1 Cylinder-on-flat configuration assuming either wear scar width or wear scar area dependence of instantaneous wear rate

**Find  $V_w$ .** As shown in Chapter 4, finding  $V_w$  can be simplified as a geometric problem, i.e.  $V_w$  can be written as a function in terms of  $R$  and  $\theta$ . For the cylinder-on-flat configuration,  $V_w$  can be approximated as the volume of a minor segment of a cylinder. Therefore, it can be shown that:

$$V_w = LR^2(\theta - \sin(\theta) \cos(\theta)) \quad (B1.1)$$

## Appendix B

---

where terms are as previously defined.

**Calculate**  $\frac{dV_w}{d\theta}$ . The derivative of  $V_w$  with respect to  $\theta$  can be shown to be:

$$\frac{dV_w}{d\theta} = LR^2(1 - \cos(2\theta)) \quad (B1.2)$$

**Determine**  $\frac{dE_d}{d\theta}$ . It was proposed in Chapter 4 that wear rate  $\left(\frac{dV_w}{dE_d}\right)$  is dependent upon the scar width ( $x$ ) in the following relationship:

$$\frac{dV_w}{dE_d} = \frac{k_1}{x} \quad (B1.3)$$

For the cylinder-on-flat configuration, wear scar width is roughly uniform throughout the damaged area. Therefore,  $x$  can be approximated as the chord length of the minor segment, which is:

$$x = 2R\sin(\theta)$$

Therefore, the wear rate expression can be rewritten as:

$$\frac{dV_w}{d\theta} \frac{d\theta}{dE_d} = \frac{k_1}{2R\sin(\theta)} \quad (B1.4)$$

Substituting Equation B1.2 into Equation B1.4 yields:

$$LR^2(1 - \cos(2\theta)) \frac{d\theta}{dE_d} = \frac{k_1}{2R\sin(\theta)}$$

which can be rearranged as follows:

$$\frac{dE_d}{d\theta} = \frac{2LR^3(1 - \cos(2\theta))\sin(\theta)}{k_1} \quad (B1.5)$$

**Integrate**  $\frac{dE_d}{d\theta}$ .  $E_d$  can be calculated by taking the integral of both sides of Equation B.1.5 with respect to  $\theta$ :

$$E_d = \frac{2LR^3}{k_1} \int (1 - \cos(2\theta))\sin(\theta) d\theta$$

By use of trigonometric identities, this can be integrated as follows:

$$\begin{aligned} \int (1 - \cos(2\theta))\sin(\theta) d\theta &\equiv \frac{1}{2} \int 3\sin(\theta) - \sin(3\theta) d\theta \\ &= \frac{1}{2} \left( \frac{1}{3} \cos(3\theta) - 3\cos(\theta) \right) + c_1 \end{aligned}$$

where  $c_1$  is a constant of integration.

Substituting the integral of  $(1 - \cos(2\theta))\sin(\theta)$  into the expression for  $E_d$  gives:

$$E_d = \frac{LR^3}{3k_1} (\cos(3\theta) - 9\cos(\theta)) + \frac{2LR^3}{k_1} c_1$$

which can be rewritten as:

$$E_d = m_1 LR^3 (\cos(3\theta) - 9 \cos(\theta)) + C_1 \quad (B1.6)$$

where  $m_1 = \frac{1}{3k_1}$  and  $C_1 = \frac{2LR^3}{k_1} c_1$ .

To evaluate the constant,  $C_1$ , it is noted that in a fretting contact, there is a threshold of energy dissipated,  $E_{th}$ , below which  $\theta = 0$  (i.e. there is no wear); in this region, Equation B1.6 does not describe the relationship between  $E_d$  and  $\theta$ . However, once  $E_d$  has exceeded  $E_{th}$ , then wear occurs (and thus  $\theta > 0$ ). Evaluating Equation B1.6 when  $E_d = E_{th}$  and  $\theta = 0$  yields the following:

$$E_{th} = -8m_1 LR^3 + C_1$$

and thus:

$$C_1 = E_{th} + 8m_1 LR^3$$

Substituting the expression of  $C_1$  into Equation B1.6, the final equation for  $E_d$  is:

$$E_d = m_1LR^3(\cos(3\theta) - 9\cos(\theta) + 8) + E_{th} \quad (B1.7)$$

A new term ( $E_{dat}$ ) can be defined, which represents the frictional energy dissipated above the threshold energy for wear to commence so that  $E_{dat} = E_d - E_{th}$  (the subscript “dat” being an acronym for “dissipated above threshold”).

In summary, a parametric function of  $V_w$  and  $E_{dat}$  in terms of  $\theta$  for the cylinder-on-flat configuration has been obtained:

$$\begin{pmatrix} V_w(\theta) \\ E_{dat}(\theta) \end{pmatrix} = \begin{pmatrix} LR^2(\theta - \sin(\theta) \cos(\theta)) \\ m_1LR^3(\cos(3\theta) - 9\cos(\theta) + 8) \end{pmatrix} \quad (B1.8)$$

**Express  $V_w$  and  $E_{dat}$  as an infinite polynomial sum (Taylor series).** With the parametric function,  $V_w$  and  $E_d$  can both be represented as a Taylor series.

The definition of a Taylor series expansion of a function  $f(x)$  at a point  $x = a$  is as follows:

$$f(x) = \sum_{n=0}^{\infty} \frac{f^{(n)}(a)}{n!} (x - a)^n$$

where  $f^{(n)}(a)$  = the  $n^{th}$  derivative of  $f(x)$  with respect to  $x$  evaluated at  $x = a$ .

Finding the Taylor series for  $V_w$  and  $E_{dat}$  at the point  $\theta = 0$  (the Taylor series of a function at 0 is also known as a Maclaurin series), then  $V_w$  and  $E_{dat}$  can be written as:

$$\begin{pmatrix} V_w(\theta) \\ E_{dat}(\theta) \end{pmatrix} = \begin{pmatrix} \sum_{n=0}^{\infty} \frac{V_w^{(n)}(0)}{n!} \theta^n \\ \sum_{m=0}^{\infty} \frac{E_{dat}^{(m)}(0)}{k!} \theta^m \end{pmatrix}$$

**Express  $V_w$  as a function of  $E_{dat}$ .** The first-degree polynomial term of each Taylor series for both  $V_w$  and  $E_{dat}$  were taken as approximations as follows:

$$\begin{pmatrix} V_w(\theta) \\ E_{dat}(\theta) \end{pmatrix} \approx \begin{pmatrix} \frac{2}{3}LR^2\theta^3 \\ 3m_1LR^3\theta^4 \end{pmatrix} \quad (B1.9)$$

Eliminating the parameter  $\theta$  from the parametric equations in Equation B1.9 yields:

$$V_w = \frac{2}{3^{1.75}} \left( \frac{L}{m_1^3} \right)^{0.25} R^{-0.25} E_{dat}^{0.75} \quad (B1.10)$$

## B2 Sphere-on-flat configuration assuming wear scar width dependence of instantaneous wear rate

**Find  $V_w$ .** For the sphere-on-flat configuration,  $V_w$  can be approximated as the volume of a spherical cap, which is given by the following equation:

$$V_w = \frac{\pi R^3}{3} (\cos^3(\theta) - 3 \cos(\theta) + 2) \quad (B2.1)$$

where terms are as previously defined.

**Calculate  $\frac{dV_w}{d\theta}$ .** Using trigonometric identities, it can be shown that:

$$\cos^3(\theta) - 3\cos(\theta) + 2 \equiv \frac{\cos(3\theta) - 9\cos(\theta) + 8}{4}$$

Accordingly, the expression for  $V_w$  for the sphere-on-flat configuration (Equation B2.1) can be written as follows:

$$V_w = \frac{\pi R^3}{12} (\cos(3\theta) - 9\cos(\theta) + 8)$$

The derivative of  $V_w$  with respect to  $\theta$  for the sphere-on-flat configuration can thus be written as follows:

$$\frac{dV_w}{d\theta} = \pi R^3 \sin^3(\theta) \quad (B2.2)$$

## Appendix B

---

**Determine**  $\frac{dE_d}{d\theta}$ . As has been shown for the cylinder-on-flat contact geometry, it is again proposed that wear rate ( $\frac{dV_w}{dE_d}$ ) is dependent upon the width of the wear scar. In this case, the shape of the wear scar approximates to that of a circle, and therefore (in contrast to the cylinder-on-flat geometry), the wear scar width in the direction of fretting displacement is not uniform. As such, it is assumed that the instantaneous wear rate is inversely proportional to a characteristic wear scar width which is defined as the maximum width of the wear scar (i.e. the wear scar diameter,  $2r$ ) as follows:

$$\frac{dV_w}{dE_d} = \frac{k_2}{2r} \quad (B2.3)$$

Using the geometrical relationship:

$$r = R\sin(\theta)$$

the expression for the wear rate can be rewritten as follows:

$$\frac{dV_w}{d\theta} \frac{d\theta}{dE_d} = \frac{k_2}{2R\sin(\theta)} \quad (B2.4)$$

Substituting Equation B2.2 into Equation B2.4 and rearranging yields:

$$\frac{dE_d}{d\theta} = \frac{2\pi R^4 \sin^4(\theta)}{k_2} \quad (B2.5)$$

**Integrate**  $\frac{dE_d}{d\theta}$ .  $E_d$  can be calculated by taking the integral of Equation B2.5 with respect to  $\theta$ :

$$E_d = \frac{2\pi R^4}{k_2} \int \sin^4(\theta) d\theta$$

By use of trigonometric identities, this can be integrated as follows:

$$\int \sin^4(\theta) d\theta \equiv \frac{1}{8} \int \cos(4\theta) - 4\cos(2\theta) + 3 d\theta = \frac{1}{32} (\sin(4\theta) - 8\sin(2\theta) + 12\theta) + c_2$$

where  $c_2$  is a constant of integration.

Substituting the integral of  $\sin^4(\theta)$  into the expression for  $E_d$  yields:

$$E_d = \frac{\pi R^4}{16k_2} (\sin(4\theta) - 8\sin(2\theta) + 12\theta) + \frac{2\pi R^4}{k_2} c_2$$

which can be rewritten as:

$$E_d = m_2 \pi R^4 (\sin(4\theta) - 8\sin(2\theta) + 12\theta) + C_2 \quad (B2.6)$$

where  $m_2 = \frac{1}{16k_2}$  and  $C_2 = \frac{2\pi R^4}{k_2} c_2$ .

As previously, it can be seen that the constant  $C_2$  can be evaluated as follows:

$$C_2 = E_{th}$$

A final equation for  $E_{dat}$  can therefore be written as follows:

$$E_{dat} = m_2 \pi R^4 (\sin(4\theta) - 8\sin(2\theta) + 12\theta) \quad (B2.7)$$

In summary, a parametric function of  $V_w$  and  $E_{dat}$  in terms of  $\theta$  for the sphere-on-flat configuration assuming wear scar width dependence of instantaneous wear rate has been obtained:

$$\begin{pmatrix} V_w(\theta) \\ E_{dat}(\theta) \end{pmatrix} = \begin{pmatrix} \frac{\pi R^3}{12} (\cos(3\theta) - 9\cos(\theta) + 8) \\ m_2 \pi R^4 (\sin(4\theta) - 8\sin(2\theta) + 12\theta) \end{pmatrix} \quad (B2.8)$$

**Express  $V_w$  and  $E_{dat}$  as an infinite polynomial sum (Taylor series).** With the establishment of the parametric function, the Taylor series for  $V_w$  and  $E_d$  can be expressed as follows:

$$\begin{pmatrix} V_w(\theta) \\ E_{dat}(\theta) \end{pmatrix} = \begin{pmatrix} \sum_{n=0}^{\infty} \frac{V_w^{(n)}(0)}{n!} \theta^n \\ \sum_{m=0}^{\infty} \frac{E_{dat}^{(m)}(0)}{k!} \theta^m \end{pmatrix}$$

**Express  $V_w$  as a function of  $E_d$ .** The first non-constant term of each Taylor series for both  $V_w$  and  $E_{dat}$  were taken as approximations as follows:

$$\begin{pmatrix} V_w(\theta) \\ E_{dat}(\theta) \end{pmatrix} \approx \begin{pmatrix} \frac{\pi R^3 \theta^4}{4} \\ \frac{32}{5} m_2 \pi R^4 \theta^5 \end{pmatrix} \quad (B2.9)$$

Eliminating the parameter  $\theta$  from the parametric equations in Equation B2.9 yields:

$$V_w = \frac{1}{4} \left( \frac{5}{32} \right)^{0.8} \left( \frac{\pi}{m_2^4} \right)^{0.2} R^{-0.2} E_{dat}^{0.8} \quad (B2.10)$$

### B3 Sphere-on-flat configuration assuming wear scar area dependence of instantaneous wear rate

**Find  $V_w$ .** The expression of  $V_w$  as a function of  $R$  and  $\theta$  remains the same as Equation B2.1:

$$V_w = \frac{\pi R^3}{3} (\cos^3(\theta) - 3 \cos(\theta) + 2) \quad (B3.1)$$

where terms are as previously defined.

**Calculate  $\frac{dV_w}{d\theta}$ .** Direct use of Equation B2.2:

$$\frac{dV_w}{d\theta} = \pi R^3 \sin^3(\theta) \quad (B3.2)$$

**Determine**  $\frac{dE_d}{d\theta}$ . The assumption here is that the wear rate  $(\frac{dV_w}{dE_d})$  is dependent upon the area of the wear scar ( $A$ ):

$$\frac{dV_w}{dE_d} = \frac{k'_2}{A} \quad (B3.3)$$

In this case, the shape of the wear scar approximates to that of a circle, and therefore, using the geometrical relationship:

$$A = \pi r^2 = \pi R^2 \sin^2(\theta)$$

the expression for the wear rate can be rewritten as follows:

$$\frac{dV_w}{d\theta} \frac{d\theta}{dE_d} = \frac{k'_2}{\pi R^2 \sin^2(\theta)} \quad (B3.4)$$

Substituting Equation B3.2 into Equation B3.4 and rearranging yields:

$$\frac{dE_d}{d\theta} = \frac{\pi^2 R^5 \sin^5(\theta)}{k'_2} \quad (B3.5)$$

**Integrate**  $\frac{dE_d}{d\theta}$ .  $E_d$  can be calculated by taking the integral of Equation B3.5 with respect to  $\theta$ :

$$E_d = \frac{\pi^2 R^5}{k'_2} \int \sin^5(\theta) d\theta$$

By use of trigonometric identities, this can be integrated as follows:

$$\begin{aligned} \int \sin^5(\theta) d\theta &\equiv \frac{1}{16} \int \sin(5\theta) - 5 \sin(3\theta) + 10 \sin(\theta) d\theta \\ &= \frac{1}{240} (-3\cos(5\theta) + 25\cos(3\theta) - 150\cos(\theta)) + c'_2 \end{aligned}$$

where  $c'_2$  is a constant of integration.

Substituting the integral of  $\sin^5(\theta)$  into the expression for  $E_d$  yields:

$$E_d = \frac{\pi^2 R^5}{240k'_2} (-3\cos(5\theta) + 25\cos(3\theta) - 150\cos(\theta)) + \frac{\pi^2 R^4}{k'_2} c'_2$$

which can be rewritten as:

$$E_d = m'_2 \pi^2 R^5 (-3\cos(5\theta) + 25\cos(3\theta) - 150 \cos(\theta)) + C'_2 \quad (B3.6)$$

where  $m'_2 = \frac{1}{240k'_2}$  and  $C'_2 = \frac{\pi^2 R^4}{k'_2} c'_2$ .

As previously, it can be seen that the constant  $C'_2$  can be evaluated as follows:

$$C'_2 = E_{th} + 128m'_2 \pi^2 R^5$$

A final equation for  $E_{dat}$  can therefore be written as follows:

$$E_{dat} = m'_2 \pi^2 R^5 (-3\cos(5\theta) + 25\cos(3\theta) - 150\cos(\theta) + 128) \quad (B3.7)$$

In summary, a parametric function of  $V_w$  and  $E_{dat}$  in terms of  $\theta$  for the sphere-on-flat configuration assuming wear scar area dependence of instantaneous wear rate has been obtained:

$$\begin{pmatrix} V_w(\theta) \\ E_{dat}(\theta) \end{pmatrix} = \begin{pmatrix} \frac{\pi R^3}{12} (\cos(3\theta) - 9\cos(\theta) + 8) \\ m'_2 \pi^2 R^5 (-3\cos(5\theta) + 25\cos(3\theta) - 150 \cos(\theta) + 128) \end{pmatrix} \quad (B3.8)$$

**Express  $V_w$  and  $E_{dat}$  as an infinite polynomial sum (Taylor series).** With the establishment of the parametric function, the Taylor series for  $V_w$  and  $E_d$  can be expressed as follows:

$$\begin{pmatrix} V_w(\theta) \\ E_{dat}(\theta) \end{pmatrix} = \begin{pmatrix} \sum_{n=0}^{\infty} \frac{V_w^{(n)}(0)}{n!} \theta^n \\ \sum_{m=0}^{\infty} \frac{E_{dat}^{(m)}(0)}{k!} \theta^m \end{pmatrix}$$

**Express  $V_w$  as a function of  $E_d$ .** The first non-constant term of each Taylor series for both  $V_w$  and  $E_{dat}$  were taken as approximations as follows:

$$\begin{pmatrix} V_w(\theta) \\ E_{dat}(\theta) \end{pmatrix} \approx \begin{pmatrix} \frac{\pi R^3 \theta^4}{4} \\ 40m'_2 \pi^2 R^5 \theta^6 \end{pmatrix} \quad (B3.9)$$

Eliminating the parameter  $\theta$  from the parametric equations in Equation B3.9 yields:

$$V_w = \frac{1}{4} \left( \frac{1}{40} \right)^{0.67} \left( \frac{1}{\pi m'_2} \right)^{0.33} R^{-0.33} E_{dat}^{0.67} \quad (B3.10)$$

#### **B4 Crossed-cylinder configuration assuming wear scar width dependence of instantaneous wear rate**

**Find  $V_w$ .** For the crossed-cylinder configuration, defining the shape of the intersection between two orthogonally crossed cylinders is not straightforward, and therefore the derivation of  $V^w$  is similarly not straightforward.

We define the system as two orthogonally crossed cylinders with the same radius ( $R$ ) in Cartesian coordinates. The shortest distance between the central axes of these two cylinders,  $2d$ , is defined as follows:

$$2d = R + R \cos(\theta)$$

The axis of one cylinder (*cylinder a*) has its axis parallel to the  $x$ -axis and crosses the  $z$ -axis at  $z = d$ , whilst the axis of the other cylinder (*cylinder b*) is parallel to the  $y$ -axis and crosses the  $z$ -axis at  $z = -d$ . This geometry is illustrated in Figure B.1.

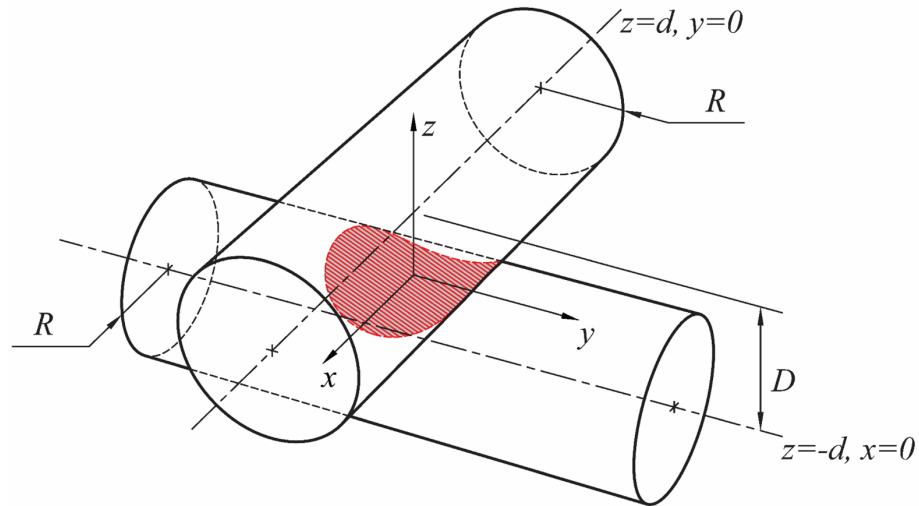


**Figure B.1: Illustration of two orthogonally crossed cylinders with identical radius ( $R$ ) in cartesian coordinates. The distance between their central axes is  $D$ .**

For *cylinder a*, all the points inside satisfy the inequality that:

$$y^2 + (z - d)^2 \leq R^2$$

For *cylinder b*, all the points inside satisfy the inequality that:

$$x^2 + (z + d)^2 \leq R^2$$

Rearranging these two inequalities gives the boundary of the intersection on  $x$ -axis and  $y$ -axis:

$$|y| \leq \sqrt{R^2 - (z - d)^2}$$

$$|x| \leq \sqrt{R^2 - (z + d)^2}$$

The limits on the  $z$ -axis are determined by the requirement that the arguments of both the square roots in the above inequalities are not negative:

$$-R \leq z - d$$

$$z + d \leq R$$

Therefore:

$$d - R \leq z \leq R - d$$

As shown in Figure B.2, every cross-section parallel to the  $x - y$  plane is a rectangle with sides of length  $l_1$  and  $l_2$ . Therefore, the volume of the intersection can be described as:

$$V_w = \lim_{n \rightarrow \infty} \sum_{j=1}^n l_1(z_j) l_2(z_j) \Delta z$$

where:

$$\Delta z = \frac{2R - 2d}{n}$$

$$z_j = (d - R) + \Delta z \cdot j$$

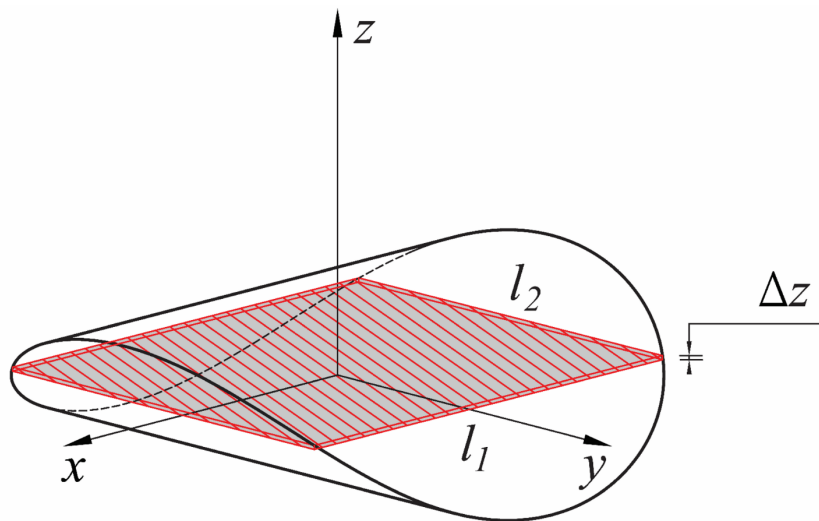


**Figure B.2:** Illustration of the intersection volume being calculated by integration of each slice parallel to the  $x - y$  plane within the boundary.

As  $n \rightarrow +\infty$ , the volume of the intersection can be written as an integral:

$$V_w = \int_{d-R}^{R-d} l_1(z) l_2(z) dz$$

## Appendix B

---

Since  $l_1$  is a line segment defined by the boundary of the intersection on  $x$ -axis, and  $l_2$  is defined by the boundary on  $y$ -axis, the following equations can be derived as:

$$l_1 = 2\sqrt{R^2 - (z + d)^2}$$

$$l_2 = 2\sqrt{R^2 - (z - d)^2}$$

Therefore,  $V_w$  can be expressed as:

$$\begin{aligned} V_w &= \int_{d-R}^{R-d} 4\sqrt{(R^2 - (z + d)^2)(R^2 - (z - d)^2)} dz \\ &= 8 \int_0^{R-d} \sqrt{(R^2 - (z + d)^2)(R^2 - (z - d)^2)} dz \end{aligned}$$

Rearranging this equation yields:

$$V_w = 8 \int_0^{R-d} \sqrt{((R - d)^2 - z^2)((R + d)^2 - z^2)} dz$$

Let:

$$z = (R - d)\sin(\theta)$$

Then:

$$dz = (R - d)\cos(\theta) d\theta$$

Changing the variable of the integration gives:

$$V_w = 8 \int_0^{\frac{\pi}{2}} \sqrt{(R - d)^2 \cos^2(\theta)} \sqrt{(R + d)^2 - (R - d)^2 \sin^2(\theta)} (R - d)\cos(\theta) d\theta$$

Rearranging this equation yields:

$$V_w = 8(R - d)^2(R + d) \int_0^{\frac{\pi}{2}} \cos^2(\theta) \sqrt{1 - \left(\frac{R - d}{R + d}\right)^2 \sin^2(\theta)} d\theta$$

To solve this integral, a standard formula [127] (Chapter 3.67 - “Square roots of expressions containing trigonometric functions”) is applied:

$$\int_0^{\frac{\pi}{2}} \sin^\alpha(x) \cos^\beta(x) \sqrt{1 - k^2 \sin^2(x)} dx$$

$$= \frac{1}{2} B\left(\frac{\alpha + 1}{2}, \frac{\beta + 1}{2}\right) F\left(\frac{\alpha + 1}{2}, -\frac{1}{2}; \frac{\alpha + \beta + 2}{2}; k^2\right)$$

for

$$\alpha > -1; \beta > -1; |k| < 1$$

In the expression of  $V_w$ , it can be found that:

$$\alpha = 0; \beta = 2; k = \frac{R - d}{R + d}$$

Therefore, an expression for  $V_w$  can be written as follows:

$$V_w = 8(R - d)^2(R + d) \cdot \frac{1}{2} B\left(\frac{1}{2}, \frac{3}{2}\right) F\left(\frac{1}{2}, -\frac{1}{2}; 2; \left(\frac{R - d}{R + d}\right)^2\right) \quad (B4.1)$$

This can be solved to yield:

$$V_w = \frac{\pi R^3}{4} (\cos^3(\theta) + \cos^2(\theta) - 5\cos(\theta) + 3) \quad (B4.2)$$

where terms are previously defined. For the detailed derivation of Equation B4.2 from Equation B4.1, see the next section, Section B5.

Using trigonometric identities, it can be shown that:

$$\cos^3(\theta) + \cos^2(\theta) - 5\cos(\theta) + 3 \equiv \frac{1}{4} (\cos(3\theta) + 2\cos(2\theta) - 17\cos(\theta) + 14)$$

which leads to:

$$V_w = \frac{\pi R^3}{16} (\cos(3\theta) + 2\cos(2\theta) - 17\cos(\theta) + 14) \quad (B4.3)$$

**Calculate**  $\frac{dV_w}{d\theta}$ . The derivative of  $V_w$  with respect to  $\theta$  can be shown to be:

$$\frac{dV_w}{d\theta} = \frac{\pi R^3}{4} \sin(\theta) (-3\cos^2(\theta) - 2\cos(\theta) + 5) \quad (B4.4)$$

**Determine**  $\frac{dE_d}{d\theta}$ . It is proposed that wear rate ( $\frac{dV_w}{dE_d}$ ) is also dependent upon the scar width ( $w$ ) for the crossed-cylinder configuration:

$$\frac{dV_w}{dE_d} = \frac{k_3}{w}$$

However, the wear scar width in the direction of fretting movement is not uniform across the damaged area for the crossed-cylinders configuration. A characteristic wear scar width is defined as the maximum width of the wear scar, which is given by the following:

$$w = 2R\sin(\theta)$$

Therefore, the wear rate expression can be rewritten as:

$$\frac{dV_w}{d\theta} \frac{d\theta}{dE_d} = \frac{k_3}{2R\sin(\theta)} \quad (B4.5)$$

Substituting Equation B4.4 into Equation B4.5 gives:

$$\frac{\pi R^3}{4} \sin(\theta) (-3\cos^2(\theta) - 2\cos(\theta) + 5) \frac{d\theta}{dE_d} = \frac{k_3}{2R\sin(\theta)}$$

which can be rearranged to yield:

$$\frac{dE_d}{d\theta} = \frac{\pi R^4 \sin^2(\theta) (-3\cos^2(\theta) - 2\cos(\theta) + 5)}{2k_3} \quad (B4.6)$$

**Integrate**  $\frac{dE_d}{d\theta}$ .  $E_d$  can be calculated by taking the integral of Equation B4.6 with respect to  $\theta$ :

$$E_d = \frac{\pi R^4}{2k_3} \int \sin^2(\theta) (-3 \cos^2(\theta) - 2\cos(\theta) + 5) d\theta$$

By use of well-known trigonometric identities, this can be integrated as follows:

$$\begin{aligned} & \int \sin^2(\theta) (-3 \cos^2(\theta) - 2\cos(\theta) + 5) d\theta \\ & \equiv \frac{1}{8} \int 3\cos(4\theta) + 4\cos(3\theta) - 20\cos(2\theta) - 4\cos(\theta) + 17 d\theta \\ & = \frac{1}{96} (9\sin(4\theta) + 16\sin(3\theta) - 120\sin(2\theta) - 48\sin(\theta) + 204\theta) + c_3 \end{aligned}$$

where  $c_3$  is a constant of integration.

Substituting the integral of  $\sin^2(\theta) (-3 \cos^2(\theta) - 2\cos(\theta) + 5)$  into the expression for  $E_d$  yields:

$$E_d = \frac{\pi R^4}{192k_3} (9\sin(4\theta) + 16\sin(3\theta) - 120\sin(2\theta) - 48\sin(\theta) + 204\theta) + \frac{\pi R^4}{192k_3} c_3$$

which can be rewritten as:

$$E_d = m_3 \pi R^4 (9\sin(4\theta) + 16\sin(3\theta) - 120\sin(2\theta) - 48\sin(\theta) + 204\theta) + C_3 \quad (A4.4.7)$$

where  $m_3 = \frac{1}{192k_3}$  and  $C_3 = \frac{\pi R^4}{192k_3} c_3$

As previously, it can be seen that the constant  $C_3$  can be evaluated as follows:

$$C_3 = E_{th}$$

A final equation for  $E_{dat}$  can therefore be written as follows:

$$E_{dat} = m_3 \pi R^4 (9\sin(4\theta) + 16\sin(3\theta) - 120\sin(2\theta) - 48\sin(\theta) + 204\theta) \quad (B4.8)$$

Therefore, a set of parametric function of  $V_w$  and  $E_d$  in terms of  $\theta$  for the crossed-cylinders configuration has been obtained:

$$\begin{pmatrix} V_w(\theta) \\ E_{dat}(\theta) \end{pmatrix} = \begin{pmatrix} \frac{\pi R^3}{16} (\cos(3\theta) + 2\cos(2\theta) - 17 \cos(\theta) + 14) \\ m_3 \pi R^4 (9\sin(4\theta) + 16\sin(3\theta) - 120\sin(2\theta) - 48\sin(\theta) + 204\theta) \end{pmatrix} \quad (B4.9)$$

**Expand  $V_w$  and  $E_{dat}$  as an infinite polynomial sum (Taylor series).** With the establishment of the parametric function, the Taylor series for  $V_w$  and  $E_d$  can be expressed as follows:

$$\begin{pmatrix} V_w(\theta) \\ E_{dat}(\theta) \end{pmatrix} = \begin{pmatrix} \sum_{n=0}^{\infty} \frac{V_w^{(n)}(0)}{n!} \theta^n \\ \sum_{m=0}^{\infty} \frac{E_{dat}^{(m)}(0)}{k!} \theta^m \end{pmatrix}$$

**Express  $V_w$  as a function of  $E_d$ .** The first non-constant term of each Taylor series for both  $V_w$  and  $E_{dat}$  were taken as approximations as follows:

$$\begin{pmatrix} V_w(\theta) \\ E_{dat}(\theta) \end{pmatrix} \approx \begin{pmatrix} \frac{\pi R^3 \theta^4}{4} \\ \frac{384}{5} m_3 \pi R^4 \theta^5 \end{pmatrix} \quad (B4.10)$$

Eliminating the parameter  $\theta$  from the parametric equations in Equation B4.10 yields:

$$V_w = \frac{1}{4} \left( \frac{5}{384} \right)^{0.8} \left( \frac{\pi}{m_3^4} \right)^{0.2} R^{-0.2} E_{dat}^{0.8} \quad (B4.11)$$

## **B5 The beta function, gamma function and hypergeometric function**

In the previous section (Section B4), an expression for  $V_w$  for a crossed-cylinders contact was written in the form of Equation B4.1. The right side of the equation involves

the use of the Beta function,  $B$ , the Gamma function,  $\Gamma$ , and the Hypergeometric function,  $F$ .

The definition of the Beta function is given by:

$$B(x, y) = \int_0^1 t^{x-1}(1-t)^{y-1} dt, \quad \operatorname{Re}(x) > 0; \operatorname{Re}(y) > 0$$

The Gamma function is an extension of the factorial function from positive integers to complex numbers, and its definition is:

$$\Gamma(z) = \int_0^\infty t^{z-1}e^{-t} dt, \quad \operatorname{Re}(z) > 0$$

There is an important relationship between Beta function and Gamma function (for a proof, see Chapter 2 of Artin's book "The Gamma Function" [128]):

$$B(x, y) = \frac{\Gamma(x)\Gamma(y)}{\Gamma(x+y)}$$

As such, the Beta function in Equation B4.1 is equal to:

$$B\left(\frac{1}{2}, \frac{3}{2}\right) = \frac{\Gamma\left(\frac{1}{2}\right)\Gamma\left(\frac{3}{2}\right)}{\Gamma(2)} \tag{B5.1}$$

With the definition of  $\Gamma$ , it can be shown that:

$$\Gamma(z+1) = \int_0^\infty t^z e^{-t} dt$$

Let:

$$\frac{du}{dt} = e^{-t}$$

$$v = t^z$$

which yields:

$$u = -e^{-t}$$

$$\frac{dv}{dt} = zt^{z-1}$$

Thus:

$$\begin{aligned} \Gamma(z + 1) &= -t^z e^{-t} \Big|_0^\infty + \int_0^\infty zt^{z-1} e^{-t} dt \\ &= \lim_{t \rightarrow \infty} (-t^z e^{-t}) - (0e^0) + \int_0^\infty zt^{z-1} e^{-t} dt \end{aligned}$$

As  $t \rightarrow +\infty$ ,  $-t^z e^{-t} \rightarrow 0$ , which means that  $\Gamma(z + 1)$  can be written as:

$$\begin{aligned} \Gamma(z + 1) &= z \int_0^\infty t^{z-1} e^{-t} dt \\ &= z\Gamma(z) \end{aligned}$$

Equation B5.1 can therefore be simplified as follows:

$$\begin{aligned} B\left(\frac{1}{2}, \frac{3}{2}\right) &= \frac{\Gamma\left(\frac{1}{2}\right)\Gamma\left(\frac{1}{2} + 1\right)}{\Gamma(1 + 1)} \\ &= \frac{1}{2} \frac{\Gamma\left(\frac{1}{2}\right)^2}{\Gamma(1)} \end{aligned} \tag{B5.2}$$

The gamma functions  $\Gamma\left(\frac{1}{2}\right)$  and  $\Gamma(1)$  can be evaluated as follows:

$$\Gamma\left(\frac{1}{2}\right) = \int_0^\infty t^{-\frac{1}{2}} e^{-t} dt$$

$$\Gamma(1) = \int_0^\infty e^{-t} dt$$

For  $\Gamma\left(\frac{1}{2}\right)$ , let:

$$t = u^2$$

then:

$$dt = 2u \, du$$

which leads to:

$$\Gamma\left(\frac{1}{2}\right) = 2 \int_0^{\infty} e^{-u^2} \, du$$

Recognizing that the right-hand side of the equation for  $\Gamma\left(\frac{1}{2}\right)$  is the Gaussian integral,

which is evaluated as follows:

$$2 \int_0^{\infty} e^{-u^2} \, du = \int_{-\infty}^{\infty} e^{-x^2} \, dx = \sqrt{\pi}$$

therefore:

$$\Gamma\left(\frac{1}{2}\right) = \sqrt{\pi} \tag{B5.3}$$

The value of  $\Gamma(1)$  can be readily evaluated as:

$$\begin{aligned} \Gamma(1) &= \int_0^{\infty} e^{-t} \, dt \\ &= \lim_{t \rightarrow \infty} (-e^{-t}) - (-e^0) \\ &= 1 \end{aligned} \tag{B5.4}$$

Substituting Equation B5.3 and Equation B5.4 into the Beta function in Equation B5.1 yields:

$$\begin{aligned} B\left(\frac{1}{2}, \frac{3}{2}\right) &= \frac{1}{2} \frac{\Gamma\left(\frac{1}{2}\right)^2}{\Gamma(1)} \\ &= \frac{1}{2} \frac{(\sqrt{\pi})^2}{1} \end{aligned}$$

$$= \frac{\pi}{2} \quad (B5.5)$$

In addition to Beta function and gamma function, Equation B4.1 requires the knowledge of Hypergeometric function, F, which is defined by the Gaussian series:

$$\begin{aligned} F(a, b; c; z) &= \sum_{n=0}^{\infty} \frac{(a)_n (b)_n}{(c)_n} \frac{z^n}{n!} \\ &= 1 + \frac{ab}{c} z + \frac{a(a+1)b(b+1)}{c(c+1)} \frac{z^2}{2!} + \dots \end{aligned}$$

Therefore, by substituting the values  $a = \frac{1}{2}$ ,  $b = \frac{3}{2}$ ,  $c = 2$  and  $z = \left(\frac{R-d}{R+d}\right)^2$ , the Hypergeometric function in Equation B4.1 can be written as follows:

$$F\left(\frac{1}{2}, -\frac{1}{2}; 2; \left(\frac{R-d}{R+d}\right)^2\right) = 1 - \frac{1}{8} \left(\frac{R-d}{R+d}\right)^2 - \frac{1}{64} \left(\frac{R-d}{R+d}\right)^4 + \dots \quad (B5.6)$$

It is noted that from the second term of the Gaussian series for  $F\left(\frac{1}{2}, -\frac{1}{2}; 2; \left(\frac{R-d}{R+d}\right)^2\right)$ , the absolute coefficient has dropped to  $\frac{1}{8}$  or even less, meaning it is reasonable to take only the first term as the approximation of the whole series. Therefore, we can simplify the Hypergeometric function in Equation B4.1 as follows:

$$F\left(\frac{1}{2}, -\frac{1}{2}; 2; \left(\frac{R-d}{R+d}\right)^2\right) \approx 1 \quad (B5.7)$$

With the knowledge of the Beta function,  $B\left(\frac{1}{2}, \frac{3}{2}\right)$ , and the Hypergeometric function,  $F\left(\frac{1}{2}, -\frac{1}{2}; 2; \left(\frac{R-d}{R+d}\right)^2\right)$ , Equation B4.1 can be evaluated as follows:

$$\begin{aligned} V_w &= 8(R-d)^2(R+d) \cdot \frac{1}{2} B\left(\frac{1}{2}, \frac{3}{2}\right) F\left(\frac{1}{2}, -\frac{1}{2}; 2; \left(\frac{R-d}{R+d}\right)^2\right) \\ &\approx 8(R-d)^2(R+d) \cdot \frac{1}{2} \frac{\pi}{2} \cdot 1 \end{aligned}$$

$$\approx 2\pi(R - d)^2(R + d) \quad (B5.8)$$

Since:

$$d = \frac{R + R\cos(\theta)}{2}$$

the expression for  $V_w$  in Equation B5.8 can be written as:

$$\begin{aligned} V_w &\approx 2\pi(R^2 - d^2)(R - d) \\ &\approx 2\pi R^3 \left( \frac{3 - 2\cos(\theta) - \cos^2(\theta)}{4} \right) \left( \frac{1 - \cos(\theta)}{2} \right) \end{aligned}$$

Finally, rearranging the equation above gives:

$$V_w \approx \frac{\pi R^3}{4} (\cos^3(\theta) + \cos^2(\theta) - 5\cos(\theta) + 3) \quad (B5.9)$$

To understand the error associated with this approximation, 3D modelling software was used to construct the shape of the intersection between two orthogonally crossed cylinders with varying  $\theta$ . Using the software, the volume of intersection was evaluated numerically, and this was then compared with the approximated values evaluated by Equation B5.9. As can be seen from Figure B.3, the differences between the normalised wear volume,  $v_w$  (where  $v_w = \frac{4V_w}{\pi R^3}$ ), calculated by these two methods are negligible across the whole range of  $\theta$ . It is therefore reasonable to assert that Equation B5.9 derived from the simplification of Equation B5.7 well describes the relationship between  $V_w$  and  $\theta$  for the crossed-cylinder contact.

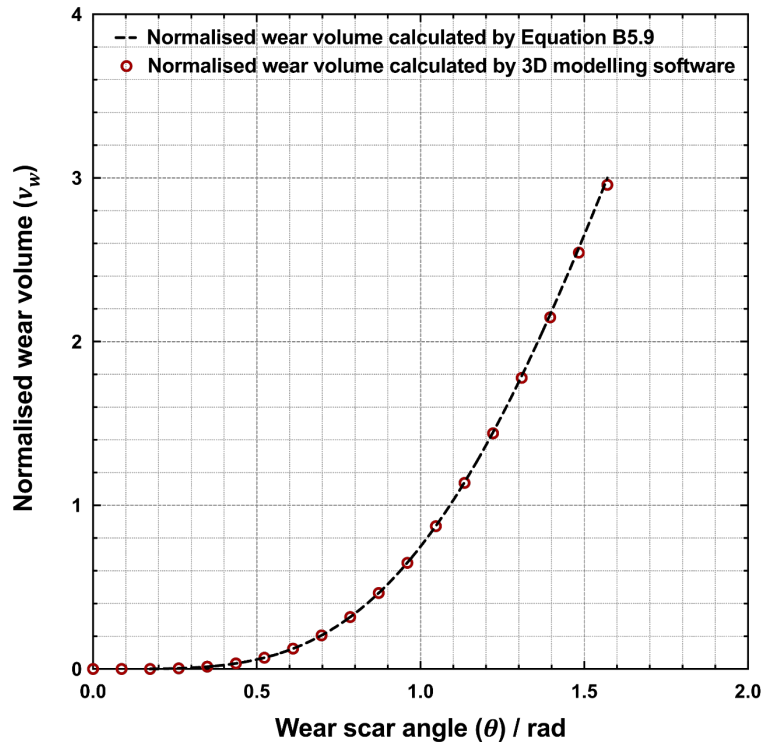


Figure B.3: Plot of normalised wear volume evaluated numerically via 3D modelling software compared with equivalent values calculated from Equation B5.9.

## Appendix C

### Dimensional analysis of the form of wear equations

Due to the nature of fretting, the slip amplitude is small compared to the size of the worn surface. This observation is crucial as it leads to the accurate approximation to relate  $V_w$ ,  $R$  and  $\theta$  by a pure geometric relationship. Such geometric relationship is assumed to be true for all the cylinder-on-flat (CF), sphere-on-flat (SF) and crossed-cylinders (CC) contact configurations, which can be approximated by adopting Taylor expansion (see Appendix B) to acquire the form of:

$$V_w \cong L^a R^b \theta^c \quad (C.1)$$

where  $a$ ,  $b$  and  $c$  are integer exponents.

The dimension of  $V_w$  (denoted as  $[V_w]$ ) is  $\mathbf{L}^3$  ( $\mathbf{L}$ , the dimensional symbol for length), and likewise,  $[L] = \mathbf{L}$  and  $[R] = \mathbf{L}$  while  $\theta$  is a dimensionless quantity, indicating that:

$$a + b = 3 \quad (C.2)$$

The CF contact produces a line contact where the length of wear scar is a constant, limited by the width of specimens (as described in Section 3.1), and thus  $a = 1$  and  $b = 2$ . In contrast, for both the SF and CC contact generating a point contact, only  $R$  is relevant when calculating the wear volume, which leads to  $a = 0$  and  $b = 3$ . The Taylor approximation as outlined in Appendix B indicates that  $c = 3$  for the CF contact, and  $c = 4$  for both the SF and CC contact. Values of  $a$ ,  $b$  and  $c$  are summarised in Table C.1.

It can be observed from Table C.1 that:

$$c = b + 1 \quad (C.3)$$

## Appendix C

---

Such relationship is safe to declare within the scope of this work, since: (i) the values of  $a$ ,  $b$  and  $c$  are obtained by the Taylor approximation for the geometric relationship between  $V_w$  and  $\theta$ , where the approximation has a high accuracy which makes those approximations almost equal to the exact equations; (ii) although  $b$  and  $c$  are not related to each other through rigorous mathematical derivation, the observation made in Equation C.3 holds true for all the cases discussed in this work, which has covered the most commonly-adopted non-conforming contact configurations for research in fretting, namely the cylinder-on-flat, sphere-on-flat and crossed-cylinders.

**Table C.1: Summary of integer exponents for CF, SF and CC contact for the Taylor approximation of the geometric relationship as indicated by Equation C.1.**

Contact configurations	$a$	$b$	$c$
Cylinder-on-flat	1	2	3
Sphere-on-flat	0	3	4
Crossed-cylinders	0	3	4

The derivative of  $V_w$  with respect to  $\theta$  can be easily found as follows:

$$\frac{dV_w}{d\theta} \cong L^a R^b \theta^{c-1} \quad (C.4)$$

Two forms of governing equations were proposed in this work which state that the instantaneous wear rate is inversely proportional to the characteristic wear scar width (Equation C.5a for all three cases) or wear scar area (Equation C.5b for CF contact, and Equation C.5c for SF; as demonstrated by Figure 5.8, the wear scar area for CC contact is complex, therefore the equation of the wear scar area in terms of  $R$  and  $\theta$  for CC contact cannot be readily defined). The validity of these assumptions has been discussed in Appendix B.

$$\frac{dV_w}{dE_d} = \frac{h_1}{R\sin(\theta)} \quad (C.5a)$$

$$\frac{dV_w}{dE_d} = \frac{h_2}{LR\sin(\theta)} \quad (C.5b)$$

$$\frac{dV_w}{dE_d} = \frac{h_2}{\pi R^2 \sin^2(\theta)} \quad (C.5c)$$

where  $h_1$  and  $h_2$  are functions of fretting parameters but are treated as constants in the current study. Please note that  $h_1$  and  $h_2$  have different dimensions as follows where **M** is the dimensional symbol for mass, and **T** is the dimensional symbol for time:

$$[h_1] = \frac{\mathbf{L}^2\mathbf{T}^2}{\mathbf{M}}$$

$$[h_2] = \frac{\mathbf{L}^3\mathbf{T}^2}{\mathbf{M}}$$

Taylor approximations can be applied to Equation C.5 to yield:

$$\frac{dV_w}{dE_d} = \frac{h_1}{R\sin(\theta)} \rightarrow \frac{dV_w}{dE_d} \cong \frac{h_1}{R\theta} \quad (C.6a)$$

$$\frac{dV_w}{dE_d} = \frac{h_2}{LR\sin(\theta)} \rightarrow \frac{dV_w}{dE_d} \cong \frac{h_2}{LR\theta} \quad (C.6b)$$

$$\frac{dV_w}{dE_d} = \frac{h_2}{\pi R^2 \sin^2(\theta)} \rightarrow \frac{dV_w}{dE_d} \cong \frac{h_2}{\pi R^2 \theta^2} \quad (C.6c)$$

## C1 Linear basis of the governing equation

When the linear basis of the governing equation is considered, combining Equation C.6a with Equation C.4 yields the following expression for  $E_d$ :

$$\begin{aligned} \frac{dE_d}{d\theta} &\cong \frac{L^a R^{b+1} \theta^c}{h_1} \\ E_d &\cong \frac{L^a R^{b+1} \theta^{c+1}}{(c+1)h_1} \end{aligned} \quad (C.7)$$

## Appendix C

---

Eliminating the internal variable  $\theta$  (so that Equation C.1 and Equation C.7 can be combined) yields:

$$\begin{aligned}
 V_w &\cong (c+1)^{\frac{c}{c+1}} h_1^{\frac{c}{c+1}} L^{a-\frac{ac}{c+1}} R^{b-\frac{(b+1)c}{c+1}} E_d^{\frac{c}{c+1}} \\
 &\cong (c+1)^{\frac{c}{c+1}} h_1^{\frac{c}{c+1}} L^{\frac{a}{c+1}} R^{\frac{b-c}{c+1}} E_d^{\frac{c}{c+1}} \\
 &\cong (c+1)^n h_1^n L^k R^m E_d^n \tag{C.8}
 \end{aligned}$$

where  $k = \frac{a}{c+1}$ ,  $m = \frac{b-c}{c+1}$  and  $n = \frac{c}{c+1}$ .

At this stage,  $V_w$  can be expressed as a function of  $L$ ,  $R$  and  $E_d$ , and the dimensions of both sides of Equation C.8 must be the same. Substituting the dimensions of each quantity into Equation C.8 yields:

$$\begin{aligned}
 \left(\frac{\mathbf{L}^2 \mathbf{T}^2}{\mathbf{M}}\right)^n \mathbf{L}^k \mathbf{L}^m \left(\frac{\mathbf{M} \mathbf{L}^2}{\mathbf{T}^2}\right)^n &= \mathbf{L}^3 \\
 k + m + 4n &= 3 \\
 \frac{a}{c+1} + \frac{b-c}{c+1} + \frac{4c}{c+1} &= 3 \\
 \frac{a+b+3c}{c+1} &= 3
 \end{aligned}$$

which can be satisfied with Equation C.2.

With the relationship declared in Equation C.3 that  $c = b + 1$ ,  $m$  can be expressed as:

$$m = \frac{b-c}{c+1} = \frac{c-1-c}{c+1} = \frac{-1}{c+1} = n-1$$

Thus, Equation C.8 can be rewritten as:

$$V_w \cong (c+1)^n h_1^n L^k R^{n-1} E_d^n \tag{C.9}$$

## C2 Area basis of the governing equation for CF contact

With the basis of the governing equation, combining Equation C.6b with Equation C.4 yields the following expression for  $E_d$ :

$$\begin{aligned}\frac{dE_d}{d\theta} &\cong \frac{L^{a+1}R^{b+1}\theta^c}{h_2} \\ E_d &\cong \frac{L^{a+1}R^{b+1}\theta^{c+1}}{(c+1)h_2}\end{aligned}\quad (C.10)$$

Eliminating the internal variable  $\theta$  yields:

$$\begin{aligned}V_w &\cong (c+1)^{\frac{c}{c+1}} h_2^{\frac{c}{c+1}} L^{a-\frac{(a+1)c}{c+1}} R^{b-\frac{(b+1)c}{c+1}} E_d^{\frac{c}{c+1}} \\ &\cong (c+1)^{\frac{c}{c+1}} h_2^{\frac{c}{c+1}} L^{\frac{a-c}{c+1}} R^{\frac{b-c}{c+1}} E_d^{\frac{c}{c+1}} \\ &\cong (c+1)^n h_2^n L^k R^m E_d^n\end{aligned}\quad (C.11)$$

where  $k = \frac{a-c}{c+1}$ ,  $m = \frac{b-c}{c+1}$  and  $n = \frac{c}{c+1}$ .

Substituting the dimensions of each quantity into Equation C.11 to assert its validity:

$$\begin{aligned}\left(\frac{\mathbf{L}^3\mathbf{T}^2}{\mathbf{M}}\right)^n \mathbf{L}^k \mathbf{L}^m \left(\frac{\mathbf{M}\mathbf{L}^2}{\mathbf{T}^2}\right)^n &= \mathbf{L}^3 \\ k + m + 5n &= 3 \\ \frac{a-c}{c+1} + \frac{b-c}{c+1} + \frac{5c}{c+1} &= 3 \\ \frac{a+b+3c}{c+1} &= 3\end{aligned}$$

which, again, is satisfied with Equation C.2.

Since the expression of  $m$  and  $n$  are identical to those in the previous section (Section C3), the relationship that  $m = n - 1$  holds, which allows Equation C.11 to be rewritten as:

$$V_w \cong (c + 1)^n h_2^n L^k R^{n-1} E_d^n \quad (C.12)$$

Notice here that, although Equation C.12 may seem similar to Equation C.9 (particularly where the expressions of  $n$  are the same), the dimension of  $h_2$  is different from that of  $h_1$  and the expression for  $k$  changes from  $\frac{a}{c+1}$  for Equation C.9 to  $\frac{a-c}{c+1}$  for Equation C.12.

### C3 Area basis of the governing equation for SF contact

Combining Equation C.6c with Equation C.4 yields the following expression for  $E_d$ :

$$\begin{aligned} \frac{dE_d}{d\theta} &\cong \frac{\pi L^a R^{b+2} \theta^{c+1}}{h_2} \\ E_d &\cong \frac{\pi L^a R^{b+2} \theta^{c+2}}{(c+2)h_2} \end{aligned} \quad (C.13)$$

Eliminating the internal variable  $\theta$  yields:

$$\begin{aligned} V_w &\cong (c+2)^{\frac{c}{c+2}} h_2^{\frac{c}{c+2}} \pi^{\frac{-c}{c+2}} L^{a-\frac{ac}{c+2}} R^{b-\frac{(b+2)c}{c+2}} E_d^{\frac{c}{c+2}} \\ &\cong (c+2)^{\frac{c}{c+2}} h_2^{\frac{c}{c+2}} \pi^{\frac{-c}{c+2}} L^{\frac{2a}{c+2}} R^{\frac{2(b-c)}{c+2}} E_d^{\frac{c}{c+2}} \\ &\cong (c+2)^n h_2^n \pi^{-n} L^k R^m E_d^n \end{aligned} \quad (C.14)$$

where  $k = \frac{2a}{c+2}$ ,  $m = \frac{2(b-c)}{c+2}$  and  $n = \frac{c}{c+2}$ .

Substituting the dimensions of each quantity into Equation C.14 to assert its validity ( $\pi$  is a dimensionless quantity):

$$\begin{aligned} \left( \frac{\mathbf{L}^3 \mathbf{T}^2}{\mathbf{M}} \right)^n \mathbf{L}^k \mathbf{L}^m \left( \frac{\mathbf{M} \mathbf{L}^2}{\mathbf{T}^2} \right)^n &= \mathbf{L}^3 \\ k + m + 5n &= 3 \\ \frac{2a}{c+2} + \frac{2(b-c)}{c+2} + \frac{5c}{c+2} &= 3 \\ \frac{2a + 2b + 3c}{c+2} &= 3 \end{aligned}$$

which, again, is satisfied with Equation C.2.

With the relationship declared in Equation C.3 that  $c = b + 1$ ,  $m$  can be expressed as:

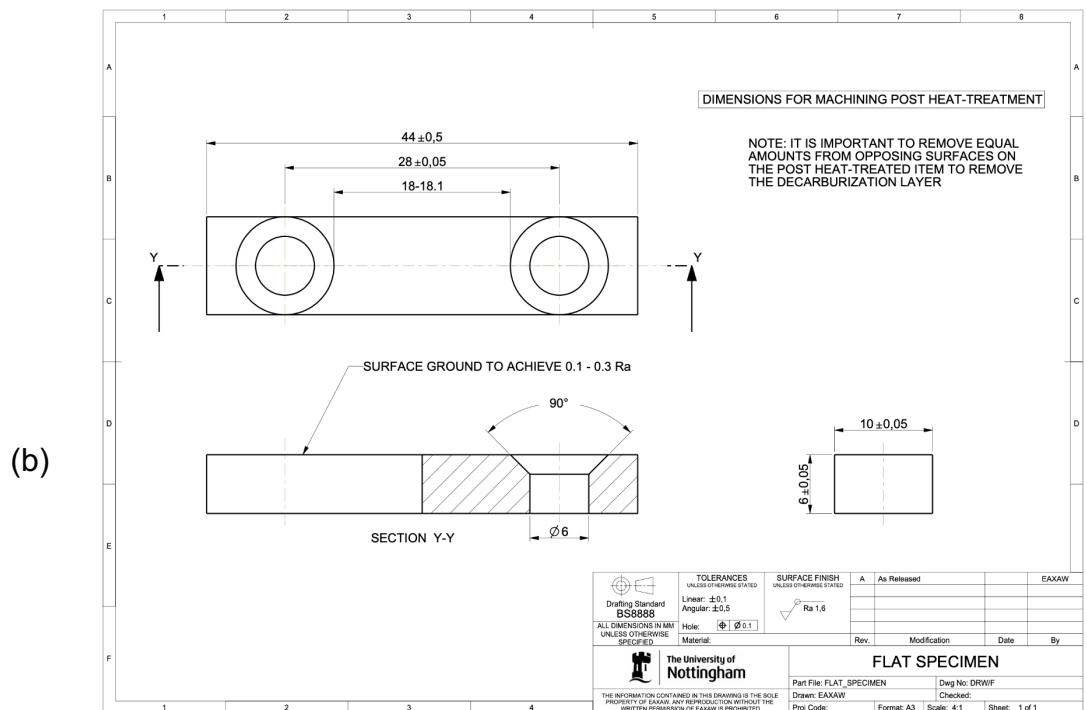
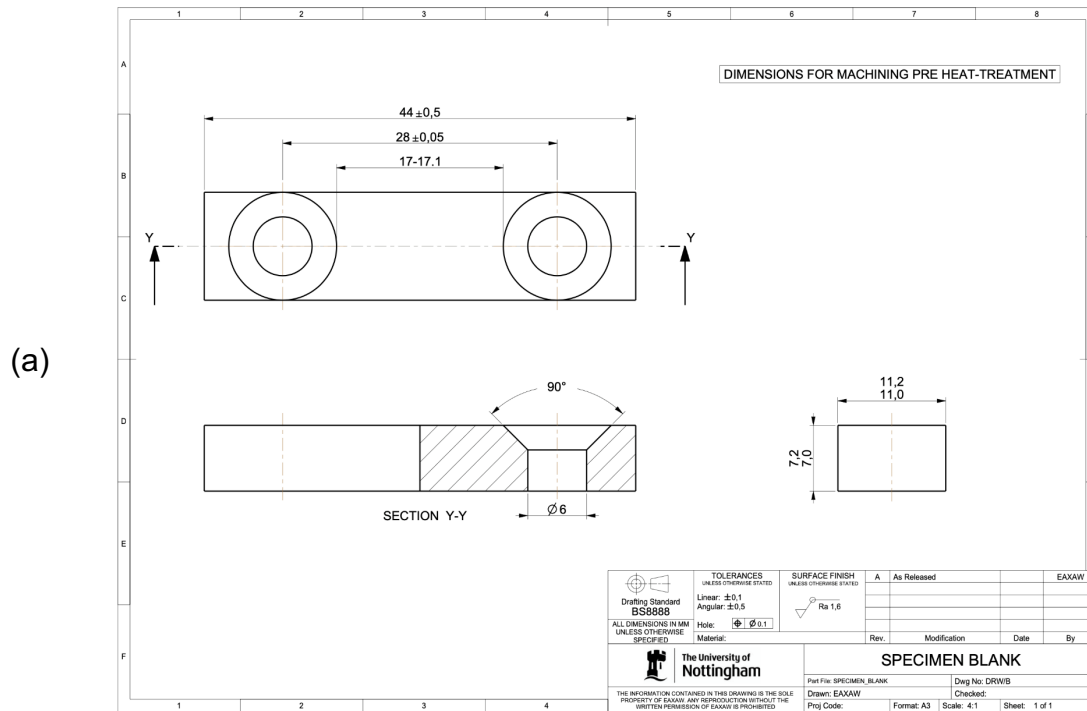
$$m = \frac{2(b - c)}{c + 2} = \frac{2(c - 1 - c)}{c + 2} = \frac{-2}{c + 2} = n - 1$$

Thus, Equation C.14 can be rewritten as:

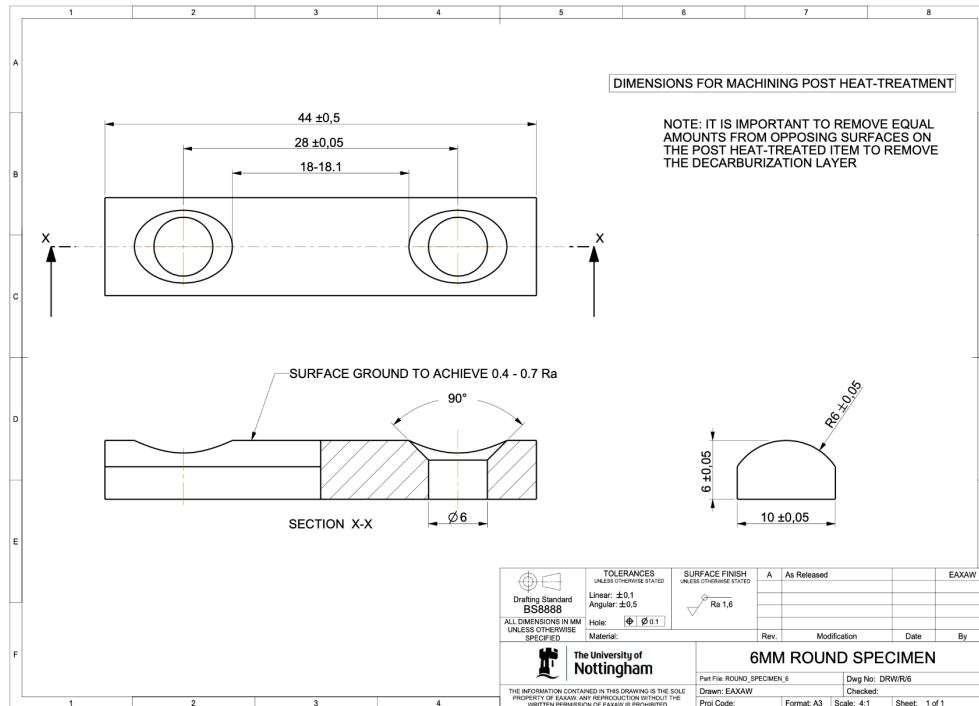
$$V_w \cong (c + 2)^n h_2^n \pi^{-n} L^k R^{n-1} E_d^n \tag{C.15}$$

# Appendix D

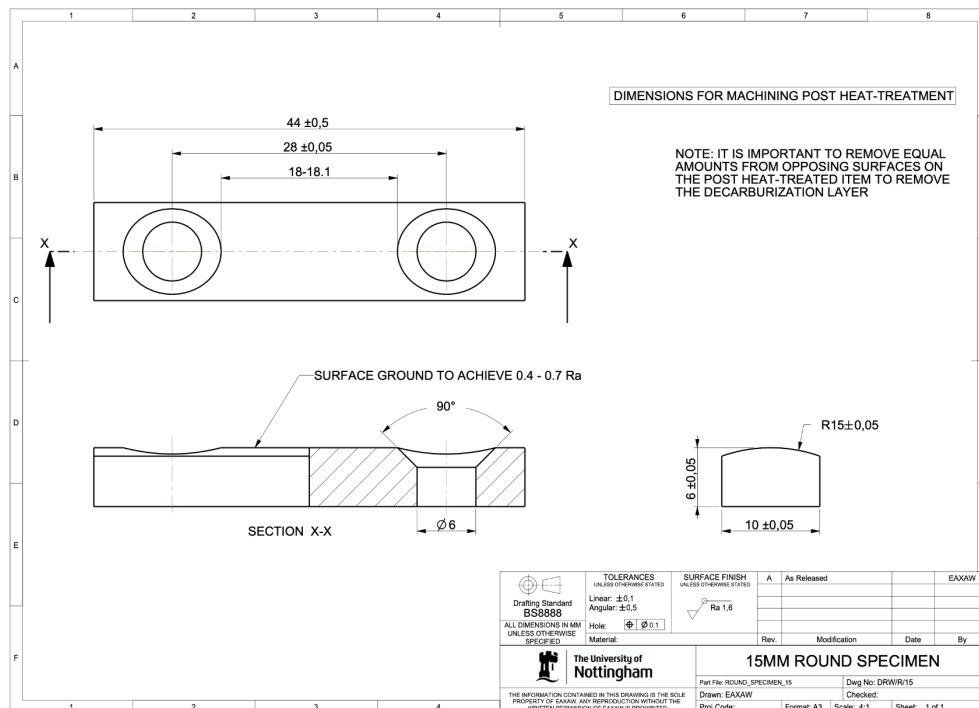
## Detail drawings of specimens



(c)



(d)



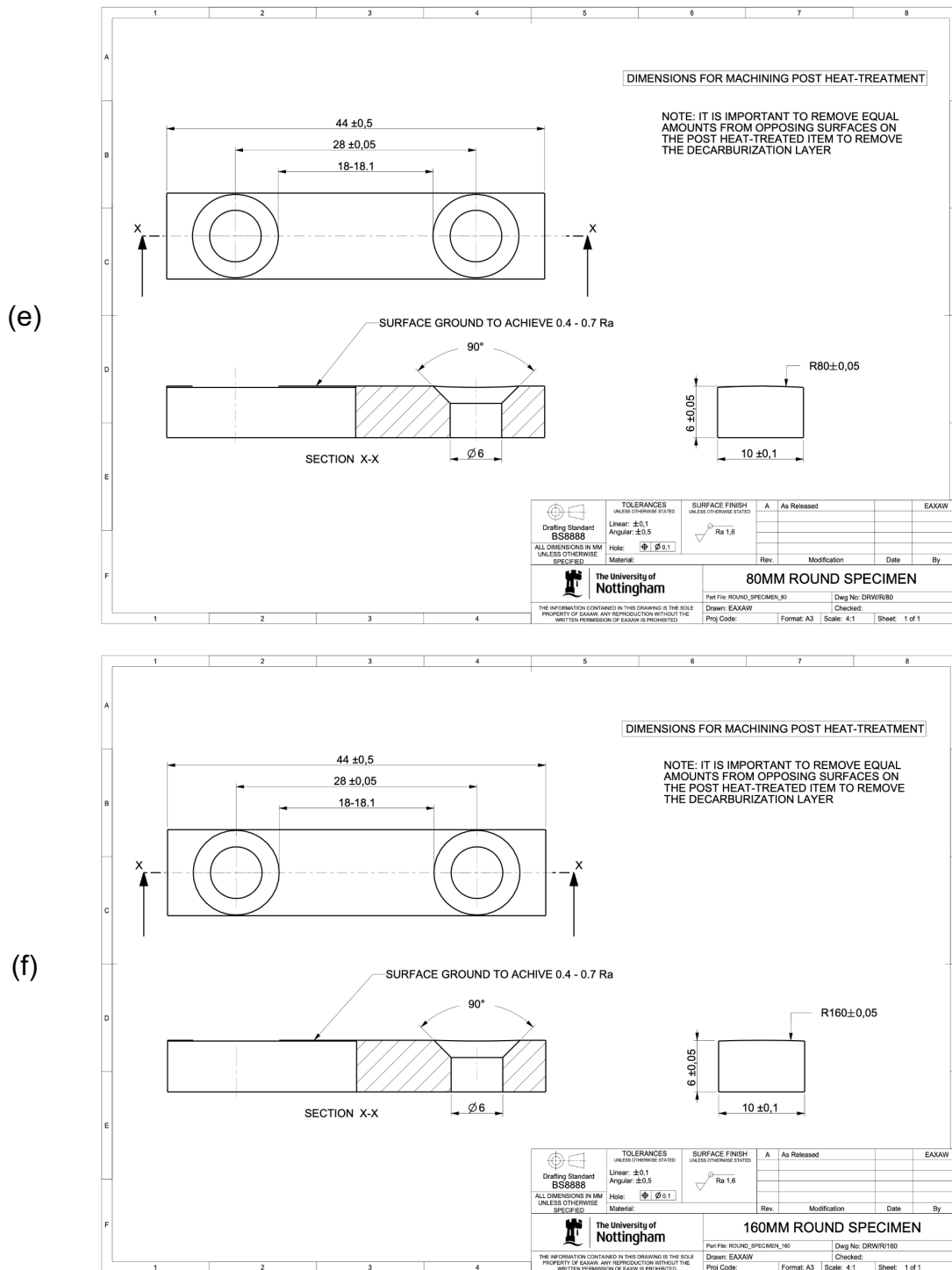


Figure D.1: Detail drawings showing the dimensions of: (a) raw specimen blanks before the heat treatment; (b) flat specimens; (c) R6 cylindrical specimens; (d) R15 cylindrical specimens; (e) R80 cylindrical specimens; (f) R160 cylindrical specimens after the heat treatment and surface finishing.